Engineering and Applied Science Theses & Dissertations

McKelvey School of Engineering

Summer 8-15-2021

Droplet and Particle Dynamics in Aerosol Reactors and Environmental System

Sukrant Dhawan
Washington University in St. Louis

Follow this and additional works at: https://openscholarship.wustl.edu/eng_etds

Part of the Chemical Engineering Commons, and the Environmental Engineering Commons

WASHINGTON UNIVERSITY IN ST. LOUIS

Department of Energy, Environmental & Chemical Engineering
McKelvey School of Engineering

Dissertation Examination Committee:
Pratim Biswas, Chair
Richard Axelbaum
Rajan Chakrabarty
Julio D'Arcy
Jian Wang

Droplet and Particle Dynamics in Aerosol Reactors and Environmental System
by
Sukrant Dhawan

A dissertation presented to
The Graduate School
of Washington University in
partial fulfillment of the
requirements for the degree
of Doctor of Philosophy

August 2021
St. Louis, Missouri

Table of Contents

List of Figures

v

List of Tables

__Acknowledgments__

I would like to express my deepest and most sincere gratitude to Prof. Pratim Biswas, my Ph.D. advisor, for his guidance and support for my scientific research. I cannot thank him enough for giving me the opportunity to join his research group. He provided me freedom to work on diverse topics, which led me to find out my true interest, and his endless support throughout encouraged me to work on the projects I was interested in. I am very grateful for the discussions I had with him regarding research and other challenges that I faced during these five years. I am sure that my entire life will benefit greatly from his guidance. His hard-work and perseverance will continue to serve as an inspiration for excellence for me.

I want to express my gratitude to all my dissertation committee members, Professors Rajan Chakrabarty, Richard Axelbaum, Jian Wang, and Julio D'Arcy for their patient advisory and kind encouragement. I am thankful Prof. Rajan Chakrabarty for his guidance and teaching me the advanced aerosol course, which motivated me to pursue the fundamentals of aerosol science and engineering. I thankful to Prof. Richard Axelbaum for teaching me the advanced concepts of combustion, which proved to be very useful in my research work. I am also thankful to Prof. Julio D'Arcy for providing critical viewpoints on my work on modeling particle synthesis using aerosol vapor polymerization. I also want to thank Prof. Mohan Sankaran and Nabiel Abuyazid for their valuable help and guidance on the plasma projects .

I would also like to thank all the colleagues in the Aerosol & Air Quality Research Laboratory for providing their help and assistance. I want to thank Dr. Yang Wang for fruitful discussions

and for helping me at the beginning of my research journey. I am thankful to Dr. Girish Sharma, Dr. Clayton Kacica, Dr. Ramesh Raliya, Dr. Nathan Reed, Dr. Huang Zhang, Dr. Jiayu Li, Abhay Vidwans, Onochie Okonkwo for helping me with my research, and making my PhD journey very smooth and fun. Especially, I am grateful to Dr. Girish Sharma for his support and assistance with my research, and many other helpful discussions.

I want to thank my funding agency, McDonnell International Scholars Academy for supporting me for my study and research at Washington University in St. Louis for 5 years. Special thanks to James V. Wertsch, Mark S. Wrighton, Kurt T. Dirks, Sarai, Teresa, Laura Benoist, Carla F. Koberna, Angie L. Rahaman, and Kristin L. Williams for their guidance, support, and kindness.

I am very thankful to all my friends in St. Louis, especially Nishit, Piyush, Anushree, Yashika, Sayan, Neha, Shubham, Girish, Priya, Jeff and Rohit, for their support and help, and making my time in St. Louis memorable and fun.

Finally, I do want to express my special gratitude to my parents, Sukhpal and Rajinder Kant, and sister, Ananya Dhawan, for their unconditional support throughout my life.

<div align="right">Sukrant Dhawan</div>

Washington University in St. Louis

August 2021

ABSTRACT OF THE DISSERTATION

Particle and Droplet Dynamics in Aerosol Reactors and Environmental Systems

by

Sukrant Dhawan

Doctor of Philosophy in Energy, Environmental and Chemical Engineering

Washington University in St. Louis, 2021

Professor Pratim Biswas, Chair

Aerosol science and engineering is an enabler for continual advances in nanomaterial synthesis. The spray-based techniques have been used extensively for the large-scale production of nanoparticles. Synthesis of particles with a desired the size and morphology is of key importance for exploiting their properties for their use in several emerging technologies. In contrast to useful nanomaterials, the aerosols from industrial flue gas, dust, indoor cooking, pathogens, and wildfire etc. are harmful to human health. It is important to understand how these harmful aerosols travel through the environment and potentially impact the health. It is also very critical to improve the accuracy of indoor aerosols sampling instruments for accurate assessment of the health impacts of these aerosols. Many potentially harmful indoor aerosols such as viruses (including the SARS-COV-2 virus) and protein fragments lie in the nanometer size ranges, and it is therefore important to improve existing technologies or develop low-cost alternatives that efficiently capture harmful, nanometer-sized aerosols. In order to control the harmful aerosol emissions, and tailor the properties of synthesized aerosols, a thorough understanding of nanoparticle formation and their dynamics in different reactor systems and environments is needed, which is the main focus of my graduate work. My dissertation is divided into three sections.

The first section of my dissertation focuses on understanding the particle formation in the aerosol reactors that employ liquid-to-particle conversion route (spray synthesis). The particles with different morphologies, mainly solid and hollow, are produced using spray drying depending on the process conditions. A model for simultaneous droplet heating, evaporation, and dynamics and transport of solute and particles within the droplet was developed, to investigate the effect of different conditions during spray drying on the dried particle morphology. The drying process was modelled in two separate stages in this work, initial drying stage before shell formation, and the transition stage, in which shell formation was modelled till the solid crust formation takes place. Using this model two cases were analyzed, 1) drying of droplet with dissolved solute, and 2) drying of droplet with suspended solids. Next, the developed droplet drying model was advanced further to understand and predict structure and conductivity of PEDOT (poly(3,4-ethylenedioxythiophene)) nanoparticles synthesized using aerosol vapor polymerization. The model was modified to additionally account for gas phase transport of monomers and polymerization reaction inside the droplet. The effect of different reactor conditions was examined on the average chain length of polymers in synthesized PEDOT nanoparticles as it directly affects their conductivity.

The second section of my dissertation focuses on understanding and accurately assessing the impact of harmful aerosols on human health. Semi-Volatile Organic Compounds (SVOCs) are very common indoor pollutant which are present in every household. These compounds can phase-partition and exists in the air in both gas and particle phase. Diffusion denuders are used to separate gas and particulate SVOCs, and measure both phases separately to accurately access their transport in an indoor environment and their subsequent health risks. However, there are artifacts associated with this sampling method. A theoretical model for simultaneous gas

diffusion and aerosol evaporation in the parallel plate denuder was developed to investigate the effects of denuder sampling artifacts on gas–particle partitioning measurements of SVOCs. The effect of the denuder design parameters and organic species properties, which may influence the evaporation of the particulate phase, was studied on sampling artifacts. The next part of my thesis focuses on understanding the spread of airborne pathogens like SARS CoV-2. A comprehensive model for respiratory emissions of droplets, droplet evaporation, and transport due to diffusion, gravitational settling, and ambient air flow, was developed. The considerations for viral load in droplets and virus decay were accounted for in the model to determine the spatiotemporal concentration of viable virus exhaled by the infected individual. The exposure to viable virus and risk of infection was determined using respiratory deposition curves and dose-response approach. The effect of the different parameters such as viral load, physical separation, ambient air velocity, mask usage etc. was determined on the risk of infection transmission.

The third section of my dissertation focuses on the fundamental understanding of particle charging in a non-thermal plasma reactor, with a vision to incorporate plasma reactors in conjunction with the conventionally used particle capture devices, thereby increasing their efficiency for particle capture. We tested a new design concept for enhancing aerosol nanoparticle charging in plasmas by introducing a DC field downstream of the plasma volume in the spatial afterglow to potentially prevent neutralization of the particles. Premade, charge-neutral nanoparticles were introduced into the plasma reactor with a downstream DC bias and the charge fraction of the particles was examined at the reactor outlet for different particle diameters as the function of reactor operating conditions. The mechanism of particle charging in plasma reactor was proposed based on experimental observation sand characteristic charging time scale calculations.

Chapter 1: Introduction and Overview

1.1   Research Objectives

Aerosols are dispersions of particles, either liquid or solid, in a gas. Aerosols are the synthetic pathway for many useful materials such as carbon black that makes tires durable, or titania that is the base material for essentially all paints manufactured today. The annual production of functional nanoparticles, including silica, titania, and carbon black, is in the millions of tons, valued at over $15 billion/year [1]. The nanomaterials synthesized using aerosol processes have very wide range of applications such as in solar cells, bio-sensing, catalysis, batteries, photocatalysts, drug delivery, cancer treatment etc. [2-8]. The properties of the materials synthesized using aerosol processes, and hence their applications, are size and morphology dependent [9-11]. So, the one of the biggest challenges that aerosol community face is to create complex materials with tailored properties of composition, size and shape [12].

In contrast to useful aerosols, the aerosols from vehicle exhaust, industrial smokestacks, indoor cooking, etc. pollute our environment and are harmful to human health [13-15]. Premature death due to aerosols is a world-wide problem. According to World Health organization, 91% of world population lives in poor air quality, and 7 million people die every year from exposure to polluted air [16]. It is very important to understand the health impact of aerosols. The advancement of the state-of the-art indoor pollutants sampling technologies is essential for accurate assessment of their health impacts. Another major challenge for the aerosol community is to understand the airborne spread of pathogens, to develop efficient prevention and control measures for airborne diseases like the coronavirus disease 2019 (COVID-19) [12].
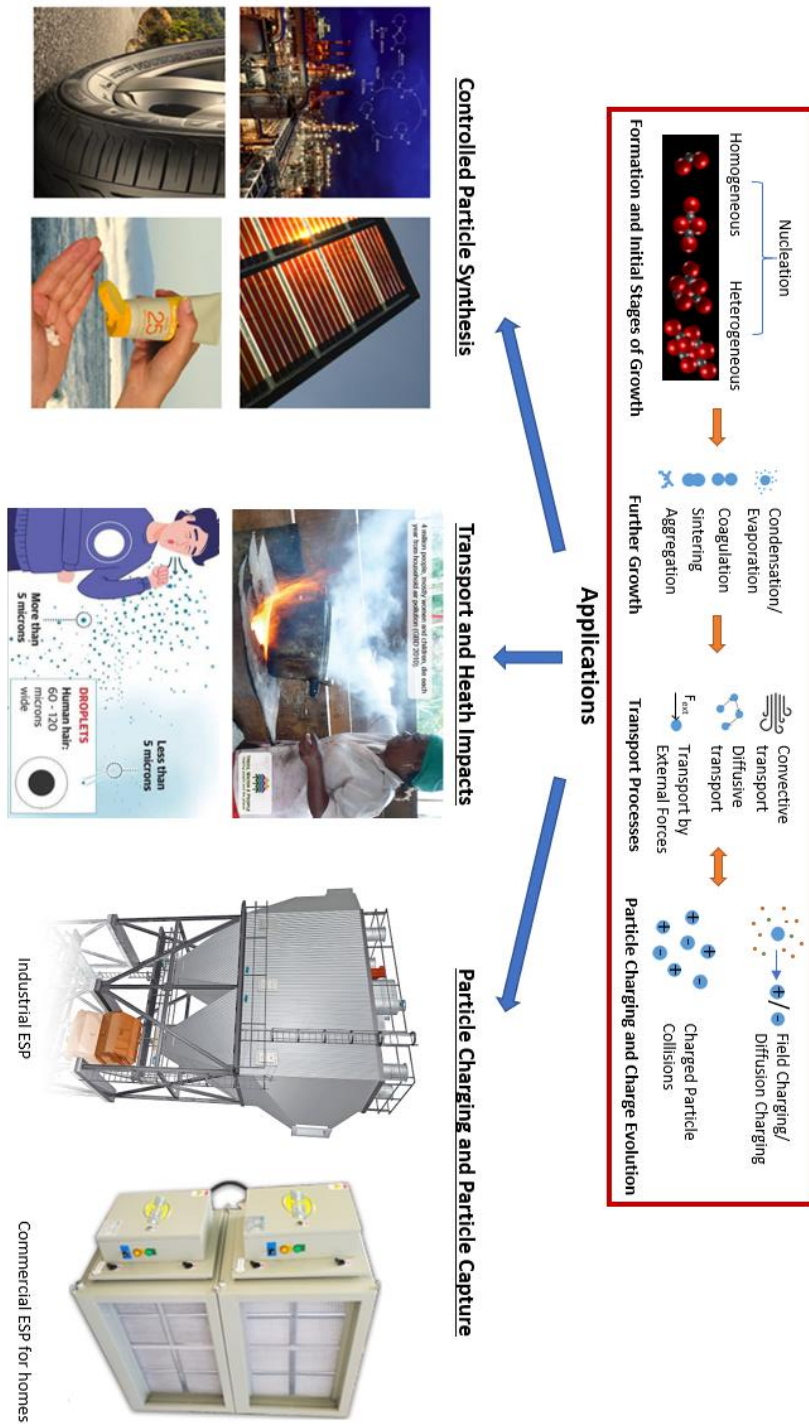
Figure 1-1 Schematic representing application of aerosol formation and growth dynamics for a) controlled synthesis of nanomaterials, b) understanding transport of atmospheric aerosols and transmission of airborne pathogens, and c) understanding particle charging to improve particle capture technologies.

To combat the issue of air pollution, and also improve the collection yield of materials synthesized using aerosol processes, there is a crucial need to improve particle capture technologies. The efficient capture of nanometer sized particles remains a major limitation of particles control technologies like HEPA filters, and Electrostatic precipitators (ESPs) [17,18]. Since many potentially harmful indoor aerosols such as viruses and protein fragments lie in the nanometer size ranges, it is therefore important to improve existing particle capture technologies or develop low-cost alternatives that efficiently capture harmful, nanometer-sized aerosols.

Aerosol science and technology paves the way for the synthesis of variety of composite materials for different applications, assessing the risk as well as, capture of indoor pollutants, thereby combating the problem of air pollution. As can be seen from Figure 1-1, a thorough understanding of aerosol formation, growth dynamics, and their interaction with the surrounding media is needed to understand their complex effects throughout all the areas reviewed above, which is the main focus of my graduate work. My dissertation is divided into three sections to address the above-mentioned challenges.

1.1.1 Controlled Synthesis of Nanoparticles in Aerosol Reactors Using Liquid-to-Particle Synthesis Process

Nanoparticles have been widely applied in areas including solar cells, bio-sensing, batteries, drug delivery, cancer treatment etc. [2-8]. They are very versatile in their applications due to their unique mechanical, thermal, electrical, magnetic, and optical properties which arise from their large specific surface area and from the quantum effects [19]. These properties are largely size dependent and morphology dependent, and the optimum particle size is in the nanoparticle size

range. The synthesis of nanoparticles with a desired the size and morphology of nanoparticles is of key importance for exploiting their properties for their use in several emerging technologies [12].

Recently, aerosol techniques are being used for large-scale commercial production of nanoparticles. The aerosol techniques for nanoparticle synthesis are continuous, one-step process with fast processing time and throughput production. The formation of nanoparticles via aerosol processes can follow one of the two formation routes: i) gas-to-particle conversion route or, ii) liquid-to-particle conversion route (spray synthesis) [20, 21]. In gas-to-particle conversion route, precursor gases react at high temperature to form product molecules. These molecules result quickly in particle formation either by molecular collisions (coagulation-driven process) or by nucleation of subcritical molecular clusters (nucleation-driven process). The particle growth takes place by further coagulation and condensation [20]. Particles made by the gas-to-particle conversion route have relatively narrow particle size distribution and consist of nonporous primary particles. The morphology of the particles depends on the competing mechanism of collision–sintering among the primary nanoparticles. There are several disadvantages of synthesizing particles using gas-to-particle conversion methods. The availability of volatile precursors at reasonable costs limits the number of materials that can be synthesized from gas-to-particle conversion method. The synthesis of multicomponent nanoparticles using this route with precise control over the composition is difficult, due to difference in chemical reaction rate, vapor pressure, nucleation and growth rate of different materials. The production rate and the size of particles generated in gas phase processes depends on the precursor concentration and the

5

residence time. Thus, the volatility of the precursors strongly limits the production rate and the size of the synthesized particles.

In liquid-to-particle conversion route (spray synthesis), solution with the dissolved precursor (solute) is usually sprayed into a carrier gas, forming small droplets [21]. Due to the high temperature of the surrounding gas, the solvent is vaporized, and the solute gets precipitated within the droplets. If the air temperature is high enough, the particles can form by the decomposition of solute. The liquid-to-particle conversion has several advantages over gas phase synthesis of nanoparticles. The ability to produce uniformly spherical particles from nano to micron size with high production rates and tunable morphologies (by controlling the precursor and solvent properties, droplet size, residence time, feed rate, surrounding gas temperature, etc.) is one of the main advantages of this method. The spray synthesis methods can readily utilize low cost and low volatility precursors such as metal nitrates, chlorides and acetates, which makes it possible to economically synthesize very large number of functional particles all across the periodic table. The spray synthesis routes have very high production rates of nanoparticles as compared to gas-to-particle formation route as it not limited by the precursor's volatility. Different synthesis techniques such as spray drying, spray pyrolysis, electrospray, aerosol vapor polymerization, etc. have been used to facilitate the nanoparticle production via droplet-to-particle conversion route. Many of these spray synthesis techniques are easily scalable and have been used in the industries for the large-scale production of functional nanoparticles [22, 23]. The controlled particle synthesis using spray drying technique and aerosol vapor polymerization technique are the focus of this work.

1.1.1 A) Particle Synthesis using Spray Drying/ Spray Pyrolysis

Spray drying has been used in the industries for the large-scale production of useful particles such as drugs, coffee powder, milk powder, detergents, etc. [24-27]. Nanoparticles with different morphologies such as spherical, hollow shell, fragmented etc. have been synthesized via spray routes depending on the properties of precursor, carrier gas flow rate and temperature etc. [21]. Figure 1-2 shows the TEM images of depicting different morphologies Eu doped Y_2O_3 nanoparticles synthesized in spray flame aerosol reactor [28]. It is very important to control the morphology of the synthesized particles, as the morphology affect their properties and hence their application. A precise control over synthesized particle thickness is essential for drug delivery applications to have better control over drug release [29, 30]. The morphology and the shell thickness of the particles also affects their sensitivity as gas sensors [31].
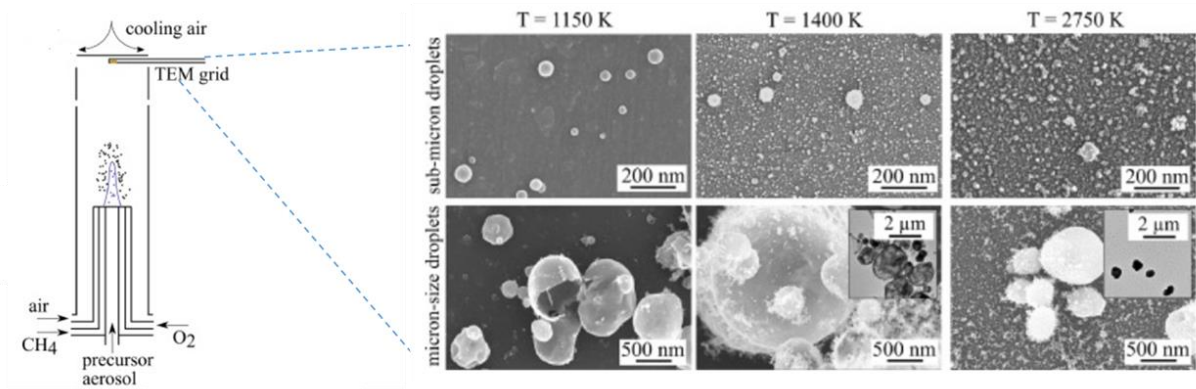
Abrams et al., *Proc. Combust. Inst.*, 2019, 37(1), 1231

Figure 1-2 TEM depicting different morphologies of nanoparticles synthesized using spray pyrolysis depending on operating conditions.

Different complex reaction and transport dynamic processes take place during the synthesis of particles via liquid-to-particle route, resulting in the formation of different morphologies. It is

crucial to understand the different dynamic processes taking place in droplet that influence the morphology of the particle in order to have better and more precise control on morphology of the synthesized particles via spray route. There is a need for a generalized droplet model which can account for all the dynamic processes such as evaporation, diffusion inside droplet, reaction, precipitation, etc. and can accurately predict for when one would form different morphologies for spray synthesis techniques.

Research Gaps: Several single droplets drying studies have been done to observe the particle formation process from the droplet. Most of these experimental procedures involve suspending a droplet using techniques such as optical traps [32], electrodynamic balances [33], acoustic levitation [34], thermal levitation [35], thin filament suspension [36], and droplet chain instruments [37]. Due to limitations such as inability to measure temperature, concentration and pressure profiles within the droplet, experimental studies fail to provide deep insight into complex processes and transport phenomena taking place within droplets. Therefore, the development of an advanced numerical model is essential to understand the effect of experimental conditions on the dried particle morphology in spray pyrolysis.

Earlier model for spray drying technique can explain the drying process and also qualitatively explain the formation of different morphologies, but these models do not account for detailed mechanisms that lead to shell formation and growth and hence do not provide accurate estimates [38-43]. There are just a handful studies that account for shell growth and morphological development inside a droplet during spray drying, but these models do not quantify the morphology in term of shell thickness and its dependance on different material and operating

8

parameters [44-46]. The limitations of both experimental and modeling studies are discussed further in more detail in Chapter 2.

1.1.1 B) Synthesis of poly(3,4-ethylenedioxythiophene) (PEDOT)Nanoparticles using Aerosol Vapor Polymerization

poly(3,4-ethylenedioxythiophene)
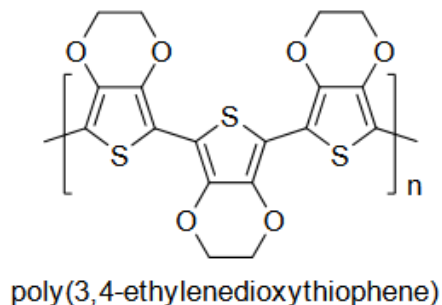
Figure 1-3 Chemical Structure of PEDOT polymer

Conductive polymers are the organic polymers that can conduct electricity [47]. poly(3,4-ethylenedioxythiophene) or PEDOT is one of the most popular conducting polymers because of its high conductivity and stability [48-51]. Most of the conductive polymers have structure similar to that of PEDOT as shown in Figure 1-3. Conductivity is imparted to these polymers through the use of a dopant ion, and the conjugated double bonds along the backbone of an otherwise insulated structure helps with conduction [51]. Although conducting polymers can possess range of conductivity, they are very light weight, and flexible as compared to metals and inorganic semiconductors [47, 51]. Because of these advantages, conducting polymers have become leading material in polymer science. They have been incorporated into commercial displays and batteries and are also promising in organic solar cells, supercapacitors, chemical sensors, organic light-emitting diodes etc. [48-55].

9
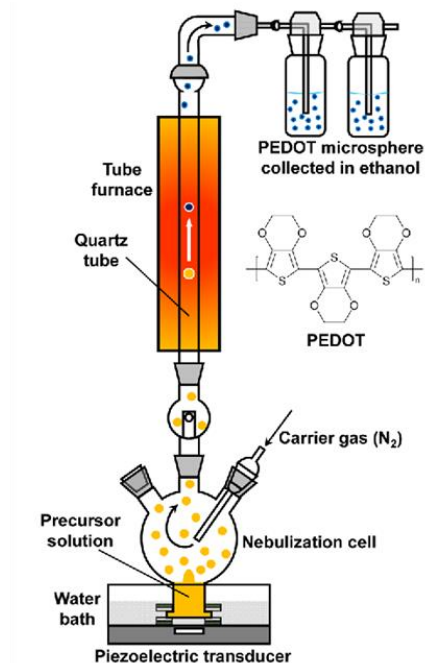
Zhang et al.. *Chem. Mater.* 2018, *27, 7559*

Figure 1-4 Schematic of ultrasonic spray polymerization to synthesize PEDOT nanoparticles.

Several techniques have been utilized to synthesize PEDOT nanoparticles with desired properties. Vapor-phase synthesis techniques have been used to form PEDOT coatings which exhibits a high electronic conductivity [50]. Different techniques that employ the use of both hard and soft templates have been used to synthesize the PEDOT nanostructures [56-58]. The major disadvantage of templates techniques is that removal of the templates is destructive to the polymer structure. Recently Zhang et al. (2018) used ultrasonic spray polymerization to synthesize PEDOT nanoparticles, where they atomized solution that consisted of EDOT monomer, ferric (initiator) and water, and passed the droplet through furnace aerosol reactor [59]. This synthesis method led to polymer particles of low conductivity. That was because, oxidative polymerization takes took in the precursor solution at room temperature, before the atomization and hence there was not very good control over polymerization.
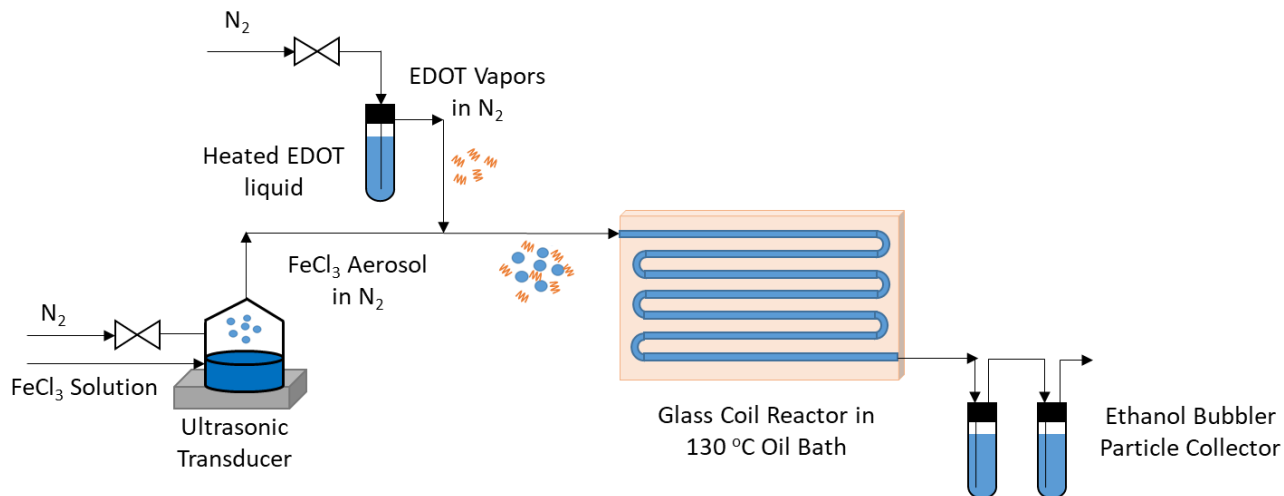
10

Figure 1-5 Schematic of PEDOT nanoparticle synthesis using Aerosol Vapor Polymerization.

A combination of aerosols technique and vapor-phase polymerization (Aerosol Vapor Polymerization or AVP) was used by Lu et al. (2019) to overcome limitations of ultrasonic spray polymerization [51]. The schematic of the setup used in this study is shown in Figure 1-5. An aerosol of oxidant droplets carried by nitrogen gas was generated by nebulizing iron(III) chloride aqueous solution using an ultrasonic transducer. Monomer (3,4-Ethylenedioxythiophene or EDOT) vapor was produced by bubbling nitrogen gas into a heated reservoir containing the liquid EDOT. Synthesis was carried out in a coiled tubular glass reactor at 130 °C under laminar flow conditions. Inside the reactor, droplet consisting of polymerization initiator is surrounded by EDOT vapors. The droplet evaporates and simultaneously EDOT vapors move to the droplet where they polymerize and result in PEDOT nanoparticle formation. These PEDOT nanoparticle were eventually collected in ethanol filled collectors [51].
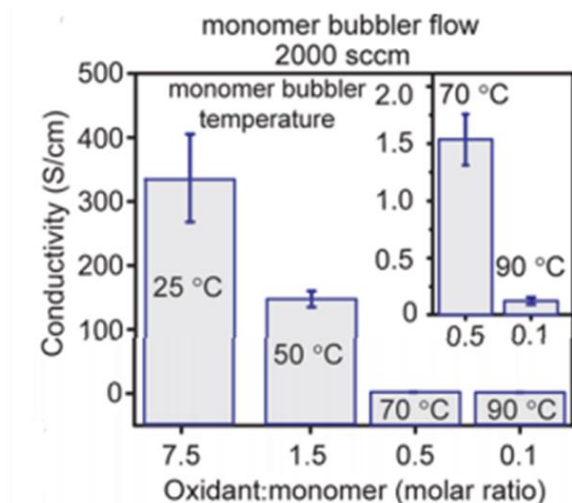
Lu el al. *Appl. Mater. Interfaces.* 2019,11, 47320

Figure 1-6 Conductivity of PEDOT nanoparticles synthesized using Aerosol Vapor Polymerization as the function of Oxidant to Monomer Ratio.

The conductivity of synthesized PEDOT particles was found to be the function of monomer to oxidant ratio in the reactor, as shown in Figure 1-6. It was proposed that the difference in conductivity based on reaction conditions could be attributed to the average conjugation chain length of polymer in the synthesized PEDOT nanoparticle. Different complex reaction and transport dynamic processes take place during the synthesis of PEDOT particles via AVP, resulting in the formation of particles with varying conductivities. It is important to understand complex processes taking place in the reactor during AVP to produce polymer particles with better control over their properties.

Research Gaps: There is a lack of experimental studies, except for the word done by D'Arcy's group [51], that relate the material and operating parameters during AVP to the conductivity of the synthesized PEDOT particles. Due to experimental limitations such as inability to measure temperature and concentration profiles within the droplet and the average conjugation chain

length in the synthesized particles, experimental studies cannot provide very deep insight into complex reactions and transport phenomena taking place inside the reactor and within the droplets. Therefore, the development of numerical model is essential to understand the effect of experimental conditions on the conductivity (average conjugation chain length) of PEDOT particles synthesized using AVP.

There are several single droplet models developed over the years that can explain the droplet drying process and the solute dynamics taking place within the droplets [38-46]. These single droplet models are insufficient to model particle synthesis using AVP process, as these models only consider droplet drying and solute/solid dynamics and transport within the droplets. The transport of EDOT (monomer vapors) from the surrounding gas phase to the droplets' surface, during AVP, cannot be considered using the single droplet models discussed above. Also, there are not any models that account for polymer formation and growth (or polymerization reaction) coupled with dynamics and transport processes taking place in a drying droplet.

1.1.2 Aerosol Transport and Health Impacts

Aerosols omnipresent in indoor air. The poor air quality affects human health in the short and long term, the consequences of this exposure range from insignificant to fatal and depend on the type of aerosols present, type of indoor environment, duration of time spent, age, gender, susceptibility, and many other factors. Due to potential severity of the associated risks, there is a need for good characterization of indoor aerosols. The understanding of the transport of these aerosols in an indoor environment is also essential to quantify their exposure and impact on health. Improving the techniques for sampling and characterization of semivolatile organic

13

compounds (SVOCs), which are common indoor pollutants; and developing the understanding of transport and exposure to bio-aerosols in an indoor environment, are the focus of this work.

1.1.2 A) Sampling Semi-Volatile Organic Compounds using Denuders for Phase-Partitioning Measurements

Semi-Volatile Organic Compounds (SVOCs) are very common indoor pollutants which are present in every household and are generated via plasticizers, pesticides, cooking, combustion products, etc. [60]. The SVOCs exists in the atmosphere in both the gas and particle phase, which are in equilibrium according to the nature of the aerosol and the ambient temperature [61-63]. The SVOCs include compounds such as polychlorinated biphenyls (PCBs), pesticides, phthalates, and polycyclic aromatic hydrocarbons (PAHs), which have been linked to serious adverse health effects [62]. The phase partitioning of SVOCs affects their transport properties, deposition rates, and the pathways by which humans are exposed to them [63, 64]. The exposure to SVOC aerosols can lead to an increase in diseases like alveolitis, asthma, cancer and can have serious detrimental effect on the reproductive, nervous, and endocrine systems [65]. The gas-phase SVOCs can be absorbed by the respiratory tract depending on their solubility in bodily fluids, whereas the particle phase can be deposited in different regions of the lung depending on their aerodynamic size. Therefore, it is important to distinguish and quantify gas- and particle-phase SVOCs to accurately access their health risks.

Therefore, while sampling SVOCs, both the phases are first separated and then analyzed. These measurements in general are typically done filter-based samplers or denuder-based samplers. are typically done using filter–sorbent-based samplers. Quartz filters are typically used for collection of particles. The gas phase passes through the filter and is subsequently adsorbed on adsorbent

material which is typically polyurethane foam or XAD resin. However, adsorption of gaseous organics could also occur on the filter, leading to overestimation of the particulate phase. Also, particles collected on the filter can volatilize leading to the underestimation of the particulate phase [66]. Thus, there is uncertainty associated with this sampling method.

In the recent studies, diffusion denuders have been employed for sampling atmospheric gases and aerosols. The walls of the denuder are internally coated with a specific reagent such as activated carbon and/or polystyrene–divinylbenzene resin that selectively adsorbs or reacts with the gas flowing through it. The denuders are designed in such a way that the gases in the sample air stream are removed almost completely by adsorption at the walls, whereas particles pass through without any significant loss due to slower diffusion rates to the wall as compared to the gas phase species. This behavior allows the separation of the gas and the particulate phase. Therefore, the denuder is placed upstream of the quartz filter to remove the gases, eliminating the potential sampling artifacts due to gases absorbing on the filter. Some of the other advantages of using denuders are that they allow high sampling velocities and have a large sampling capacity as compared to the filter–sorbent samplers. Although the use of denuder overcomes many of the measurement artifacts in the filtration device, measurement biases or artifacts are still possible and may be significant in denuder sampling. The removal of gas phase in the denuder distorts the gas-particle equilibrium and leads to dissociation of the particulate phase. This phenomenon is particularly true for volatile organic species and lead to significant error in determining gas-to-particle phase partitioning of organic aerosols due to underestimation of the particle phase.

Research Gaps: Several studies have been carried out to understand the artifacts caused by decomposition of inorganic aerosols in diffusion denuders. These studies evaluate sampling artifacts by modeling gas diffusion and decomposition of monodisperse inorganic aerosol inside a denuder. However, in all of the above studies, the analysis was done for single species inorganic aerosols. There are not many studies that have examined the measurement artifacts arising from the evaporative loss of semi-volatile organic aerosols in the diffusion denuder. There are several challenges associated with modeling semi-volatile organic aerosols as these aerosols exist in the atmosphere as a mixture of thousands of species. For a realistic simulation, all of the compounds that are present in the aerosol need to be considered and it is impractical to incorporate separate equations for thousands of these compounds.

1.1.2 B) Understanding Airborne Transmission of Infectious Pathogens

Airborne diseases are bacteria or viruses that are most commonly transmitted through small respiratory droplets. These droplets are expelled when someone with the airborne disease sneezes, coughs, or even speaks [67]. These infectious droplets can travel along air currents, deposit to nearby surfaces, or linger in the air where they are eventually inhaled by someone else. Few diseases such as measles, tuberculosis, influenza, coronavirus disease (2019) etc. are predominantly airborne [68]. COVID-19 outbreak created a global public health emergency [69]. With the recent COVID-19 pandemic, people have become more conscious about the air they breathe and the surfaces they touch. Initially, airborne transmission was disregarded as the primary modes of spread of infection. Extensive measures were implemented to reduce the direct and indirect transmission, but the rapid spread of SARS-CoV-2 despite these measures suggested the airborne transmission as the dominant transmission pathway. Several research studies support

the transmission of SARS-CoV-2 virus through the air [70, 71]. The World Health Organization (WHO) prescribed using masks or maintaining a physical distance of 6 ft (1.8 m) from each other to minimize the risk of infection from airborne transmission. The recommendation of 6 ft distancing is based on outdated studies, and several recently published studies support the hypothesis of virus transmission well over a distance of 1.8 m from an infected person [72]. An enhanced understanding of pathogen transmission via aerosolized sputum and saliva droplets is vital to develop effective public health measures aiming at reducing the infection risks from airborne diseases.

Research Gaps: There are many CFD based modeling studies conducted on the airborne spread of viruses causing diseases such as SARS and measles [73-75]. These models for the droplet transport are based on aerosol dynamics and do not account for the initial viral load in the droplets and the virus viability and hence fail to give any quantitative information regarding the risk of transmission. Several studies have used a dose−response approach to assess the risk of infection from airborne viruses [76-78]. However, in all of these studies, a key assumption in the model is that it considers the air to be well-mixed within the modeled space, but in reality, exhaled particles travel in a plume, and their transport depends on the initial velocity during exhalation and the background air motion. It is essential to develop a comprehensive model which combines virology and aerosol science and can accurately estimate the probability of transmission of the airborne diseases.

1.1.3 Particle Charging and Particle Capture
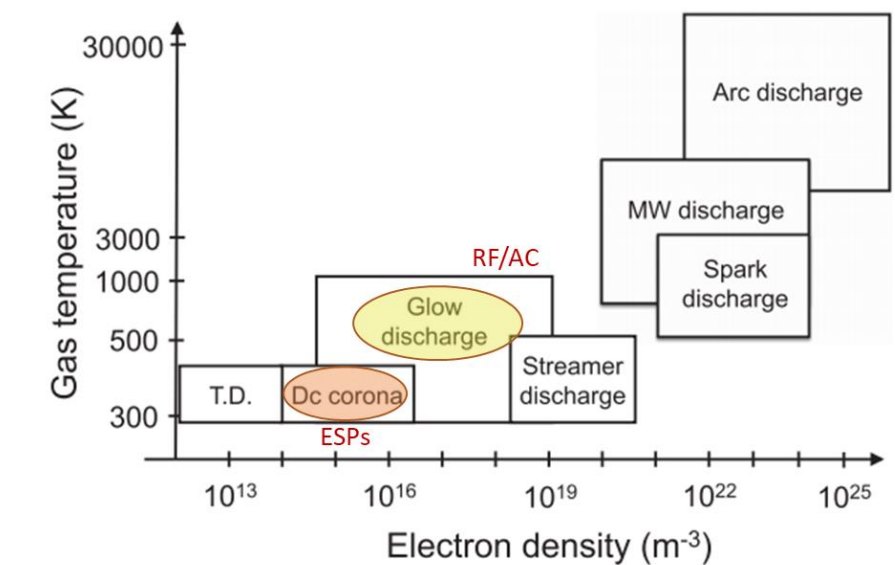
Bruggeman, *Plasma Sources Sci. Technol. 2017,* 26 (12) 123002

Figure 1-7 Different types of plasmas based on gas temperature, and electron density.

Several aerosol devices are developed to get rid of harmful nanoparticles from a gas stream, to address the problem of polluted air. Electrostatic Precipitators (ESP) have been widely employed in hospitals, coal power plants etc. to capture fine aerosol particles. An ESP uses a corona discharge for charging the particles, which are then captured with the DC electric field [17]. The efficiency of an ESP depends on its ability to charge particles, and the charging and thus removal of smaller sized particles (sub 200 nm), has been a challenge in corona-based devices [17]. Coronas are a type of gas discharge formed by partial breakdown of gas under high electric field, with ion concentration of the order of 10^{14}-10^{16} #/m^3, whereas the ion concentration in atmospheric pressure glow discharge plasmas is usually 2-3 orders of magnitude higher than that in corona discharges, as shown in Figure 1-7 [79]. Also, it is very easy to integrate

radiofrequency (RF) and alternating current (AC) powered atmospheric pressure flow-through versions of these plasmas with existing particle control systems such as ESPs. So, these plasmas have potential to be better than DC corona for particle capture.

Research Gaps: There are few studies that report particle charging in low pressure plasmas and even fewer studies exist on atmospheric pressure glow discharges for particle charging and particle control applications. Particle charge distribution in complex plasma afterglow have been studied widely, but only for low pressure plasmas [80-82]. The particle charge measurement setup in these studies consisted of laser and video cameras for the observation of the particle oscillation in the plasma afterglow. Therefore, only larger micro-meter sized particles, which can be observed using cameras, were the focus of these studies. Chen et al (2018 and 2020) measured particles at the outlet of low-pressure RF plasma which they measured using low pressure particle mobility sizers [83, 84]. This study reported the presence of the presence of bipolarly charged nanoparticles, but the detailed charging characteristics were not reported.

Sharma et al., *J. Phys. D.* 2020, 53(24) 254204
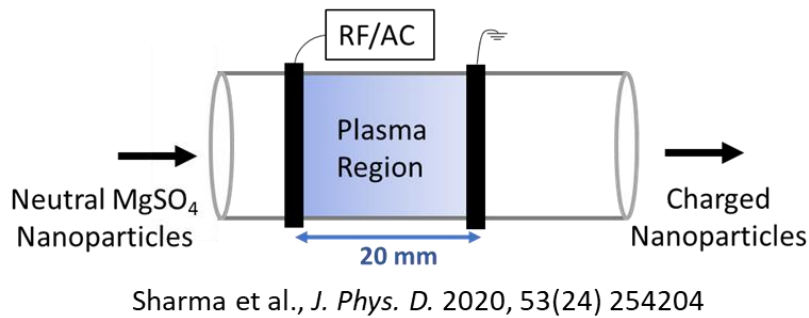
Figure 1-8 Schematic of RF/AC powered flow-through, atmospheric pressure plasma reactor.

Power Source | Electron flux to surface dominates | Electrons lost to walls quickly due to high mobility

Flux to Surface

Photoelectric Emission

Thermo-ionization

Thermal Radiation

Neutral Particles

Ion Flux to Surface

Bipolarly Charged Particles

● Particle
+ Ar⁺ ion
• Electron

Stage 1: Charging in Plasma Region

Stage 2: Discharging in Plasma Downstream

$\tau_{1,RF} < \tau_{1,AC} < t_{residence}$

$\tau_{2,RF} \sim t_{residence} < \tau_{2,AC}$

Sharma et al., *J. Phys. D.* 2020, 53(24) 254204

Figure 1-9 Two- stage mechanism for particle charging inside and outside the plasma volume.

Recently, our group systematically characterized particle charging in AC- and RF-powered flow-through, atmospheric-pressure, plasma systems [85]. Premade, charge-neutral nanoparticles are introduced into the plasma as shown in Figure 1-8. The charge fraction and distribution of the particles are examined at the reactor outlet for different mobility diameters (10-250 nm) as a function of plasma power. High charging efficiencies (>90%) were found for particles larger than 100 nm. However, the charging efficiency of particles smaller than 100 nm was low, with a charging efficiency of less than 40% for 20 nm sized particles and 0% for particles of size 10 nm. The charge distribution of particles exiting the plasma reactor was revealed to be bipolar with particles supporting multiple charges. A two-stage charging mechanism based on a characteristic time scale analysis, as shown in Figure 1-9, suggested that while particles were predominantly charged negatively in the plasma volume, the relatively faster rate of loss of the electrons in the spatial afterglow (downstream of the plasma region) resulted in neutralization by positive ions, and even subsequent positive charging of some of the particles [85]. Thus, the

decrease in particle charging efficiency due to neutralization in spatial afterglow region in the plasma reactor was the major limitation this work.

1.2 Research Objectives
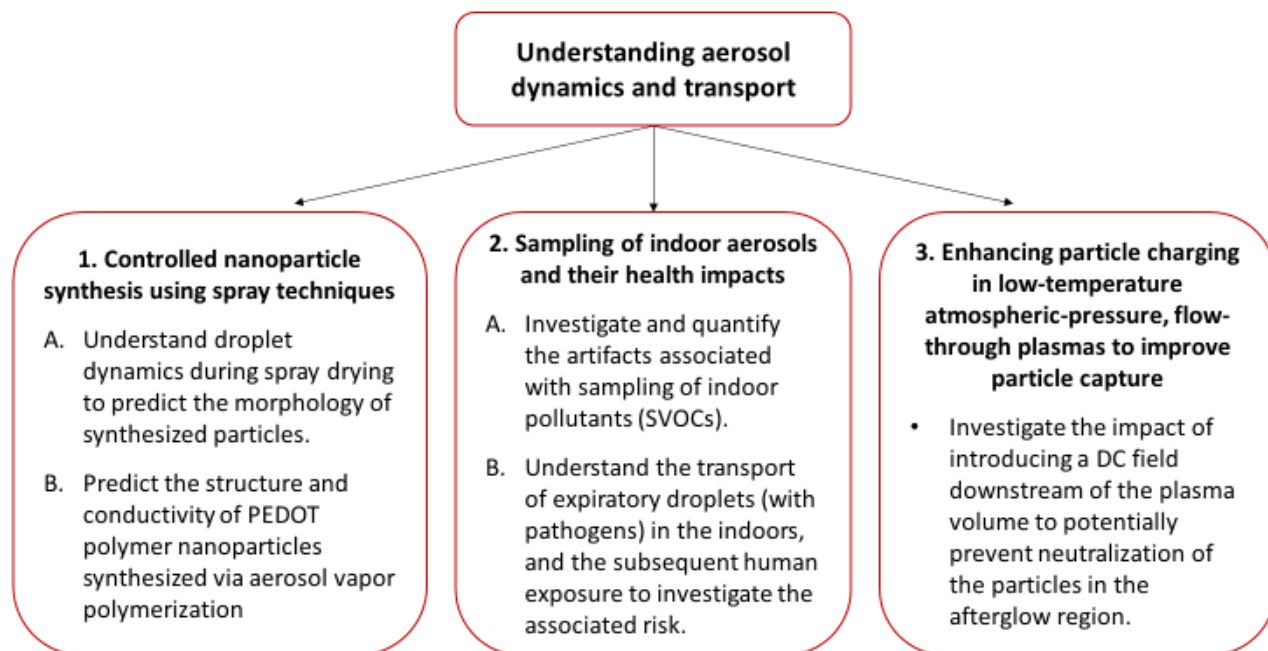
Figure 1-10 Flowchart representing the summary of the research objectives.

A thorough understanding of aerosol science, especially aerosol formation, growth dynamics, and their interaction with the surrounding media, was applied to address the scientific gaps throughout all the areas reviewed in Section 1.1. This dissertation has three main objectives:

Objective 1: The first objective was to develop an understanding of droplet and particle dynamics in aerosol reactors, for controlled synthesis of nanomaterials using spray techniques. This objective is divided into two sub-objectives:

1A) To predict the morphology of particles synthesized via spray drying depending on material and process parameters.

- A model for simultaneous droplet heating, evaporation, and dynamics and transport of solute and particles within the droplet was developed, to investigate the effect of different conditions during spray pyrolysis on the dried particle morphology. Using this model two cases were analyzed, 1) drying of droplet with dissolved solute, and 2) drying of droplet with suspended solids. The developed model could help to choose efficient operating conditions during spray pyrolysis to produce particles of desired properties.

1B) To predict the structure and conductivity of PEDOT polymer nanoparticles synthesized via aerosol vapor polymerization as the function of material and process parameters.

- A model for simultaneous monomer transport in gas phase to droplets, droplet heating, evaporation, and dynamics, transport and reaction of monomers and polymers within the droplet, was developed to investigate the effect of different conditions during AVP on the synthesized particle structure (average chain length or conductivity).

Objective 2: The second objective of my thesis was to investigate the artifacts associated with sampling and characterization of indoor pollutants (SVOCs), and to understand the transport of bio-aerosols in the indoor environment and the subsequent human exposure to evaluate the associated risk. This objective is divided into two sub-objectives:

2A) To estimate the sampling artifacts in denuders during phase partitioning measurements of semi-volatile organic compounds.

- A theoretical multi-component model for simultaneous gas diffusion and aerosol evaporation in the parallel plate denuder was developed to investigate the effects of denuder sampling artifacts on gas–particle partitioning measurements of SVOCs. The effect of the denuder design parameters and organic species properties, which may influence the evaporation of the particulate phase, was studied on sampling artifacts.

2B) To estimate the risk from airborne transmission and inhalation of pathogen laden expiratory droplets.

- A model, based on aerosol dynamics of the droplets combined with the respiratory deposition and a dose−response model, was developed to accurately evaluate the risk of airborne transmission. The risk of infection was evaluated as a function of different parameters such as viral load, infectivity factor, emission sources, physical separation, exposure time, ambient air velocity, and mask usage.

Objective 3: The third objective of my thesis was to enhance the particle charging in low-temperature atmospheric-pressure, flow-through plasmas, by introducing DC bias in the plasma afterglow region to mitigate the neutralization.

- A new design concept for enhancing aerosol nanoparticle charging in plasmas, was tested in this work, by introducing a DC field downstream of the plasma volume in the spatial afterglow to potentially prevent neutralization of the particles. Premade, charge-neutral nanoparticles were introduced into the plasma reactor with a downstream DC bias, and

the charge fraction of the particles was examined at the reactor outlet for different particle diameters as the function of applied DC voltage.

An understanding of aerosol dynamics, transport, and their interaction with the surrounding media, was applied to the accomplish my thesis objectives. The research objectives of my thesis are summarized in Figure 1-10.

1.3   Dissertation Outline

The three objectives of my thesis are studied and described in the 6 chapters of the dissertation. Each chapter is self-contained, with and introduction, methodology, results, discussion, and conclusions section. Chapter 2 and Chapter 3 describe the systematic studies to predict final particle structure, size and morphology as the function of different reaction parameters for the particles synthesized using spray drying and aerosol vapor polymerization, respectively. Chapter 4 describes numerical investigation of the artifacts during sampling of semi-volatile organic compounds using diffusion denuders, aiming to obtain a comprehensive criterion for denuder design and operating conditions to minimize the artifacts. Chapter 5 describes in detail the comprehensive approach for estimating the risk from airborne transmission and inhalation of expiratory droplets of SARS-CoV-2 by combining aerosol dynamics with respiratory deposition and dose-response approach. Chapter 6 investigates the application of a low temperature, atmospheric pressure RF plasma with DC bias in the afterglow region, as a device for particle charging and capture. Chapter 7 lists the conclusions and the future work that can be done to gain better understanding of existing systems and enable new work.

Appendix A lists the detailed derivation for the multi-modal model. Appendix B and Appendix C provide supplementary information for Chapter 5 and Chapter 6, respectively. Appendix D includes the computational codes used in this thesis. Appendix E includes my curriculum vitae and Appendix F includes my transcript.

1.4   References

1. Li, S., Ren, Y., Biswas, P., & Stephen, D. T. (2016). Flame aerosol synthesis of nanostructured materials and functional devices: Processing, modeling, and diagnostics. *Progress in Energy and Combustion Science*, *55*, 1-59.

2. Huisman, C. L., Goossens, A., & Schoonman, J. (2003). Aerosol synthesis of anatase titanium dioxide nanoparticles for hybrid solar cells. *Chemistry of materials*, *15*(24), 4617-4624.

3. Loiseau, A., Asila, V., Boitel-Aullen, G., Lam, M., Salmain, M., & Boujday, S. (2019). Silver-based plasmonic nanoparticles for and their use in biosensing. *Biosensors*, *9*(2), 78.

4. Strobel, R., Baiker, A., & Pratsinis, S. E. (2006). Aerosol flame synthesis of catalysts. *Advanced Powder Technology*, *17*(5), 457-480.

5. Sung, J. C., Pulliam, B. L., & Edwards, D. A. (2007). Nanoparticles for drug delivery to the lungs. *Trends in biotechnology*, *25*(12), 563-570.

6. Wen, Y., Zhu, Y., Langrock, A., Manivannan, A., Ehrman, S. H., & Wang, C. (2013). Graphene-bonded and-encapsulated Si nanoparticles for lithium ion battery anodes. *Small*, *9*(16), 2810-2816.

7. Teoh, W. Y. (2013). A perspective on the flame spray synthesis of photocatalyst nanoparticles. *Materials*, *6*(8), 3194-3212.

8. Lee, W. H., Loo, C. Y., Traini, D., & Young, P. M. (2015). Inhalation of nanoparticle-based drug for lung cancer treatment: advantages and challenges. *Asian Journal of Pharmaceutical Sciences*, *10*(6), 481-489.

9. Tsapis, N., Bennett, D., Jackson, B., Weitz, D. A., & Edwards, D. A. (2002). Trojan particles: large porous carriers of nanoparticles for drug delivery. *Proceedings of the National Academy of Sciences*, *99*(19), 12001-12005.

10. Li, Z., Fredin, L. A., Tewari, P., DiBenedetto, S. A., Lanagan, M. T., Ratner, M. A., & Marks, T. J. (2010). In situ catalytic encapsulation of core-shell nanoparticles having variable shell thickness: dielectric and energy storage properties of high-permittivity metal oxide nanocomposites. *Chemistry of Materials*, *22*(18), 5154-5164.

11. Khanchandani, S., Kundu, S., Patra, A., & Ganguli, A. K. (2012). Shell thickness dependent photocatalytic properties of ZnO/CdS core–shell nanorods. *The Journal of Physical Chemistry C*, *116*(44), 23653-23662.

12. Sorensen, C. M., Flagan, R. C., Baltensperger, U., & Pui, D. Y. (2019). Grand challenges for aerosol science and technology. *Aerosol Science and Technology*, *53*(7), 731-734.

13. Tie, X., & Cao, J. (2009). Aerosol pollution in China: Present and future impact on environment. *Particuology*, *7*(6), 426-431.

14. Burger, H. (1990). Bioaerosols: prevalence and health effects in the indoor environment. *Journal of Allergy and Clinical Immunology*, *86*(5), 687-701.

15. Hussein, T., Korhonen, H., Herrmann, E., Hämeri, K., Lehtinen, K. E., & Kulmala, M. (2005). Emission rates due to indoor activities: indoor aerosol model development, evaluation, and applications. *Aerosol Science and Technology*, *39*(11), 1111-1127.

16. World Health Organization. (2016). Ambient air pollution: A global assessment of exposure and burden of disease.

17. Zhuang, Y., Kim, Y. J., Lee, T. G., & Biswas, P. (2000). Experimental and theoretical studies of ultra-fine particle behavior in electrostatic precipitators. *Journal of electrostatics*, *48*(3-4), 245-260.

18. Gupta, A., Novick, V. J., Biswas, P., & Monson, P. R. (1993). Effect of humidity and particle hygroscopicity on the mass loading capacity of high efficiency particulate air (HEPA) filters. *Aerosol Science and Technology*, *19*(1), 94-107.

19. Volokitin, Y., Sinzig, J. D., De Jongh, L. J., Schmid, G., Vargaftik, M. N., & Moiseevi, I. I. (1996). Quantum-size effects in the thermodynamic properties of metallic nanoparticles. *Nature*, *384*(6610), 621-623.

20. Swihart, M. T. (2003). Vapor-phase synthesis of nanoparticles. *Current opinion in colloid & interface science*, *8*(1), 127-133.

21. Okuyama, K., & Lenggoro, I. W. (2003). Preparation of nanoparticles via spray route. *Chemical engineering science*, *58*(3-6), 537-547.

22. Gharsallaoui, A., Roudaut, G., Chambin, O., Voilley, A., & Saurel, R. (2007). Applications of spray-drying in microencapsulation of food ingredients: An overview. *Food research international*, *40*(9), 1107-1121.

23. Wegner, K., Schimmoeller, B., Thiebaut, B., Fernandez, C., & Rao, T. N. (2011). Pilot plants for industrial nanoparticle production by flame spray pyrolysis. *KONA Powder and Particle Journal*, *29*, 251-265.

24. Broadhead, J., Edmond Rouan, S. K., & Rhodes, C. T. (1992). The spray drying of pharmaceuticals. *Drug development and industrial pharmacy*, *18*(11-12), 1169-1206.

25. Frascareli, E. C., Silva, V. M., Tonon, R. V., & Hubinger, M. D. (2012). Effect of process conditions on the microencapsulation of coffee oil by spray drying. *Food and bioproducts processing*, *90*(3), 413-424.

26. Kim, E. H. J., Chen, X. D., & Pearce, D. (2009). Surface composition of industrial spray-dried milk powders. 2. Effects of spray drying conditions on the surface composition. *Journal of Food Engineering*, *94*(2), 169-181.

27. Ali, M., Mahmud, T., Heggs, P. J., Ghadiri, M., Bayly, A., Ahmadian, H., & Martin de Juan, L. (2017). CFD modeling of a pilot-scale countercurrent spray drying tower for the manufacture of detergent powder. *Drying Technology*, *35*(3), 281-299.

28. Abram, C., Mezhericher, M., Beyrau, F., Stone, H. A., & Ju, Y. (2019). Flame synthesis of nanophosphors using sub-micron aerosols. *Proceedings of the Combustion Institute*, *37*(1), 1231-1239.

29. Chang, M. W., Stride, E., & Edirisinghe, M. (2010). Controlling the thickness of hollow polymeric microspheres prepared by electrohydrodynamic atomization. *Journal of the Royal Society Interface*, *7*(suppl_4), S451-S460.

30. Kho, K., & Hadinoto, K. (2010). Aqueous re-dispersibility characterization of spray-dried hollow spherical silica nano-aggregates. *Powder Technology*, *198*(3), 354-363.

31. Jeong, H. M., Kim, J. H., Jeong, S. Y., Kwak, C. H., & Lee, J. H. (2016). Co_3O_4–SnO_2 hollow heteronanostructures: facile control of gas selectivity by compositional tuning of sensing materials via galvanic replacement. *ACS applied materials & interfaces*, *8*(12), 7877-7883.

32. Ashkin, A., & Dziedzic, J. M. (1975). Optical levitation of liquid drops by radiation pressure. *Science*, *187*(4181), 1073-1075.

33. Chan, C. K., Flagan, R. C., & Seinfeld, J. H. (1998). In situ study of single aqueous droplet solidification of ceramic precursors used for spray pyrolysis. *Journal of the American Ceramic Society*, *81*(3), 646-648.

34. Schiffter, H., & Lee, G. (2007). Single-droplet evaporation kinetics and particle formation in an acoustic levitator. Part 1: Evaporation of water microdroplets assessed using boundary-layer and acoustic levitation theories. *Journal of pharmaceutical sciences*, *96*(9), 2274-2283

35. Tsapis, N., Dufresne, E. R., Sinha, S. S., Riera, C. S., Hutchinson, J. W., Mahadevan, L., & Weitz, D. A. (2005). Onset of buckling in drying droplets of colloidal suspensions. *Physical review letters*, *94*(1), 018302.

36. Lin, J. C., & Gentry, J. W. (2003). Spray drying drop morphology: experimental study. *Aerosol Science & Technology*, *37*(1), 15-32.

37. Baldelli, A., Power, R. M., Miles, R. E., Reid, J. P., & Vehring, R. (2016). Effect of crystallization kinetics on the properties of spray dried microparticles. *Aerosol Science and Technology*, *50*(7), 693-704.

38. Brenn, G., Wiedemann, T., Rensink, D., Kastner, O., & Yarin, A. L. (2001). Modeling and experimental investigation of the morphology of spray dryed particles. *Chemical engineering & technology*, *24*(11), 1113-1116.

39. Messing, G. L., Zhang, S. C., & Jayanthi, G. V. (1993). Ceramic powder synthesis by spray pyrolysis. *Journal of the American Ceramic Society*, *76*(11), 2707-2726.

40. Jayanthi, G.V.; Zhang, S.C; Messing, G.L. Modeling of solid particle formation during solution aerosol thermolysis: The evaporation stage. *Aerosol Sci. Technol.*, **1993,** *19*(4), 478-490.

41. Zhang, S. C., Messing, G. L., Lee, S. Y., & Santoro, R. J. (1994). Formation of solid and hollow spherical particles by spray pyrolysis. *MRS Online Proceedings Library (OPL)*, *372*.

42. Ozturk, A., & Cetegen, B. M. (2005). Experiments on ceramic formation from liquid precursor spray axially injected into an oxy-acetylene flame. *Acta materialia*, *53*(19), 5203-5211.

43. Basu, S., Jordan, E. H., & Cetegen, B. M. (2008). Fluid mechanics and heat transfer of liquid precursor droplets injected into high-temperature plasmas. *Journal of Thermal Spray Technology*, *17*(1), 60-72.

44. Mezhericher, M., Levy, A., & Borde, I. (2011). Modelling the morphological evolution of nanosuspension droplet in constant-rate drying stage. *Chemical Engineering Science*, *66*(5), 884-896.

45. Maurice, U., Mezhericher, M., Levy, A., & Borde, I. (2013). Drying of droplet containing insoluble nanoscale particles: Numerical simulations and parametric study. *Drying Technology*, *31*(15), 1790-1807.

46. Handscomb, C. S., & Kraft, M. (2010). Simulating the structural evolution of droplets following shell formation. *Chemical Engineering Science*, *65*(2), 713-725.

47. Janata, J., & Josowicz, M. (2003). Conducting polymers in electronic chemical sensors. *Nature materials*, *2*(1), 19-24.

48. Dupont, S. R., Novoa, F., Voroshazi, E., & Dauskardt, R. H. (2014). Decohesion kinetics of PEDOT: PSS conducting polymer films. *Advanced functional materials*, *24*(9), 1325-1332.

49. Diao, Y., Lu, Y., Yang, H., Wang, H., Chen, H., & D'Arcy, J. M. (2020). Direct Conversion of Fe2O3 to 3D Nanofibrillar PEDOT Microsupercapacitors. *Advanced Functional Materials*, *30*(32), 2003394.

50. Wang, H., Diao, Y., Lu, Y., Yang, H., Zhou, Q., Chrulski, K., & D'Arcy, J. M. (2020). Energy storing bricks for stationary PEDOT supercapacitors. *Nature communications*, *11*(1), 1-9.

51. Lu, Y., Kacica, C., Bansal, S., Santino, L. M., Acharya, S., Hu, J., Izima, C., Chrulski, K., Diao, Y., Wang, H. & D'Arcy, J. M. (2019). Synthesis of Submicron PEDOT Particles of High Electrical Conductivity via Continuous Aerosol Vapor Polymerization. *ACS applied materials & interfaces*, *11*(50), 47320-47329.

52. Das, P. R., Komsiyska, L., Osters, O., & Wittstock, G. (2015). PEDOT: PSS as a functional binder for cathodes in lithium ion batteries. *Journal of The Electrochemical Society*, *162*(4), A674.

53. Kawahara, J., Ersman, P. A., Engquist, I., & Berggren, M. (2012). Improving the color switch contrast in PEDOT: PSS-based electrochromic displays. *Organic electronics*, *13*(3), 469-474.

54. Kim, Y., Ballantyne, A. M., Nelson, J., & Bradley, D. D. (2009). Effects of thickness and thermal annealing of the PEDOT: PSS layer on the performance of polymer solar cells. *Organic Electronics*, *10*(1), 205-209.

55. Sakamoto, S., Okumura, M., Zhao, Z., & Furukawa, Y. (2005). Raman spectral changes of PEDOT–PSS in polymer light-emitting diodes upon operation. *Chemical physics letters*, *412*(4-6), 395-398.

56. Zhang, Z., Chen, G., Wang, H., & Li, X. (2015). Template-directed in situ polymerization preparation of nanocomposites of PEDOT: PSS-coated multi-walled carbon nanotubes with enhanced thermoelectric property. *Chemistry–An Asian Journal*, *10*(1), 149-153.

57. Liang, L., Fan, J., Wang, M., Chen, G., & Sun, G. (2020). Ternary thermoelectric composites of polypyrrole/PEDOT: PSS/carbon nanotube with unique layered structure prepared by one-dimensional polymer nanostructure as template. *Composites Science and Technology*, *187*, 107948.

58. Somboonsub, B., Srisuwan, S., Invernale, M. A., Thongyai, S., Praserthdam, P., Scola, D. A., & Sotzing, G. A. (2010). Comparison of the thermally stable conducting polymers PEDOT, PANi, and PPy using sulfonated poly (imide) templates. *Polymer*, *51*(20), 4472-4476.

59. Zhang, Y., & Suslick, K. S. (2015). Synthesis of poly (3, 4-ethylenedioxythiophene) microspheres by ultrasonic spray polymerization (USPo). *Chemistry of Materials*, *27*(22), 7559-7563.

60. Wang, L., Zhao, B., Liu, C., Lin, H., Yang, X., & Zhang, Y. (2010). Indoor SVOC pollution in China: a review. *Chinese Science Bulletin*, *55*(15), 1469-1478.

61. Pankow, J. F. (1994). An absorption model of the gas/aerosol partitioning involved in the formation of secondary organic aerosol. *Atmospheric Environment*, *28*(2), 189-193.

62. Brasher, A. M. D., & Wolff, R. H. (2004). Relations between land use and organochlorine pesticides, PCBs, and semi-volatile organic compounds in streambed sediment and fish on the Island of Oahu, Hawaii. *Archives of Environmental Contamination and Toxicology*, *46*(3), 385-398.

63. Bidleman, T. F. (1988). Wet and dry deposition of organic compounds are controlled by their vapor-particle partitioning. *Environ. Sci. Technol.*, *22*, 361-367.

64. Longnecker, M. P., Rogan, W. J., & Lucier, G. (1997). The human health effects of DDT (dichlorodiphenyltrichloroethane) and PCBS (polychlorinated biphenyls) and an overview of organochlorines in public health. *Annual review of public health*, *18*(1), 211-244.

65. Heudorf, U., Mersch-Sundermann, V., & Angerer, J. (2007). Phthalates: toxicology and exposure. *International journal of hygiene and environmental health*, *210*(5), 623-634.

66. Galarneau, E., & Bidleman, T. F. (2006). Modelling the temperature-induced blow-off and blow-on artefacts in filter-sorbent measurements of semivolatile substances. *Atmospheric Environment*, *40*(23), 4258-4268.

67. Eames, I., Tang, J. W., Li, Y., & Wilson, P. (2009). Airborne transmission of disease in hospitals. *Journal of the Royal Society Interface*, *6*(suppl_6), S697-S702.

68. Zemouri, C., Awad, S. F., Volgenant, C. M. C., Crielaard, W., Laheij, A. M. G. A., & De Soet, J. J. (2020). Modeling of the transmission of coronaviruses, measles virus, influenza virus, Mycobacterium tuberculosis, and Legionella pneumophila in dental clinics. *Journal of dental research*, *99*(10), 1192-1198.

69. Wimalawansa, S. J. (2020). Global epidemic of coronavirus—Covid-19: what can we do to minimize risks. *Eur J Biomed*, *7*(3), 432-8.

70. Lednicky, J. A., Lauzard, M., Fan, Z. H., Jutla, A., Tilly, T. B., Gangwar, M., ... & Wu, C. Y. (2020). Viable SARS-CoV-2 in the air of a hospital room with COVID-19 patients. *International Journal of Infectious Diseases*, *100*, 476-482.

71. Greenhalgh, T., Jimenez, J. L., Prather, K. A., Tufekci, Z., Fisman, D., & Schooley, R. (2021). Ten scientific reasons in support of airborne transmission of SARS-CoV-2. *The lancet*, *397*(10285), 1603-1605.

72. Bourouiba, L. (2020). Turbulent gas clouds and respiratory pathogen emissions: potential implications for reducing transmission of COVID-19. *Jama*, *323*(18), 1837-1838.

73. Redrow, J., Mao, S., Celik, I., Posada, J. A., & Feng, Z. G. (2011). Modeling the evaporation and dispersion of airborne sputum droplets expelled from a human cough. *Building and Environment*, *46*(10), 2042-2051.

74. Li, X., Shang, Y., Yan, Y., Yang, L., & Tu, J. (2018). Modelling of evaporation of cough droplets in inhomogeneous humidity fields using the multi-component Eulerian-Lagrangian approach. *Building and environment*, *128*, 68-76.

75. Gao, N. P., Niu, J. L., Perino, M., & Heiselberg, P. (2008). The airborne transmission of infection between flats in high-rise residential buildings: tracer gas simulation. *Building and Environment*, *43*(11), 1805-1817.

76. Wells, W. F. (1934). On air-borne infection. Study II. Droplets and droplet nuclei. *American Journal of Hygiene*, *20*, 611-18.

77. Yan, Y., Li, X., Shang, Y., & Tu, J. (2017). Evaluation of airborne disease infection risks in an airliner cabin using the Lagrangian-based Wells-Riley approach. *Building and environment*, *121*, 79-92.

78. Rudnick, S. N., & Milton, D. K. (2003). Risk of indoor airborne infection transmission estimated from carbon dioxide concentration. *Indoor air*, *13*(3), 237-245.

79. Bruggeman, P. J., Iza, F., & Brandenburg, R. (2017). Foundations of atmospheric pressure non-equilibrium plasmas. *Plasma Sources Science and Technology*, *26*(12), 123002.

80. van Minderhout, B., Peijnenburg, T., Blom, P., Vogels, J. M., Kroesen, G. M. W., & Beckers, J. (2019). The charge of micro-particles in a low pressure spatial plasma afterglow. *Journal of Physics D: Applied Physics*, *52*(32), 32LT03.

81. Couëdel, L., Mikikian, M., Boufendi, L., & Samarian, A. A. (2006). Residual dust charges in discharge afterglow. *Physical Review E*, *74*(2), 026403.

82. Couëdel, L., Samarian, A. A., Mikikian, M., & Boufendi, L. (2008). Dust charge distribution in complex plasma afterglow. *EPL (Europhysics Letters)*, *84*(3), 35002.

83. Chen, X., Ghosh, S., Buckley, D. T., Sankaran, R. M., & Hogan Jr, C. J. (2018). Characterization of the state of nanoparticle aggregation in non-equilibrium plasma synthesis systems. *Journal of Physics D: Applied Physics*, *51*(33), 335203.

84. Chen, X., Seto, T., Kortshagen, U. R., & Hogan Jr, C. J. (2020). Size and structural characterization of Si nanocrystal aggregates from a low pressure nonthermal plasma reactor. *Powder Technology*, *373*, 164-173.

85. Sharma, G., Abuyazid, N., Dhawan, S., Kshirsagar, S., Sankaran, R. M., & Biswas, P. (2020). Characterization of particle charging in low-temperature, atmospheric-pressure, flow-through plasmas. *Journal of Physics D: Applied Physics*, *53*(24), 245204.

Chapter 2: Understanding morphological evolution in the droplets to predict the structure of particles synthesized via spray techniques.

Dhawan, S. & Biswas, P. A numerical model to predict the morphology of particles synthesized via spray pyrolysis. Drying Technology, Submitted (2021).

Abstract

The spray synthesis techniques have been used in the industries for the large-scale production of functional nanoparticles, as these techniques can readily utilize economical and low volatility precursors and have very high production rates. Particles with different morphologies, mainly solid and hollow, are produced using spray pyrolysis depending on the process conditions. Since the properties of nanoparticles and hence their applications depend on their morphology, it is important to understand the different dynamic processes taking place in the droplet during spray pyrolysis, that influence the morphology of the particle. In this study, a model for simultaneous droplet heating, evaporation, and transport of solute and particles within the droplet, was developed, to investigate the effect of different conditions during spray pyrolysis on the dried particle morphology. The drying process was modelled in two separate stages, initial drying stage before shell formation, and the transition stage, in which shell formation will modelled till the solid crust formation takes place. The model equations were cast into dimensionless form for generalization, and the effects of governing dimensionless groups on the particle morphology were evaluated by performing a sensitivity analysis. Using this model two cases were analyzed, 1) drying of droplet with dissolved solute, and 2) drying of droplet with suspended solids. The important parameters that affect the particle morphology were identified for each case. The developed model could help to choose efficient operating conditions during spray pyrolysis to produce particles of desired properties.

2.1   Introduction

Nanotechnology has received enormous attention in the past few decades. The annual production of functional nanoparticles, including silica, titania, and carbon black, is in the millions of tons, valued at over $15 billion/year [1]. Nanoparticles have extensive applications in solar cells, sensors, catalysis, batteries, drug delivery, cancer treatment etc. [2-13]. They are very versatile in their applications due to their unique mechanical, thermal, electrical, magnetic and optical properties, which arise from their large specific surface area and from the quantum effects [14]. These properties are largely size dependent and morphology dependent, and the synthesis of nanoparticles with a desired the size and morphology of nanoparticles is of key importance for exploiting their properties for their use in several emerging technologies. Therefore, it is important to develop a process in which particles having controlled characteristics including size, morphology, and composition can be produced.

Large number of aerosol techniques for the preparations of particles with narrow size distributions and desired morphologies have been developed over the years [9, 15-18]. The aerosol techniques of particle synthesis are continuous and one-step process with fast processing times, and overcome many drawbacks of conventional wet chemistry synthesis techniques which are usually batch processes involving a large number of processing steps [19]. The formation of nanoparticles via aerosol processes can follow one of the two formation routes: I) gas-to-particle conversion route [15] or, II) liquid-to-particle conversion route (spray synthesis) [20]. In gas-to-particle aerosol synthesis processes, volatile precursors are used, which react in gaseous state at high temperature to form product molecules. These molecules quickly result in particle formation via nucleation, and the particle growth takes place by further coagulation and

condensation. The primary advantages of the gas-to-particle conversion methods are the small particle size with narrow size distribution and high purity [15]. However, the availability of volatile precursors at reasonable costs limits the materials that can be synthesized from gas-to-particle conversion method. Also, the volatility of the precursors limits the production rate and the size of the synthesized particles. Spray synthesis of nanoparticles overcome several of these drawbacks [20]. In liquid-to-particle aerosol synthesis processes, precursor is dissolved in a solution which is sprayed into hot carrier gas, forming small droplets. Due to the high temperature of the carrier gas, the solvent is vaporized, and the solute (precursor) gets precipitated and reacts to form particles. The spray synthesis methods can readily utilize low cost and low volatility precursors such as metal nitrates, chlorides and acetates, which makes it possible to economically synthesize very large number of functional particles all across the periodic table. Also, nano to micron sized particles can be synthesized with very high production rates as the production rate is not limited by precursor's volatility. Different synthesis techniques such as spray drying, spray pyrolysis, electrospray, flame assisted spray aerosol reactor, furnace aerosol reactor, etc. have been used to facilitate the nanoparticle production via droplet-to-particle conversion route. Many of these spray synthesis techniques are easily scalable and have been used in the industries for the large-scale production of functional nanoparticles [21, 22].

In spray pyrolysis, the particle formation can broadly follow two different routes depending on solute and solvent (precursor) physical properties [23]. If the melting point of solute is very low as compared to the decomposition/reaction temperature of the solute, then after the complete evaporation of the solvent, the solute particle will melt, resulting in a liquid solute droplet. This droplet then reacts at higher temperature and can result in either solid or hollow particle. The

reaction of molten precursor can also result in gas release which can puff up the particles, favoring the formation of hollow particles. If the melting point of solute is higher than the decomposition temperature of solute, the precipitation of solute results in either hollow or solid particle formation. If temperature is very high, sintering can then densify the particles and make them solid.

Nanoparticles with different morphologies such as spherical, hollow shell, fragmented etc. have been synthesized via spray routes depending on the properties of precursor, carrier gas flow rate and temperature etc. Abram et al. 2019 [24] observed the formation of different morphologies of Eu doped Y_2O_3 nanoparticles synthesized in spray flame aerosol reactor depending on their operating conditions. Cho et al. 2013 [25] prepared hollow spheres of WO_3 using spray pyrolysis for trimethylamine detection, as the hollow structures with thin and porous shells act as excellent nano-architectures for gas sensors. Bang et al. 2008 [26] synthesized solid and hollow $ZnS:Ni^{2+}$ nanoparticles using spray pyrolysis and compared their photocatalytic activity for water splitting. The solid nanoparticles performed better than hollow nanoparticles due to their good crystallinity and high surface area. It can be seen from all these studies that the properties of the nanoparticles and hence their application are strongly dependent on their morphology. Therefore, it is crucial to understand the different dynamic processes taking place in droplet that influence the morphology of the particle in order to have better and more precise control on morphology of the synthesized particles via spray route.

The control of particle morphology in the spray processes has been the goal of several studies over the years. Several single droplets drying studies have been done to observe the particle formation process from the droplet. Most of these experimental procedures involve suspending a

droplet using techniques such as optical traps [27], electrodynamic balances [28], acoustic levitation [29], thermal levitation [30], thin filament suspension [30], and droplet chain instruments [32]. The major drawback of all these experimental techniques is that large droplets, at least a few hundred micrometers, are required, and that the flow and temperature field in the vicinity of the droplet are usually different from those of a free-flowing droplet during spray pyrolysis. Also due to experimental limitations such as inability to measure temperature, concentration and pressure profiles within the droplet, these studies fail to provide deep insight into complex processes and transport phenomena taking place within droplets. Therefore, the development of an advanced numerical models, that can account for heat and mass transfer in the droplet, is essential to understand the effect of experimental conditions on the dried particle morphology in spray pyrolysis.

Numerous single droplets drying models have been developed over the past few decades. Jain et al. 1997 developed a criterion based on percolation theory to predict the morphology of particle for the spray pyrolysis systems where solute melts before decomposition. There has been a lot of modeling studies in the literature for the systems are where solutes do not melt, since they are the most common spray pyrolysis systems. The brief summary of these models can be seen in Table 2-1. Brenn et al. 2001 [33] proposed one-dimensional model for solute's transport inside the droplet based on Fick's diffusion. The derived equations were nondimensionalized and empirical relation was derived to predict the particle morphology in terms of Sherwood number, which was identified to be the characteristic parameter controlling particle morphology. Messing et al. 1993 [34], Jayanthi et al. 1993 [35] and Zhang et al. 1994 [36] developed a model of particle formation during solution aerosol thermolysis was proposed to study the obtained particle

morphology at the evaporation stage of the process. Equations describing the evolution of droplet temperature (assumed to be radially uniform) and internal concentration profile in spherical droplet were derived and the criterion for solid and hollow particle formation was postulated. Solid particles were considered to from if the precipitation of the solute takes place in whole droplet volume or if the concentration of the solute at the droplet center greater than critical value when the concentration at the droplet's surface reached critical saturation concentration. Ozturk and Cetegen 2005 [37] and Basu et al. 2008 [38] integrated the model developed by Jayanthi et al. 1993 [35] with the computational fluid dynamics model to investigate the effects of effects of droplet size, injection velocity and surrounding conditions on the particle morphology. Mezhericher et al. 2007 [39] further modified the model developed by Jayanthi et al. 1993 [35] by considering internal temperature profile within the droplet. These droplet drying models were able to describe the evaporation of droplet before the solute precipitation but were not able to accurately predict the final particle structure as they do not account for precipitation, shell growth and particle dynamics within the droplet. Based on the population balance approach developed by Seydel et al. 2006, [40] Handscomb and Kraft 2010 [43] developed model that took into account the solute precipitation and particle dynamics within the droplet. However, the major drawback of this model was that the simulated evolution of the solids volume fraction demonstrated a negative solids gradient immediately under the crust region. Recently, Mezhericher et al. 2011[41] and Maurice et al. 2013 [42] have developed a two-stage drying model to simulate droplet evaporation and the shell growth. However, their models do not distinguish between the dissolved phase and precipitated or phase of the solute. There is no study in literature that have identified and examined key governing parameters on the particle morphology during spray pyrolysis.

Table 2-1 Mass & energy conservation spray pyrolysis models in increasing order of complexity.

	References	Description
I.	Brenn *et al.* 2001[33]	• non-dimensionalized the equation for solute's transport • identified important parameter from the non-dimensionalized equation • derived empirical dependence of morphology on non-dimensional parameter
II.	Messing *et al.* 1993,[34] Jayanthi *et al.* 1993[35] and Zhang *et al.* 1994[36]	• solute diffusion, droplet heating, and solvent evaporation • constant surrounding conditions • uniform droplet temperature
III.	Ozturk and Cetegen 2005[37] and Basu *et al.* 2008[38]	• modified the above models by considering shear on droplet • used CFD to get accurate surrounding conditions
IV.	Mezhericher *et al.* 2007[39]	• updated previous models by considering temperature profile within droplet
V.	Seydel *et al.* 2006[40]	• added equations for solid formation, diffusion and growth • modelled till shell formation
VI.	Mezhericher *et al.* 2011[41] and Maurice *et al.* 2013[42]	• developed two-stage drying model to simulate droplet evaporation and the shell formation and growth • do not distinguish between the dissolved phase and precipitated or phase
VII.	Handscomb and Kraft 2010[43]	• considered three component system: solvent, dissolved solute, solid • modelled solute precipitation, solid growth, shell formation and growth

In this study, a comprehensive and generalized two-stage model for droplet drying and subsequent particle growth is developed for the process of spray pyrolysis where the solute does not melt. For the first stage, equations for simultaneous heat transfer, droplet evaporation, solute diffusion, solute precipitation and particle dynamics were derived. The equations for shell formation and growth till solid crust formation, were derived for the second stage. The equations were non dimensionalized and the effects of governing parameters and operating conditions of spray pyrolysis on particle morphology are quantified. This model is applicable for drying of droplets of any size with insoluble solids as well as droplets with dissolved solute. The developed model can be a guide for determining efficient operating conditions for the production of particles with desired properties.

2.2   Model Development
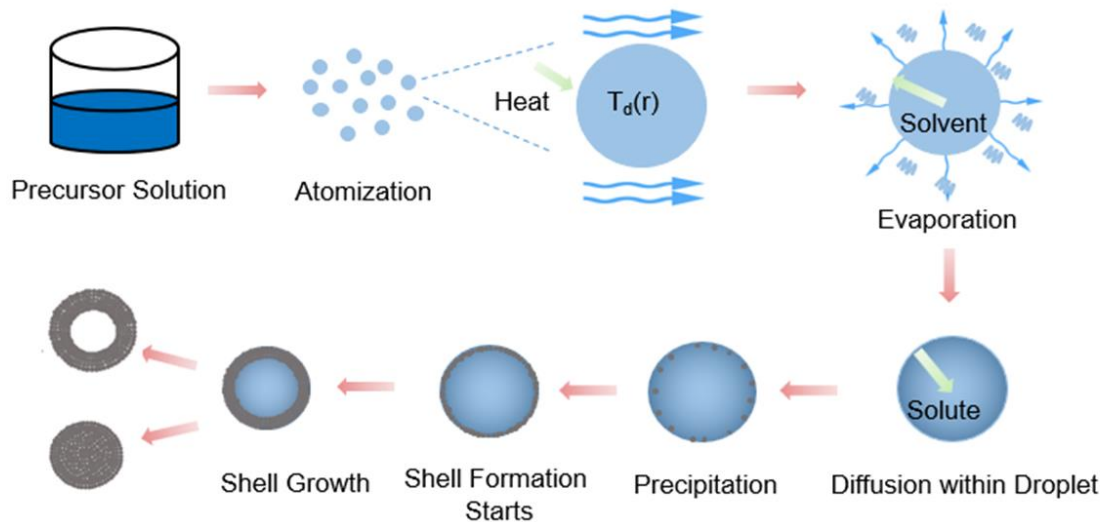
Figure 2-1 Schematic diagram of the various processes taking place during spray pyrolysis.

In the present study, two-stage model of droplet drying is considered. In spray pyrolysis, precursor usually consist of a dissolved metal salt or suspended particles in some solvent. This solution is atomized and sprayed into a carrier gas. In the initial drying stage, the droplet gains sensible heat and begins to evaporate, and droplet's diameter starts to reduce. Due to evaporation of the solvent, the solute/particle concentration starts to increase near the droplet's surface. This results in diffusion of solute/particles towards the droplet's center. When the concentration of dissolved solute in droplet increases above the critical saturation value, the precipitation of solute will take place. The transition drying stage begins when the concentration of solids at the droplets surface rises above the critical concentration. Shell formation and growth till solid crust formation, is modelled in this drying stage. The schematic of these processes occurring in the droplets is shown in Figure 2-1. In this study, drying model considers the system to be made of

three components: 1) solvent, 2) solute dissolved in the solvent, and 3) precipitated solute or particles inside the droplet. The solvent and dissolved solute was assumed to be an ideal binary solution. Thus, the system under consideration has two phases i.e. continuous phase, which is the ideal binary mixture of solute and solvent, and solid phase, which comprises of precipitated solute or particles inside the droplet. It is assumed that the droplets maintain spherical symmetry throughout the drying process and that the temperature of the droplet is spatially uniform.

2.2.1   Initial Drying Stage before Shell Formation

The heat transferred to the droplet results in the increase in droplet temperature with time. It is also used as the latent heat of vaporization as the droplet evaporates. The evolution of droplet temperature with time can be evaluated using the energy balance equation, given by:

$$A(t)\,h\,(T_\infty - T_d(t)) = m(t)S\frac{dT_d(t)}{dt} + L\frac{dm(t)}{dt} \tag{2.1}$$

where, A is the surface area of the droplet, h is the heat transfer coefficient, T_∞ is the surrounding gas temperature, T_d is the droplet temperature, m is the mass of droplet, S is the specific heat capacity of the droplet and L is the latent heat of vaporization of the solvent. The term of left-hand side is the total heat transferred to the droplet from the surroundings. The first term on right-hand side refers to the transferred heat which results in the increase in droplet temperature, while the second term refers to the rate at which heat transferred to droplet is used as latent heat to evaporate the solvent. In majority of the spray pyrolysis systems, droplet move with no relative velocity with respect to carrier gas. Therefore, Nusset number can be assumed to be 2, and the heat transfer coefficient is given by:

$$h = {}^k/_{R(t)}$$ (2.2)

Here, k is the thermal conductivity of the surrounding gas and R is the droplet radius. The rate of change of droplet radius, moving with the same velocity as the surrounding gas, is given by:

$$\frac{dR(t)}{dt} = \frac{D_v v_m}{R(t)k_B} \left(\frac{p_\infty}{T_\infty} - \frac{p_d}{T_d}\right) F(Kn)$$ (2.3)

where D_v is the diffusivity of solvent vapor in carrier gas, k_B is the Boltzmann constant, p_∞ is the partial pressure of solvent vapor in the surrounding gas, p_d is the pressure of solvent vapor at the droplet's surface and F is the Fuchs-Sutugin correction factor for transport to/from a droplet surface in the transition-free molecule regime, given by [44]:

$$F(Kn) = \frac{1 + Kn}{1 + 1.71Kn + 1.333Kn^2}$$ (2.4)

where Kn is the Knudsen number (= $2\lambda/d_p$, where λ is the mean-free-path of the vapor molecules). The pressure of solvent vapor at droplet's surface can be given by:

$$p_d(t) = p_{sat}\left(1 - \varepsilon(R, t)\right) * \left(1 - x_s(R, t)\right)$$ (2.5)

Here, p_{sat} is the saturation pressure of solvent, $\varepsilon(R,t)$ is the volume fraction of solids at droplet's surface, and $x_s(R,t)$ is the mole fraction of dissolved solute at the droplet's surface. The continuous phase is assumed to be an ideal binary solution of solute dissolved in solvent. Therefore, the evolution of continuous phase can be described by volume averaged transport equation for solute. The differential mass balance for the solute can be written as:

$$\frac{\partial\left[(1-\varepsilon(r,t))\rho_c(r,t)w_s(r,t)\right]}{\partial t} + \frac{1}{r^2}\frac{\partial}{\partial r}\left[-r^2 D_s\rho_c(r,t)\frac{\partial}{\partial r}\left[(1-\varepsilon(r,t))w_s(r,t)\right]\right]$$

$$- \rho_s\frac{\partial\varepsilon(r,t)}{\partial t} = 0 \quad (2.6)$$

where, r is the radial direction, ε is the volume fraction of solid in the droplet, ρ_c is the continuous phase density, w_s is the mass fraction of solute in the continuous phase, D_s is the solute diffusivity in solvent, and ρ_s is the density of solute. The first term on left hand side of this equation represents the rate of change of the density of solute dissolved in the continuous phase. The second term accounts for the diffusion of solute which is induced by the concentration gradients of solute inside the droplet caused by solvent evaporation. The last term accounts for the loss of solute from the continuous phase to the solid phase due to precipitation and crystallite growth. The continuous phase density ρ_c at any time could be calculated by:

$$\rho_c = \frac{1}{\frac{w_s(r,t)}{\rho_s} + \frac{1-w_s(r,t)}{\rho_l}} \quad (2.7)$$

50

where, ρ_l is the pure solvent density. The solid phase in droplet was modelled by a solving population balance equation of particles. The particles in the droplet considered in the model are assumed to be spherical. The solid phase concentration will evolve in droplet due to diffusive transport, precipitation and growth from dissolved solute and coagulation. The general form of the size distribution function of solid particles inside the droplet is given by [45]:

$$\frac{\partial n(v,r,t)}{\partial t} - \frac{1}{r^2}\frac{\partial}{\partial r}\left(r^2 D \frac{\partial n(v,r,t)}{\partial r}\right) + \frac{\partial(Gn)}{\partial v} - I(v^*)\delta(v - v^*)$$

$$- \frac{1}{2}\int_0^v \beta(v - \tilde{v}, \tilde{v})n(v - \tilde{v}, r, t)n(\tilde{v}, r, t)d\tilde{v} + n(v,r,t)\int_0^\infty \beta(\tilde{v}, v)n(\tilde{v}, r, t)d\tilde{v} = 0 \quad (2.8)$$

In this equation, n is the size distribution function, v is the particle volume, D is the diffusivity of solid particles, G is the growth rate, I is the nucleation rate, v^* is the critical volume of nucleated particle and β is the collision coefficient. The first term on the left-hand side is the rate of change of the particle size distribution in the volume interval, v to $v + dv$, the second term considers the particle diffusion in the droplet, the third term accounts for particle growth, the fourth term describes the formation of new particles of critical volume v* due to precipitation and the last term accounts for the Brownian Coagulation of particles. To simplify the model, it was assumed that the particles were monodisperse and the particle size was the function of radial position and time. The condensational growth rate G, is given by [44]:

$$G = 2\pi \left(\frac{6}{\pi}v\right)^{\frac{1}{3}}\frac{D_s k_B T_d \rho_c}{\rho_s}[w_s - w_{s,sat}] \quad (2.9)$$

where, $w_{s,sat}$ is the saturation mass fraction of the solute in the solvent. The expression developed by Dirksen and Ring (1991) [46] for homogeneous nucleation rate was used in this study. The expression for nucleation/precipitation rate I is given by:

$$I = I_{max} \exp\left[-\left(\frac{200}{(\ln S)^2}\right)\right]$$
(2.10)

where I_{max} is a constant representing the maximum nucleation rate, and S is the saturation ratio. For nearly monodisperse systems, the collision frequency function is given by:

$$\beta = \frac{8k_B T_d}{3\mu}$$
(2.11)

Here, μ is the solvent's viscosity. equation (2.7) can be written in the terms of moments and the ith moment is defined as:

$$m_i(r,t) = \int_{vmin}^{\infty} v^i(n(v,r,t))dv$$
(2.12)

The zeroth moment represents the number concentration and the first moment represents the volume fraction of solids (ε). Using the monodisperse assumption and by integrating the equation (2.8), the equations for the zeroth and first moment can be derived as:

$$\frac{\partial m_0(r,t)}{\partial t} = \frac{1}{r^2}\frac{\partial}{\partial r}\left(r^2 D \frac{\partial m_0(r,t)}{\partial r}\right) - \frac{1}{2}\beta(m_0(r,t))^2 + I \tag{2.13}$$

$$\frac{\partial m_1(r,t)}{\partial t} = \frac{\partial \varepsilon(r,t)}{\partial t} = \frac{1}{r^2}\frac{\partial}{\partial r}\left(r^2 D \frac{\partial m_1(r,t)}{\partial r}\right) + Iv^* + m_0(r,t)G \tag{2.14}$$

It is assumed that both dissolved solute and the solid particles do not leave the droplet during evaporation. Therefore, the mass flux of dissolved solute and particles across the droplet receding surface is zero, and accordingly, the boundary conditions at droplet's surface are given by:

$$\frac{\partial w_s(R,t)}{\partial r} = -\frac{w_s(R,t)}{D_s}\frac{dR(t)}{dt} \tag{2.15}$$

$$\frac{\partial m_0(R,t)}{\partial r} = -\frac{m_0(R,t)}{D}\frac{dR(t)}{dt} \tag{2.16}$$

$$\frac{\partial m_1(R,t)}{\partial r} = -\frac{m_1(R,t)}{D}\frac{dR(t)}{dt} \tag{2.17}$$

The zero gradient boundary condition is used at the center of the droplet because of the spherical symmetry. Hence at r = 0,

$$\frac{\partial w_B(0,t)}{\partial r} = \frac{\partial m_0(0,t)}{\partial r} = \frac{\partial m_1(0,t)}{\partial r} = 0 \tag{2.18}$$

The system of ordinary and partial differential equations (2.1), (2.3), (2.6), (2.13), (2.14) along with the boundary conditions (2.15-2.18) can be solved simultaneously using numerical methods to obtain the evolution of droplet temperature, droplet radius, concentration profiles of dissolved solute and the volume fraction profile of solids within the droplet in the initial stage of drying before shell formation. Since, the droplet's radius decreases with time, the spatial domain which lies between $0 \leq r \leq R(t)$ changes with time. To handle the moving boundary, coordinate transformation from (r,t) to (z,t_n) was used, given by

$$z = \frac{r}{R(t)} \quad and \quad t_n = t; \quad 0 \leq z \leq 1 \tag{2.19}$$

$$\frac{\partial}{\partial r} = \frac{\partial}{\partial z}\frac{\partial z}{\partial r} + \frac{\partial}{\partial t_n}\frac{\partial t_n}{\partial r} = \frac{1}{R(t_n)}\frac{\partial}{\partial z} \tag{2.20}$$

$$\frac{\partial}{\partial t} = \frac{\partial}{\partial t_n}\frac{\partial t_n}{\partial t} + \frac{\partial}{\partial z}\frac{\partial z}{\partial t} = \frac{\partial}{\partial t_n} - \frac{z}{R(t_n)}\frac{dR(t_n)}{\partial t_n}\frac{\partial}{\partial z} \tag{2.21}$$

This transformation was applied to all the equations.

2.2.2   Transition stage

When the volume fraction of solids at the droplet's surface reaches a saturated value, the shell formation is deemed to begin. The saturated value corresponds to the point when solid volume fraction reaches material packing factor. The saturation value of solid volume fraction ($\varepsilon_{critical}$) was assumed to be 0.65 in this study, similar to Handscomb and Kraft 2010. When the shell is formed, it undergoes compressive stresses in both tangential and radial directions, as the particles

on the droplet surface are drawn inwards by the surface tension. Thus, the liquid inside the droplet relatively passes through the layer of shell and moves towards the droplet surface. Minoshima, Matsushima et al. (2001) [47] related this liquid movement through the shell to filtration process through the porous medium. Using this analogy, the compressive pressure acting on the shell was related to the pressure arising due to the movement of the liquid through the shell and, Darcy's law was used to calculate the compressive pressure. The compressive pressure acting on shell (P_{shell}) is given by [47]:

$$P_{shell} = \frac{\mu}{\kappa} \frac{dR(t)}{dt} \frac{R(t)}{(R(t) - T(t))} T(t) \tag{2.22}$$

where, κ is the permeability of the shell and T is the shell thickness. The permeability of the shell (κ) can be estimated using the Carmen-Kozeny relation [48]:

$$\kappa = \frac{1}{5} \frac{(1 - \varepsilon)^3}{S_v^2} \tag{2.23}$$

where, S_v is the surface area of solids per unit volume. The compressive pressure on shell results in the droplet shrinkage which continues till the shell becomes structurally capable of supporting itself. The maximum pressure that the shell can sustain without buckling is given by [49]:

$$P_{max} = \left(\frac{T(t)}{R(t) - T(t)} \right)^2 \frac{2E}{\sqrt{3(1 - v^2)}} \tag{2.24}$$

where, E is the Young's Modulus of the shell and v is the Poisson's ratio. Both P_{shell} and

P_{max} increases with time as the shell thickness increases. The shell will shrink if P_{max} is less than

P_{shell} and will continue to shrink till P_{max} becomes equal to P_{shell}. Since, the shell is structurally

capable to support the compressive stresses acting on it when $P_{max} \geq P_{shell}$, the shell turns to a

solid crust with unchangeable outer radius. The shrinking of shell stops and evaporation interface

retreats inside the droplet. This marks the end of transition stage, and the size of the particle

remains unchanged if further drying continues.

During the transition regime, the modelling domain is divided into two regions: 1) shell region

which lies between $R_{in}(t)$ and $R(t)$, and 2) inner region which starts from the droplet's center

till $R_{in}(t)$, where $R_{in}(t)$ is the inner radius of the shell. The volume fraction of solids in the

inner region is less than the saturated or maximum packing fraction ($\varepsilon_{critical}$) while the volume

fraction of solids in the shell region is assumed to be saturated value ($\varepsilon_{critical}$). Also, the

concentration of dissolved solute is assumed to be saturated in the shell region. Equations (2.1),

(2.3), (2.6), (2.13), (2.14) can be used to describe the evolution of droplet temperature, droplet's

radius, concentration profiles of dissolved solute and the volume fraction profile of solids within

the inner region of the droplet ($0 \leq r < R_{in}$). Since the concentration of both solid particles and

dissolved solute is assumed to be saturated in the shell region, the partial pressure of the solvent

at the droplet surface during transition regime is given by:

$$p_d(t) = p_{sat}\left(1 - \varepsilon_{critical}(R, t)\right) * \left(1 - x_{s,sat}(R, t)\right) \qquad (2.25)$$

Here, $x_{s,sat}$ is the mole fraction of the solute in the solvent under saturation conditions. As the droplet shrinks, the concentration of sold increases resulting in the thickening of shell. The rate of change of the inner shell radius is derived in the Appendix B of study by Mezhericher, Levy et al. 2011. In that study, a simple shell balance was performed by equating increment of shell volume to the sum of volume of solids adjacent to the shell which are adhered to the shell during the shrinkage and solids volume pushed under the liquid layer by capillary forces, and the rate of change in inner shell radius was derived as:

$$\frac{dR_{in}(t)}{dt} = \frac{\varepsilon_{critical}}{\varepsilon_{critical} - \varepsilon(R_{in}, t)} \frac{R(t)^2}{R_{in}(t)^2} \frac{dR(t)}{dt} \tag{2.26}$$

The boundary conditions at the inner radius of shell are assumed to be:

$$\frac{\partial w_s}{\partial r} = \frac{\partial m_0}{\partial r} = \frac{\partial m_1}{\partial r} = 0 \quad at \; r = R_{in}(t) \tag{2.27}$$

These boundary conditions conserve the net mass of dissolved solute and solid in the droplet as they do not leave the droplet boundary. Similar to the initial drying stage, the spatial domain of the inner region changes with time in the transition stage of drying. Therefore, to handle the moving boundary, similar coordinate transformation from (r, t) to (z_2, t_m) was used, given by

$$z_2 = \frac{r}{R(t)} \quad and \; t_m = t; \quad 0 \leq z_2 \leq 1 \tag{2.28}$$

2.2.3   Criteria for different morphologies and test plan
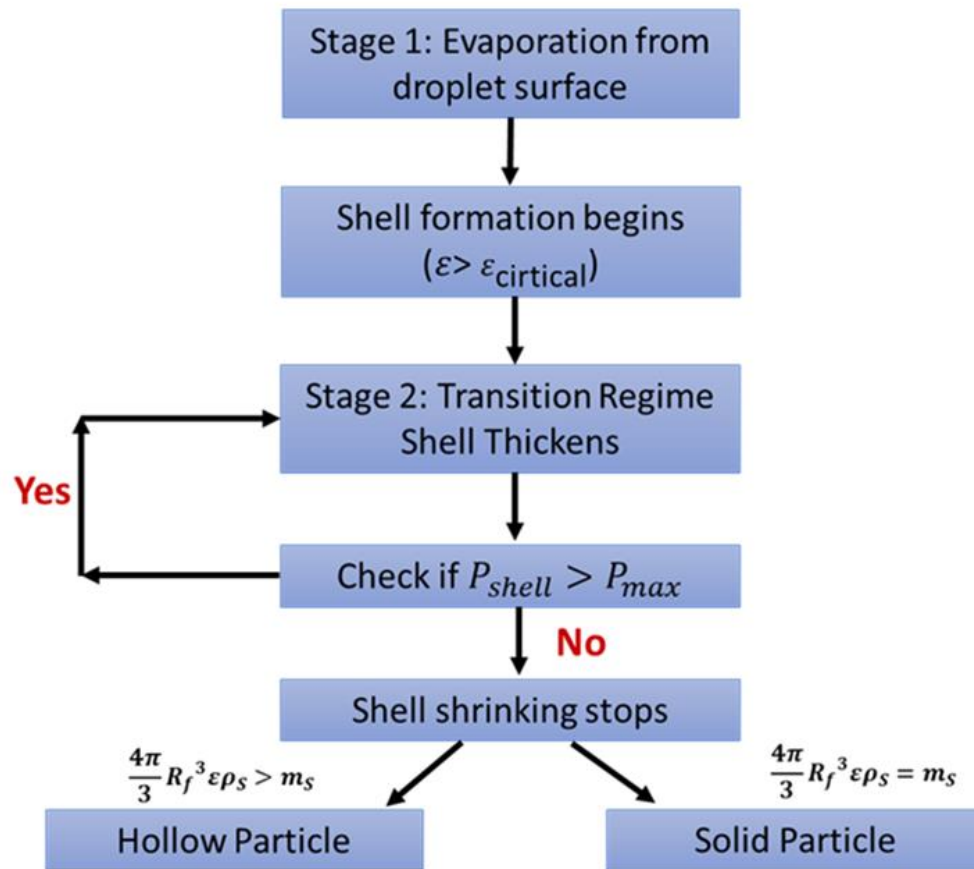
Figure 2-2 Algorithm for predicting particle morphology during spray pyrolysis.

The algorithm for the developed model is presented in Figure 2-2. Initially, the equations listed in Section 2.2.1 are solved to get the droplet temperature, radius and the concentration profiles of solute and solids in the droplet, till the solid volume fraction at the droplet's surface reaches a saturation value. After the first drying stage, transition stage begins, and the equations for the transition stage, as listed in Section 2.2.2, are solved numerically as the function of time. At each time step P_{shell} and P_{max} are calculated and compared. When, P_{shell} and P_{max} are equal i.e. when

the shell becomes capable of structurally supporting itself, shrinking stops and the transition stage ends. However, if P_{shell} remains higher than P_{max} until the shell spreads over the entire droplet's radius, the concentration throughout the droplet will reach saturated value, resulting in the formation of solid particles. The particles with hollow morphology can form if P_{max} becomes greater than P_{shell} during droplet shrinkage, before the shell spreads over the entire radius. After the end of the transition stage, the particle diameter does not change on further drying and the shell grows further inwards. For the case when P_{max} becomes greater than P_{shell} during droplet shrinkage, before the shell spreads over the entire radius., assuming the uniform shell porosity, the inner shell radius can be evaluated by using the mass balance given by:

$$m_{solute+solids} = \frac{4\pi}{3}\left(R_f{}^3 - R_{in,f}{}^3\right)\varepsilon_{critical}\,\rho_s \tag{2.29}$$

Here, $m_{solute+solids}$ is the total mass of dissolved solute and suspended solids in the droplet, R_f is the final outer radius of the particle and $R_{in,f}$ is the final inner radius of the shell. After calculating $R_{in,f}$ from equation 2.29, relative shell thickness, R' can be calculated as:

$$R' = \frac{R_f - R_{in,f}}{R_f} \tag{2.30}$$

For the purpose of this study, if the relative shell thickness of the particle is less than 0.95, the morphology of particle is considered to be hollow otherwise it is considered to be solid.

Table 2-2 Simulation Plan.

Simulation Plan	
3.1 Non-dimensionalization	- Non-dimensionalized all equations - Identify key parameters that can affect particle morphology
3.2 Model Verification	- Comparison with experimental results of Nesik and Vodnik (1991) - Mass Balance Confirmation
3.3 Sensitivity Analysis	- Two drying cases: - particles suspended in droplet - solute dissolved in droplet - For both cases, evaluated the effect of key non-dimensional parameters on particle morphology

In this study, the equations are first nondimensionalized for mathematical simplicity and to combine model parameters into a smaller set of governing dimensionless groups. Before the system analysis, the consistency of the model was first established by validating its numerical scheme. Then, the simulations were carried out to investigate the effect of dimensionless governing parameters on the particle morphology for two different cases: 1) drying of droplet with suspended particles and 2) drying of droplet with dissolved solute. The effect of governing parameters on morphology were quantified in terms of the relative shell thickness, R'. The test plan and the set of all the simulations performed for this work are listed in Table 2-2.

2.2.4 Non-Dimensionalization

The model equations were nondimensionalized for mathematical simplicity to identify the key governing parameters, that affect the particle morphology during spray pyrolysis, by combining model parameters into key dimensionless groups. For the first drying stage, the dimensionless equations are given by:

$$\frac{dT_d{}^*}{dt^*} = 3\left(\frac{\frac{1}{\tau_{hc}{}^*}R^*(1-T_d{}^*) + \frac{1}{J_A}R^{*2}\frac{dR^*}{dt^*}}{R^{*3} + \rho_c{}^* - 1}\right) \tag{2.31}$$

$$\frac{dR^*}{dt^*} = \frac{1}{2R^*}\left(p_\infty{}^* - \frac{p_d{}^*}{T_d{}^*}\right)F(Kn) \tag{2.32}$$

$$\frac{\partial[(1-\varepsilon)\rho_c{}^*w_s]}{\partial t^*} + \frac{1}{z^2 R^{*2}\,\tau_{diffn,s}{}^*}\frac{\partial}{\partial z}\left[-z^2\rho_c{}^*\frac{\partial}{\partial z}[(1-\varepsilon)w_s]\right]$$

$$-\frac{1}{R^*}\frac{\partial}{\partial z}\left[z\frac{dR^*}{dt^*}\frac{\partial}{\partial z}[(1-\varepsilon)\rho_c{}^*w_s]\right] + \frac{\partial\varepsilon}{\partial t^*} = 0 \tag{2.33}$$

$$\frac{\partial m_0{}^*}{\partial t^*} = \frac{z}{R^*}\frac{dR^*}{dt^*}\frac{\partial m_0{}^*}{\partial z} + \frac{1}{z^2 R^{*2}\,\tau_{diffn,p}{}^*}\frac{\partial}{\partial z}\left(z^2\frac{\partial(m_0{}^*)^{\frac{4}{3}}(m_1{}^*)^{\frac{-1}{3}}}{\partial z}\right) - \frac{m_0{}^{*2}}{\tau_{coag}{}^*}$$

$$+S^2\exp\left(\frac{-1}{(lnS)^2}\right) \tag{2.34}$$

61

$$\frac{\partial m_1^*}{\partial t^*} = \frac{z}{R^*} \frac{dR^*}{dt^*} \frac{\partial m_1^*}{\partial z} + \frac{1}{z^2 R^{*2} \tau_{diffn,p}^*} \frac{\partial}{\partial z} \left(z^2 \frac{\partial (m_0^*)^{\frac{1}{3}} (m_1^*)^{\frac{2}{3}}}{\partial z} \right)$$

$$+ I_{max}^* \exp\left(\frac{-200}{(lnS)^2}\right) + \frac{m_0^{*\frac{2}{3}} m_1^{*\frac{1}{3}} T_d^* \rho_c^*}{\tau_{cond}^*} (S-1) \quad (2.35)$$

with the boundary conditions:

$$\frac{\partial w_s}{\partial z} = -w_s \, \tau_{diffn,s} R^* \frac{dR^*}{dt^*} \quad at \; z = 1 \tag{2.36}$$

$$\frac{\partial m_0^*}{\partial z} = -m_0^* \, \tau_{diffn,p} R^* \frac{dR^*}{dt^*} \quad at \; z = 1 \tag{2.37}$$

$$\frac{\partial m_1^*}{\partial z} = -m_1^* \, \tau_{diffn,p} R^* \frac{dR^*}{dt^*} \quad at \; z = 1 \tag{2.38}$$

$$\frac{\partial w_s}{\partial z} = \frac{\partial m_0^*}{\partial z} = \frac{\partial m_1^*}{\partial z} = 0 \quad at \; z = 0 \tag{2.39}$$

For the transition stage, equations (2.31-2.35) are valid used for the inner region, with the boundary conditions:

$$\frac{\partial w_s}{\partial z_2} = \frac{\partial m_0^*}{\partial z_2} = \frac{\partial m_1^*}{\partial z_2} = 0 \quad at \; z_2 = 1 \tag{2.40}$$

The equation for the rate of change in inner shell radius can be non-dimensionalized as:

$$\frac{dR_{in}^*}{dt^*} = \frac{\varepsilon_{critical}}{\varepsilon_{critical} - \varepsilon(1, t^*)} \frac{R^{*2}}{R_{in}^{*2}} \frac{dR^*}{dt^*} \tag{2.41}$$

The shell shrinking stops when $P_{max} \geq P_{shell}$. After substituting the expressions for P_{max} & P_{shell}, this inequality can be non-dimensionalized as

$$\frac{1}{\tau_{shell}^*} \left(\frac{R^* - R_{in}^*}{R_{in}^*} \right) \geq R^{*3} \left(-\frac{dR^*}{dt^*} \right) \tag{2.42}$$

where, $t^* = t/\tau_{evap}$, $T_d^* = T_d/T_\infty$, $\rho_c^* = \rho_c/\rho_s$, $p_i^* = p_i/p_{sat}$, $m_0^* = m_0/N_{ref}$, $m_1^* = m_1/(v_{ref}N_{ref})$, $R^* = R/R_{initial}$ and $R_{in}^* = R_{in}/R_{initial}$, are the dimensionless variables, and $\tau_{diffn,s}^*$, $\tau_{diffn,p}^*$, τ_{hc}^*, J_A, τ_{coag}^*, τ_{cond}^*, I^* and τ_{shell}^* are the dimensionless parameters that govern the morphology of the particles during spray pyrolysis. The definition and expressions for these dimensionless parameters are given in Table 2-3. Here, N_{ref} is the reference number concentration of particles and v_{ref} is the reference volume of particles in the droplet. In Table 2-3, τ_{evap} is the characteristic evaporation time of pure droplet, given by

$$\tau_{evap} = \frac{2R_{initial}^2 k_B T_\infty}{D_V v_m p_{sat}} \tag{2.43}$$

Table 2-3 Dimensionless parameters and their definitions.

Parameters	Definition	Expression
$\tau_{diffn,s}{}^{*}$	Ratio of characteristic diffusion time of the dissolved solute to evaporation time of pure droplet	$\dfrac{R_{initial}{}^{2}/D_s}{\tau_{evap}}$
$\tau_{diffn,p}{}^{*}$	Ratio of characteristic diffusion time of the suspended solids to evaporation time of pure droplet	$\dfrac{R_{initial}{}^{2}/D}{\tau_{evap}}$
$\tau_{hc}{}^{*}$	Ratio of characteristic time to achieve wet bulb temperature to evaporation time of pure solvent	$\dfrac{\rho S R_{initial}{}^{2}}{k\tau_{evap}}$
J_A	Ratio of sensible heat to latent heat of vaporization	$\dfrac{S T_\infty}{L}$
$\tau_{coag}{}^{*}$	Ratio of characteristic coagulation time to evaporation time of pure solvent	$\dfrac{2/\beta N_{ref}}{\tau_{evap}}$
$\tau_{cond}{}^{*}$	Ratio of characteristic time for solids to grow to evaporation time of pure solvent	$\dfrac{1/\left(2\pi \left(\dfrac{6}{\pi}\right)^{\frac{1}{3}} \dfrac{D_s k_B T_\infty}{w_{s,sat} v_{ref}^{\frac{2}{3}}}\right)}{\tau_{evap}}$
I^{*}	Ratio of nucleation rate to the product of evaporation time and reference concentration	$\dfrac{I_{max}\tau_{evap}}{N_{ref}}$
τ_{shell}^{*}	Ratio of characteristic time of shell thickening to the evaporation time of pure droplet	$\dfrac{\mu}{\kappa}\dfrac{\sqrt{3(1-v^2)}}{2E}\dfrac{R_{initial}{}^{2}}{\tau_{evap}}$

Here, D_V is the diffusivity of solvent in the vapor phase and v_m is the molecular volume of the solvent. Equations (2.31-2.35) and (2.36), along with the appropriate boundary conditions, constitute a set of coupled ordinary differential equations (ODE) and partial differential equations (PDEs). This set of coupled ODEs and PDEs is solved by finite difference technique (MATLAB in this work).

2.3　　　Results and Discussions
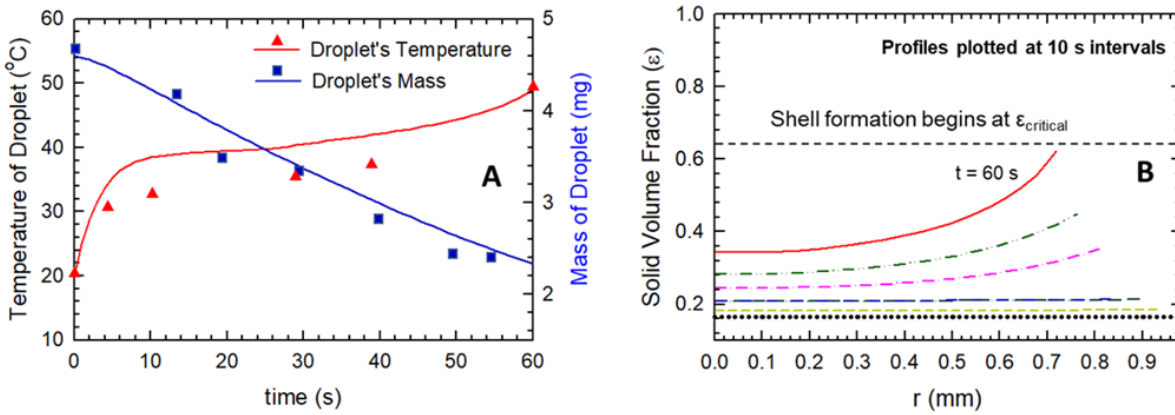
Figure 2-3 (a) Simulated (this work) versus experimental (Nesik and Vodnik 1991) temperature and droplet mass with time for drying of droplet containing silica particles. (b) Simulated (this work) profile of solid volume fraction inside droplet at 10 seconds interval.

The numerical scheme of this model is validated by comparing to experimental results of Nešić and Vodnik 1991 [50]. The drying of a water droplet with an initial size of 1 mm containing 30% by weight, 16 nm colloidal silica particles was simulated. The temperature of the carrier gas was considered to be 101°C. Figure 2-3 shows the simulated results of drying of droplet with colloidal silica particles. In Figure 2-3a, the evolution of droplet mass and temperature with time were plotted, while in Figure 2-3b, simulated solids volume fraction profiles during the drying of a colloidal silica were plotted at 10 second intervals. It can be seen from Figure 2-3a that the simulated temperature and droplet's mass evolution were in reasonable agreement with the experimental results of Nešić and Vodnik 1991 [50]. However, the experimental data for the evolution of solid fraction profile inside the droplet was not available due to experimental limitations. Also, the mass balance was carried out on the numerical solutions of the present

model. The total solid and solute mass was found to be conserved at each time step as they do not escape from the droplet.

After establishing the numerical consistency of the present model, a parametric analysis was carried out to investigate the effects of the dimensionless governing parameters listed on Table 2-3, on the morphology of the particle. Two different cases were considered: 1) drying of droplet with suspended particles, and 2) drying of droplet with dissolved solute, and the effects of dimensionless governing parameters on the particle morphology were evaluated for both the cases. The values of the parameters examined here were in the typical range for spray pyrolysis experiments.

2.3.1   Case I: Drying of droplet with suspended particles

Table 2-4 Simulation Parameters

Dissolved Particles	Silica
Solvent	Water
Initial Droplet Temperature (K)	298
Relative Humidity	0
Density of solvent (kg m^{-3})	1000
Density of solute (kg m^{-3})	2660
Latent Heat of Solvent (kJ/kg)	2258
Specific Heat of Solvent (kJ/(kg.K))	4.184
Suspended particle diameter (nm)	5 nm
Initial Solid Fraction	0.25
Initial droplet radius (nm)	1000

The first test case simulated is the drying of a droplet containing suspended particles. To simulate, the initial mass fraction of dissolved solute was set to be zero in the model equations. Thus, for this case, solute transport equation as well as, the nucleation and particle growth terms are not considered. The effect of different parameters, ambient temperature, diameter of particles suspended in droplets, initial volume fraction of particles in droplets and Young's modulus, on particle morphology was quantified by calculating the relative shell thickness of the final dried particle. The parameters used in the simulations are listed in Table 2-4.
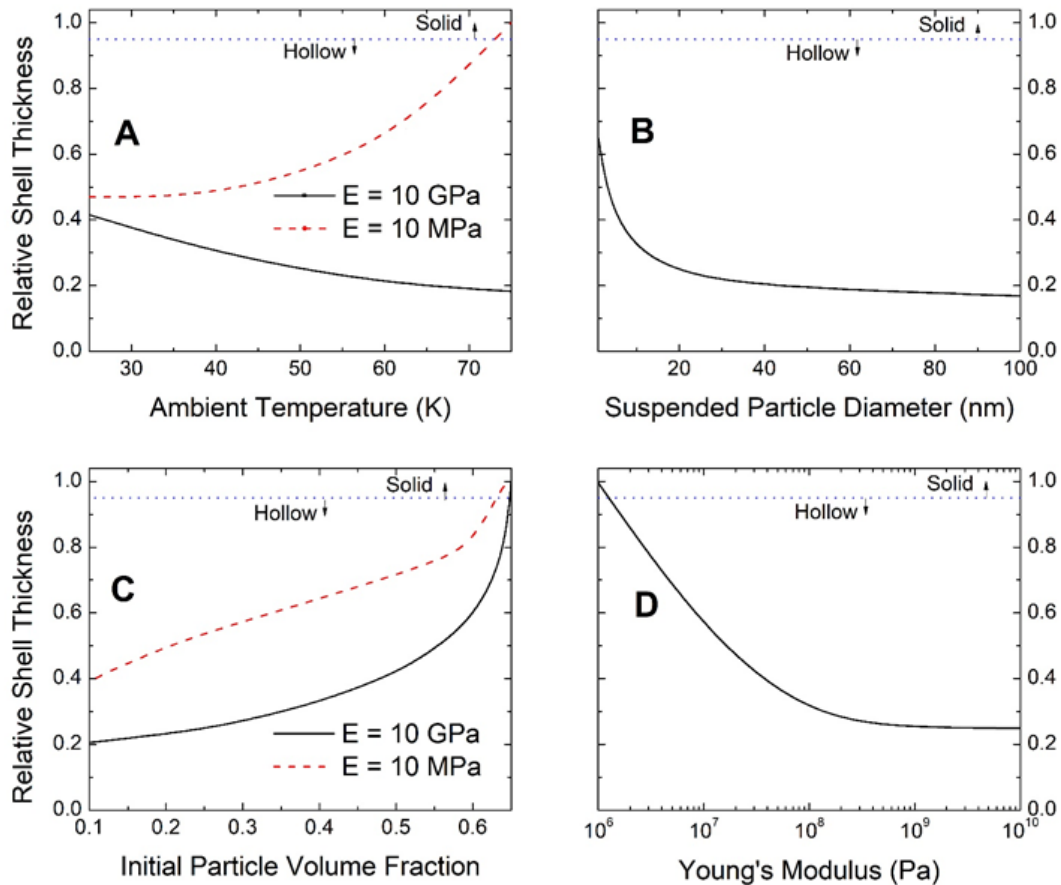
Figure 2-4 Calculated relative shell thickness of the final dried particles as a function of (a) ambient temperature (b) suspended particle diameter (c) initial solid volume fraction and (d) Young's modulus of shell. The simulation parameters are given in Table 2-4.

67

Figure 2-4 shows the calculated relative shell thickness of final dried particles as the function of the above-mentioned parameters. The impact of ambient temperature on the particle morphology is shown in Figure 2-4(a). It can be seen that the influence of ambient temperature on particle morphology is dependent on Young's Modulus of the shell. When Young's Modulus of shell is large (10 GPa), the relative shell thickness of the dried particle decreases with increase in temperature, which means that as the temperature increases, formation of particles with hollow morphology is favored. However, if Young's Modulus of shell is low (10 MPa), the relative shell thickness of the dried particle decreases with increase in temperature, favoring the formation of particles with solid morphology. At higher ambient temperature, evaporation of droplets is faster as compared to transport of particles towards the droplet's center, resulting in higher concentration of particles near the droplet's surface. However, compressive pressure acting on shell during the transition stage also increases with the increase in evaporation rate (Equation 2.22), which increases the time of droplet shrinkage. If Young's Modulus of shell is large, the shell is easily able to structurally support any increase in the compressive stresses caused by increase in evaporation rate at higher temperatures, and therefore hollow particle formation is favored due to increased concentration gradients between droplet's surface and center. But if Young's Modulus of shell is low, the transition stage or shell shrinkage before crust formation will last longer at higher ambient temperature and shell will continue to deform for long time, leading to thicker shells, thus favoring the formation of solid particles.

Figure 2-4(b) shows relative thickness of final dried particle as a function of the diameter of suspended particles, while keeping the initial volume fraction of suspended particles at 0.25. If the diameter of suspended particles increases, the relative shell thickness of the final dried

particle decreases favoring the particle formation with hollow morphology. This is because diffusivity of particles decreases with increase in their diameter. As droplet shrinks, transport of solid towards the droplet center will be slow resulting in higher concentration solids near the droplet surface as compared to its center. Therefore, formation of particles with hollow morphology is favored when diameter of suspended particles is high.

Figure 2-4(c) shows the relative thickness of final dried droplet as a function of the initial volume fraction of suspended particles, while keeping the diameter of suspended particles to 5 nm. It can be seen that as the initial concentration increases, the relative shell thickness of dried droplet increases, favoring the formation of particles with solid morphology as particle concentration remain high throughout the droplet volume. Figure 2-4(d) shows the relative thickness of final dried droplet as the function of shell's Young's Modulus. As can be seen from the figure, larger Young's Modulus favors the formation of particles with hollow morphology. This is because if Young's Modulus of the shell is large, during transition stage, shell become capable of supporting itself faster thus shortening the shell thickening regime. Therefore, droplets which from shells with larger Young's Modulus produce larger particles with narrower shells.

Next the effect of different non-dimensional parameters on the particle morphology was evaluated. The effect of the dimensionless parameters, $\tau_{coag}{}^*$, $\tau_{diffn,p}{}^*$, J_A, τ_{shell}^*, and $\tau_{hc}{}^*$, on particle morphology was quantified by calculating the relative shell thickness of the final dried particle. J_A did not have any significant effect on the morphology of the particle. Figure 2-5 shows the calculated relative shell thickness of the final dried particles as the function of

$\tau_{diffn,p}{}^*$, τ_{shell}^*, $\tau_{hc}{}^*$ and τ_{coag}^* for initial solid fractions of 0.15 and 0.25. As can be seen from Figure 2-5(a), the relative shell thickness of the dried particle decreases with increase in $\tau_{diffn,p}{}^*$, which means that as the $\tau_{diffn,p}{}^*$ increases, formation of particles with hollow morphology is favored. A higher value of $\tau_{diffn,p}{}^*$ implies the higher ratio of characteristic diffusion time of solid particles as compared to the characteristic evaporation time of pure solvent. As the droplet evaporates, the concentration of the solids at the droplet's surface increases which results in the transport of solid towards the droplets center. If the diffusivity of solids within the droplets is very low, i.e. characteristic diffusion time of solids high, the transport of solid towards the droplet center will be slow and the concentration solids near the droplet surface will remain high as compared to the droplet's center. Therefore, formation of particles with hollow morphology is favored when $\tau_{diffn,p}{}^*$ is high.

Figure 2-5(b) shows the relative thickness of final dried particle as the function of τ_{shell}^*, while keeping the other dimensionless parameters constant. τ_{shell}^* is the ratio of characteristic time of shell thickening or the time for shell to become structurally capable of supporting itself to the evaporation time of pure droplet. It can be seen from Figure 2-5(b) that an increase in increase in τ_{shell}^* results in the increase in relative shell thickness of the final dried particle favoring the solid morphology. The high value of τ_{shell}^* implies that the shrinking of shell continues for relatively long time. For such cases, concentration throughout the droplet will reach high values, favoring the formation of solid particles. τ_{shell}^* depends on the mechanical properties of the shell such as permeability, Young's Modulus, Poisson's ratio, and viscosity of the solvent. In order to preferentially synthesize solid particles, τ_{shell}^* should be high during spray pyrolysis.
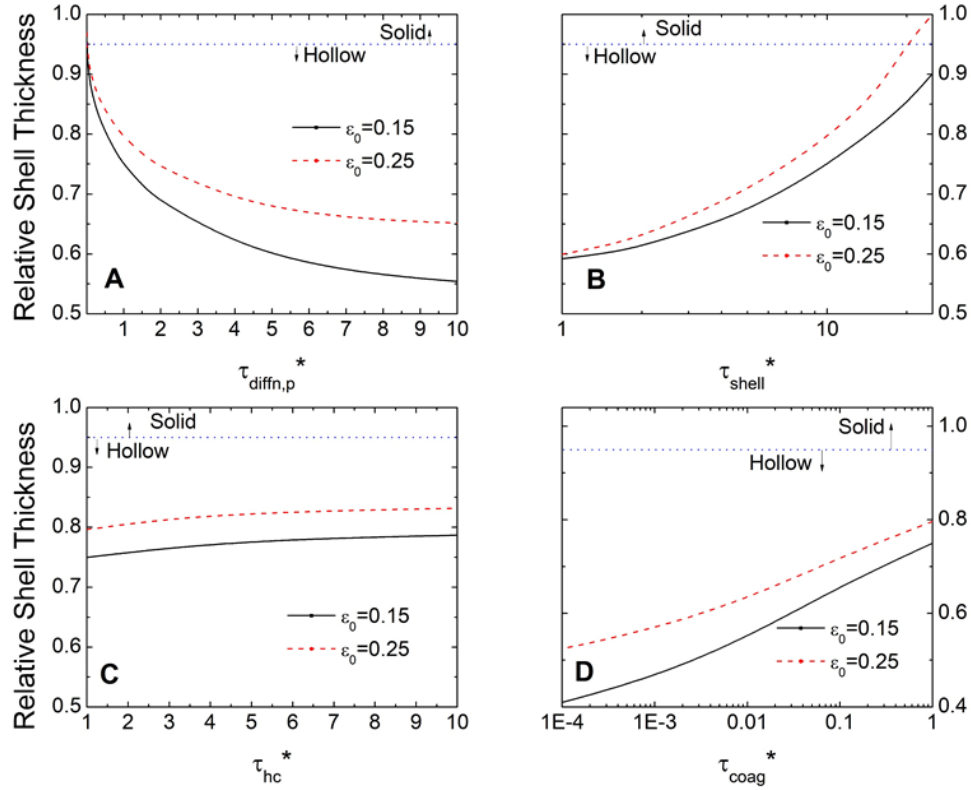
Figure 2-5 Calculated relative shell thickness of the final dried particles as the function of (a) $\tau_{diffn,p}^{*}$, (b) τ_{shell}^{*}, (c) τ_{hc}^{*} and (d) τ_{coag}^{*} for initial solid fraction of 0.15 and 0.25. The base case values for J_A, $\tau_{diffn,p}^{*}$, τ_{shell}^{*}, τ_{hc}^{*} and τ_{coag}^{*} are 5, 1, 10, 1 and 1 respectively.

Figure 2-5(c) shows the relative thickness of final dried particle as the function of τ_{hc}^{*} while keeping the other dimensionless parameters constant. τ_{hc}^{*} is the ratio of characteristic time to achieve wet bulb temperature to the characteristic evaporation time of pure solvent. It can be seen from Figure 2-5(c) that an increase in τ_{hc}^{*} results in the increase in relative shell thickness, favoring the formation of particles with solid morphology. This is because, when τ_{hc}^{*} is high, droplet temperature rises slowly resulting in slower evaporation of the droplets. τ_{hc}^{*} depends on the thermal properties of the droplet and the surrounding air.

Figure 2-5(d) shows the relative thickness of final dried particle as the function of τ^*_{coag} while keeping the other dimensionless parameters constant. τ^*_{coag} is the ratio of characteristic coagulation time to the characteristic evaporation time of pure solvent. It can be seen from Figure 2-5(d) that decrease in τ^*_{coag} results in the decrease in relative shell thickness, favoring the formation of particles with hollow morphology. This is because, when τ^*_{coag} is small, particles undergo collisions and coagulate faster to form aggregates with larger size, which restricts their mobility as particle diffusivity decreases with particle size. Therefore, the formation of particles with hollow morphology is favored when τ^*_{coag} is low. The simulations were also performed for the different initial concentrations of the solids within the droplet. It can be seen from Figure 2-5 that higher initial concentration of solids inside the droplet results in the formation of particles with higher shell thickness, thus favoring the formation of particles with solid morphology.
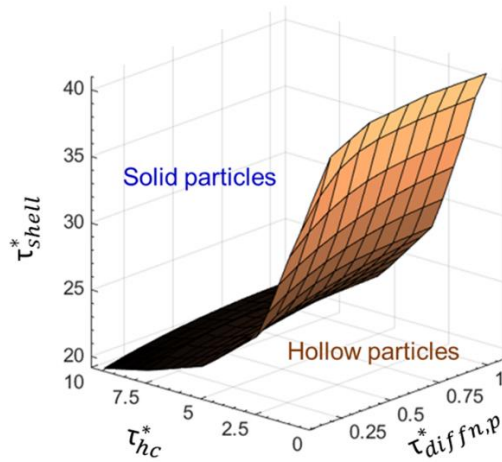
Figure 2-6 Surface plot representing the characteristic time combinations (, ,) respectively when relative thickness of shell is 0.95 (limiting case) for initial solid fraction of 0.15. for this simulation was chosen to be 1.

The developed model can be used for choosing the appropriate operating conditions during spray pyrolysis, such that the particles with the desired morphology can be synthesized. For the objective of guiding the operating conditions of the process, the combinations of the dimensionless parameters, $\tau_{diffn,p}{}^{*}$, τ_{shell}^{*}, and $\tau_{hc}{}^{*}$, were calculated, that would result in limiting case of particle morphology i.e. relative shell thickness = 0.95. Figure 2-6 show the surface plot representing the characteristic time combinations when relative thickness of shell is 0.95 (limiting case). It can be seen from the plot that any combination of $\tau_{diffn,p}{}^{*}$, τ_{shell}^{*}, and $\tau_{hc}{}^{*}$ lying above the limiting surface will result in the formation of particles with solid morphology, while any point below the surface will result in the formation of the particle with hollow morphology. This surface plot can be used for choosing conditions, required to synthesize desired particle morphology during the drying of droplet containing suspended solids.

2.3.2   Case II: Drying of droplet with dissolved solute

The second test case simulated is the drying of a droplet containing dissolved solute. It was assumed that initially droplet is free of any solid particles. Eventually as the droplet radius decrease due to evaporation, the concentration of solids in the droplet will increase due to precipitation, which is modelled in this case. The effect of the different parameters, i.e. the ambient temperature, diameter of particles suspended in droplets, initial volume fraction of particles in droplets and Young's modulus, on particle morphology is similar as Case I. The effect of all the dimensionless parameters listed in Table 2-3 on particle morphology was quantified by calculating the relative shell thickness of the final dried particle. The effects of $\tau_{diffn,p}{}^{*}$, τ_{shell}^{*}, $\tau_{hc}{}^{*}$ and τ_{coag}^{*} on particle morphology will be similar to Case I.
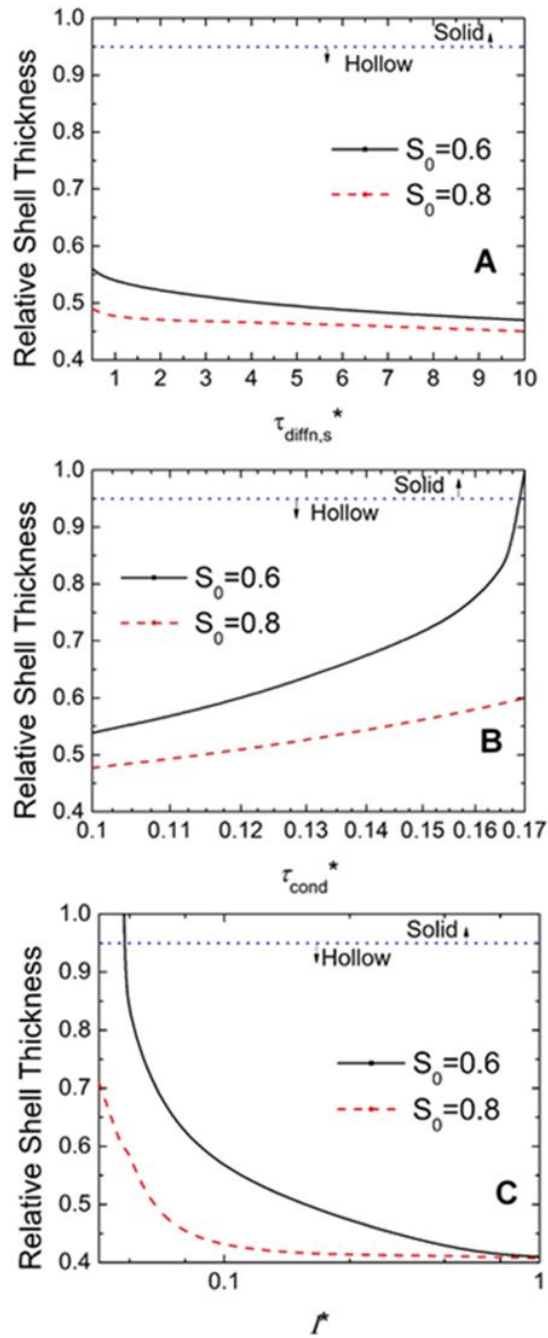
Figure 2-7 Calculated Relative shell thickness of the final dried particles as the function of (a) $\tau_{diffn,s}{}^*$, (b) τ_{cond}^*, and (c) I^* for initial saturation of 0.6 and 0.6. The base case values for $\tau_{diffn,s}$, $\tau_{diffn,p}{}^*$, τ_{shell}^*, $\tau_{hc}{}^*$, τ_{cond}^*, I^* and $\tau_{coag}{}^*$ are 1, 10, 1, 1, 0.1, 1, 0.1 and 1 respectively. The saturation mass fraction of solute was considered to be 0.16.

Figure 2-7 shows the calculated relative shell thickness of the final dried particles as the function of $\tau_{diffn,s}^*$, τ_{cond}^* and I^*, for the initial solute saturation ratio of 0.6 and 0.8. As can be seen from Figure 2-7(a), the relative shell thickness of the dried particle increases with decrease in $\tau_{diffn,s}^*$. A higher value of $\tau_{diffn,s}^*$ implies the higher ratio of characteristic diffusion time of dissolved solute as compared to the characteristic evaporation time of pure solvent. If the solute diffusion rate is higher, solute transport inside the droplet will be faster, resulting in relative decrease in difference between the droplet's surface and center concentration gradients during evaporation. This will result in precipitation of solute throughout the droplet volume, favoring the formation of solid dried particles. Conversely, if the solute diffusion rate is low, the concentration of solute will be higher near the droplet surface as compared to its center, resulting in precipitation only near the droplet's surface.

Figure 2-7(b) shows the relative thickness of final dried particle as the function of τ_{cond}^* while keeping the other dimensionless parameters constant. τ_{cond}^* is the ratio of characteristic condensation/growth time of solids in the droplets to the characteristic evaporation time of pure solvent. It can be seen from Figure 2-7(b) that the relative shell thickness of final dried particle decreases with decrease in τ_{cond}^*. This is because, when τ_{cond}^* is lower, particles inside the droplets will grow to larger size faster which limits their mobility. As a result of low mobility, particles remain concentrated near the droplet's surface and favors the formation of particles with hollow morphology.

Figure 2-7(c) shows the relative thickness of final dried particle as the function of I^*, while keeping the other dimensionless parameters constant. I^* is the dimensionless nucleation rate. It

can be seen from Figure 2-7(c) that the relative shell thickness of final dried particle increases with decrease in I^*. This is because, when I^* is small, precipitation rates of solids inside the droplets is lower. As a result, the solid fraction inside the droplets increases slowly while the droplet evaporates, and the final size of the dried droplet will be smaller, thus favoring the formation of solid particles.

2.4   Conclusions

Particles with different morphologies, mainly solid and hollow, can be produced using spray pyrolysis depending on the process conditions. A comprehensive model that accounts for simultaneous droplet heating, evaporation, and transport of solute and particles within the droplet was developed in this study, to investigate the effect of process conditions during spray pyrolysis on the resultant particle morphology. The model equations were also cast into dimensionless form for mathematical simplicity, and a sensitivity analysis was carried out to investigate the effects of important governing parameters on the morphology of the dried particle. The cases of drying of droplet with dissolved solute and the drying of droplet with suspended solids were analyzed. The sensitivity analysis showed that = dimensionless parameters, τ_{cond}^*, τ_{coag}^*, I^*, $\tau_{diffn,s}^*$, $\tau_{diffn,p}^*$, τ_{shell}^*, and τ_{hc}^*, which are a function of the surrounding gas properties as well as droplet's (solute, solid and solvent) physical and thermal properties have a strong influence on the morphology of the particle synthesized during spray pyrolysis. The impact of these governing parameters on particle morphology was evaluated in this study by quantifying their impact on the relative shell thickness of the final dried particle. These results can be used to help choose operating conditions during spray pyrolysis to produce particles of desired properties.

2.5   References

1. Li, S., Ren, Y., Biswas, P., & Stephen, D. T. (2016). Flame aerosol synthesis of nanostructured materials and functional devices: Processing, modeling, and diagnostics. *Progress in Energy and Combustion Science*, *55*, 1-59.

2. Kim, H., Kim, J., Yang, H., Suh, J., Kim, T., Han, B., Kim, S., Kim, D.S., Pikhitsa, P.V. & Choi, M. (2006). Parallel patterning of nanoparticles via electrodynamic focusing of charged aerosols. *Nature nanotechnology*, *1*(2), 117-121.

3. Kavadiya, S., Niedzwiedzki, D. M., Huang, S., & Biswas, P. (2017). Electrospray-Assisted Fabrication of Moisture-Resistant and Highly Stable Perovskite Solar Cells at Ambient Conditions. *Advanced Energy Materials*, *7*(18), 1700210.

4. Slowing, I. I., Trewyn, B. G., Giri, S., & Lin, V. Y. (2007). Mesoporous silica nanoparticles for drug delivery and biosensing applications. *Advanced Functional Materials*, *17*(8), 1225-1236.

5. Abokifa, A. A., Haddad, K., Fortner, J., Lo, C. S., & Biswas, P. (2018). Sensing mechanism of ethanol and acetone at room temperature by SnO 2 nano-columns synthesized by aerosol routes: theoretical calculations compared to experimental results. *Journal of Materials Chemistry A*, *6*(5), 2053-2066.

6. Astruc, D., Lu, F., & Aranzaes, J. R. (2005). Nanoparticles as recyclable catalysts: the frontier between homogeneous and heterogeneous catalysis. *Angewandte Chemie International Edition*, *44*(48), 7852-7872.

7. Nie, Y., Wang, W. N., Jiang, Y., Fortner, J., & Biswas, P. (2016). Crumpled reduced graphene oxide–amine–titanium dioxide nanocomposites for simultaneous carbon

dioxide adsorption and photoreduction. *Catalysis Science & Technology*, *6*(16), 6187-6196.

8. Wu, Z. S., Ren, W., Wen, L., Gao, L., Zhao, J., Chen, Z., Zhou, G., Li, F.& Cheng, H. M. (2010). Graphene anchored with Co3O4 nanoparticles as anode of lithium ion batteries with enhanced reversible capacity and cyclic performance. ACS nano, 4(6), 3187-3194.

9. Kacica, C. T., Wang, L. S., Chadha, T. S., & Biswas, P. (2018). Oriented, One-Dimensional Tin Dioxide–Titanium Dioxide Composites as Anode Materials for Lithium-Ion Batteries. *Energy Technology*, *6*(10), 1966-1974.

10. Karakoçak, B. B., Raliya, R., Davis, J. T., Chavalmane, S., Wang, W. N., Ravi, N., & Biswas, P. (2016). Biocompatibility of gold nanoparticles in retinal pigment epithelial cell line. *Toxicology in Vitro*, *37*, 61-69.

11. Singh, R., & Lillard Jr, J. W. (2009). Nanoparticle-based targeted drug delivery. *Experimental and molecular pathology*, *86*(3), 215-223.

12. Davis, M. E., Chen, Z., & Shin, D. M. (2010). Nanoparticle therapeutics: an emerging treatment modality for cancer. *Nanoscience and technology: A collection of reviews from nature journals*, 239-250.

13. Kennedy, L. C., Bickford, L. R., Lewinski, N. A., Coughlin, A. J., Hu, Y., Day, E. S., ... & Drezek, R. A. (2011). A new era for cancer treatment: gold-nanoparticle-mediated thermal therapies. *Small*, *7*(2), 169-183.

14. Volokitin, Y., Sinzig, J. D., De Jongh, L. J., Schmid, G., Vargaftik, M. N., & Moiseevi, I. I. (1996). Quantum-size effects in the thermodynamic properties of metallic nanoparticles. *Nature*, *384*(6610), 621-623.

15. Swihart, M. T. (2003). Vapor-phase synthesis of nanoparticles. *Current opinion in colloid & interface science*, *8*(1), 127-133.

16. Mädler, L. (2004). Liquid-fed aerosol reactors for one-step synthesis of nano-structured particles. *KONA Powder and Particle Journal*, *22*, 107-120.

17. Basak, S., Chen, D. R., & Biswas, P. (2007). Electrospray of ionic precursor solutions to synthesize iron oxide nanoparticles: modified scaling law. *Chemical engineering science*, *62*(4), 1263-1268.

18. Boissiere, C., Grosso, D., Chaumonnot, A., Nicole, L., & Sanchez, C. (2011). Aerosol route to functional nanostructured inorganic and hybrid porous materials. *Advanced Materials*, *23*(5), 599-623.

19. Pratsinis, S. E. (2010). Aerosol-based technologies in nanoscale manufacturing: from functional materials to devices through core chemical engineering. *AIChE journal*, *56*(12), 3028-3035.

20. Okuyama, K., & Lenggoro, I. W. (2003). Preparation of nanoparticles via spray route. *Chemical engineering science*, *58*(3-6), 537-547.

21. Gharsallaoui, A., Roudaut, G., Chambin, O., Voilley, A., & Saurel, R. (2007). Applications of spray-drying in microencapsulation of food ingredients: An overview. *Food research international*, *40*(9), 1107-1121.

22. Wegner, K., Schimmoeller, B., Thiebaut, B., Fernandez, C., & Rao, T. N. (2011). Pilot plants for industrial nanoparticle production by flame spray pyrolysis. *KONA Powder and Particle Journal*, *29*, 251-265.

23. Jain, S., Skamser, D. J., & Kodas, T. T. (1997). Morphology of single-component particles produced by spray pyrolysis. *Aerosol science and technology*, *27*(5), 575-590.

24. Abram, C., Mezhericher, M., Beyrau, F., Stone, H. A., & Ju, Y. (2019). Flame synthesis of nanophosphors using sub-micron aerosols. *Proceedings of the Combustion Institute*, *37*(1), 1231-1239.

25. Cho, Y. H., Kang, Y. C., & Lee, J. H. (2013). Highly selective and sensitive detection of trimethylamine using WO3 hollow spheres prepared by ultrasonic spray pyrolysis. *Sensors and Actuators B: Chemical*, *176*, 971-977.

26. Bang, J. H., Helmich, R. J., & Suslick, K. S. (2008). Nanostructured ZnS: Ni2+ photocatalysts prepared by ultrasonic spray pyrolysis. *Advanced Materials*, *20*(13), 2599-2603.

27. Ashkin, A., & Dziedzic, J. M. (1975). Optical levitation of liquid drops by radiation pressure. *Science*, *187*(4181), 1073-1075.

28. Chan, C. K., Flagan, R. C., & Seinfeld, J. H. (1998). In situ study of single aqueous droplet solidification of ceramic precursors used for spray pyrolysis. *Journal of the American Ceramic Society*, *81*(3), 646-648.

29. Schiffter, H., & Lee, G. (2007). Single-droplet evaporation kinetics and particle formation in an acoustic levitator. Part 1: Evaporation of water microdroplets assessed using boundary-layer and acoustic levitation theories. *Journal of pharmaceutical sciences*, *96*(9), 2274-2283

30. Tsapis, N., Dufresne, E. R., Sinha, S. S., Riera, C. S., Hutchinson, J. W., Mahadevan, L., & Weitz, D. A. (2005). Onset of buckling in drying droplets of colloidal suspensions. *Physical review letters*, *94*(1), 018302.

31. Lin, J. C., & Gentry, J. W. (2003). Spray drying drop morphology: experimental study. *Aerosol Science & Technology*, *37*(1), 15-32.

32. Baldelli, A., Power, R. M., Miles, R. E., Reid, J. P., & Vehring, R. (2016). Effect of crystallization kinetics on the properties of spray dried microparticles. *Aerosol Science and Technology*, *50*(7), 693-704.

33. Brenn, G., Wiedemann, T., Rensink, D., Kastner, O., & Yarin, A. L. (2001). Modeling and experimental investigation of the morphology of spray dryed particles. *Chemical engineering & technology*, *24*(11), 1113-1116.

34. Messing, G. L., Zhang, S. C., & Jayanthi, G. V. (1993). Ceramic powder synthesis by spray pyrolysis. *Journal of the American Ceramic Society*, *76*(11), 2707-2726.

35. Jayanthi, G.V.; Zhang, S.C; Messing, G.L. Modeling of solid particle formation during solution aerosol thermolysis: The evaporation stage. *Aerosol Sci. Technol.*, **1993,** *19*(4), 478-490.

36. Zhang, S. C., Messing, G. L., Lee, S. Y., & Santoro, R. J. (1994). Formation of solid and hollow spherical particles by spray pyrolysis. *MRS Online Proceedings Library (OPL)*, *372*.

37. Ozturk, A., & Cetegen, B. M. (2005). Experiments on ceramic formation from liquid precursor spray axially injected into an oxy-acetylene flame. *Acta materialia*, *53*(19), 5203-5211.

38. Basu, S., Jordan, E. H., & Cetegen, B. M. (2008). Fluid mechanics and heat transfer of liquid precursor droplets injected into high-temperature plasmas. *Journal of Thermal Spray Technology*, *17*(1), 60-72.

39. Mezhericher, M., Levy, A., & Borde, I. (2007). Theoretical drying model of single droplets containing insoluble or dissolved solids. *Drying technology*, *25*(6), 1025-1032.

40. Seydel, P., Blömer, J., & Bertling, J. (2006). Modeling particle formation at spray drying using population balances. *Drying Technology*, *24*(2), 137-146.

41. Mezhericher, M., Levy, A., & Borde, I. (2011). Modelling the morphological evolution of nanosuspension droplet in constant-rate drying stage. *Chemical Engineering Science*, *66*(5), 884-896.

42. Maurice, U., Mezhericher, M., Levy, A., & Borde, I. (2013). Drying of droplet containing insoluble nanoscale particles: Numerical simulations and parametric study. *Drying Technology*, *31*(15), 1790-1807.

43. Handscomb, C. S., & Kraft, M. (2010). Simulating the structural evolution of droplets following shell formation. *Chemical Engineering Science*, *65*(2), 713-725.

44. Friedlander, S. K. (2000). *Smoke, dust, and haze*. Oxford university press.

45. Biswas, P.; Wang, Y. The wonder world of aerosol science and engineering. Amazon Press, 2019, ISBN-13: 978-1533264954.

46. Dirksen, J. A., & Ring, T. A. (1991). Fundamentals of crystallization: kinetic effects on particle size distributions and morphology. *Chemical Engineering Science*, *46*(10), 2389-2427.

47. Minoshima, H., Matsushima, K., Liang, H., & Shinohara, K. (2001). Basic model of spray drying granulation. *Journal of chemical engineering of Japan*, *34*(4), 472-478.

48. Coulson, J. M., Richardson, J. F., Backhurst, J. R., & Harker, J. H. (1991). *Particle technology and separation processes* (Vol. 2). Headington Hill Hall, Oxford: Pergamon Press.

49. Timoshenko, S. P., & Gere, J. M. (2009). *Theory of elastic stability*. Courier Corporation.

50. Nešić, S., & Vodnik, J. (1991). Kinetics of droplet evaporation. *Chemical Engineering Science*, *46*(2), 527-537.

Chapter 3: Modeling vapor and droplet dynamics to predict the properties of PEDOT nanoparticles synthesized via aerosol vapor polymerization

Abstract

Aerosol Vapor Polymerization is a technique for synthesizing scalable submicron-sized particles of the conducting polymer poly(3,4-ethylenedioxythiophene) (PEDOT), which overcomes the problems associated with current state-of-the-art synthesis techniques and produces particle with very high processability and environmental stability. The synthesis using this technique is based on a hybrid approach utilizing an aerosol of aqueous oxidant droplets and monomer vapor to engineer a scalable synthetic scheme. The electrical conductivity of the PEDOT particles synthesized using aerosol vapor polymerization is strongly dependent on the reaction parameters and conditions, as any change in the reaction conditions affect the conjugation length of polymers in the synthesized particle. It is important to understand the different dynamic processes taking place in the reactor and the droplet during aerosol vapor polymerization, that influence the conjugation length of polymers in the synthesized particle, as it affects the conductivity of synthesized particles and hence their application. In this study, a model for monomer transport from gas phase to droplet, droplet heating and evaporation, transport of polymers and reaction within the droplet, was developed, to investigate the effect of different conditions during aerosol vapor polymerization on the average conjugation length in the synthesized particle. The effects of governing parameters like reactor temperature, oxidant and monomer concentration etc. on the average conjugation length and the conductivity of particle, were evaluated by performing a sensitivity analysis and the results were compared with the experimental observations. The developed model could help to choose efficient operating conditions during aerosol vapor polymerization process to produce particles of desired properties.

3.1   Introduction

Conductive polymers are the organic polymers that can conduct electricity. These polymeric materials have electrical properties such as conductivity similar to those of metals and inorganic semiconductors. Conductivity is imparted to these polymers through the use of a dopant ion, and the conjugated double bonds along the backbone of an otherwise insulated structure helps with conduction [1-3]. These compounds possess several advantages associated with conventional polymers over inorganic materials, such as ease of synthesis, light weight, tunable conductivity and flexibility in processing [4-5]. Because of these advantages, conducting polymers have become a leading material in polymer science. They have been used in artificial muscles [6], flexible electronic devices [7], organic light-emitting diodes [8], organic solar cells [9], commercial displays [10], rechargeable batteries [11], and sensors [12]. The fast-growing organic electronics industry has an estimated worth of more than \$75 billion by 2020 [13]. Poly(3,4-ethylenedioxythiophene) (PEDOT) has been recognized as one of the most promising CPs because of its remarkable electrical conductivity when doped with suitable dopants (300–600 $S.cm^{-1}$), physical and chemical stability, processibility, flexibility, superior optical transparency and low thermal conductivity, etc. [13-15]. PEDOT is generally considered a superior supercapacitor within the field of conjugated polymers [16]. The application of PEDOT as a supercapacitor requires mass transport of counterions into and out of the polymer structure. The efficiency of PEDOT-based supercapacitors is generally limited by slow ion diffusion [16]. Therefore, in recently years, the synthesis of PEDOT nanostructures which possess high surface area have obtained increasing research and attention. Several template-based synthesis techniques have been used to synthesize PEDOT nanostructures using templates such as surfactant micelles, or hard materials like mesoporous silica, silica microspheres, or polystyrene

[17-19]. Sacrificial templates are cumbersome and expensive, and the removal of these templates is destructive to the polymer structure. The ability to synthesize PEDOT nanostructures in a template-free fashion is ideal as it would reduce synthetic steps and cost.

There are very limited reports on template-free synthesis of PEDOT nanoparticles. Scalable aerosol technologies such spray pyrolysis/drying, chemical aerosol flow synthesis etc. have been readily utilized to synthesize inorganic nanoparticles with high throughput and low downstream processing steps. Zhang et al. 2015 [16] used spray pyrolysis approach to synthesize PEDOT nanoparticles, but the uncontrolled polymerization within the precursor solution before atomization lead to particles of low conductivity. To prevent uncontrollable polymerization in the precursor solution during spray pyrolysis, aerosol vapor polymerization technique was developed by Lu et al. 2019 (D'Arcy's group) [13]. The schematic of the experimental setup for aerosol vapor polymerization is shown in Figure 3-1. In aerosol vapor polymerization, an aerosol of oxidant droplets carried by nitrogen gas is generated by nebulizing iron(III) chloride (oxidant and polymerization initiator) aqueous solution using an ultrasonic transducer. Monomer vapor is produced by bubbling nitrogen gas into a heated reservoir containing the liquid 3,4-Ethylenedioxythiophene (EDOT). The oxidant droplet stream and the monomer vapor stream are mixed at the inlet of a coiled tubular glass reactor at 130 °C. Inside the reactor, droplet consisting of initiator (or oxidant) is surrounded by EDOT vapors. The droplet evaporates, and simultaneously, EDOT vapors move to the droplet where they polymerize and result in PEDOT nanoparticle formation. These synthesized PEDOT nanoparticles are eventually collected in ethanol filled collectors at the reactor's outlet. In this technique, the limitations of spray synthesis due to uncontrolled polymerization in the precursor solution [16] was overcome by delivering

each reactant (monomer and oxidant) independently to the reactor [13]. Aerosol vapor polymerization (AVP) is a scalable continuous batch-processing technique that can produce spherical submicron-sized PEDOT particles. PEDOT particles synthesized by Lu et al. 2019 [13] possessed very high electrical conductivity. The synthesized particles also exhibited extended chemical and physical stability characterized by a high doping level and surface charge that enabled solution processing without the need for surfactants.
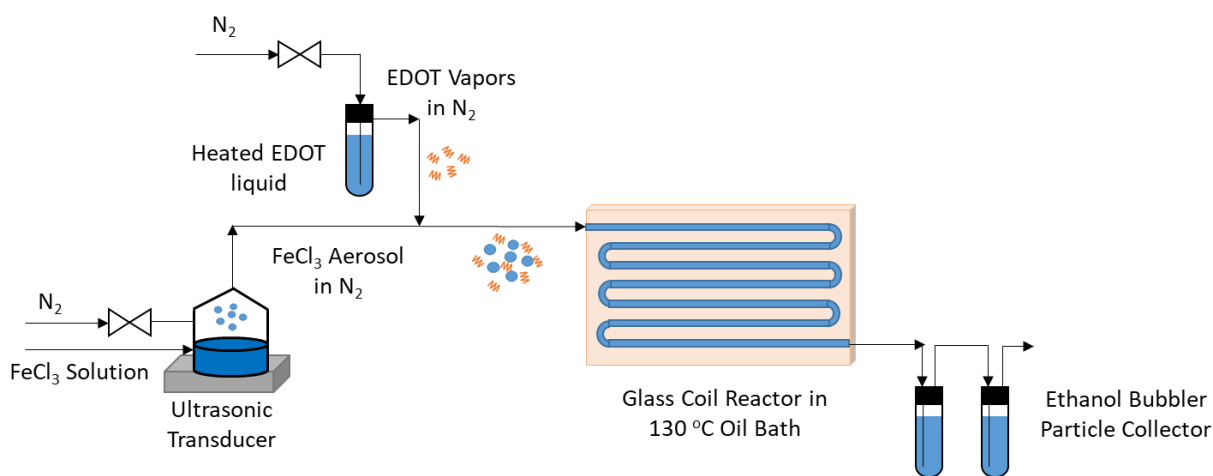
Figure 3-1 The schematic of the experimental setup for PEDOT synthesis using aerosol vapor polymerization.

PEDOT particles with varying electrical conductivity can be synthesized via aerosol vapor polymerization, depending on the properties of precursors, carrier gas flow rates, residence time, and the temperature of the reactor etc. Lu et al. (2019) [13] observed the formation of particles of different conductivities, synthesized using aerosol vapor polymerization process, by varying the ratio of oxidant and monomer entering the reactor. It was observed that the conductivity of the synthesized PEDOT particles decreased with the decrease in oxidant to monomer ratio [13]. The high electrical conductivity at higher oxidant to monomer ratio was attributed to longer

conjugation length. It was observed by Lu et al. (2019) [13], that a 7.5 oxidant-to monomer ratio produces a doped polymer of long conjugation length and blue PEDOT particles, whereas a ratio of 0.1 lead to purple PEDOT particles comprising short chained oligomers [13]. It can be concluded from this study that the properties of the PEDOT nanoparticles synthesized using AVP are strongly dependent on the reactor conditions and parameters. Therefore, it is crucial to understand the different vapor and droplet dynamic processes taking place in reactor that influence the conductivity of the particle, in order to have better and more precise control on conductivity of the particles synthesized via AVP.

Since, AVP is a relatively new synthesis technique, there aren't any modeling studies in literature to understand the vapor and droplet dynamics within the reactor, to predict the properties of synthesized PEDOT particles, and have better control over the synthesis process. However, numerous single droplets drying models have been developed over the past few decades for particle formation during spray pyrolysis process [20-29]. We recently developed a comprehensive model to predict particle morphology during spray pyrolysis (refer to Chapter 2), which accounted for simultaneous droplet heating, evaporation, transport of solute and particles within the droplet as well as shell formation and thickening. These models, for particle formation during spray drying, could be modified further by accounting for vapor phase dynamics of monomers and polymerization kinetics in the droplet to understand the PEDOT particle formation during AVP.

In this study, a comprehensive and generalized model accounting for monomer transport from gas phase to droplet, droplet heating and evaporation, transport of polymers and polymerization reaction within the droplet, was developed, to investigate the effect of different conditions during

90

aerosol vapor polymerization on the average conjugation length and the conductivity of the synthesized particle. The effects of governing parameters like temperature, oxidant and monomer concentration etc. on the average conjugation length in particle were evaluated by performing a sensitivity analysis, and the results were compared with the experimental observations. The developed model could help to choose efficient operating conditions during aerosol vapor polymerization process to produce particles of desired properties.

3.2 Model Development
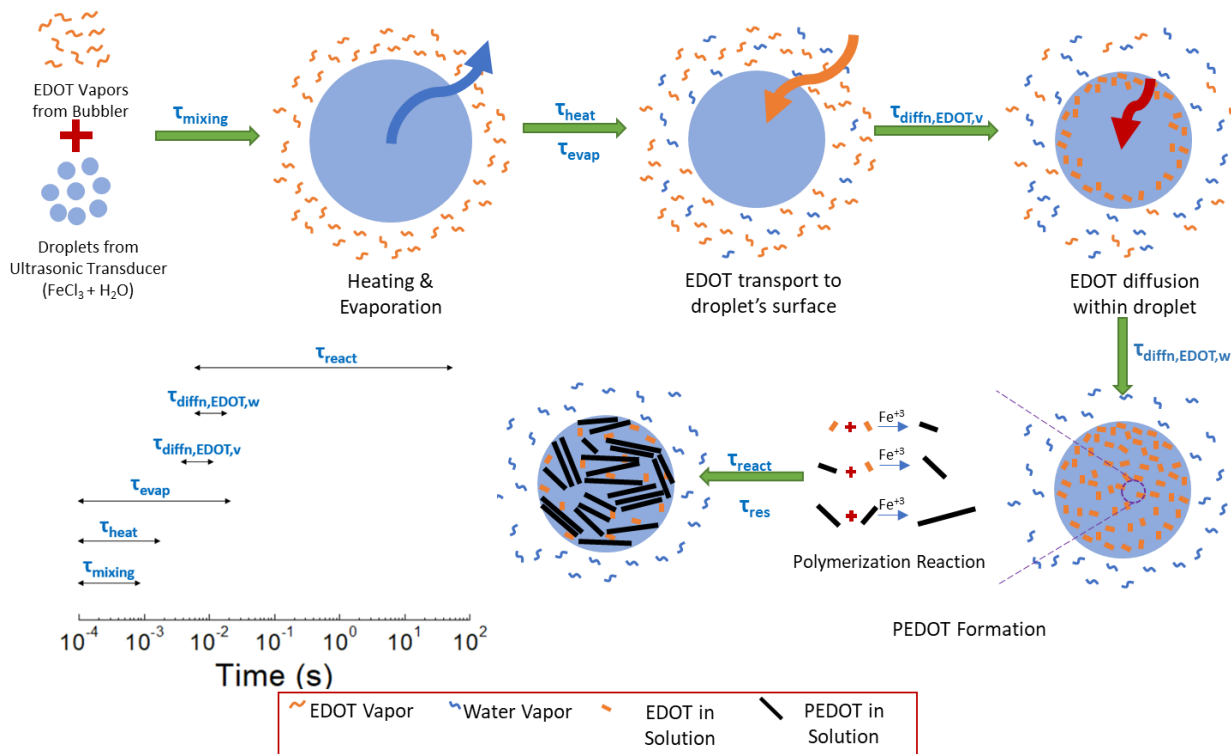
Figure 3-2 Schematic diagram of the various processes taking place during aerosol vapor polymerization.

Figure 3-2 is a schematic representing different processes taking place inside the reactor and the droplet during PEDOT synthesis via aerosol vapor polymerization. The aerosol droplets consisting of aqueous solution of iron chloride (III) (oxidant and polymerization initiator) are atomized using an ultrasonic transducer. The monomer vapors of EDOT are generated by bubbling nitrogen gas through heated EDOT liquid. The temperature of the liquid EDOT is controlled to regulate the amount of EDOT vapor going to the reactor. The aerosolized droplet stream and the monomer vapor stream are mixed together just before they enter the reactor. Inside the reactor, the droplet is heated. As the result the droplet evaporation starts which will result in decrease in droplet size due to loss of water (solvent). Due to evaporation, the

92

concentration of water vapor in the gas surrounding the droplet increases, which will increase the relative humidity (RH) of the carrier gas surrounding the droplet. Eventually due to increase in RH, the vapor pressure of water at the droplet surface will reach in equilibrium with the environment, and the further evaporation will stop. Simultaneous to droplet heating and evaporation, EDOT vapors will be transported by diffusion from carrier gas to the droplet's surface, and the rate of transport will be governed by Henry's Law. As a result, EDOT concentration inside droplet will start to increase near the surface. This will result in concentration gradients inside droplet and will cause the diffusion of EDOT towards the droplet's center. Inside the droplet, due to presence of EDOT and the initiator, the polymerization reaction will start, and the polymers will grow in size by step growth polymerization process. Polymers chains of different chain length will be present throughout the droplet. As the reaction progresses, these chains grow and interact with each other due to van der waal forces and pi-pi interaction. These interactions make the particle very stable, and it does not decompose into individual polymer chains when suspended in any solvent. Thus, a single droplet results in formation of one particle. These PEDOT droplets are eventually collected at the reactor's outlet in ethanol filled collectors by bubbling.

In this study, both gas phase (carrier gas) and the droplet phase are modeled, to fully understand the complex dynamics taking place during AVP. The gas phase is considered to be made of three components: 1) EDOT vapors, 2) water vapors from evaporation, and 3) suspended droplets. The droplet phase is also considered to be made of three components: 1) solvent (water), 2) dissolved species which consists of iron chloride (II and III), and 3) undissolved species which comprise of EDOT and PEDOT polymer of chains. The solvent and dissolved solute was assumed to be an

ideal binary solution. Thus, the droplet further has two phases i.e. the continuous phase, which is the ideal binary mixture of solute and solvent, and the solid phase, which comprises of undissolved species inside the droplet i.e. EDOT and PEDOT chains. It is assumed that the droplets maintain spherical symmetry throughout the drying process and that the temperature of the droplet is spatially uniform. Different aspects of model formulation are discussed in this section.

3.2.1   Droplet heating and evaporation

The heat transferred to the droplet results in the increase in droplet temperature with time. It is also used as the latent heat of vaporization as the droplet evaporates. The evolution of droplet temperature with time can be evaluated using the energy balance equation, given by [30]:

$$A(t)\, h\, (T_\infty - T_d(t)) = m(t)S\frac{dT_d(t)}{dt} + L\frac{dm(t)}{dt} \tag{3.1}$$

where, A is the surface area of the droplet, h is the heat transfer coefficient, T_∞ is the surrounding gas temperature, T_d is the droplet temperature, m is the mass of droplet, S is the specific heat capacity of the droplet and L is the latent heat of vaporization of the solvent. The term of left-hand side is the total heat transferred to the droplet from the surroundings. The first term on right-hand side refers to the transferred heat which results in the increase in droplet temperature, while the second term refers to the rate at which heat transferred to droplet is used as latent heat to evaporate the solvent. In majority of the spray pyrolysis systems, droplet move with no relative velocity with respect to carrier gas. Therefore, Nusset number can be assumed to be

94

$2\ln(1 + B_T)/_{B_T}$, where B_T is the heat transfer Spalding number which takes into consideration

the Stefan flow in the droplet boundary layer. The heat transfer coefficient is given by [30]:

$$h = {}^{2k}/_{Nu\ R(t)} \qquad (3.2)$$

Here, k is the thermal conductivity of the surrounding gas and R is the droplet radius. The rate of

change of droplet radius, moving with the same velocity as the surrounding gas, is given by [31]:

$$\frac{dR(t)}{dt} = \frac{D_v v_m}{R(t) k_B} \left(\frac{p_\infty}{T_\infty} - \frac{p_d}{T_d}\right) F(Kn) \qquad (3.3)$$

where D_v is the diffusivity of solvent vapor in carrier gas, k_B is the Boltzmann constant, p_∞ is

the partial pressure of solvent vapor in the surrounding gas, p_d is the pressure of solvent vapor at

the droplet's surface and F is the Fuchs-Sutugin correction factor for transport to/from a droplet

surface in the transition-free molecule regime, given by [31]:

$$F(Kn) = \frac{1 + Kn}{1 + 1.71Kn + 1.333Kn^2} \qquad (3.4)$$

where Kn is the Knudsen number ($= 2\lambda/d_p$, where λ is the mean-free-path of the vapor

molecules). The pressure of solvent vapor at droplet's surface can be given by:

$$p_d(t) = p_{sat}\big(1 - \varepsilon(R, t)\big) * \big(1 - x_s(R, t)\big) \tag{3.5}$$

Here, p_{sat} is the saturation pressure of solvent, $\varepsilon(R, t)$ is the volume fraction of solids at droplet's surface, and $x_s(R, t)$ is the mole fraction of dissolved solute at the droplet's surface.

3.2.2   EDOT transport to the droplet

Initially, droplet consisting of the aqueous solution of iron chloride (III) will be surrounded by EDOT vapors in the carrier gas. EDOT vapors will be transported from the carrier gas to the droplet surface and the flux of EDOT vapors to the droplet surface ('F') is given by [31]:

$$F = \frac{4\pi D_{EDOT,v} R\,(t)}{k_B} \left(\frac{p_{\infty,EDOT}}{T_\infty} - \frac{p_{d,EDOT}}{T_d} \right) \tag{3.6}$$

where $D_{EDOT,v}$ is the diffusivity of EDOT vapor in carrier gas, k_B is the Boltzmann constant, $p_{\infty,EDOT}$ is the partial pressure of EDOT vapor in the surrounding gas, $p_{d,EDOT}$ is the pressure of EDOT vapor at the droplet's surface. The pressure of EDOT vapor at the droplet's surface is governed by Henry's Law:

$$p_{d,EDOT}(t) = \frac{c_{d,EDOT}(t)}{H} \tag{3.7}$$

where, $c_{d,EDOT}$ is the concentration of the suspended EDOT monomer at the droplet's surface and H is the Henry's constant (4.52×10^{-6} bar-m^3/mole). Using gas phase mass balance and

equation 3.6, the evolution of EDOT vapor concentration in the carrier gas could be evaluated as the function of time. The flux represented by equation 3.6 also serve as boundary condition for evolution of EDOT concentration inside the droplet.

3.2.3 Dissolved phase and solid phase evolution inside droplet

The continuous phase is assumed to be an ideal binary solution of solute (ferrous and ferric chloride) dissolved in solvent. The droplet initially consists of only ferric ions while the ferrous ions are the byproduct of polymerization and oxidation reaction, and are inert. So, only the evolution of concentration of ferric ions was modeled using transport equations. The evolution of ferric ion concentration (or solute) inside the droplet can be described by volume averaged transport equation for solute. The differential mass balance for the solute can be written as:

$$\frac{\partial[\rho_c(r,t)w_s(r,t)]}{\partial t} + \frac{1}{r^2}\frac{\partial}{\partial r}\left[-r^2 D_s \rho_c(r,t)\frac{\partial}{\partial r}[w_s(r,t)]\right] - r_{Fe+3} = 0 \qquad (3.8)$$

where, r is the radial direction, ρ_c is the continuous phase density, w_s is the mass fraction of solute in the continuous phase, D_s is the solute diffusivity in solvent, and ρ_s is the density of solute. The first term on left hand side of this equation represents the rate of change of the density of solute dissolved in the continuous phase. The second term accounts for the diffusion of solute, driven by the concentration gradients inside the droplet caused by solvent evaporation. The last term accounts for the loss of ferric ions from the continuous phase due to polymerization, and oxidation reaction. The solid phase was modeled by using similar transport equation given by:

$$\frac{\partial [N_i(r,t)]}{\partial t} + \frac{1}{r^2}\frac{\partial}{\partial r}\left[-r^2 D_i \frac{\partial}{\partial r}[N_i(r,t)]\right] - r_i = 0 \tag{3.9}$$

where, N_i is the number concentration of PEDOT polymer of chain length 'i', D_i is the diffusivity of PEDOT polymer of chain length 'i', and r_i refers to the change in concentration due to polymerization reaction.

3.2.4   Polymerization Kinetics

During polymerization, monomer vapor is oxidized upon contact with ferric ions dissolved in suspended water droplets, resulting in the formation of monomer radical cations (Figure 3-3). The radical cations combine to form oligomers. Radical coupling promotes the assembly of oligomers and formation of the conjugated backbone via kinetically controlled deprotonation where water serves as the proton scavenger [13]. The oxidation of polymer (or monomer)to the radical cation is the slowest and the rate determining step, as it exhibits the highest-energy barrier [32]. The coupling of radical cations, and the following deprotonation step are several orders of magnitude faster than the rate determining step [32]. So, in generalized form, the rate limiting step is formation of radical cation from polymer of chain length '*i*'. These radical cation of length '*i*' will combine with radical cation of length '*j*' to form polymer of length '*i+j*'(fast step). The reactions can be represented as follows:

$$P_i + Fe^{+3} \xrightarrow{ki} P_i^* + Fe^{+2} \qquad (Rate\ Limiting) \tag{3.10}$$

$$P_i^* + P_j^* \rightarrow P_{i+j} \qquad (Fast) \tag{3.11}$$
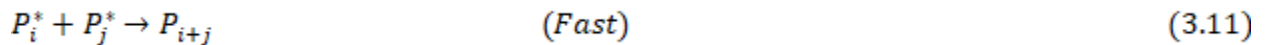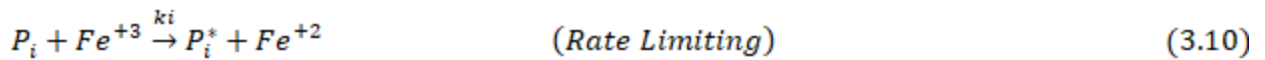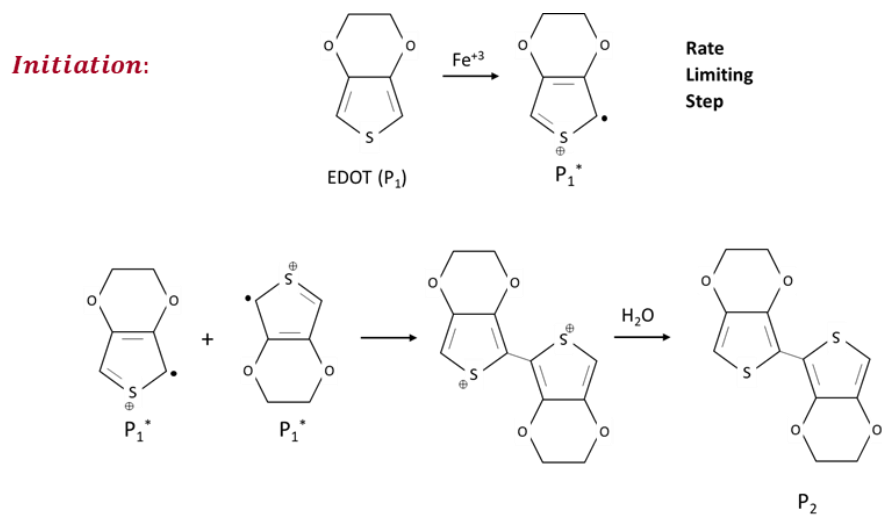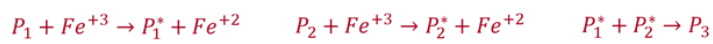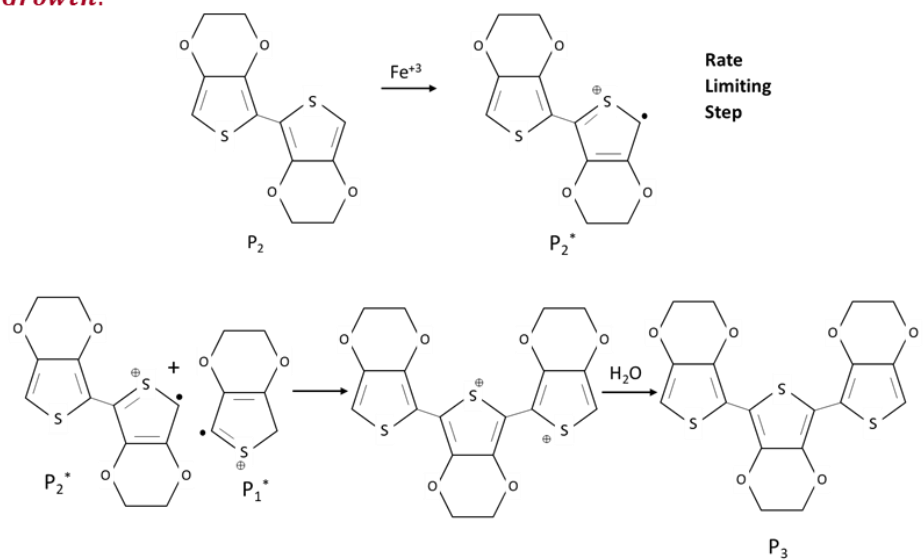
Figure 3-3 Schematic representing PEDOT polymerization kinetics.

Equation 3.10 represents the rate limiting step, while equation 3.11 is the combination of radical coupling and deprotonation steps which are very fast. Here, P_i refers to polymer of chain length 'i' and P_i^* refers to radical cation of chain length 'i'. k_i is the rate constant of the rate limiting step, which is the oxidation of EDOT and PEDOT oligomers to radical cations. The rate of oxidation to form radical cation depends on the chain length. The oxidation of the oligomer (i.e.

99

chains of length greater than equal to 2) is energetically favorable compared to that of EDOT. This can be related to a higher HOMO level of the oligomer in comparison to the monomer due to a longer π conjugation length [32]. Kirchmeyer & Reuter (2005) reported that the rate constants 'k_i' are similar for oligomers of chain length $i \geq 2$, and $k_1 < k_i$ for all $i \geq 2$ [32].

The rate of generation of radical cation can be quantified using the following rate expression:

$$\frac{dN_i^*}{dt}_{generation} = k_i[N_i][Fe^{+3}] \tag{3.12}$$

Here, N_i^* refers to number concentration of radical cation of chain length 'i'. The steady-state approximation method was used to derive a rate law expression. It was assumed that since radical cations are intermediate species in the reaction mechanism, they are consumed as quickly as they are generated. Thus, the rate of change of concentration of radical cation can be expressed as:

$$\frac{dN_i^*}{dt} = \frac{dN_i^*}{dt}_{generation} + \frac{dN_i^*}{dt}_{consumption} = 0 \tag{3.13}$$

The radical cation of length 'i' combine with radical cation of length 'j' to form polymer of length '$i+j$'. It was assumed that the combination reaction (3.11) is not selective i.e., it is probability of combination of radical cation with other cation is independent of their chain length. Thus, the rate of formation ($\dot{N}_{i,j}$) of polymer of chain length '$i+j$' by the combination of chains of length 'i' and 'j' is given by:

$$N_{ij} = \frac{\frac{dN_i^*}{dt}\Big|_{generation} \times \frac{dN_j^*}{dt}\Big|_{generation}}{\sum_k \frac{dN_k^*}{dt}\Big|_{generation}} \qquad (3.14)$$

By using the population balance, the rate of change in concentration of polymer chains can be written as:

$$\frac{dN_k}{dt} = \left(\sum_{i+j=k} \alpha \dot{N}_{ij}\right) - \sum_{i+j=k} \dot{N}_{ij} \qquad (3.15)$$

Here, N_k represents the number concentration of polymer of chain length 'k' (P_k). The first term on right hand side represents the rate of formation of polymer of chain length 'k' by the combination of two radical cations. In equation 3.15, $\alpha = 1$, if $i \neq j$ and $\alpha = \frac{1}{2}$, if $i = j$. The second term on right hand side represents the rate of loss of polymer of chain length 'k' due to formation of radical cation and further reaction.

It can be seen from equation 3.10, one Fe^{+3} ion is consumed during formation of a radical cation. Thus, formation of one P_{i+j} by generation and subsequent combination of P_i^* and P_j^* will involve two Fe^{+3} ion. Fe^{+3} also gets consumed in oxidative doping of PEDOT chain. Therefore, to account for Fe^{+3} concentration, it is important to know the amount Fe^{+3} that is consumed in the oxidative doping step. Kim and Zozoulenko (2019) used DFT to determine the oxidation level of PEDOT chains when doped [33]. For chain lengths >6, 33% oxidation level was reported. Therefore, in the model, it is important to consider that when polymers of chain length <6 are

formed, additional Fe^{+3} is consumed due to oxidative doping. Therefore, the rate of change in Fe^{+3} ion concentration is given by:

$$\frac{d[Fe^{+3}]}{dt} = -\sum_i \sum_j \dot{N}_{ij} - r_{doping} \tag{3.16}$$

r_{doping} in this equation refers to the rate of consumption of Fe^{+3} ions during oxidative doping. The expression of r_{doping} could be evaluated by doing simple charge balance, by assuming the 33% oxidation level for PEDOT chains (for chain lengths >6).

To see how the polymerization reaction proceeds, the set of equations 3.15 and 3.16 need to be solved simultaneously. Equation 3.15 is a set of equations representing evolution of concentration of polymer of all the possible chain lengths, which can vary from 1 to theoretically infinity. The computational expense of the model increases, if the polymerization reaction proceeds for a long time.
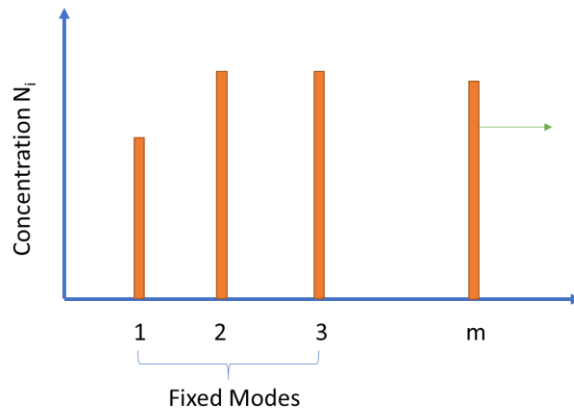
Figure 3-4 Schematic representing the formulation of modal method.

In order to reduce the number of equations while maintaining accuracy, modal method was used to numerically solve equation 3.15. In this method, equations for polymer of chain lengths 1, 2 and 3 were considered, while the larger polymers were all lumped to one size chain size 'm'. 'm' grows as the reaction progresses. Thus, three fixed mode and one growth mode is considered in this numerical formulation. The schematic representing the formulation of modal method used here is shown in Figure 3-4. If the polymer formed via combination from mode 'i' and 'j' lies between two nodes, the new polymer is split into two adjacent nodes in accordance with mass conservation. The modal scheme is discussed in more detail in Appendix A and the details for apportionment are also discussed in Appendix A. This reduces the number of variables to be solved for (N_1 N_2 N_3 N_m and m & $[Fe^{+3}]$). The expression for r_s and r_i in equations 3.8 and 3.9 are given by rates in equations 3.15 and 3.16. The accurate values of reaction rate constants are not known for the PEDOT synthesis by the polymerization of EDOT in the presence of $Fe+^3$ ions in an aqueous solution. Lu et al. (2019) reported the reaction time scale for PEDOT polymerization to be the order of 10 s, at the reactor temperature of 130 ^0C [13]. Rough estimates for k_1 (16 $cm^3mol^{-1}s^{-1}$) and k_2 (20 $cm^3mol^{-1}s^{-1}$) were used in this work, so that the reaction time comes out to be of the similar order, as reported by Lu et al. (2019) [13].

3.2.5 Simulation Plan

Table 3-1 Simulation Plan

I. Model Verification	• Mass Balance Confirmation • Comparison with experimental results of Lu et al. 2019

		The simulations were performed for experimental conditions from Lu et al. 2019. The following were evaluated:
II.	Base Case Simulation	▪ Droplet evaporation & heating ▪ Transport of EDOT from gas phase to droplet ▪ Evolution of concentration of EDOT inside droplet (average and radial) ▪ Time scale analysis and particle morphology prediction
		The effect of following was evaluated on avg. chain length in particle and hence conductivity:
III.	Sensitivity Analysis	▪ Oxidant to Monomer ratio ▪ Residence time in the reactor ▪ Reactant concentration

The equations listed in Section 3.2.1-3.2.3 are solved simultaneously to account for all the processes taking place during aerosol vapor polymerization. The simulation plan is listed in Table 3-1. Before the system analysis, the consistency of the model was first established by validating its numerical scheme by doing mass balance verifications. The conditions used in work done by Lu et al. (2019) [13] were used as the base case in this study, and the model results were validated against the experimental observations. For the base case, the evolution of droplet size and relative humidity inside the reactor was evaluated, and the time scales for evaporation and droplet heating were discussed. Then, the transport of EDOT from gas phase to droplet was discussed. Following that, evolution of average and radial concentration inside the droplet was examined, to determine the EDOT transport and diffusion time scale inside the droplet. The comparison of different timescales of processes taking place during AVP was done, and the predictions regarding synthesized particle morphology were made. Next, the simulations were

carried out to investigate the effect of different governing parameters on the average chain length of polymers in the synthesized nanoparticle. The average chain length of polymers in the synthesized particles was evaluated as it is representative of the conjugation chain length in the synthesized particles on which the conductivity of the particle depends. The effect of different parameters, like residence time, oxidant to monomer ratio, reactant concentration, number concentration of droplets, reactor temperature etc., on the conductivity of the synthesized PEDOT particle, was examined.

3.3   Results and Discussion

Table 3-2 Simulation Parameters

Initial Relative Humidity	0
Ultrasonic Nebulizer Generation Rate	7 ml/min
Flow Rate through Monomer Bubbler	2000 sccm
Flow Rate through Ultrasonic Diffuser	2000 sccm
Droplet Size generated by Ultrasonic Diffuser	1.5 micrometers
Initial Fe^{+3} Concentration	0.266 M
Temperature of EDOT Bubbler (Affects initial EDOT vapor concentration)	90^0C
Temperature inside the glass coil reactor	130^0C
Residence Time	20 s

The numerical scheme of this model was validated by doing mass balance verification and by comparing to experimental results of Lu et al. 2019 [13]. The comparison with experimental observations is discussed later in this section. After establishing the numerical consistency of the present model, using the experimental conditions from Lu et. al 2019 as base conditions, the relative timescales of different taking place during the aerosol vapor polymerization were established. The parameters used in the base case simulations are listed in Table 3-2.

3.3.1   Timescale Analysis

Figure 3-5 shows the evolution of the droplet temperature, the relative humidity (RH) of the carrier gas surrounding the droplets inside the reactor, and the evolution of the droplet diameter as the function of time. Initial RH of the carrier gas entering the reactor is close to zero. As the

droplets enter the heated reactor, the temperature of the droplets increases. The increase of droplet temperature is very fast as can be seen from Figure 3-5 A , and the temperature of droplet saturates within 0.5 ms. The heating of the droplets, and the resulting difference in RH at droplet's surface and the carrier gas, results in the evaporation of the droplets and the reduction of their size. As the droplets evaporate, the concentration of the water vapor in the carrier gas surrounding droplets will increase. Hence, the driving force for the droplet evaporation will decrease with time. As can be seen from Figure 3-5 B and C , as the RH of the droplets increases to 1, equilibrium is reached, and there is no further decrease in droplet diameter. It can be seen from Figure 3-5 B and C, that the evaporation time scale is of the order of 1 ms. The final size of the evaporated droplet calculated from this simulation was found to be 843 nm, and it agrees well with experimentally observed average final particle size 750 nm by Lu et al. (2019) [13].
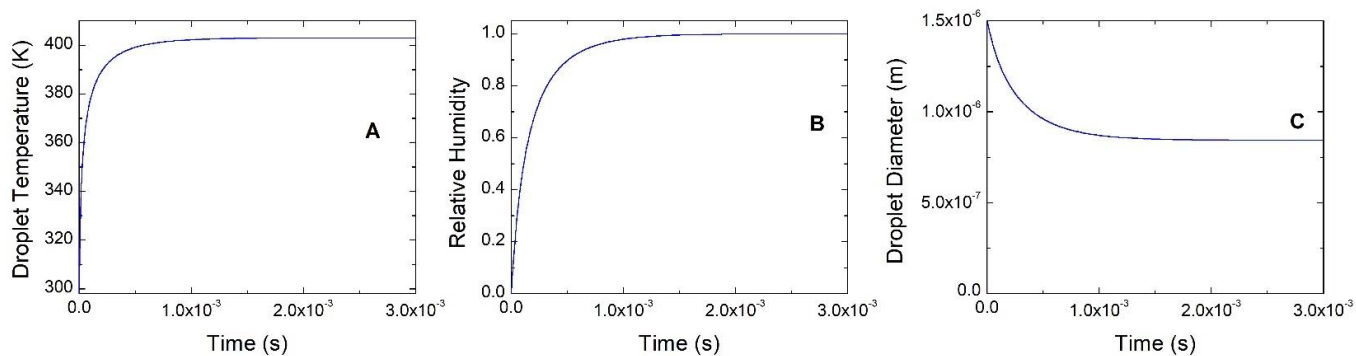
Figure 3-5 Evolution of a) droplet temperature, b) relative humidity of the carrier gas surrounding the droplets inside the reactor, and c) droplet diameter as the function of time. The parameters used are listed in Table 3-2.

Next, the transport of EDOT vapors from the carrier gas to the droplet was considered. The initial concentration of EDOT vapor in the carrier gas was calculated from the temperature of liquid EDOT bubbler, by using Clausius–Clapeyron relation. Figure 3-6 shows the evolution of

EDOT vapor concentration in the carrier gas surrounding the droplet, and the average concentration of EDOT monomers inside the droplets. Initially the EDOT concentration inside the droplets is zero. The transport of EDOT vapor from the carrier gas to the droplet surface occurs, and the concentration of EDOT vapor in the carrier gas eventually decrease with time. It can be seen from Figure 3-6 that the complete transport of EDOT vapors from gas phase to droplet takes place in ~0.05 s.
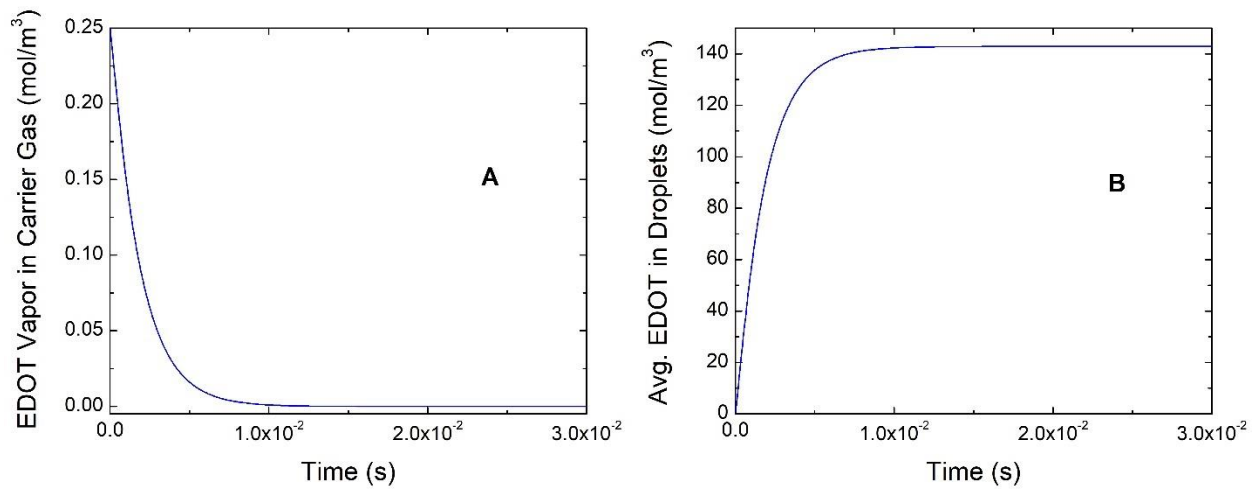
Figure 3-6 Evolution of a) EDOT vapor concentration in the carrier gas surrounding the droplet, and b) the average concentration of EDOT monomers inside the droplets. The parameters used are listed in Table 3-2.

Figure 3-7 shows the evolution of EDOT concentration inside the droplet as the function of radial position, at t = 0.1 ms. and at t = 5 ms. Initially, the EDOT concentration inside the droplets is zero. As the transport of EDOT vapor from carrier gas to the droplets' surface occurs, the concentration at the droplet's surface increases. The concentration at the droplet surface at t = 0.1 ms is therefore higher than the concentration at the center. The concentration gradient between the center of the droplet, and its surface results in the diffusion of EDOT towards the center of the droplet. It can be seen from Figure 3-7 that the concentration of EDOT becomes

uniform inside the droplet. Thus, the internal diffusion of EDOT inside the droplet is very fast and the characteristic diffusion time for internal diffusion is less than 5 ms.
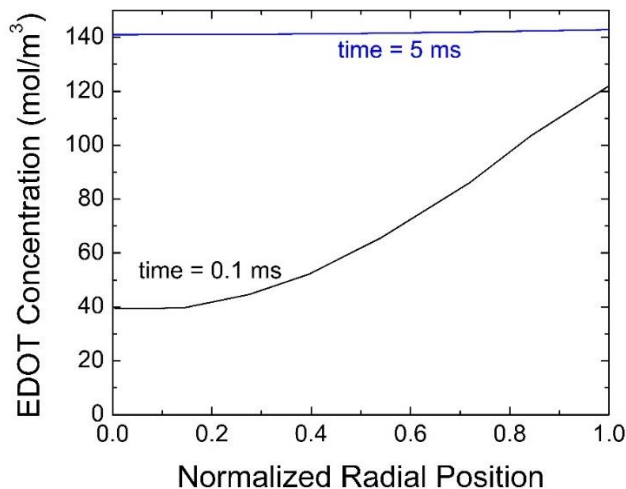
Figure 3-7 Evolution of EDOT concentration inside the droplet as the function of radial position, at t = 0.1 ms and at t = 5 ms. The parameters used are listed in Table 3-2.

Based on the relative characteristic times of different dynamic processes happening during AVP, comments can be made on the morphology of the synthesized particles. Lu et al. (2019) reported the characteristic time for polymerization reaction to be the order of 10 s [13]. The characteristic times for heating, evaporation, diffusion of EDOT from gas to vapor, and internal diffusion of EDOT are 0.5 ms, 1 ms, 5 ms, and < 5 ms for our base case simulation. The reaction time is a few orders of magnitude larger than other time scales. Therefore, it can be concluded that before any significant reaction take place, the droplet is equilibrated (no change in diameter), and there will be constant concentration of EDOT distributed throughout the droplet volume. Since EDOT will be distributed uniformly throughout the droplet before any significant reaction, the formation of solid particles will take place, provided residence time inside the reactor is enough.

3.3.2   Sensitivity Analysis

The developed model was then used to quantify the effect of different process parameters on the conductivity of PEDOT particles synthesized using aerosol vapor polymerization. The average chain length of polymer in the synthesized PEDOT particles was used as a representative of particle conductivity, since the conductivity of the PEDOT particle depends on the conjugation chain length which is a function of average polymer chain length. The parameters evaluated here are listed in Table 3-1. The simulation parameters were taken to be same as base case parameters (Table 3-2) unless specified.
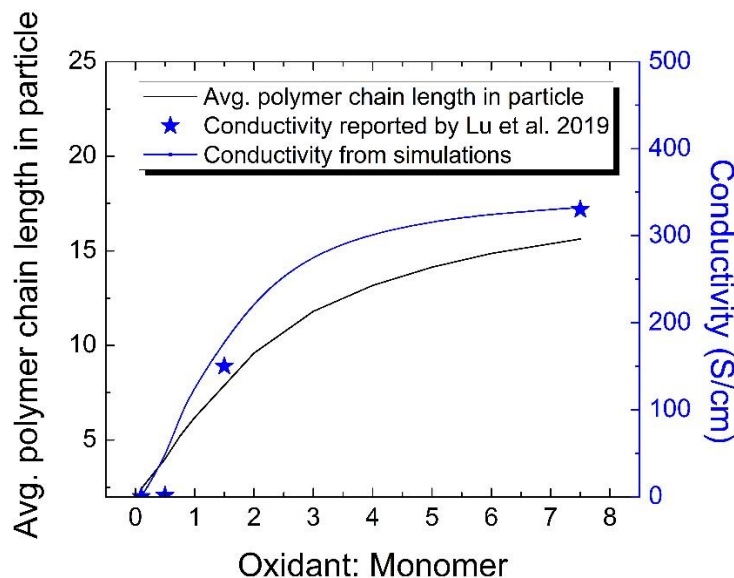
Figure 3-8 The average polymer chain length and conductivity of PEDOT particle synthesized via AVP as the function of oxidant to monomer ratio.

Figure 3-8 shows the average polymer chain length in PEDOT particles synthesized via AVP obtained via simulation. The oxidant to monomer ratio can be varied by changing the temperature of liquid EDOT bubbler, or by changing initial oxidant concentration in the

precursor solution. In the simulations, the initial concentration of Fe^{+3} was set to 0.266 M in the droplets and the concentration of EDOT in the carrier gas was varied. It can be seen, that with an increase in oxidant to monomer ratio, the average polymer chain length increases which should result in increase in particle conductivity. Lu et. al. (2019) [13] reported that the conductivity of PEDOT particles increased as a function of oxidant to monomer ratio. Thus, the experimental observations qualitatively agree with the simulation results. To obtain the relationship between average polymer chain length in PEDOT particle to its conductivity, regression analysis was performed and the simulated polymer chain length as the function of oxidant to monomer ratio was correlated to conductivity of PEDOT particles as reported by Lu et al. (2019) [13]. The following expression for conductivity was obtained as the function of average polymer chain length in PEDOT particle *'l'*:

$$Conductivity \left(\frac{S}{cm}\right) = (-1.372 \pm 24.528)l^2 + (51.65 \pm 464.75)l - (139.6 \pm 1508) \quad (3.17)$$

This regression equation is accurate at a 95% confidence level and have the adjusted $R^2 \approx 0.96$. Figure 3-8 shows comparison between the conductivity of predicted PEDOT particles obtained from simulation and equation 3.17, with the experimentally measured conductivity by Lu et al. (2019) [13]. It can be seen that the with the increase in oxidant to monomer ratio, the conductivity of synthesized PEDOT particle increases, but the increase in conductivity is not very significant on increasing the oxidant to monomer ratio more than 3.

Next, the effect of residence time inside the reactor on particle conductivity was evaluated. The simulations were performed for ethanol bubbler temperature at 50 ^{0}C and at 70 ^{0}C (oxidant to

monomer ratio 1.5 and 0.5 respectively). It can be seen from Figure 3-9 that as the residence time increases, the average polymer chain length in PEDOT particle and hence their conductivity, increases. However, the increase in conductivity also saturates with further increase in residence time. It can be seen from Figure 3-9 that the saturation point is reached early when ethanol bubbler temperature is set at 70 ^{0}C (oxidant to monomer ratio 0.5) as compared to when ethanol bubbler temperature is set at 50 ^{0}C (oxidant to monomer ratio 1.5). This is because saturation point is reached when reaction slows down due to the consumption of oxidant (Fe^{+3}), and the oxidant is consumed faster when the oxidant to monomer ratio is low.
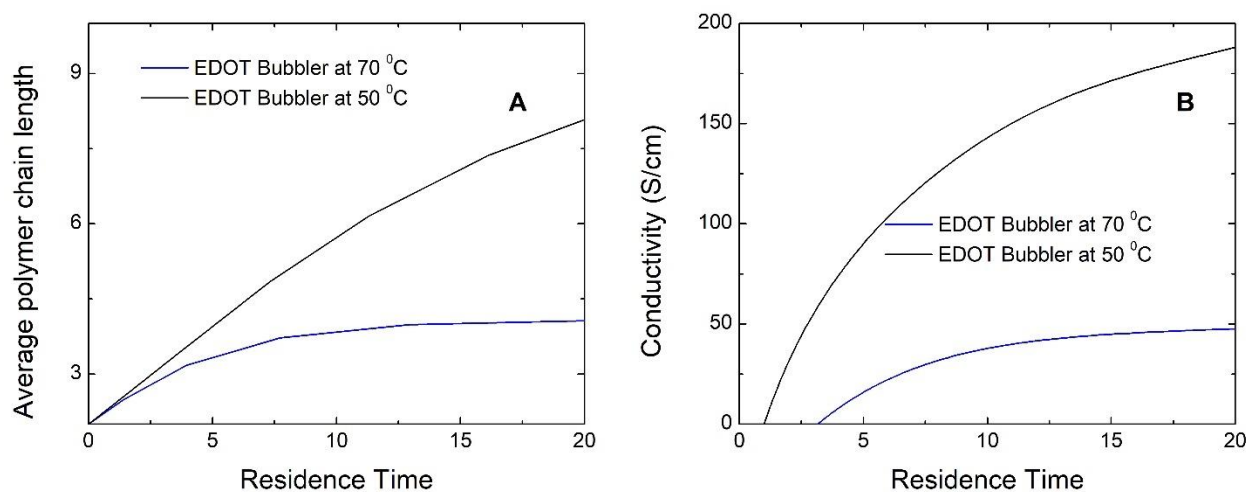
Figure 3-9 a) The average polymer chain length, and b) conductivity of PEDOT particle synthesized via AVP as the function of residence time.

Next, the effect of concentration of reactants on the conductivity of synthesized PEDOT particle was evaluated. The oxidant to monomer ratio was fixed to 1.5, and the concentration of oxidant and EDOT was varied accordingly, in these simulations. It can be seen from Figure 3-10 that increasing the reactant concentration results in increase in average polymer chain length in synthesized particles and hence increase in their conductivity. It should be noted that the gain in

increase in conductivity of the particles on increasing the reactant concentration diminishes at higher concentrations (0.35 M oxidant concentration in this case). Thus, using this model appropriate concentrations of reactants could be chosen based on conductivity vs cost considerations.
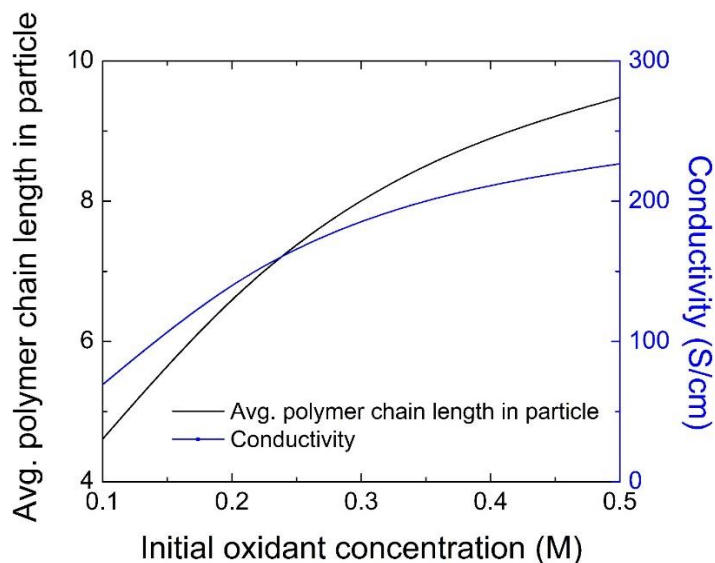
Figure 3-10 The average polymer chain length, and conductivity of PEDOT particle synthesized via AVP as the function of initial oxidant concentration. The oxidant to monomer ratio was fixed to 1.5.

In Lu et al. (2019) [13], the main parameters that were varied to control the synthesized PEDOT particle conductivity are the EDOT vapor concentration (oxidant monomer ratio), and the residence time in the reactor. To have more control over the synthesized PEDOT particle morphology, the additional input and design parameters could be varied, that were not explored in the previous study. The humidity of the droplet stream at the reactor inlet is one such important control parameter. In the experiments by Lu et al. (2019) [13], the stream at the inlet of the reactor has low relative humidity, which results in the evaporation of droplets as they enter the heated reactor. The relative humidity of the stream at the reactor's inlet could be controlled to control the evaporation process, thus controlling the final particle size and the polydispersity.

The evaporation increases the polydispersity of the particles at the reactor outlet. Higher humidity at the reactor's inlet would prevent the evaporation of the droplets inside the heated reactor. Thus, increasing the humidity would not result in any further increase in polydispersity of the synthesized particles and provide better control over the size of synthesized particle. Since the evaporation depends on the size of the droplets, the concentration of initiator in the evaporated droplet would be a function of initial droplet size. As the nebulizer creates polydisperse droplets, the reaction rate would not be uniform in all the generated droplets, and would depend on droplet initial size. Thus, limiting the evaporation by increasing the initial humidity would preserve the initial concentration of initiator in the droplet and provide better control over the synthesis process.

The temperature and the pressure of the reactor are also very important parameters that can affect the conductivity of the synthesized PEDOT particles. The temperature and pressure of the reactor can influence evaporation of droplets, transport of EDOT vapors from carrier gas to droplet, and also the reaction rate. The impact of temperature on reaction rate would be significant as the rate constants are exponentially dependent on temperature. The rate of reaction could also be controlled by changing the pressure of the system. The influence of pressure on polymerization in the liquid phase has been investigated by many studies and in some cases, large effects have been reported. Thus, increasing the temperature and pressure increases the reaction rate, which can improve the synthesized particle conductivity by the formation of larger polymers. It would also reduce the residence time required to synthesize the particles which would help with scalability and efficiency. The morphology of the synthesized particle could also be controlled by changing the temperature and pressure as discussed in Section 3.3.1.

114

3.4   Conclusions

PEDOT particles with varying electrical conductivity can be synthesized via aerosol vapor polymerization depending on the properties of precursors, carrier gas flow rates, residence time, and the temperature of the reactor etc. A comprehensive model that accounts for monomer transport from gas phase to droplet, droplet heating and evaporation, transport of polymers and polymerization reaction within the droplet, was developed, to investigate the effect of different conditions during aerosol vapor polymerization on the average conjugation length, and the conductivity of the synthesized particle. The modal model was developed to numerically solve polymerization kinetics inside the droplet.

The simulation results were compared with Lu et. al (2019) [13] and were used to explain experimental observations regarding particle morphology and conductivity. A sensitivity analysis was carried out to investigate the effects of important governing parameters on the conductivity of particle synthesized via AVP. The present study demonstrated that the change in process parameters and operating conditions during AVP result in significant difference in the conductivity of synthesized particle. The model equations developed in this study can be used to design the operating conditions of aerosol vapor polymerization process so that the particles with desired properties can be obtained while minimizing the cost of production.

3.5　References

1. Das, T. K., & Prusty, S. (2012). Review on conducting polymers and their applications. *Polymer-plastics technology and engineering*, *51*(14), 1487-1500.

2. Skotheim, T. A. (Ed.). (1997). *Handbook of conducting polymers*. CRC press.

3. Wynne, K. J., & Street, G. B. (1982). Conducting polymers. A short review. *Industrial & Engineering Chemistry Product Research and Development*, *21*(1), 23-28.

4. Ates, M., Karazehir, T., & Sezai Sarac, A. J. C. P. C. (2012). Conducting polymers and their applications. *Current Physical Chemistry*, *2*(3), 224-240.

5. Saxena, V., & Malhotra, B. D. (2003). Prospects of conducting polymers in molecular electronics. *Current Applied Physics*, *3*(2-3), 293-305.

6. Otero, T. F., & Sansinena, J. M. (1995). Artificial muscles based on conducting polymers. Bioelectrochemistry and Bioenergetics, 38(2), 411-414.

7. Hohnholz, D., Okuzaki, H., & MacDiarmid, A. G. (2005). Plastic electronic devices through line patterning of conducting polymers. *Advanced functional materials*, *15*(1), 51-56.

8. Kim, W. H., Mäkinen, A. J., Nikolov, N., Shashidhar, R., Kim, H., & Kafafi, Z. H. (2002). Molecular organic light-emitting diodes using highly conducting polymers as anodes. *Applied Physics Letters*, *80*(20), 3844-3846.

9. R Murad, A., Iraqi, A., Aziz, S. B., N Abdullah, S., & Brza, M. A. (2020). Conducting polymers for optoelectronic devices and organic solar cells: A review. *Polymers*, *12*(11), 2627.

10. Wang, P. C., Liu, L. H., Mengistie, D. A., Li, K. H., Wen, B. J., Liu, T. S., & Chu, C. W. (2013). Transparent electrodes based on conducting polymers for display applications. *Displays*, *34*(4), 301-314.

11. Kim, J., Park, H. S., Kim, T. H., Kim, S. Y., & Song, H. K. (2014). An inter-tangled network of redox-active and conducting polymers as a cathode for ultrafast rechargeable batteries. *Physical Chemistry Chemical Physics*, *16*(11), 5295-5300.

12. Janata, J., & Josowicz, M. (2003). Conducting polymers in electronic chemical sensors. *Nature materials*, *2*(1), 19-24.

13. Lu, Y., Kacica, C., Bansal, S., Santino, L. M., Acharya, S., Hu, J., Izima, C., Chrulski, K., Diao, Y., Wang, H. & D'Arcy, J. M. (2019). Synthesis of Submicron PEDOT Particles of High Electrical Conductivity via Continuous Aerosol Vapor Polymerization. *ACS applied materials & interfaces*, *11*(50), 47320-47329.

14. Wang, Y. (2009, March). Research progress on a novel conductive polymer–poly (3, 4-ethylenedioxythiophene)(PEDOT). In *Journal of Physics: Conference Series* (Vol. 152, No. 1, p. 012023). IOP Publishing.

15. Yue, R., & Xu, J. (2012). Poly (3, 4-ethylenedioxythiophene) as promising organic thermoelectric materials: A mini-review. *Synthetic metals*, *162*(11-12), 912-917.

16. Zhang, Y., & Suslick, K. S. (2015). Synthesis of poly (3, 4-ethylenedioxythiophene) microspheres by ultrasonic spray polymerization (USPo). *Chemistry of Materials*, *27*(22), 7559-7563.

17. Xu, Y., Sui, Z., Xu, B., Duan, H., & Zhang, X. (2012). Emulsion template synthesis of all conducting polymer aerogels with superb adsorption capacity and enhanced electrochemical capacitance. *Journal of Materials Chemistry*, *22*(17), 8579-8584.

18. Luo, S. C., Yu, H. H., Wan, A. C., Han, Y., & Ying, J. Y. (2008). A General Synthesis for PEDOT-Coated Nonconductive Materials and PEDOT Hollow Particles by Aqueous Chemical Polymerization. *Small*, *4*(11), 2051-2058.

117

19. Zhang, S., Ren, J., Zhang, Y., Peng, H., Chen, S., Yang, F., & Cao, Y. (2020). PEDOT hollow nanospheres for integrated bifunctional electrochromic supercapacitors. *Organic Electronics*, *77*, 105497.

20. Brenn, G., Wiedemann, T., Rensink, D., Kastner, O., & Yarin, A. L. (2001). Modeling and experimental investigation of the morphology of spray dryed particles. *Chemical engineering & technology*, *24*(11), 1113-1116.

21. Messing, G. L., Zhang, S. C., & Jayanthi, G. V. (1993). Ceramic powder synthesis by spray pyrolysis. *Journal of the American Ceramic Society*, *76*(11), 2707-2726.

22. Jayanthi, G.V.; Zhang, S.C; Messing, G.L. Modeling of solid particle formation during solution aerosol thermolysis: The evaporation stage. *Aerosol Sci. Technol.*, **1993,** *19*(4), 478-490.

23. Zhang, S. C., Messing, G. L., Lee, S. Y., & Santoro, R. J. (1994). Formation of solid and hollow spherical particles by spray pyrolysis. *MRS Online Proceedings Library (OPL)*, *372*.

24. Ozturk, A., & Cetegen, B. M. (2005). Experiments on ceramic formation from liquid precursor spray axially injected into an oxy-acetylene flame. *Acta materialia*, *53*(19), 5203-5211.

25. Basu, S., Jordan, E. H., & Cetegen, B. M. (2008). Fluid mechanics and heat transfer of liquid precursor droplets injected into high-temperature plasmas. *Journal of Thermal Spray Technology*, *17*(1), 60-72.

26. Mezhericher, M., Levy, A., & Borde, I. (2007). Theoretical drying model of single droplets containing insoluble or dissolved solids. *Drying technology*, *25*(6), 1025-1032.

27. Mezhericher, M., Levy, A., & Borde, I. (2011). Modelling the morphological evolution of nanosuspension droplet in constant-rate drying stage. *Chemical Engineering Science*, *66*(5), 884-896.

28. Maurice, U., Mezhericher, M., Levy, A., & Borde, I. (2013). Drying of droplet containing insoluble nanoscale particles: Numerical simulations and parametric study. *Drying Technology*, *31*(15), 1790-1807.

29. Handscomb, C. S., & Kraft, M. (2010). Simulating the structural evolution of droplets following shell formation. *Chemical Engineering Science*, *65*(2), 713-725.

30. Incropera, F., & DeWitt, D. (1985). Introduction to heat transfer.

31. Friedlander, S. K. (2000). *Smoke, dust, and haze* (Vol. 198). New York: Oxford university press.

32. Kirchmeyer, S., & Reuter, K. (2005). Scientific importance, properties and growing applications of poly (3, 4-ethylenedioxythiophene). *Journal of Materials Chemistry*, *15*(21), 2077-2088.

33. Kim, D., & Zozoulenko, I. (2019). Why is pristine PEDOT oxidized to 33%? A density functional theory study of oxidative polymerization mechanism. *The Journal of Physical Chemistry B*, *123*(24), 5160-5167.

Chapter 4. Estimating sampling artifacts in denuders during phase partitioning measurements of semi-volatile organic compounds

Abstract

The partitioning of semi-volatile organic compounds (SVOCs) between the gas and particle phase plays an important role in understanding the formation of secondary organic aerosols (SOAs) in the atmosphere. There are uncertainties and problems associated with measurements during the simultaneous sampling of both gas and particle phases. In recent studies, diffusion denuders have been used for separate sampling of gas and particle phases of organic compounds. The removal of the gaseous species in the denuder distorts the gas-particle equilibrium and leads to the dissociation of the particulate phase during the sampling. This phenomenon is particularly true for volatile organic species and leads to significant error in determining gas-to-particle phase partitioning of organic aerosols due to underestimation of the particle phase. In this study, a model for simultaneous gas diffusion and aerosol decomposition/evaporation in the parallel plate denuder was developed to investigate the effects of sampling artifacts on gas–particle partitioning measurements of semi-volatile organic compounds. The model equations were cast into dimensionless form for generalization, and the effects of governing dimensionless groups on the denuder sampling artifacts were evaluated by performing a sensitivity analysis. Also, regression correlations for denuder sampling artifacts as the function of governing dimensionless groups were obtained. It was observed that the sampling of SVOCs could result in substantial particulate phase loss due to evaporation in the denuder, resulting in significant errors in the phase partitioning measurements. Also, the operating conditions for the denuder, so that the denuder sampling artifacts lie within tolerable limits, were evaluated.

4.1 Introduction

Organic compounds are typically classified based on their volatility and oxidation state. The phase in which these compounds exist in the atmosphere depends primarily on their volatility. Semi-volatile organic compounds (SVOCs) are a subgroup of volatile organic compounds (VOCs) that have higher molecular weights and higher boiling points. SVOCs exists in the atmosphere in both the gas and particle phase, which are in equilibrium according to the nature of the aerosol and the ambient temperature [1, 2]. The phase partitioning of SVOCs affect their transport properties, deposition rates, and the pathways by which humans are exposed to them [2]. SVOCs include compounds such as polychlorinated biphenyls (PCBs), pesticides, phthalates and polycyclic aromatic hydrocarbons (PAHs), which have been linked to serious adverse health effects. The exposure to SVOC aerosols can lead to an increase in diseases like alveolitis, asthma, cancer etc. and can have serious detrimental effect on the reproductive, nervous, and endocrine systems [3-5]. The gas phase SVOCs can be absorbed by the respiratory tract depending on their solubility in bodily fluids whereas the particle phase can be deposited in different regions of the lung depending on their aerodynamic size. Therefore, it is important to distinguish and quantify gas and particle phase SVOCs to accurately access their health risks. Furthermore, the partitioning of SVOCs between the gas and particle phases plays an important role in the formation of secondary organic aerosols and their chemical aging in the atmosphere [6, 7]. Therefore, knowing the phase partitioning is helpful in understanding the chemistry of secondary organic aerosol formation in the atmosphere.

Several field studies have been carried out to measure the gas and particle phase distribution of SVOCs in the atmosphere [8, 9]. These measurements in general are typically done using filter-

sorbent based samplers. Quartz filters are typically used for collection of particles. The gas phase passes through the filter and is subsequently adsorbed on adsorbent material which is typically polyurethane foam or XAD resin. However adsorption of gaseous organics could also occur on the filter, leading to overestimation of the particulate phase. Also, particles collected on the filter can volatilize leading to the underestimation of the particulate phase [10]. Thus, there is uncertainty associated with this sampling method. In recent years, diffusion denuders have been used as an important tool for assessing the gas-particle phase partitioning of semi-volatile compounds in the atmosphere [11-13].

Diffusion denuders are routinely employed for sampling and collecting various atmospheric gases such as ammonia, nitric acid, sulphur dioxide and organic vapors [14, 15]. The walls of the denuder are internally coated with a specific reagent such as activated carbon and/or polystyrene-divinylbenzene resin that selectively adsorbs or reacts with the gas flowing through it. The denuders are designed in such a way that the gases in the sample air stream are removed almost completely by adsorption at the walls, whereas particles pass through without any significant loss due to slower diffusion rates to the wall as compared to the gas phase species. This behavior allows us to separate the gas and particulate phase. Therefore, the denuder is placed upstream of the quartz filter to remove the gases, eliminating the potential sampling artifacts due to gases absorbing on the filter. Some of the other advantages of using denuders are that they allow high sampling velocities and have a large sampling capacity as compared to the filter-sorbent samplers.

The advantages of diffusion denuders over filter-sorbent samplers have made them widely employed devices for sampling atmospheric gases and aerosols. Although the use of denuder

overcomes many of the measurement artifacts in the filtration device, measurement biases or artifacts are still possible and may be significant in denuder sampling. At the denuder inlet, the gases are usually in equilibrium with the suspended particulates. During the flow through the denuder, the gas diffuses and is adsorbed by the denuder walls. The removal of gas by the denuder walls may distort the gas-particle equilibrium. A concentration gradient between gas and particles is created which acts as a driving force for the evaporation of the particles. Thus, there is a transfer of species from the particle to the gas phase and eventually to the denuder walls. Due to the evaporation of particles in the denuder, the mass of particles collected is less than their actual mass and results in higher gas fraction estimates. Several studies have been carried out to understand the artifacts caused by decomposition of inorganic aerosols in diffusion denuders. Biswas and co-workers [16] developed a computational model to evaluate sampling artifacts by incorporating gas diffusion and decomposition of monodisperse inorganic aerosol (ammonium nitrate) in their equations. Bai et al. [17] further modified the model developed by Biswas et al. [16] to include the effects of polydispersity and diffusion of inorganic aerosols; and Lu et al. [18] later incorporated aerosol coagulation in these equations. In these studies, the shape of the particle size distribution was approximated as lognormal, and the equation for the aerosol moments and the mass balance equations for were associated gases were solved.

In all of the above studies, the analysis was done for single species inorganic aerosols. There are not many studies that have examined the measurement artifacts arising from the evaporative loss of semi-volatile organic aerosols in the diffusion denuder. The semi-volatile organic aerosols exist in the atmosphere as a mixture of thousands of species [19, 20]. For a realistic simulation, all of the volatile compounds that are present need to be considered. However, it is impractical to

incorporate separate equations for thousands of these compounds. Therefore, to simplify, organic compounds with similar properties and/or origin are lumped together. The volatility basis set (VBS) approach developed by Donahue et al. [21] allows for an elegant and unified framework for modeling organic aerosols. In the VBS approach, individual organic compounds are grouped together based on their saturation concentration into equally spaced bins in a logarithmic scale (the basis set). The VBS approach has been widely implemented in many global and regional scale air quality models [22-24]. The advantages of the volatility basis-set approach include that it is systematic and can describe the partitioning of hundreds of compounds with a smaller number of parameters [21].

In this study, a comprehensive model to evaluate and quantify measurement artifacts in the denuder sampling of phase-partitioned multi-component semivolatile organic compounds is developed. The equations for simultaneous gas diffusion and aerosol decomposition/ evaporation in a parallel plate diffusion denuder were derived. The VBS approach is used to group different SVOCs into distinct bins based on their volatility: $\{C_{sat.i}\} = \{1, 10, 100, 1000\}$ μg m^{-3} as our basis set, as the saturation concentrations of SVOCs lie within this range. The effects of denuder design parameters and organic species properties, which influence the evaporation of the particulate phase, are quantitatively determined on the measurement artifacts. This model is also applied to simulate the sampling of SVOCs in a multiple parallel plate denuder documented by Delgado-Saborit et al. [25].

4.2 Model
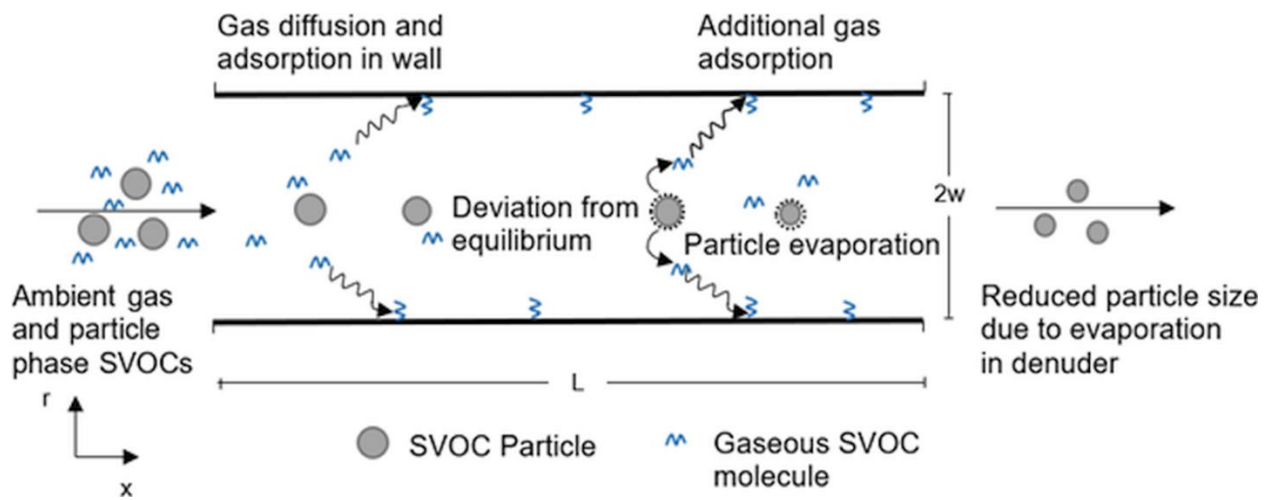
Figure 4-1 Schematic of diffusion denuder channel showing gas diffusion to walls and particle evaporation/decomposition.

The aerosol is assumed to be in equilibrium with the gaseous phase constituents at the inlet of the denuder. Inside the denuder, the gas preferentially diffuses to the denuder walls and is removed therein, thus the gas concentration drops and the equilibrium conditions for the particles with the surrounding gas is disturbed. This creates a concentration gradient between gas and particles which acts as a driving force for evaporation of the particles. Due to evaporation, there is transfer of species from the particle phase to the gas phase, which is subsequently adsorbed by the denuder walls. The schematic of these processes occurring in the denuder is shown in Figure 4-1.

The model for simultaneous gas diffusion and aerosol evaporation in a parallel plate diffusion denuder was developed to evaluate and quantify measurement artifacts in the sampling of phase-partitioned multi-component semivolatile organic compounds. It is assumed that the gas phase species is distributed over bins (i) based on the volatility basis set (VBS); whereas the particle is

126

a mixture of all the species in the various VBS. For the flow between parallel plates, the mass

balance equation for the gas-phase molecules diffusing to the denuder walls is:

$$v(r)\frac{\partial C_{g,i}(x,r)}{\partial x} = D_{g,i}\left(\frac{\partial^2 C_{g,i}(x,r)}{\partial r^2} + \frac{\partial^2 C_{g,i}(x,r)}{\partial x^2}\right)$$

$$-2\pi N D_{g,i} d_p(x,r)\left(C_{g,i}(x,r) - C_{d,i}(x,r)\right)F(Kn) \qquad (4.1)$$

where x is the direction of flow, r is the direction normal to the plates, $D_{g,i}$ is the diffusivity of

the species corresponding to i^{th} VBS bin in air, v is the velocity profile in the channel between

two denuder plates, $C_{g,i}$ is the gas-phase concentration of species corresponding to i^{th} bin, N is the

particle number concentration, d_p is the particle diameter, $C_{d,i}$ is the concentration of the gaseous

species corresponding to i^{th} bin at the particle's surface, and F is the Fuchs-Sutugin correction

factor for transport to/from a droplet surface in the transition-free molecule regime, given by:

$$F(Kn) = \frac{1 + Kn}{1 + 1.71Kn + 1.333Kn^2} \qquad (4.2)$$

where Kn is the Knudsen number (= $2\lambda/d_p$, where λ is the mean-free-path).

The left-hand side of equation (5.1) accounts for the convection of the gaseous species due to the

flow in the axial direction in the denuder. The first term on the right-hand side of equation (4.1)

describes the diffusion of the gas-phase species, while the second term accounts for the gain in

gas phase molecules from the evaporation of aerosols/particulate phase. The particle diffusion terms and any loss to the wall is neglected in equation (4.1) because the diffusivity of the particles is several orders of magnitude lower than that of the gaseous species, and the residence time in the denuder is low (typically < 5 s). Also, the axial diffusion of gas in the denuder could be neglected because of the higher axial velocity in the denuder. Therefore, in equation (4.1) the term $D_{g,i}\left(\partial^2 C_{g,i}/\partial x^2\right)$ could be ignored for practical purposes. The velocity profile in the channel is assumed to be laminar and fully developed, and is given by:

$$v(r) = \frac{3}{2} v_{avg} \left(1 - \left(\frac{r}{w}\right)^2\right) \tag{4.3}$$

where v_{avg} is the average gas velocity in the denuder, and w is half the width of the denuder channel. The concentration of species i, $C_{d,i}$ (equation (5.1)) on the surface of the particle can be related to the saturation concentration by the following equation while accounting for the Kelvin effect [26]:

$$C_{d,i}(x,r) = y_i(x,r) C_{sat,i} exp\left(\frac{4\sigma_i v_{m,i}}{k_B T d_p(x,r)}\right) \tag{4.4}$$

Here, y_i is the mole fraction of species belonging to VBS bin 'i' in the particle phase, $C_{sat,i}$ is the saturation concentration, σ_i is the surface tension and $v_{m,i}$ is the molecular volume of the species belonging to bin 'i', k_B is Boltzmann's constant, and T is the ambient temperature.

As the particles move along the denuder axis with the flow, there is transfer of species from the particle to the gas phase which will reduce the size of the particles. Hence, the change in the size of the particle is given by solving the equation [26]:

$$v(r)\frac{\partial C_{p,i}(x,r)}{\partial x} = 2\pi D_{g,i}d_p(x,r)\left(C_{g,i}(x,r) - C_{d,i}(x,r)\right)F(Kn) \tag{4.5}$$

where $C_{p,i}$ is the moles of species corresponding to i^{th} bin in the particle phase and d_p is the particle diameter, given by:

$$d_p(x,r) = \left(\frac{6}{\pi}\sum_i\left(C_{p,i}(x,r)\frac{Mwt_i}{\rho_i}\right)\right)^{\frac{1}{3}} \tag{4.6}$$

Here, Mwt_i is the molecular weight and ρ_i is the density corresponding to species in i^{th} bin. At the denuder inlet, the particle and the gas phase are assumed to be in equilibrium. The walls of the denuder are assumed to be a perfect sink for gases, the boundary conditions are set to the axis of symmetry, and a zero wall concentration. Therefore, the initial and boundary conditions for the process described by equations (4.1) and (4.5) are:

$$at\ x = 0, \quad C_{g,i\,0} = y_{i0}C_{sat,i}exp\left(\frac{4\sigma_i v_{m,i}}{k_B T d_{p0}}\right), \quad for\ 0 \leq r \leq w \tag{4.7}$$

$$at\ x = 0, \quad C_{p,i} = y_{i0}\left(\frac{\pi}{6}d_{p0}{}^3\right)\bigg/\left(\sum_i\left(y_{i0}\frac{Mwt_i}{\rho_i}\right)\right), \quad for\ 0 \leq r \leq w \tag{4.8}$$

129

$$at\ r = 0, \qquad \partial C_{g,i}/\partial r = 0, \qquad\qquad for\ 0 \le x \le L \qquad\qquad (4.9)$$

$$at\ r = w, \qquad C_{g,i} = 0, \qquad\qquad for\ 0 \le x \le L \qquad\qquad (4.10)$$

where d_{po} and y_{io} are the inlet particle diameter and the inlet mole fraction of species belonging to bin 'i' in the particle phase, respectively.

These equations are further nondimensionalized for mathematical simplicity and to combine model parameters into a smaller set of governing dimensionless groups. The dimensionless equations are given by:

$$v^*(x^*,r^*)\frac{\partial C_{g,i}^*(x^*,r^*)}{\partial x^*} = \left(\frac{1}{Pe_{m,i}}\right)\frac{\partial^2 C_{g,i}^*(x^*,r^*)}{\partial r^{*2}}$$

$$-t_i^* d_p^*(x^*,r^*)\left(C_{g,i}^*(x^*,r^*) - C_{d,i}^*(x^*,r^*)exp\left(\frac{K_i}{d_p^*(x^*,r^*)}\right)\right) F \qquad (4.11)$$

$$v^*(x^*,r^*)\frac{\partial C_{p,i}^*(x^*,r^*)}{\partial x^*}$$

$$= t_i^* R_i d_p^*(x^*,r^*)\left(C_{g,i}^*(x^*,r^*) - C_{d,i}^*(x^*,r^*)exp\left(\frac{K_i}{d_p^*(x^*,r^*)}\right)\right) F \qquad (4.12)$$

$$d_p^*(x^*,r^*) = \left(\sum_i \left(C_{p,i}^*(x,r)\frac{Mwt_i}{\rho_i}\right)\right)\Bigg/\left(\sum_i \left(y_i(x,r)\frac{Mwt_i}{\rho_i}\right)\right) \qquad (4.13)$$

130

with the boundary conditions

$$at\ x = 0, \qquad C^*_{g,i0} = 1, \qquad\qquad for\ 0 \le r \le w \qquad\qquad\qquad (4.14)$$

$$at\ x = 0, \qquad C^*_{p,i0} = 1, \qquad\qquad for\ 0 \le r \le w \qquad\qquad\qquad (4.15)$$

$$at\ r = 0, \qquad \partial C^*_{g,i}/\partial r^* = 0, \qquad for\ 0 \le x \le L \qquad\qquad\qquad (4.16)$$

$$at\ r = w, \qquad C^*_{g,i} = 0, \qquad\qquad for\ 0 \le x \le L \qquad\qquad\qquad (4.17)$$

Table 4-1 Dimensionless parameters and their definitions.

Parameters	Definition	Expression
$Pe_{m,i}$	Ratio of the characteristic diffusion time towards channel wall to the residence time	$\dfrac{(w^2/D_{g,i})}{(L/v_{avg})}$
t^*_i	Ratio of residence time in the denuder to characteristic evaporation time	$\dfrac{(L/v_{avg})}{(1/2\ \pi\ ND_{g,i}dp_0)}$
R_i	Ratio of the species present in gas phase to that in the particle phase at the inlet	$\dfrac{C_{g,i,in}}{C_{p,i,in}}$
K_i	Kelvin effect factor	$\dfrac{4\ \sigma_i\ v_{m,i}}{k_B T dp_0}$

where $x^* = x/L$, $r^* = r/w$, $d^*_p = d_p/d_{p,0}$, $C^*_{g,i} = C_{g,i}/C_{g,i0}$, $C^*_{p,i} = C_{p,i}/C_{p,i0}$, $C^*_{d,i} = C_{d,i}/C_{g,i0}$ and

$v^* = v/v_{avg}$ are the dimensionless variables, and $Pe_{m,i}$, t^*_i, K_i and R_i are the dimensionless

parameters that govern the performance of denuder. The definition and expressions for these

dimensionless parameters are given in Table 4-1. $Pe_{m,i}$, the modified Peclet number, is the ratio

131

of the characteristic time for diffusion towards the channel wall (w^2/D_g) to the residence time in the denuder (L/v_{avg}). The dimensionless time t_i^*, is the ratio of residence time in the denuder (L/v_{avg}) to the characteristic evaporation time in the continuum regime ($1/(2\pi N\,dp_0\,DL)$). K_i is the Kelvin effect factor, and R_i is the ratio of the species present in the gas phase to that in the particle phase at the denuder inlet.

Equations (4.11) and (4.12), along with the appropriate boundary conditions, constitute a set of coupled ordinary differential equations (ODE) and partial differential equations (PDEs). These PDEs are transformed to ODEs using an explicit-finite difference scheme at points along r, across the denuder. This set of coupled ODEs is then solved by a stiff ordinary differential equation solver (MATLAB in this work), and $C_{p,i}$ and $C_{g,i}$ are calculated as a function of both x and r. The cup-mixing average is used to evaluate the effects of process parameters on the evolution of the particle size and the amount of gas collected in the denuder, which is calculated using:

$$C_{avg}(x) = \frac{\int_0^w v(r)\,C(x,r)\,dr}{\int_0^w v(r)\,dr} = \frac{\int_0^1 (1-(r^*)^2)\,C(x,r)\,dr}{\int_0^1 (1-(r^*)^2)\,dr} \tag{4.18}$$

Before the system analysis, the consistency of the model was first established by validating its numerical scheme. Then, the simulations were carried out to investigate the effect of dimensionless governing parameters on the denuder sampling artifacts. The measurement artifacts were quantified in terms of the percentage mass lost from the particle phase (ML_i),

percentage excess gas adsorbed at denuder walls (EG_i), and the percentage error in fraction of the total SVOC in gas phase ($GF_{error,i}$). The expressions for these are given below:

$$ML_i = 100 \left(1 - C^*_{p,i\ avg}(x = L)\right) \tag{4.19}$$

$$EG_i = 100 \left(\frac{1}{R_i}ML_i - C^*_{g,i\ avg}(x = L)\right) \tag{4.20}$$

$$GF_{error,i} = 100 \left(\frac{GF_i(measured) - GF_i(actual)}{GF_i(actual)}\right) \tag{4.21}$$

where GF_i is the ratio of the species corresponding to i^{th} bin present in the gas phase to the total amount of ith species present in both phases. The regression correlations for denuder sampling artifacts as the function of governing dimensionless parameters were obtained. These equations were used to choose appropriate operating conditions for the denuder so that the error due to sampling artifacts lie within the allowable limit. Finally, the developed model was applied to evaluate the SVOCs sampling artifacts for a typical denuder used in the field and the operating conditions were calculated for which the error due to sampling artifacts are negligible. The test plan and the set of all the simulations performed for this work are listed in Table 4-2.

Table 4-2 Simulation Plan

I.	Model Verification	• Comparison with analytical solution (Tan and Thomas 1972) for flow between parallel plates
		• Mass Balance Confirmation
II.	Sensitivity Analysis	• Investigation of the effects of the dimensionless governing parameters on the sampling artifacts.
III.	Regression Correlations	• Obtain regression correlations for denuder sampling artifacts as the function of Pe_m and t^*
		• Determine the operating region (Pe_m and t^* values) such that error in denuder measurements lie below 10%.
IV.	Model Application	• Investigation of sampling artifacts in sampling of SVOCs using the multi-parallel plate denuder developed by Delgado-Saborit et al. [25]
		• Determination of operating flowrates so that errors in measurements are within allowable limits.

4.3   Results and Discussions

The numerical scheme of this model is validated by comparing to analytical solutions for limited conditions. First, the numerical solutions of the present model's predictions for gas concentrations in the absence of evaporating particles were compared with the analytical solution given by Tan and Thomas [27] for flow between parallel plates, and both were in excellent agreement. Second, a mass balance was carried out on the numerical solutions of the present model in the presence of evaporating particles. The net difference between the inlet and the outlet gas concentrations was calculated to be equal to the net difference between the net gas adsorbed in the denuder walls and the additional gas released due to particle evaporation.

After establishing the numerical consistency of the present model, a parametric analysis was carried out to investigate the effects of the dimensionless governing parameters $Pe_{m,i}$, t_i^*, K_i and R_i (in equations (4.11) and (4.12)) on the artifacts caused by evaporation of the particulate phase in the parallel plate denuder. For this simulation, it is assumed that the mole fractions of species in the various bins in the particle phase are same at the inlet and that both the phases are in equilibrium. Also, D_{gi}, σ_i and $v_{m,i}$ were assumed to not vary across different bins so that the dimensionless parameters $Pe_{m,i}$, t_i^* and K_i depended only on the denuder parameters and operating conditions, but not on the bin. The values of the parameters examined here are in the typical range for denuders used in the field.
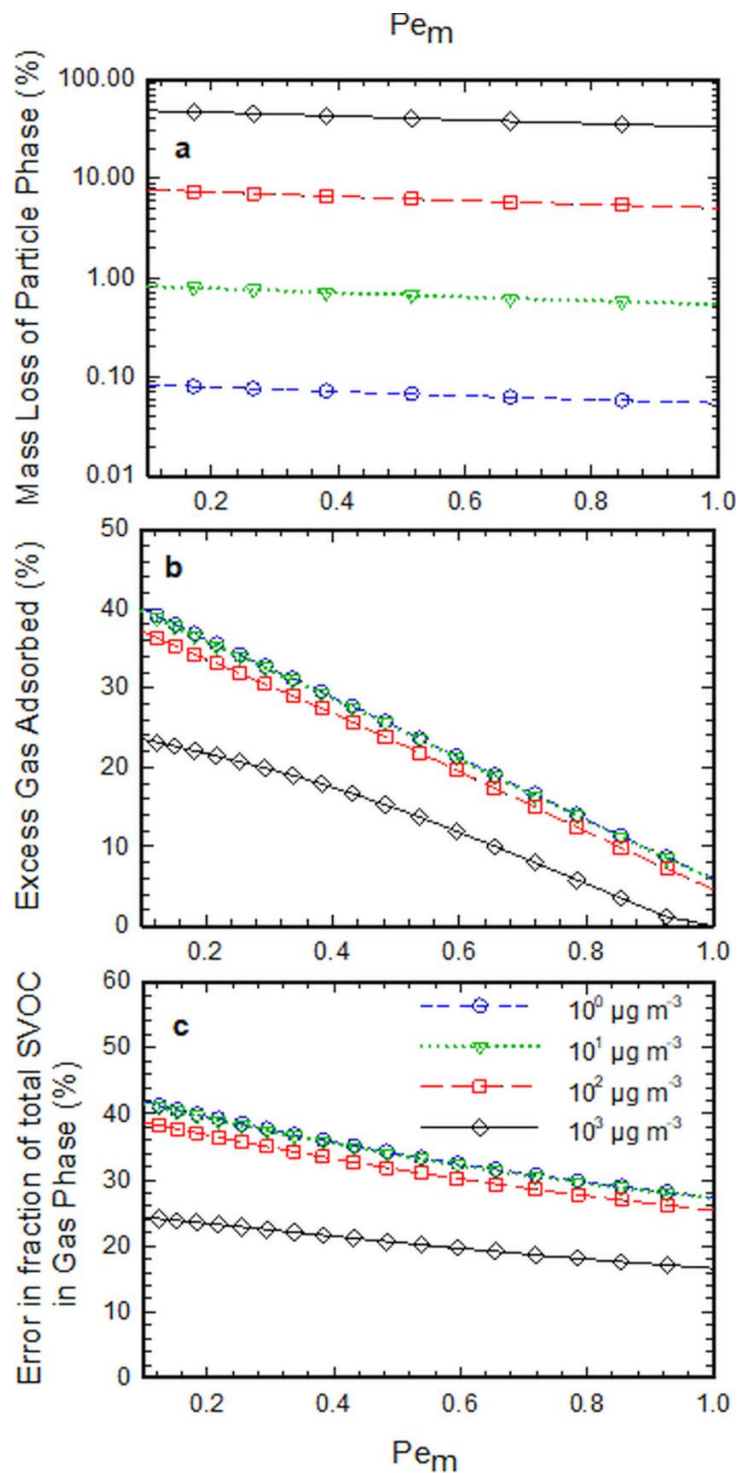
Figure 4-2 (a) Calculated mass loss percentage of SVOCs particles at the exit of the parallel plate denuder as a function of Pe_m for each volatility bin, (b) Excess adsorbed gas in the denuder in the presence of evaporating SVOCs particles as a function of Pe_m for each volatility bin, (c) Error in gas fraction measurements of phase-partitioned SVOCs as a function of Pe_m for each volatility bin. Note that in this simulation $t^* = 1.0$, $K = 0.05$ and R_i is defined according to the equilibrium condition at the inlet.

Figure 4-2 shows the measurement artifacts in the denuder sampling as the function of $Pe_{m,i}$. As the diffusivity of species corresponding to all the bins are assumed to be same for this simulation, $Pe_{m,i}$ is same for all the volatility bins as can be seen from the expression in Table 5-1. The mass lost from the particle phase (ML_i), excess gas adsorption at denuder walls (EG_i) and the error in measured gas fraction ($GF_{error,i}$) were evaluated for each distinct bin as the function of Pe_m while keeping the other dimensionless parameters t_i^*, K_i and R_i constant. As can be seen from Figure 4-2, with an increase in Pe_m mass lost from the particle phase, the adsorption of excess gas in the denuder and error in gas fraction measurements decreases. It can also be seen from Figure 4-2 that the mass lost from the particle phase is higher for the bin with higher volatility which can be attributed to higher evaporative losses for the species with higher volatility. However, the percentage of excess gas adsorbed at denuder walls is higher for the species with low volatility. The gas and the particle phase were assumed to be in equilibrium at the inlet of the denuder for this simulation. Hence R_i, which is the ratio of the species present in gas phase to that in the particle phase at the inlet, will be higher for bins with higher volatility. The higher value of R_i of the higher volatility bin will contribute to relatively less amount of excess gas adsorbed, as can be seen from equation (4.20).

An increase in Pe_m implies a lower evaporative loss of the particulate phase. Therefore, to minimize the sampling artifacts, it is desirable to have larger Pe_m values for the denuder, provided all the gas phase species can be removed. Higher values of Pe_m are due to the larger channel width, lower gas diffusivity, shorter length or higher velocity, which results in the characteristic diffusion time towards the channel wall to be higher or the residence time of gas to

be shorter. In terms of controllable parameters, larger channel widths, higher flow rates and lower volume of the denuders, or a larger value for $\frac{Q\,w^2}{V}$, where Q is the volumetric flow rate, and V is the volume of the denuder, can be selected to minimize particle evaporative loss.
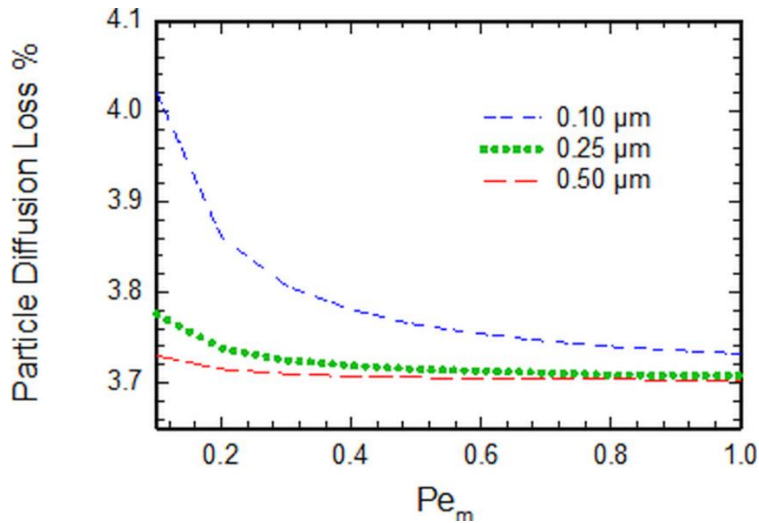
Figure 4-3 Percentage of particle lost in the parallel plate denuder due to diffusion as the function of Pe_m. Note that for Pe_m calculation, D_g was assumed to be 6×10^{-2} cm^2/s.

An additional factor to be considered is loss of particles by diffusion. While the diffusion denuder is designed to minimize particle loss and ensure gas removal, it is important to evaluate the loss of small particles. It is also important to estimate this and compare to evaporative losses arising from the particulate phase. The diffusion loss of the particles in the parallel plate denuder was calculated as the function of the modified Peclet number for different particle diameters using the expression given by DeMarcus and Thomas [28]. Figure 4-3 shows the percentage of particles that are lost in the denuder due to diffusion as the function of Pe_m for three different diameters: 0.1 µm, 0.25 µm and 0.5 µm, which is typical size range for atmospheric aerosols [29, 30]. Diffusive losses of particles are very low as compared to evaporative loss of particles,

except for very low volatility species for which both losses are comparable yet still insignificant $< 5\%$. (Figure 4-2, 4-3).
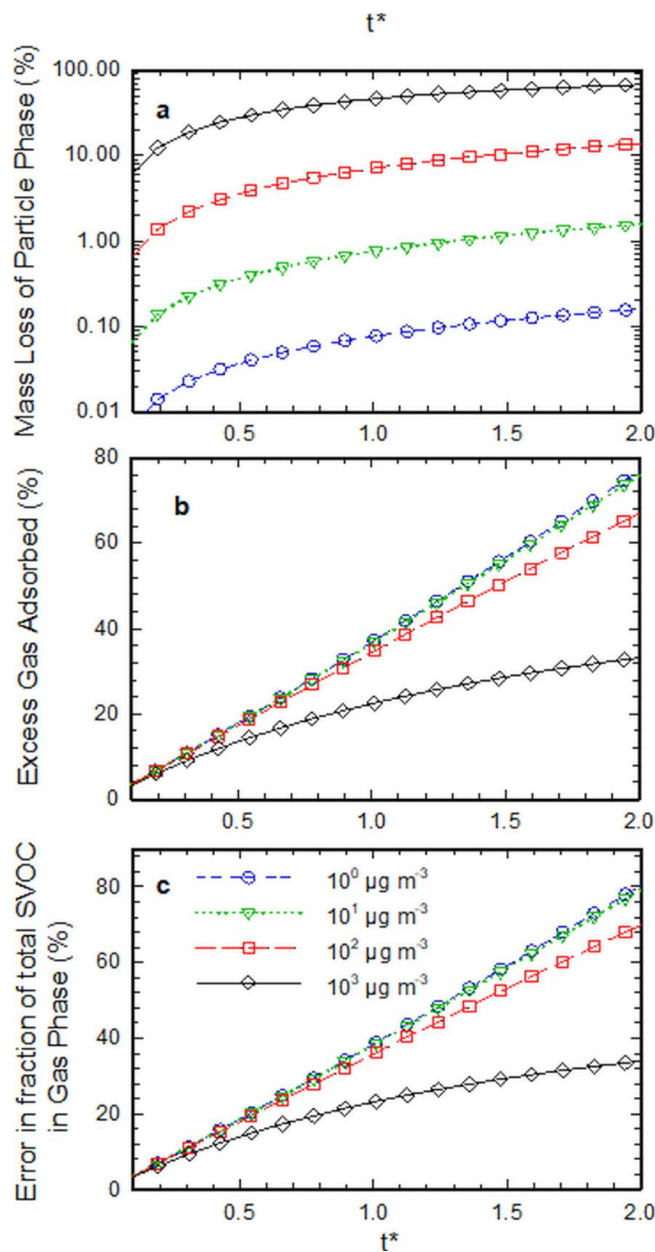
Figure 4-4 (a) Calculated mass loss percentage of SVOCs particles at the exit of the parallel plate denuder as a function of t* for each volatility bin, (b) Excess adsorbed gas in the denuder in the presence of evaporating SVOCs particles as a function of t* for each volatility bin, (c) Error in gas fraction measurements of phase-partitioned SVOCs as a function of t* for each volatility bin. Note that for this simulation $Pe_m = 0.1$, $K = 0.05$ and R_i is defined according to the equilibrium condition at the inlet.

139
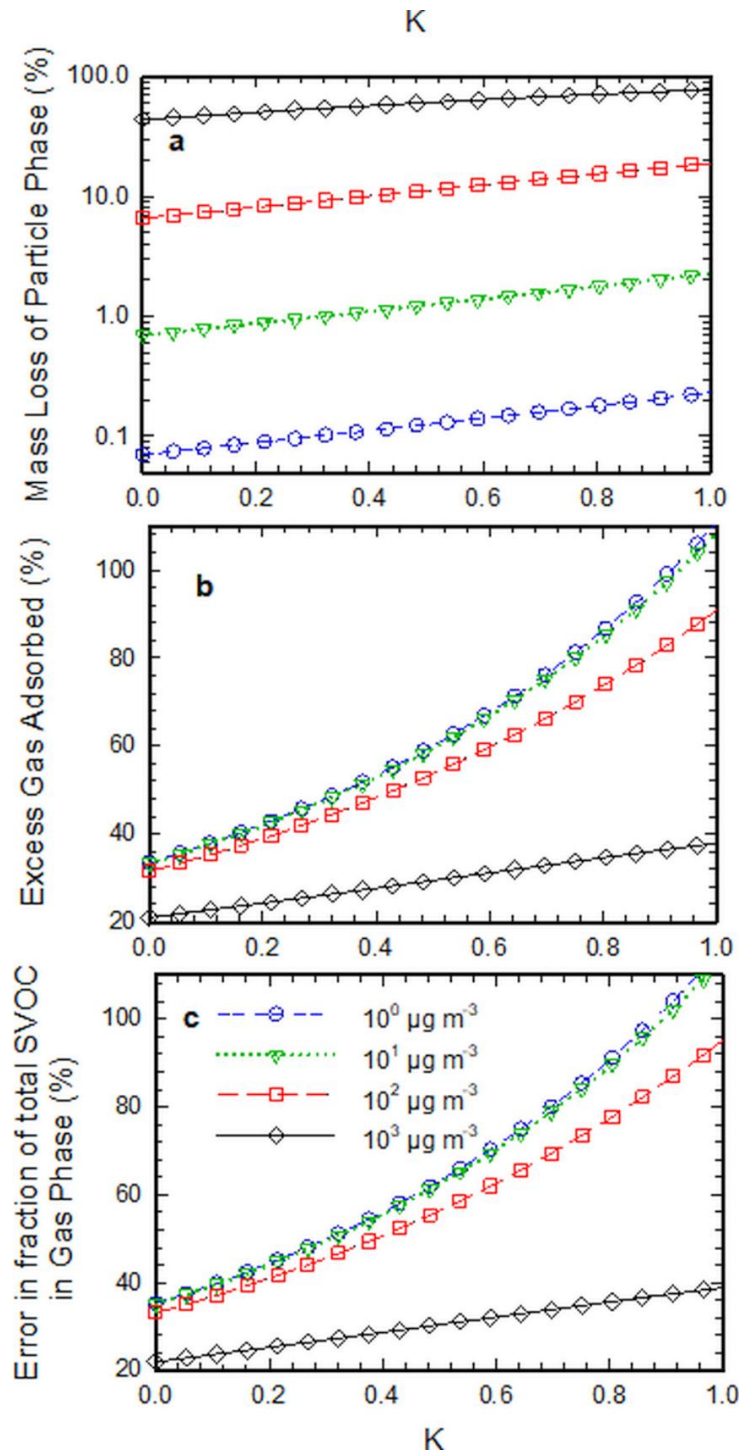
Figure 4-5 (a) Calculated mass loss percentage of SVOCs particles at the exit of the parallel plate denuder as a function of K for each volatility bin, (b) Excess adsorbed gas in the denuder in the presence of evaporating SVOCs particles as a function of K for each volatility bin, (c) Error in gas fraction measurements of phase-partitioned SVOCs as a function of K for each volatility bin. Note that for this simulation $Pe_m = 0.1$, $t^* = 1.0$ and R_i is defined according to the equilibrium condition at the inlet.

140
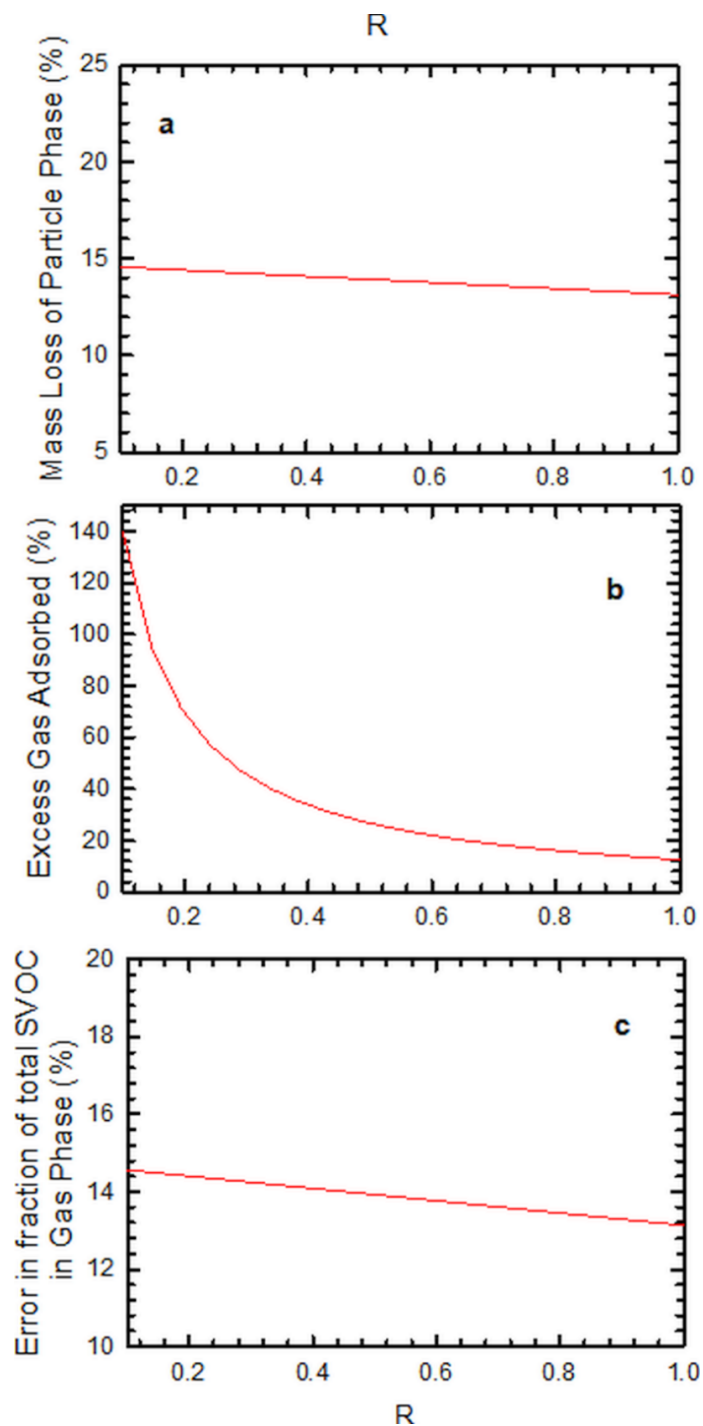
Figure 4-6 (a) Calculated mass loss percentage of SVOCs particles at the exit of the parallel plate denuder as a function of R, (b) Excess adsorbed gas in the denuder in the presence of evaporating SVOCs particles as a function of R, (c) Error in gas fraction measurements of phase-partitioned SVOCs as a function of R. Note that for this simulation $Pe_m = 0.1$, $t^* = 1.0$ and $K = 0.05$.

Figure 4-4 shows the measurement artifacts in the denuder sampling as the function of t_i^*. As the diffusivity of species corresponding to all the bins are assumed to be same for this simulation, t_i^* is same for all the bins as can be seen from the expression in Table 4-1. The measurement artifacts were evaluated as the function of t^* while keeping the other dimensionless parameters $Pe_{m,i}$, K_i and R_i constant. It can be seen from Figure 4-4 that an increase in t^* results in the increase in denuder measurement artifacts. The higher value of t^* implies the higher ratio of the residence time to the characteristic evaporation time. Therefore, the increase in t^* results in more aerosol evaporation and hence higher measurement artifacts. So, to minimize the sampling artifacts, t^* should be kept low while operating the denuder.

Figure 4-5 shows the measurement artifacts in denuder sampling as the function of K_i^*. As σ_i and $v_{m,i}$ are assumed to not vary across different bins so K_i depend only on the denuder parameters and operating conditions but not on the bin as can be seen from the expression in Table 4-1. It can be seen from Figure 4-5 that an increase in K results in the increase in the denuder measurement artifacts. The higher value of K implies higher saturation concentration at the particle's surface due to the Kelvin effect. This results in the higher driving force, which causes evaporation of particles. Therefore, an increase in K increases the evaporative losses as seen in Figure 4-5.

R_i , the ratio of the species present in the gas phase to that in the particle phase, at the inlet will be higher for bins with higher volatility. Therefore, it is different for distinct bins, and it defines the initial conditions (actual gas-particle phase values) for our simulation. Therefore, to see the

effect of R_i on measurement artifacts, the particle was assumed to be composed of species belonging to bin $C_{sat.\,i} = 100$ μg m^{-3}. Figure 4-6 shows the measurement artifacts in the denuder sampling as the function of R. It can be seen that an increase in R results in the decrease in the evaporative losses in the denuder. This is because at the higher value of R, the gas present at the inlet is higher than the equilibrium value and hence the driving force that causes evaporation of particles is lower. Therefore, an increase in R decreases the sampling artifacts as seen in Figure 4-6.

The developed model can be used for two different purposes- (1) designing a denuder and, (2) choosing the appropriate operating conditions for an existing denuder, such that the error due to sampling artifacts are low. For the objective of designing the denuder, a set of regressions equations were obtained, relating Pe_m and t^* to percentage mass loss from the particle phase due to evaporation in the denuder and the excess gas adsorbed on denuder walls, for SVOC with C_{sat} = 1000 μg m^{-3}, number concentration of 10^5 #/cm³ for three different diameters: 0.1 μm, 0.25 μm and 0.5 μm.

For the particle diameter of 0.1 μm and (0.1<Pe_m<1, and 0.01 <t*<0.2), the regression equations are given by:

$$Mass\ Loss\ \% = (310.56 \pm 3.09)\,(0.736 \pm 0.005)^{Pe_m}\,(t^*)^{(0.757 \pm 0.005)} \tag{4.22}$$

$$Excess\ Gas\ Adsorbed\ \% = (0.468 \pm 0.028) + (5.034 \pm 0.106)Pe_m$$

$$+(-13.48 \pm 0.09)\,(Pe_m)^{(2)} + (16.33 \pm 0.12)t^* \tag{4.23}$$

For the particle diameter of 0.25 µm and ($0.1 < Pe_m < 1$, and $0.1 < t^* < 1$), the regression equations are given by:

$$Mass\ Loss\ \% = (60.10 \pm 0.50)\,(0.643 \pm 0.008)^{Pe_m}\,(t^*)^{(0.833 \pm 0.010)} \qquad (4.24)$$

$$Excess\ Gas\ Adsorbed\ \% = (57.96 \pm 2.51)\,(0.217 \pm 0.021)^{Pe_m}\,(t^*)^{(0.889 \pm 0.063)} \qquad (4.25)$$

For the particle diameter of 0.5 µm and ($0.1 < Pe_m < 1$, and $0.1 < t^* < 1$), the regression equations are given by:

$$Mass\ Loss\ \% = (11.10 \pm 0.00)\,(0.607 \pm 0.004)^{Pe_m}\,(t^*)^{(0.941 \pm 0.006)} \qquad (4.26)$$

$$Excess\ Gas\ Adsorbed\ \% = (83.59 \pm 3.23)\,(0.235 \pm 0.020)^{Pe_m}\,(t^*)^{(1.035 \pm 0.061)} \qquad (4.27)$$

All these regression equations are accurate at a 95% confidence level. The regression equations for percentage mass loss for the particle diameters have the adjusted $R^2 \approx 1$, and the equations for the excess gas adsorbed in denuder walls have the adjusted $R^2 \approx 0.96$. For desired (allowable) error in the measurements, one can choose Pe_m and t^* values from these equations. For example, if the aerosol entering the denuder is monodisperse with diameter = 0.25 µm, then, for $Pe_m = 0.1$ and $t^* = 1.0$, the particle will lose 57% of its mass due to evaporation in the denuder, and the amount of excess gas adsorbed by the denuder walls will be 45%.
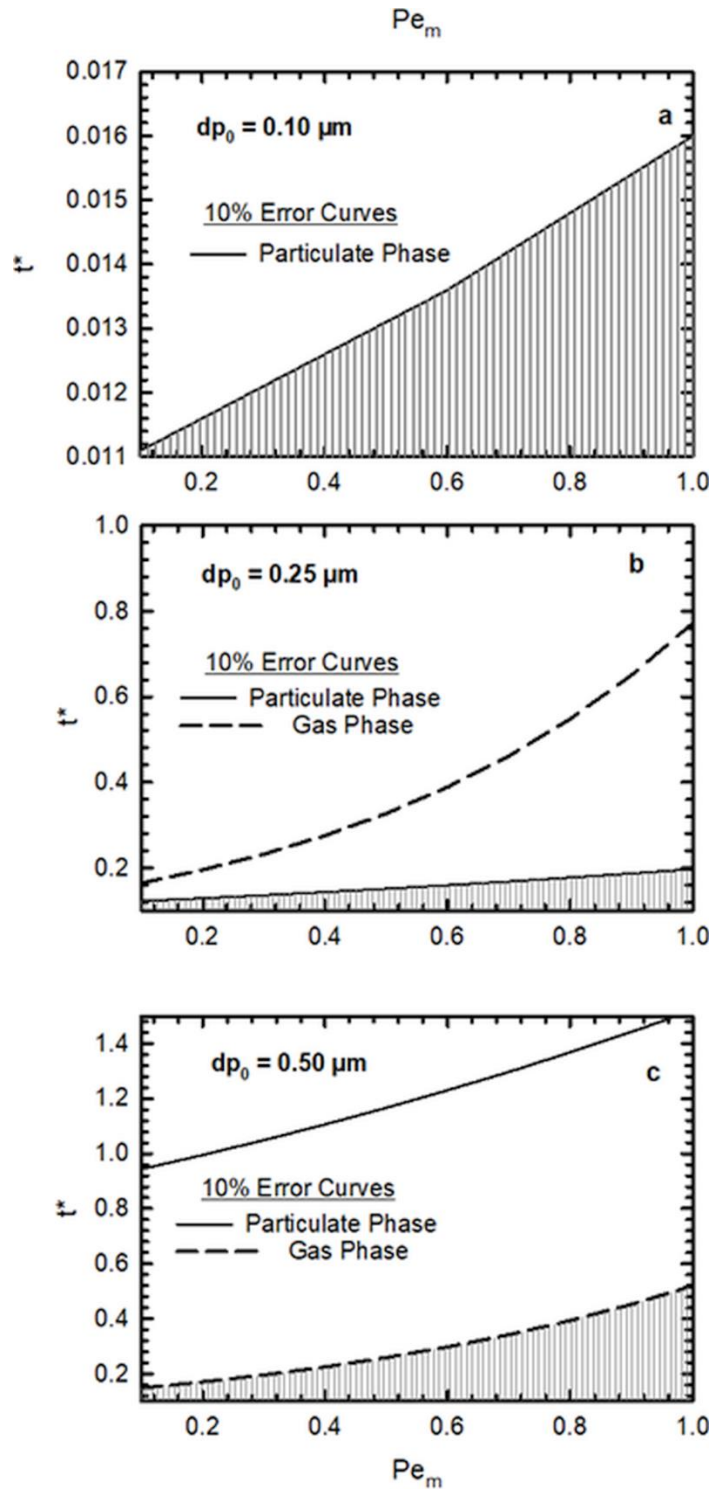
Figure 4-7 Pe_m and t* curves corresponding to 10% error in gas and particulate phase measurements for inlet particle diameters of a) 0.1 μm, b) 0.25 μm and c) 0.5 μm. The shaded area corresponds to the region where the error due to denuder sampling artifacts lie below 10%. For this simulation, $C_{sat} = 1000$ μg m^{-3}, $N = 10^{11}$ # m^{-3}.

These equations are very useful in designing a denuder such that the error due to sampling artifacts lie within an allowable limit (e.g. 10%). The saturation concentrations of SVOCs lie within 1-1000 $\mu g \ m^{-3}$. Among the SVOCs, species with saturation concentrations of 1000 $\mu g \ m^{-3}$ will have the maximum possible error due to evaporative losses. Therefore, the sampling artifacts in SVOCs measurement will be negligible if errors for the worst-case scenario i.e. for $C_{sat} = 1000 \ \mu g \ m^{-3}$, lie within the acceptable limits. The regression equations (5.22-5.25) were used to evaluate the Pe_m and t^* values (operating region) such that error in both the particle and gas phase measurements lie below 10% (assuming that this is an acceptable level of error). The shaded area in Figure 4-7 corresponds to the region in which the errors due to sampling artifacts are within the acceptable limit of 10%. It can be seen from Figure 4-7 that the error in particulate phase is the dominant error for the particles of size 0.1 µm and 0.25 µm whereas the error in gas phase is the dominant error for the particles of size 0.50 µm. Thus, the error which defines the boundary of operating region of the denuder is a function of particle diameter and, shifts from particulate phase to gas phase as the controlling parameter with the increase in the particle diameter. Figure 4-7 can be used as a guide for designing the denuder and for selecting appropriate operating conditions so that the sampling artifacts are reasonably small.

Table 4-3 Simulation Parameters and Denuder Dimensions

Parameters	
Flow rate – High (lpm)	30
Flow rate – Low (lpm)	3
Temperature (K)	298
Measured Diameter (µm) (assumption)	0.2
Dimensions of the denuder	
Length (cm)	14.5
Width (cm)	9.5
Depth (cm)	4.2
Number of spacings	21
Width plate (cm)	0.0559
Channel Spacing 'w' (cm)	0.15

The developed model was then used to evaluate SVOCs sampling artifacts for a typical denuder used in the field. In this work, the multi-parallel plate denuder developed by Delgado-Saborit et al. [25] for the sampling of PAHs was selected for the analysis. The denuder parameters and the operating conditions are listed in Table 4-3. The authors report a result assuming no biases. The developed model was used to calculate the error in measurements due to sampling artifacts for the experimental SVOCs phase partitioning data. The simulations were carried out for two of the cases listed in the paper: (1) Indoors Combustion (ETS), where the denuder was operated at the flow rate of 3 lpm and, (2) Outdoors Traffic (Roadside), where the denuder was operated at the higher flow rate of 30 lpm. Although the measured aerosol was polydisperse, the majority of the particles were reported to be less than 0.56 µm in size. Therefore, the calculation is done for an

average particle diameter of 0.2 µm. Initially, the concentrations of each species in the gas and particulate phase, as measured by denuder, were used as the input for the simulation. The mass loss for each species due to denuder sampling and the inlet concentration were updated based on difference between the simulation output and the experimental data. The initial conditions were updated by repeating the above process until the output of the simulation matched the experimental data.

Table 4-4 The experimental data for SVOCs concentrations in the gas and particulate phase (Delgado-Saborit, Stark, and Harrison (2014)) vs the gas and particulate phase concentrations calculated in this study obtained by correcting for particle evaporation in the denuder.

SVOCs	Volatility Bin C ($\mu g/m3$)	Experimentally Measured		Calculated by Simulation	
		Particulate Phase (ng/m³)	Gas Phase (ng/m³)	Particulate Phase (ng/m³) (% Error)	Gas Phase (ng/m³) (% Error)
Low Flow Case - INDOORS Combustion (ETS)					
phenanthrene	10^3	0.08	37.90	0.58 (86.1%)	37.40 (1.3%)
anthracene	10^2	0.01	1.95	0.01 (16.1%)	1.95 (0.2%)
fluoranthene	10^2	0.07	8.04	0.08 (16.1%)	8.02 (0.2%)
pyrene	10^2	0.07	4.66	0.08 (16.1%)	4.65 (0.2%)
High Flow Case - OUTDOORS (Traffic Roadside)					
phenanthrene	10^3	0.27	13.80	0.32 (15.6%)	13.75 (0.3%)
anthracene	10^2	0.05	0.34	0.05 (1.7%)	0.34 (0.1%)
fluoranthene	10^2	0.21	1.47	0.21 (1.7%)	1.47 (0.1%)
pyrene	10^2	0.22	4.62	0.22 (1.7%)	4.62 (0.1%)

Clearly, the inlet conditions (or the ambient state) are different than that measured at the outlet due to the potential biases inside the denuder. This error was calculated for each species based on the process described earlier for both high and low flow cases. The errors of the volatile organic species with the saturation concentration >1000 μg m^{-3} were very high; while the error in measurements of species with the saturation concentration <100 μg m^{-3}, were negligible. The simulation results are listed in Table 4-4 for various SVOCs. It can be seen from Table 4-4 that for the low flow case, the error in particle phase measurements of SVOCs are as high as 86.1% for phenanthrene. For the high flow case, error in particle phase measurements for phenanthrene is 15.6%. It can be concluded from these results that measurement of SVOCs using a denuder and just attributing these to the ambient values could involve substantial artifacts. The magnitude of these artifacts depends on the sampling flow rate and the volatility of the particles and, as expected, are significant at lower flow rate and for the species with higher volatility.
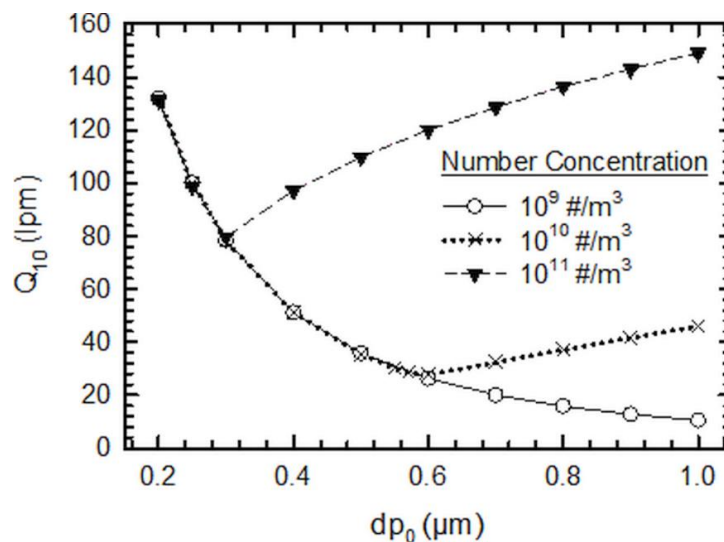
Figure 4-8 Flow rate corresponding to 10% error in denuder measurements as the function of inlet particle diameter at various particle concentrations. For this simulation, the species diffusivity, molecular weight, density and Kelvin effect factor are 4×10^{-6} $m^2 s^{-1}$, 200 g mol^{-1}, 1000 kg m^{-3} and 0 respectively. Gas and particles are assumed to be in equilibrium at the denuder inlet.

To demonstrate the usefulness of our model, operating conditions (flow rate, Q_{10}) for the Delgado-Saborit et al. [25] denuder that would result in low errors ($< 10\%$) were established for a range of inlet diameters of the particle at various number concentrations. The saturation concentration of SVOC was assumed to be the limiting case of 1000 $\mu g\ m^{-3}$. It can be seen from Figure 4-8 that for the particle number concentration of 10^9 # m^{-3}, Q_{10} decreases with an increase in the particle diameter. The error in particle phase measurement due to evaporative losses dominates the error in gas phase measurements for the particle number concentration of 10^9 # m^{-3} over the diameter range shown in the Figure 4-8. As the error in particle phase measurement due to evaporative losses decreases with the increase in particle diameter, Q_{10} decreases with increase in particle diameter for the particle number concentration of 10^9 # m^{-3}. However, it can be observed that for the number concentration of 10^{10} # m^{-3} and 10^{11} # m^{-3}, Q_{10} first decreases and then increases with the increase in inlet particle diameter. This is so because for these number concentrations, there is a switch in the dominant error from the particle phase (at smaller diameters) to error in gas phase due to excess gas adsorption (at larger particle diameters). The error in particle phase measurement decreases while the error in gas phase measurement increases with the increase in particle diameter. This results in decrease and then eventual increase of Q_{10} with the increase in inlet particle diameter. The denuder should be operated at the flow rate which is greater than or equal to Q_{10} so that the error due to sampling artifacts is not significant ($\leq 10\%$).

4.4   Conclusions

A comprehensive model that accounts for simultaneous gas diffusion, and aerosol evaporation was developed to evaluate and quantify the artifacts in the denuder sampling of the gas and particulate phase of semi-volatile organic compounds. The model equations were also cast into dimensionless form for mathematical simplicity, and a sensitivity analysis was carried out to investigate the effects of important governing parameters, Pe_m, t^*, K and R, on the sampling artifacts. The sensitivity analysis showed that these parameters, which are the function inlet particle diameter, particle concentration, flow rate, and species properties have a strong influence on the denuder sampling artifacts.

The present study demonstrated that the sampling of a variety of SVOCs could result in significant particulate phase loss and excess gas adsorption due to aerosol evaporation in the denuder. The developed model was used to evaluate the SVOCs sampling artifacts for a typical denuder used in the field and it was observed that the species can undergo a substantial loss from particle phase due to evaporation, depending on the volatility of the species. The error could be significant for those species in VBS space with saturation concentration greater than 1000 $\mu g\ m^-$ ^{3} Thus, significant artifacts (positive for gases and negative for particle mass) can occur during sampling organic aerosols in a diffusion denuder, which can lead to errors in determining gas-to-particle phase partitioning of these compounds. The model equations developed in this study can also be used to design a denuder so that the sampling artifacts are minimized.

4.5   References

1. Pankow, J. F. (1987). Review and comparative analysis of the theories on partitioning between the gas and aerosol particulate phases in the atmosphere. *Atmospheric Environment*, *21*(11), 2275-2283.

2. Bidleman, T. F. (1988). Atmospheric processes. *Environmental science & technology*, *22*(4), 361-367.

3. Longnecker, M. P., Rogan, W. J., & Lucier, G. (1997). The human health effects of DDT (dichlorodiphenyltrichloroethane) and PCBS (polychlorinated biphenyls) and an overview of organochlorines in public health. *Annual review of public health*, *18*(1), 211-244.

4. Boström, C. E., Gerde, P., Hanberg, A., Jernström, B., Johansson, C., Kyrklund, T., Rannug, A., Törnqvist, M., Victorin, K. & Westerholm, R. (2002). Cancer risk assessment, indicators, and guidelines for polycyclic aromatic hydrocarbons in the ambient air. *Environmental health perspectives*, *110*(suppl 3), 451-488.

5. Heudorf, U., Mersch-Sundermann, V., & Angerer, J. (2007). Phthalates: toxicology and exposure. *International journal of hygiene and environmental health*, *210*(5), 623-634.

6. Kroll, J. H., Chan, A. W., Ng, N. L., Flagan, R. C., & Seinfeld, J. H. (2007). Reactions of semivolatile organics and their effects on secondary organic aerosol formation. *Environmental science & technology*, *41*(10), 3545-3550.

7. Hallquist, M., Wenger, J. C., Baltensperger, U., Rudich, Y., Simpson, D., Claeys, M., Dommen, J., Donahue, N.M., George, C., Goldstein, A.H. & Wildt, J. (2009). The formation, properties and impact of secondary organic aerosol: current and emerging issues. *Atmospheric chemistry and physics*, *9*(14), 5155-5236.

8. Cincinelli, A., Pieri, F., Martellini, T., Passaponti, M., Del Bubba, M., Del Vento, S., & Katsoyiannis, A. A. (2014). Atmospheric occurrence and gas-particle partitioning of PBDEs in an industrialised and urban area of Florence, Italy. *Aerosol and Air Quality Research*, *14*(4), 1121-1130.

9. Xie, M., Hannigan, M. P., & Barsanti, K. C. (2014). Gas/particle partitioning of n-alkanes, PAHs and oxygenated PAHs in urban Denver. *Atmospheric Environment*, *95*, 355-362.

10. Galarneau, E., & Bidleman, T. F. (2006). Modelling the temperature-induced blow-off and blow-on artefacts in filter-sorbent measurements of semivolatile substances. *Atmospheric Environment*, *40*(23), 4258-4268.

11. Possanzini, M., Di Palo, V., Gigliucci, P., Scianò, M. C. T., & Cecinato, A. (2004). Determination of phase-distributed PAH in Rome ambient air by denuder/GC-MS method. *Atmospheric Environment*, *38*(12), 1727-1734.

12. Zhao, Y., Kreisberg, N. M., Worton, D. R., Teng, A. P., Hering, S. V., & Goldstein, A. H. (2013). Development of an in situ thermal desorption gas chromatography instrument for quantifying atmospheric semi-volatile organic compounds. *Aerosol Science and Technology*, *47*(3), 258-266.

13. Isaacman-VanWertz, G., Yee, L.D., Kreisberg, N.M., Wernis, R., Moss, J.A., Hering, S.V., De Sá, S.S., Martin, S.T., Alexander, M.L., Palm, B.B. and Hu, W. (2016). Ambient gas-particle partitioning of tracers for biogenic oxidation. *Environmental science & technology*, *50*(18), 9952-9962.

14. Ianniello, A., Spataro, F., Esposito, G., Allegrini, I., Rantica, E., Ancora, M. P., Hu, M. & Zhu, T. (2010). Occurrence of gas phase ammonia in the area of Beijing (China). *Atmospheric Chemistry and Physics*, *10*(19), 9487-9503.

15. Li, Y., Schwandner, F.M., Sewell, H.J., Zivkovich, A., Tigges, M., Raja, S., Holcomb, S., Molenar, J.V., Sherman, L., Archuleta, C. & Lee, T. (2014). Observations of ammonia, nitric acid, and fine particles in a rural gas production region. *Atmospheric Environment*, *83*, 80-89.

16. Biswas, P., Lu, C. S., Xu, M., & Pratsinis, S. E. (1990). Design equations for gas sampling in diffusion denuders and the effects of particle dissociation. *In Transactions on Visibility and Fine Particles C.V., Ed., AWMA*. TR-17: 131-145

17. Bai, H., Lu, C., & Ling, Y. M. (1995). A theoretical study on the evaporation of dry ammonium chloride and ammonium nitrate aerosols. *Atmospheric Environment*, *29*(3), 313-321.

18. Lu, C., Bai, H., & Lin, Y. M. (1995). A model for predicting performance of an annular denuder system. *Journal of aerosol science*, *26*(7), 1117-1129.

19. Hildemann, L. M., Mazurek, M. A., Cass, G. R., & Simoneit, B. R. (1991). Quantitative characterization of urban sources of organic aerosol by high-resolution gas chromatography. *Environmental science & technology*, *25*(7), 1311-1325.

20. Goldstein, A. H., & Galbally, I. E. (2007). Known and unexplored organic constituents in the earth's atmosphere. *Environmental science & technology*, *41*(5), 1514-1521.

21. Donahue, N. M., Robinson, A. L., Stanier, C. O., & Pandis, S. N. (2006). Coupled partitioning, dilution, and chemical aging of semivolatile organics. *Environmental science & technology*, *40*(8), 2635-2643.

22. Lane, T. E., Donahue, N. M., & Pandis, S. N. (2008). Simulating secondary organic aerosol formation using the volatility basis-set approach in a chemical transport model. *Atmospheric Environment*, *42*(32), 7439-7451.

23. Shrivastava, M., Fast, J., Easter, R., Gustafson Jr, W. I., Zaveri, R. A., Jimenez, J. L., Saide, P. & Hodzic, A. (2011). Modeling organic aerosols in a megacity: comparison of simple and complex representations of the volatility basis set approach. *Atmospheric Chemistry and Physics*, *11*(13), 6639-6662.

24. Jo, D. S., Park, R. J., Kim, M. J., & Spracklen, D. V. (2013). Effects of chemical aging on global secondary organic aerosol using the volatility basis set approach. *Atmospheric Environment*, *81*, 230-244.

25. Delgado-Saborit, J. M., Stark, C., & Harrison, R. M. (2014). Use of a versatile high efficiency multiparallel denuder for the sampling of PAHs in ambient air: gas and particle phase concentrations, particle size distribution and artifact formation. *Environmental science & technology*, *48*(1), 499-507.

26. Friedlander, S. K., Smoke, D., & Haze, J. W. (1977). Sons. *New York*.

27. Tan, C. W., & Thomas, J. W. (1972). Aerosol penetration through a parallel-plate diffusion battery. *Journal of Aerosol Science*, *3*(1), 39-43.

28. DeMarcus, W., & Thomas, J. W. (1952). *Theory of a diffusion battery* (No. ORNL-1413). Oak Ridge National Lab., Y-12 Area.

29. Cabada, J. C., Rees, S., Takahama, S., Khlystov, A., Pandis, S. N., Davidson, C. I., & Robinson, A. L. (2004). Mass size distributions and size resolved chemical composition of fine particulate matter at the Pittsburgh supersite. *Atmospheric Environment*, *38*(20), 3127-3141.

30. Liu, Z., Hu, B., Zhang, J., Yu, Y., & Wang, Y. (2016). Characteristics of aerosol size distributions and chemical compositions during wintertime pollution episodes in Beijing. *Atmospheric Research*, *168*, 1-12.

Chapter 5. Aerosol dynamics model for estimating risk from short range airborne transmission and inhalation of expiratory droplets of SARS-CoV-2

Abstract

The highly infectious SARS-CoV-2 novel coronavirus has resulted in a global pandemic. More than a hundred million people are already impacted, with infected numbers expected to go up. Coughing, sneezing and even talking emit respiratory droplets which can carry infectious viruses. It is important to understand how the exhaled particles move through air to an exposed person to better predict the airborne transmission impacts of SARS-CoV-2. There are many studies conducted on the airborne spread of viruses causing diseases such as SARS and measles, however, there are very limited studies that couple the transport characteristics with the aerosol dynamics of the droplets. In this study, a comprehensive model, for simultaneous droplet evaporation and transport due to diffusion, convection and gravitational settling, is developed to determine the near spatial and temporal concentration of viable virus exhaled by the infected individual. The exposure to the viable virus is estimated by calculating the respiratory deposition, and the risk of infection is determined using a dose-response model. The developed model is used to quantify the risk of short-range airborne transmission of SARS-CoV-2 from inhalation of virus laden droplets, when an infected individual is directly in front of the person exposed and the surrounding air is stagnant. The effect of different parameters, such as viral load, infectivity factor, emission sources, physical separation, exposure time, ambient air velocity, dilution and mask usage is determined on the risk of exposure.

5.1   Introduction

The severe acute respiratory syndrome coronavirus 2 (SARS-CoV-2) is a novel strain of coronavirus that causes respiratory illness ranging from mild to severe disease and death. This is highly transmissible and has resulted in a global coronavirus disease pandemic (COVID-19). As of May 2021, more than hundred million people have been impacted, and the pandemic has resulted in more than 3,300,000 deaths globally [1]. SARS-CoV-2 has the potential of being a long-lasting global pandemic, and it is important to follow prevention and control measures to minimize the spread [2,3]. It is critical to understand how the transmission of SARS-CoV-2 virus takes place, in order to develop effective public health and infection prevention and control measures. The transmission of SARS-CoV-2 can occur mainly through aerosol transmission and less commonly through surface transmission and contact transmission [3]. The public health authorities initially marginalized the significance of airborne transmission of SARS-CoV-2 throughout the pandemic and considered the person-to-person transmission and the contact with contaminated surfaces as the primary modes of the spread of the infection. This was because, about 44% of the documented cases have been identified to be infected by asymptomatic carriers [4-7]. Since asymptomatic people typically do not sneeze or cough, the airborne mode was disregarded as a mode of transmission. Extensive measures have been implemented to reduce the direct and indirect transmission, but the rapid spread of SARS-CoV-2 despite these measures suggests and has now confirmed that airborne transmission is the dominant pathway.

Several research studies have been conducted recently that support the transmission of SARS-CoV-2 virus through the air. Not only coughing and sneezing but breathing and speaking also result in the emission of respiratory droplets laden with viruses [8-10]. Thus, asymptomatic

carriers can also spread the infectious droplets in the air while breathing and speaking. The infected person exhales the virus laden droplets which can remain suspended for several hours and carry infectious viruses to several of meters away from where they were emitted [11]. Several recent studies have proven the presence of airborne infectious SARS-CoV-2 viruses [12-15]. Lednicky et al. [16] isolated viable virus from air samples collected up to 4.8 m away from the patients infected with SARS-CoV-2. This virus has also shown to remain viable in the aerosolized form for several hours. van Doremalen et al. [17] aerosolized virus-laden droplets, and showed that this virus can survive aerosolization process, and found that the virus remained viable during a 3 hr testing period. Fears et al. [18] reported that the virus remained viable in the laboratory generated aerosol droplets up to 16 hr testing period. Thus, people with respiratory manifestations of COVID-19 produce aerosols that contain viable SARS-CoV-2 during expiration, which survive in the air for several hours and these aerosols serve as a potential source of transmission of the virus. Recent studies in animal models have demonstrated SARS-CoV-2 transmission in the absence of contact between animals, which affirms that the SARS-CoV-2 infection can be transmitted through the air [19-21].

The World Health Organization has prescribed maintaining a physical distance of 6 ft (1.8 m) from each other to minimize the risk of infection from airborne transmission. However, several recently published studies support the hypothesis of virus transmission over a distance of 2 m from an infected person [22, 23]. An enhanced understanding of pathogen transmission via aerosolized sputum and saliva droplets is vital to develop effective public health measures aiming at reducing the infection risks. Therefore, it is essential to develop a comprehensive model which combines virology and aerosol science, and can accurately estimate the probability

of transmission of the SARS-CoV-2 virus that is emitted. Several transport models have been developed over the years based on aerosol physics that simulate the aerosol dynamics and transport of the exhaled droplets. These models range from simple trajectory calculations to CFD scale simulations, to represent realistic breathing cycles [24-30]. These models for the droplet transport are based on aerosol dynamics and do not account for the initial viral load in the droplets and the virus viability, and hence fail to give any quantitative information regarding the risk of transmission. Several studies have used dose-response approach to assess the risk of infection from airborne viruses [31-35]. However, in all of these studies, a key assumption in the model is that it considers the air to be well-mixed within the modeled space, but in reality, exhaled particles (either indoors or outdoors) travel in a plume, and their transport depends on the initial velocity during exhalation and the background air motion. Therefore, a model, based on aerosol dynamics of the droplets combined with the respiratory deposition and a dose-response model, is needed to accurately evaluate the risk of airborne transmission.

A comprehensive model, for simultaneous droplet evaporation and transport by diffusion, gravitational settling, and ambient air flow, is developed. Time scale analysis is used to establish the importance of evaporation in the settling process, thus accurately determining the lifetime of the airborne droplet. Size distribution data reported in the literature for sneezes, coughs, and speech is used to quantitatively determine the transport and exposure. The viral load in the droplets and their decay parameters are used in the model to determine the spatial and temporal concentration of the viable virus in the vicinity of an infected individual. The exposure to viable virus and the risk of infection is determined using a dose-response approach, after accounting for the size dependent deposition in the respiratory tract. There continues to be a confusion in the

161

terminology used, and often aerosols are used to only refer to the smaller size droplets. In this paper, we will use the term "aerosols" to describe all airborne droplets. Clearly, these droplets will be of varying (and changing) sizes, and have different airborne lifetimes. Thus, the evaluated risk of the infection from the inhalation of virus laden droplets includes the risk from the deposition of small airborne droplets as well as large droplets in the respiratory region of the exposed individual. The cases considered in this study refer to the situation when an infected individual is directly in front of the person exposed, and there are no obstacles nearby where the droplets can deposit (except for the ground). The risk of infection is evaluated as a function of different parameters such as viral load, infectivity factor, emission sources, physical separation, exposure time, ambient air velocity and mask usage.

5.2   Materials and Methods

When an infected individual breathes, speaks, coughs, or sneezes, respiratory droplets containing the virus, are emitted. The emitted droplets then travel through the air, and eventually settle to the ground due to gravity. Droplets larger than 200 µm settle to the ground very quickly in less than a second. The emitted droplets also undergo evaporation resulting in decrease in their size due to water loss, which increases the time they remain suspended; those with emitted size < 15 µm can remain suspended in air for several hours, and can travel long distances. Also, the SARS-CoV-2 can remain viable in the droplets for several hours [17, 18]. The suspended droplets can be deposited on different surfaces near the infected individual depending on the room layout and the air flow within the room. These droplets carrying the infectious virus can also potentially be inhaled by a person in the vicinity. The inhaled droplets with infectious viruses then deposit in the respiratory region of the exposed person, potentially resulting in an infection. If the infected person is wearing a mask, the concentration of emitted droplet decreases, lowering the risk of infection.   Similarly, a mask worn by the exposed individual will reduce the inhalation of droplets laden with infectious virus, and further minimize the risk of infection. The concentration of the infectious aerosols can also be reduced by increasing the ventilation (dilution) rate and by using higher efficiency filtration in the buildings. Figure 5-1 depicts the dynamics of the airborne transmission of the infection, outlining the process of transport of virus laden droplets exhaled by an infected individual to their deposition in the respiratory system of a susceptible person. In this study, the risk of transmission is evaluated for the situation when an infected individual is directly in front of the person exposed. The evaluated risk of infection includes the risk from inhalation and subsequent deposition of virus laden droplets in the respiratory region of the exposed individual.

163
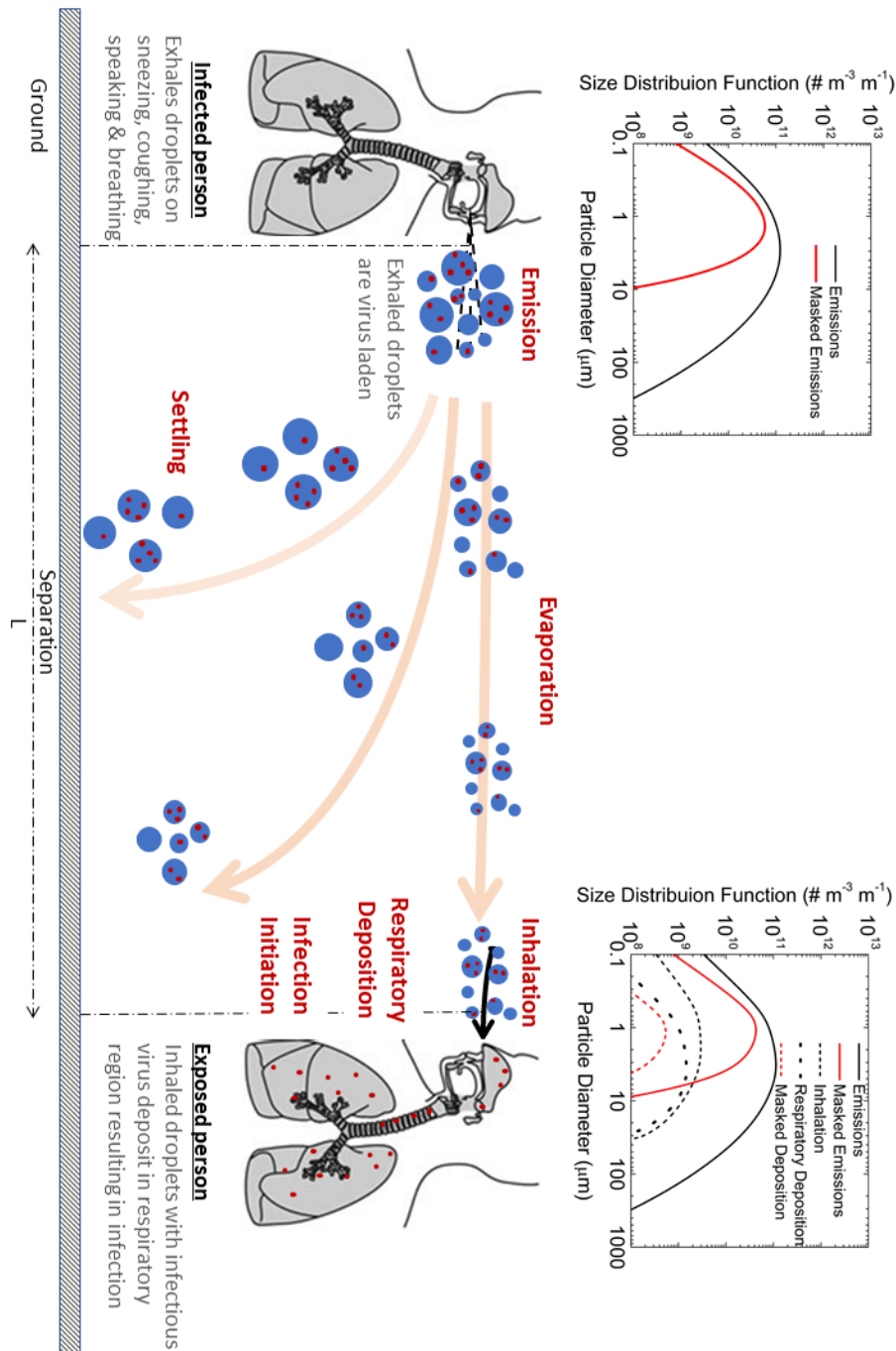
Figure 5-1 Schematic depicting dynamics of airborne transmission of infection, outlining the process of transport of virus laden droplets (virus represented by red dots) exhaled by an infected individual to their deposition in the respiratory system of a susceptible person. The virus laden droplets exhaled by an infected person undergo evaporation as soon as they are expired. The larger droplets (>200 μm) settle immediately, while the smaller droplets (<15 μm) remain suspended for several hours. The suspended droplets with infectious virus can eventually be inhaled and deposited in the respiratory region of the exposed person, thus initiating the infection. The exposure to infectious virus can be reduced by the usage of masks. The size distributions presented here are hypothetical.

164

5.2.1 Transport and aerosol dynamics

A generalized comprehensive model is developed to quantify the risk of airborne transmission of SARS-CoV-2 from inhalation of virus laden droplets, when an infected individual is directly in front of the person exposed. The transport and dynamics of the emitted droplets is expressed by the generalized aerosol dynamics equation, given by [36]:

$$\frac{\partial n(v,t)}{\partial t} + \nabla.(\overrightarrow{v_p}\, n(v,t)) - \nabla^2(D\, n(v,t)) = \frac{\partial(G\, n(v,t))}{\partial v} + I(v^*)\delta(v - v^*)$$

$$+ \left(\frac{1}{2}\int_0^v \beta(v - \hat{v}, \hat{v})n(v - \hat{v}, t)n(\hat{v}, t)d\hat{v} - n(\hat{v}, t)\int_0^v \beta(v, \hat{v})n(\hat{v}, t)d\hat{v}\right) + \dot{n} \qquad (5.1)$$

where, n is the droplet/particle size distribution function (PSD), which is a function of spatial position and time, v is the droplet volume (metric for size), $\overrightarrow{v_p}$ is the particle velocity, D is the diffusion coefficient , G is the evaporation rate , I is the nucleation rate, v^* is the critical nuclei size, β is the coagulation kernel and $\dot{n}$ is the emission rate . The first term on the left-hand side (LHS) is the rate of change of the PSD in the volume interval, v to $v + dv$, the second term considers the aerosol convection, and the third term considers the diffusion. The first term on the right-hand side (RHS) accounts for aerosol evaporation, the second term describes the formation of new particles [37], the third term describe the effect of Brownian coagulation and the final term on the RHS is the emission term.

The droplets released during expiration activities (speaking, coughing, sneezing), from an infected individual, will be transported by diffusion and convection by the air. Gravitational

165

forces result in the settling of the droplets [36]. Depending on the surrounding relative humidity, the evaporation will take place till the vapor pressure of water at the surface of the expired droplets becomes equal to the ambient relative humidity. The cases considered in this study refer to the situation when an infected individual is in close vicinity directly in front of the person exposed, and there are no obstacles/surfaces nearby both individuals where the droplets can deposit (except for the ground). The evaluated risk of infection includes the risk from deposition of small airborne droplets as well as large droplets in the respiratory region of the exposed individual. Since there is no nucleation (new particle formation) taking place during this process, the second term on RHS in equation (5.1) is neglected. The total number concentrations of droplets emitted during respiratory activities is very low. Therefore, the coagulation term, which is the third term on RHS in equation (5.1), can also be neglected. Thus, for this particular case, the equation for droplet transport can be rewritten as:

$$\frac{\partial n}{\partial t} = \nabla^2 (D\,n) - \nabla \cdot (\vec{v}_p n) + \frac{\partial (Gn)}{\partial v} + \dot{n} \tag{5.2}$$

The particle velocity $\vec{v_p}$ is described by:

$$\vec{v}_p = (\vec{u}_{air} - \vec{u}_{ext}) \tag{5.3}$$

where, $\vec{u}_{air}$ is the air velocity while, $\vec{u}_{ext}$ is the velocity of droplet due to external forces (in this case is gravity) and given by [36]:

$$\vec{u}_{ext} = \frac{m_{droplet}\, g}{3\pi\mu d_p\, C} \quad towards\ the\ ground \tag{5.4}$$

where, $m_{droplet}$ is the mass of droplet, g is acceleration due to gravity, μ is air viscosity, d_p is droplet diameter and C is Cunningham's slip correction factor, which accounts for non-continuum effects while calculating the drag on small particles. The air velocity, $\vec{u}_{air}$ is given by:

$$\vec{u}_{air} = \vec{u}_{expiration} + \vec{u}_w \tag{5.5}$$

where, $\vec{u}_{expiration}$ is the initial velocity field of the emitted droplets, and $\vec{u}_w$ is the ambient air velocity. Savory et al. [38] measured the velocity fields during cough using Particle Image Velocimetry, and developed an expression for cough front velocity as the function of distance from mouth:

$$\vec{u}_{cough} = \frac{0.875}{(x + 0.333)^2} \quad in\ direction\ of\ coughing \tag{5.6}$$

where, x is the horizontal distance form infected individual in the direction of coughing. For simplicity, cough velocity is assumed to only be a function of horizontal distance from the point of emission. Nishimura et. al. [39] reported the expiration jet velocities are similar during coughing and sneezing, so $\vec{u}_{sneeze}$ was assumed to be same as $\vec{u}_{cough}$. Chao et al. [40] reported

that the expiration jet velocities during speaking is about a third of during coughing, so $\vec{u}_{speech}$ was assumed to be $\frac{1}{3}\vec{u}_{cough}$.

Respiratory droplets emitted by the infected individuals are composed of an aqueous solution containing inorganic and organic ions, glycoproteins, and suspended viruses [41]. The presence of the dissolved ions will affect the evaporation of the emitted droplets. However, the effect of organic species on evaporation will be negligible because of their low mole fraction, since their molecular weight is very high. The total ion content can be approximated as 150 mM of NaCl [41]. The modal numerical scheme was used in this study to solve the droplet transport equation (Eq. 5.2), as it is easily applicable for multicomponent systems and can account for solute's effect on evaporation. In this approach, a modal form of size distribution was assumed wherein the total volume range for the aerosol droplets is divided into discrete modes [42]. Thus, from Eq. 5.2, the evolution of number concentration of each mode with time and spatial position can be described by:

$$\frac{\partial N_i(x,y,z,t)}{\partial t} = \nabla^2 (D N_i(x,y,z,t)) - \nabla \cdot \left(\vec{v_p} N_i(x,y,z,t) \right) + \dot{N}_i(x,y,z,t) \tag{5.7}$$

Here, $N_i(x,y,z,t)$ is the number concentration of droplets belonging to the ith mode, which will change due to convection, diffusion, and emissions. Evaporation will result in the change in diameter of each mode. The change in diameter of the ith mode $(d_{p,i}(t))$ due to evaporation can be described using [36, 43]:

$$\frac{dd_{p,i}(t)}{dt} = \frac{4D_v v_m}{d_{p,i}(t)k_B T}\left(RH.P_{sat} - P_{d,i}(t)\right)F(Kn) \tag{5.8}$$

where,

$$P_{d,i}(t) = P_{sat}\left(1 - x_{solute,i}(t)\right)\exp\left(\frac{4\sigma_s v_m}{d_{p,i}(t)k_B T}\right) \tag{5.9}$$

where, $d_{p,i}$ is the diameter of droplets belonging to i^{th} mode, D_v is the diffusivity of water vapor, v_m is the molecular volume of water, k_B is the Boltzmann's constant, T is the temperature, RH is the ambient relative humidity, P_{sat} is the saturation vapor pressure of water, $P_{d,i}$ is the vapor pressure of water at droplet's surface, $x_{solute,i}$ is the mole fraction of solute, σ_s is the surface tension of water, and F is the Fuchs-Sutugin correction factor for transport to/from a droplet surface in the transition-free molecule regime, given by [36]:

$$F(Kn) = \frac{1 + Kn}{1 + 1.71Kn + 1.333Kn^2} \tag{5.10}$$

where Kn is the Knudsen number ($= 2\lambda/d_{p,i}$, where λ is the mean-free-path of the vapor molecules). Before the droplet expiration, the concentration of droplets will be zero over the whole simulation domain. Also, at all times the concentration will be zero at the ground, and at very large distances from the mouth. Therefore, the initial and the boundary conditions for the process described by Eq. 5.7 are:

$$N_i(x,y,z,t) = 0 \text{ at } t = 0 \text{ for all } x, y, z \tag{5.11}$$

$$N_i(x,y,z,t) = 0 \text{ at } y = 0 \text{ and at large } x, y \text{ and } z, \text{ for all } t \tag{5.12}$$

The number concentration in the vicinity will increase due to the emissions from the infected person over time. The person will expire droplets at t = 0 and the expiration activity is assumed to last for time, t_{exp}. Thus, it is assumed that there will be constant emissions $\dot{N}_i(x,y,z,t)$ at an infected person's mouth (x = 0, y = H, z = 0) from t = 0 till t_{exp}. To simplify, $\dot{N}_i(x,y,z,t)$ can be considered to be composed of superposition of impulse emissions:

$$\dot{N}_i(x,y,z,t) = \sum_{i=0}^{texp/dt} \left(\delta(t - i \times dt) \right) \tag{5.13}$$

Since, the system of Eq. 5.7 is linear and time invariant wrt N_i, the solution of these equations $(N_{i,(\delta(t-i\times dt))})$ to a shifted input emission impulse $\delta(t - i \times dt)$ is just same as the solution to $\delta(t)$ $(N_{i,\delta(t)})$ but shifted in time by $i \times dt$ (i.e. $N_{i,(\delta(t-i\times dt))}(t) = N_{i,(\delta(t))}(t - i \times dt)$). And so, the response to a sum of such shifted emission impulses is just a sum of the resulting shifted outputs. Using this method, we can compute the output (N_i) from Eq. 5.7, in response to step emissions $\dot{N}_i(x,y,z,t)$, by calculating the output in response to impulse emission at t = 0 $(N_{i,\delta(t)})$, and then taking the summation of time shifted outputs. Therefore, $N_{i,\delta(t)}$ was calculated first using these equations.

Several studies have reported distribution of the sizes and numbers of particles emitted during speaking, coughing, and sneezing (see Appendix B) [40,44-53]. Most of these studies report only the sizes distribution of the emitted particles while the total number concentration of the exhaled droplets is not reported. Chao et al. [40] reported in a detailed manner the sizes and number of particles emitted during speaking and coughing, and Duguid [44]reported the detailed size distribution of droplets emitted during sneezing. The particle size distributions from Chao et al. [40] and Duguid [44] were used in this study and these are shown in Appendix B. Approximately 0.4 L of air is assumed to be exhaled in a cough and sneeze over a time period of ~500 ms [40]. A constant emission rate was assumed during this time period of emissions. The air volume emitted during speech is almost a third of the volume emitted during a cough over the same time period. The input emission impulse is based on the size distribution function as shown in Appendix B and the volume of air expired. The calculations for coughing, sneezing and speech input emission impulse are discussed in more detail in Appendix B.

5.2.2 Respiratory deposition

The droplets exhaled by an infected person that reach another individual, can eventually be inhaled. The droplets in the air passages of the respiratory system deposit by various mechanisms that are size dependent. The total deposition fraction (DF) in the respiratory system according to the model developed by the International Commission on Radiological Protection (ICRP model) [54] is:

$$DF = IF\left(0.0587 + \frac{0.911}{1 + \exp(4.77 + 8.91 \ln d_{p,i})} + \frac{0.943}{1 + \exp(0.503 + 15.48 \ln d_{p,i})}\right) \quad (5.14)$$

where, $d_{p,i}$ is in m, and IF is the inhalable fraction defined as:

$$IF = \left(1 - \frac{1}{1 + 4.8 \times 10^{13} \, d_{p,i}^{2.8}}\right) \tag{5.15}$$

The rate of deposition of these droplets for each mode, in the respiratory tract of an exposed individual at any position as the function of time can be calculated using:

$$N_{inh,rate,i,\delta(t)}(x,y,z,t) = N_{i,\delta(t)}(x,y,z,t) \times IR \times DF \tag{5.16}$$

where, IR is the inhalation rate (= 1.5 m³/hr) [55]. If the exposed individual is wearing a mask, the LHS of Eq. 5.16 will be multiplied by the particle penetration efficiency of the mask.

5.2.3   Viral load and inactivation rate considerations

The concentration of virus in the sputum/saliva (V_{load}) is representative of the virus concentration in the emitted droplets [56]. Assuming that virus does not leave the droplet during evaporation, this average number of virus for each mode will not change as the function of time. The rate of deposition of infectious viruses in the respiratory tract of the susceptible individual at any position as the function of time can be calculated using:

$$V_{inh,rate,i,\delta(t)}(x,y,z,t) = N_{inh,rate,i,\delta(t)}(x,y,z,t) \times V_{load} \left(\frac{\pi}{6} d_{p,i,0}^{3}\right) \times \left(\frac{1}{2}\right)^{\frac{t}{T_{1/2}}} \tag{5.17}$$

172

where, V_{load} is the initial viral load, $d_{p,i,0}$ is the initial diameter of ith mode, and $T_{1/2}$ is the half

life of the viruses. The factor of $(1/2)^{\frac{t}{T_{1/2}}}$ represents the ratio of virus that remain infectious at

time 't' to the initial number of infectious of viruses. van Doremalen et al. [17] measured the

concentration of airborne infectious viruses as a function of time at 23°C and 40% relative

humidity, and it was reported that 50% of the viruses became non-viable after 1.1 hrs under the

given experimental conditions (i.e. $T_{1/2} = 1.1$ hr).

$V_{inh,rate,i,\delta(t)}$ corresponds to the output in response to impulse emission at $t = 0$. $V_{inh,rate,i}$

(assuming no filtration and deposition losses except for the ground) for continuous emissions till

time t_{exp} was calculated using:

$$V_{inh,rate,i}(x,y,z,t) = \sum_{i=0}^{\frac{texp}{dt}} V_{inh,rate,i,\delta(t-i\times dt)}(x,y,z,t) \qquad (5.18a)$$

$$= \sum_{i=0}^{texp/dt} V_{inh,rate,i,\delta(t)}(x,y,z,t-i\times dt) \qquad (5.18b)$$

The total viruses deposited in the respiratory system of a susceptible individual at a position (X,

Y,Z) up to a time 'T', is given by:

$$V_{total}(X,Y,Z,T) = \int_0^T \sum_i V_{inh,rate,i}(X,Y,Z,t)\, dt \qquad (5.19)$$

5.2.4   Risk of infection

A dose-response model can be used to estimate the probability of getting infected on exposure to pathogens. A limitation of conducting risk assessment of SARS-CoV-2 is the lack of quantitative dose-response information for this particular coronavirus. Therefore, in this work, dose response was approximated from the data available for similar viruses. Existing dose-response models are available for SARS-CoV-1. Watanabe et al., 2010 [57] reported an exponential dose-response relationship for SARS-CoV-1. According to this model, if the total expected number of pathogens deposited in the visitor's alveolar region, is μ, then the actual integer number of pathogens deposited would follow a Poisson probability distribution. Therefore, if the deposition of just one pathogen can initiate infection, the risk of infection 'R' is given by the expression:

$$R = 1 - \exp(-\mu) \tag{5.20}$$

However, not every virus results in an infection. Therefore, to account for actual infectious dose, Eq. 5.20 can be modified as:

$$R = 1 - \exp(-\sigma \, \mu) \tag{5.21}$$

where, the factor 'σ' is the infectivity factor which is the inverse of the number of viruses that can initiate an infection. It is representative of the infectious dose. This factor can also be used to describe different variants of the virus which may be more infective. Eq. 4.21 can be combined with the transport model to estimate the probability that a susceptible individual at a position (X,Y,Z) will get infected, when exposed for time 'T'. It is given by:

$$R(X, Y, Z, t) = 1 - \exp\left(-\sigma\, V_{total}(X, Y, Z, T)\right) \qquad (5.22)$$

5.2.5   Simulation plan

Table 5-1 Test Plan

Sr No.	Objective	Parameters	Results
I	Size distribution of emitted droplets	Exhalation activities: speaking, coughing, and sneezing	Appendix B
II	Lifetime of Droplet	Settling time as the function of emitted particle size (accounting for diameter)	Figure 5-2.A.
III	Distance traversed	Distance traversed by droplets as the function of their size for different exhalation activities	Figure 5-2.B.
IV	Infectivity factor 'σ' and viral load on risk of infection	Risk from coughing (with no background wind) at a distance of 2.4 m as a function of 'σ' and viral load	Figure 5-3
V	Impact of time and distance on risk of infection	Risk, as a function of exposure time and distance, from different exhalation activities (with no background wind)	Figure 5-4
VI	Impact of ambient wind velocity on risk of infection	Risk as a function of wind velocity at distance of 2.4 m, 4.8 m	Figure 5-5
VII	Impact of mask usage on risk of infection	Risk from sneezing and coughing at a distance of 2.4 m when: A) No one is wearing masks B) Exposed person is wearing mask C) Infected person is wearing mask D) Both are wearing masks	Figure 5-6

The ambient temperature and relative humidity were assumed to be 298 K and 50% respectively, as the representative parameters for the results in this paper. These parameters can be readily varied to examine their effects. The time scales of settling of droplets and their evaporation were evaluated, and the effect of evaporation of droplets on their settling time was examined. After determining the settling time of the evaporating droplets, the horizontal distance travelled by droplets before they settle, was calculated as the function of the droplet size. Then, simulations were carried out to investigate the effect of governing parameters on the airborne transmission of SARS-CoV-2. The airborne transmission was quantified in terms of the risk of infection (Eq. 5.22). The effect of different parameters such as infectivity parameter, viral load, source, physical separation, time of exposure, ambient air velocity, and mask usage, was examined on the risk of infection. The test plan and the set of all the simulations performed are listed in Table 5-1.

5.3   Results and Discussions

5.3.1   Lifetime of droplets and distance traversed
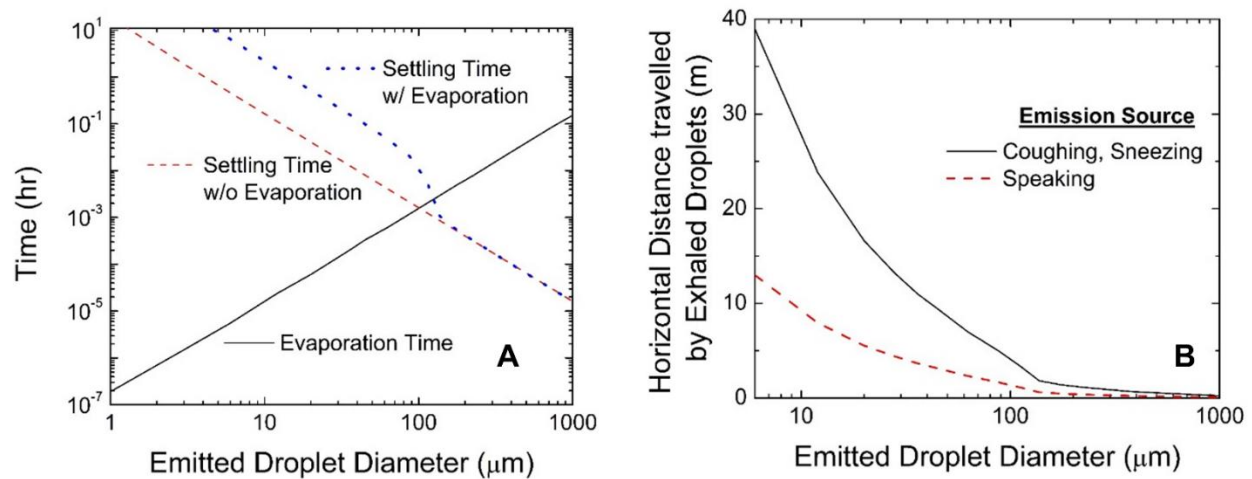
Figure 5-2 A.) Representative evaporation time and settling time calculated for droplets of different initial sizes. B.) Horizontal distances travelled by emitted droplets with a typical initial velocity of release during coughing, sneezing, and speaking in quiescent ambient. Simultaneous droplet evaporation and settling is considered in the trajectory calculations.

When the droplet containing infectious virus are emitted, they move and spread with the flow of the ambient air. These droplets are acted on by the force of gravity, and as a result, droplets larger than 200 µm settle to the ground very quickly in less than a second, while droplets smaller than 15 µm can remain suspended for several hours. The distance traversed by these droplets depend on their time of suspension (settling time) or lifetime, which depends on the droplet size. The droplets also undergo evaporation as soon as they are expired. It is important to understand the effect of evaporation on the lifetime of droplets to accurately estimate the droplet transport process. Figure 5-2.A. outlines a comparison of the evaporation time and the settling time for droplets. The evaporation time of the droplets was calculated by solving Eq. 5.6 till the final diameter of the droplets stopped changing due to attaining equilibrium with the surrounding

ambient. The settling time of the non-evaporating droplet, was evaluated by dividing the height from which droplets (typical value of H ~ 1.75 m) are emitted to the settling velocity of the droplets ($\overrightarrow{u_{ext}}$ from Eq. 5.4) and is therefore given by:

$$t_{lifetime} = \frac{18\,H\,\mu\,C}{\rho_p\,d_p^2\,g} \tag{5.23}$$

As can be seen from Figure 4-2.A., for the droplets larger than 100 µm, the settling time is smaller than the evaporation time of the droplets. Thus, large droplets (> 100 µm) take longer to evaporate than to settle, and evaporation does not significantly impact the droplet trajectory, since it is a few orders of magnitude higher than the settling time. However, for droplets smaller than 100 µm, evaporation occurs very fast before the droplet settles. Since, large number of droplets exhaled during different expiration activities lie below 100 µm (Appendix B), the evaporation of the emitted or exhaled droplets has to be considered to accurately evaluate the droplet transport characteristics.

The evaporation of the droplet was coupled with the settling (see Appendix B), and we estimated the settling time of the evaporating droplets. As expected, for any particle larger than ~ 140 µm, the settling time of evaporating droplets is same as the settling time of non-evaporating droplet with same initial diameter. This is because for particles larger than 140 µm, the settling time is a few orders of magnitude of lower than the evaporation time and, the droplets settle before any significant evaporation has taken place. It can be seen from Figure 5-2.A. that, for particles smaller than 90 µm, the settling time of an evaporating droplet is higher than the settling time of a non-evaporating droplet with same initial diameter. However, the settling time of an

evaporating droplet has similar dependence on the emitted droplet diameter as the settling time of a non-evaporating droplet. This is because for droplets smaller than 90 μm, evaporation takes place very fast as compared to settling. The droplets reach equilibrium diameter very quickly and settle at that diameter for a relatively longer time. Thus, the settling time of an evaporating droplet of some initial diameter smaller than 90 μm is same as the settling time of non-evaporating droplet with equilibrium diameter. For the respiratory droplets under evaporation at 298 K and 50% RH, the equilibrium diameter is 0.14 times the initial diameter. The settling time of evaporating droplets of size 'd_p' can be calculated by dividing height from which droplets (H ~ 1.75 m) are emitted to the settling velocity of the droplets (u_{ext}) evaluated for an effective diameter 'd_{eff}', where:

$$t_{lifetime} = \frac{18\,H\,\mu\,C}{\rho_p\,d_{eff}^2\,g}$$

$$= \frac{18\,H\,\mu\,C}{\rho_p\,(0.14\,d_p)^2\,g}, \qquad \text{when } d_p < 90 \text{ μm, and} \quad (5.24a)$$

$$= \frac{18\,H\,\mu\,C}{\rho_p\,(d_p)^2\,g}, \qquad \text{when } d_p > 140 \text{ μm} \qquad (5.24b)$$

There is a transition region between 90 μm and 140 μm. It can be seen from Figure 5-2.A., that evaporating droplets with emission diameter < 60 μm can remain suspended in air for several minutes and the droplets < 10 μm can remain suspended for several hours.

After determining the settling time of evaporating droplets, the trajectory of the droplets was determined by solving the equation of motion while simultaneously considering droplet evaporation and settling (see Appendix B). Based on the trajectory calculations, the horizontal

distance traversed by droplets before settling, expired during coughing, sneezing, and speaking, was evaluated as the function of their size. As can be seen from Figure 5-2.B., the lifetime of the 100 μm droplet is 44 s and it can travel 1.6 m and 4.9 m when released during speaking and coughing/sneezing respectively; while the 10 μm droplet can stay suspended for 2.2 hrs and can travel 9.1 m and 27.4 m when released during speaking and coughing/sneezing respectively. The distance traversed by droplets before settling, emitted during speaking is about a third of when emitted during coughing/sneezing as the expiration velocity of droplets released during speaking is $1/3^{rd}$ of the velocity of particles emitted during coughing/sneezing. The expired droplets <50 μm can traverse distances larger than 10 m, and can potentially spread infection to these large distances.

5.3.2 Effect of infectivity factor and viral load on risk of infection
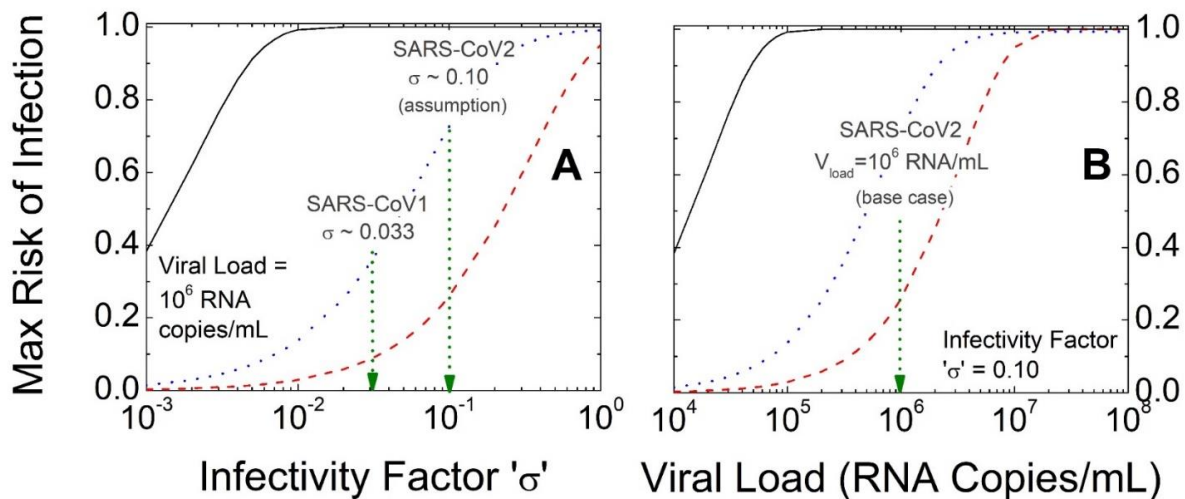
Figure 5 Error! No text of specified style in document.**-3** Maximum risk of infection from a single sneeze (———), cough (— — —)and speaking for 1min (·········) from infected individual, at a separation of 2.4 m as the function of A). infectivity factor 'σ', and B). viral load in exhaled droplets, in quiescent ambient. The left vertical line in A) represents the 'σ' for SARS-CoV-1 (Watanabe et al. 2010) and while the right

vertical line represents the assumed 'σ' for SARS-CoV-2 in the simulations in this study. The vertical line in B) represents the assumed initial viral load of emitted droplets for SARS-CoV-2, in this study.

The infectivity factor, 'σ', is not known for SARS-CoV-2. To determine the effect of 'σ' on the risk of infection, the transport equations coupled with dose response model were solved, and the risk of infection (when exposed to long time or max. risk) from droplets released during coughing, sneezing and speaking (for 1 min) was evaluated at the distance of 2.4 m in front of the infected individual in the quiescent ambient air (zero background velocity) as a worst-case scenario. The viral concentration in the saliva was assumed to be 10^6 infectious copies per mL. It can be seen from Figure 5-3.A. that the risk rises from zero at lower 'σ', increases and eventually saturates to 1 at higher 'σ' values. For SARS-CoV-1, this 'σ' lies in range 0.01-0.10 [57]. At σ = 0.033 (representative value for SARS-CoV-1), the risk of infection at 2.4 m distance is ~ 10% from a cough, 100% from a sneeze, and ~ 40% from speaking for 1 min. Since SARS-CoV-2 is highly infectious, 'σ' was assumed to be 0.10 for the base cases in our simulations. At σ = 0.1, the risk of infection at 2.4 m distance is higher than 20% from a cough, 100% from sneeze, and higher than 70% from speaking for 1 min. Clearly, as more representative values are obtained by experimentation later, the appropriate values of 'σ' can be used. It should also be noted that different variants of the virus (such as being found in recent times) have different infectivity rates, and appropriate values of 'σ' can be used to represent this effect.

The risk of infection also depends on the number of infectious viruses present in the droplets expired. The viral load is variable among different people and also in the same patient during the course of the disease. It lies between 10^3-10^{11} copies per mL of the saliva [58-63]. Figure 5-3.B. shows the effect of viral load on the risk of infection (when exposed for long time) at the

distance of 2.4 m in front of the infected individual in the quiescent ambient from coughing and talking for 1 min. The infectivity factor was assumed to be 0.1. The viral load has a similar effect on the risk of infection as 'σ'. The risk rises with increase in viral load and eventually saturates to 1 at higher values (> 2 x 10^7 infectious RNA copies per mL). The viral concentration in the saliva was assumed to be 10^6 infectious copies per mL in our simulations, since it averages to that value [58-63].

5.3.3 Effect of exposure time and physical separation on risk of infection
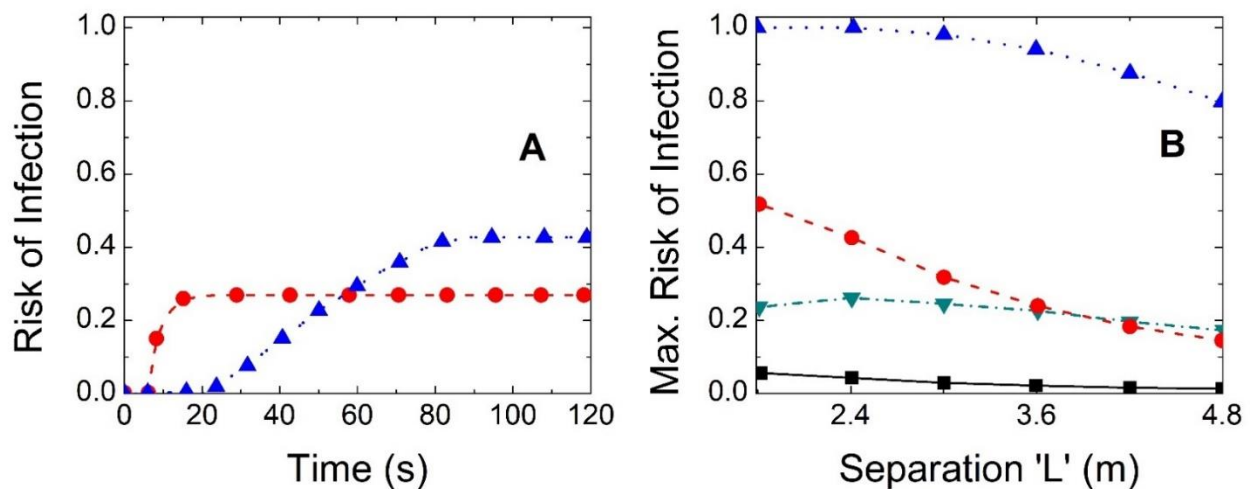
Figure 5-4 A.) Risk of infection from cough (0.5 s — — ● — —) and speaking (1 min ⋯ ▲ ⋯), by infected individual, at a separation of 2.4 m in quiescent ambient air (no background air velocity) as the function of time; time of 0s corresponds to the start of exhalation activity. The risk increases with time and saturates to the maximum at time >10 s for cough, and >80 for speaking. B.) Maximum risk of infection from a single cough (— · ▼ · —), speaking (10s —■—, 1 min — — ● — — & 10 min ⋯ ▲ ⋯), as the function of physical separation.

The simulations were performed for the cases of single cough, and speaking for 1 min in the quiescent ambient conditions without any ventilation, and the risk of infection was evaluated as the function of time. Figure 4-4.A. shows the risk of infection at a distance of 2.4 m as the

function of time. Here, t = 0 corresponds to the start of expiration activity. It can be seen from Figure 5-4.A. that the risk of infection increases from zero and saturates to a maximum value with time. When infected person expires droplets containing the infectious virus, it takes some time for the droplets to reach the susceptible person, and till then, the risk of infection is zero. The droplets released travel as a pulse and when they reach the susceptible individual, the risk starts to increase and reaches a maximum when the pulse completely passes further ahead. It can also be seen from Figure 5-4.A. that the risk of infection rises quickly from zero to the saturation value in (< 10 s) for coughing but, rises slowly from zero at 20 s to the saturation value at ~90 s for the case of speaking. This is because the velocity of expired droplets is higher in case of coughing as compared to speaking. Since, for coughing, the droplets are released within 500 ms, the width of pulse in which droplets travel is thinner and passes through the position of infected individual faster. Hence, the risk of infection rises from zero to the saturation value very fast for the case of coughing. However, during speaking, the droplets are released over a longer period of time (1 min in this case), and the susceptible individual is exposed to the virus over the longer period of time. Hence, the risk of infection slowly increases from zero to the saturation value.

The risk of infection will also depend on the physical separation between the infected and the exposed individual. Figure 5-4.B. shows the risk of infection in the quiescent ambient from a single cough, and talk (10 s, 1 min and 10 min), from infected individual as the function of physical separation between the infected and the exposed individual. The height of exposed individual is assumed to be same as the infected individual. The risk of infection at 6 ft or 1.8 m is very high (Figure 4-4.B.); it is 1 for speaking (10 min), 0.52 for speaking (1 min), 0.25 for coughing and 0.07 for speaking (10 s). Thus, the widely recommended physical separation of 6 ft

(1.8 m) is not enough to prevent the spread of SARS-CoV-2. The risk of infection from speaking

for longer periods of time is high and comparable to risk from coughing, and it increases with the

increase in speech time. This supports the hypothesis that asymptomatic individuals who do not

cough or sneeze can spread the infection [4-7].

It can also be seen that the risk of infection reduces as the distance increases from 1.8 m to 5 m.

This is because as the expiratory droplets travel further, settling of particles takes place resulting

in lower net inhalation and respiratory deposition of the infectious viruses. The regression

equations were used to evaluate the safe physical distance from the infected person such that the

risk of infection lie below 10% (assuming that this is an acceptable level of risk). The regression

equations are given by:

$$L = \left(exp(R) - (1.91186 \pm 0.04775)\right)/(-0.16497 \pm 0.01349)$$

$$for\ speaking\ (1\ min) \quad (5.25)$$

$$L = \ln\left((R - (1.01613 \pm 0.00878))/(-0.00319 \pm 0.00173)\right)/(0.88757 \pm 0.10886)$$

$$for\ speaking\ (10\ min) \quad (5.26)$$

$$L = \left(exp(R) - (1.41248 \pm 0.00555)\right)/(-0.04497 \pm 0.0107)$$

$$for\ coughing \quad (4.27)$$

Here, L is the physical separation (m) from the infected individual and R is the risk of infection

when exposed for long times. Substituting acceptable level of risk in these equations will give

the safe physical distance above which risk is low. All these regression equations are accurate at

a 95% confidence level. The regression equations for have the adjusted $R^2 > 0.97$. The risk of infection becomes lower than 10% at a distance of 6.9 m for coughing, and 4.9 m and 6.4 m for speaking for 1 min and 10 mins respectively.

The cases considered in this study (Figure 5-4) represents a scenario when infected individual is directly in front of the person exposed and the surrounding air is stagnant or there is no dilution by mixing. The concentration of the infectious aerosols can be reduced by increasing the ventilation rate in the buildings, thus reducing the risk of infection. The effect of dilution on the risk of transmission is discussed in more detail in Appendix B.

5.3.4   Effect of ambient air velocity on risk of infection
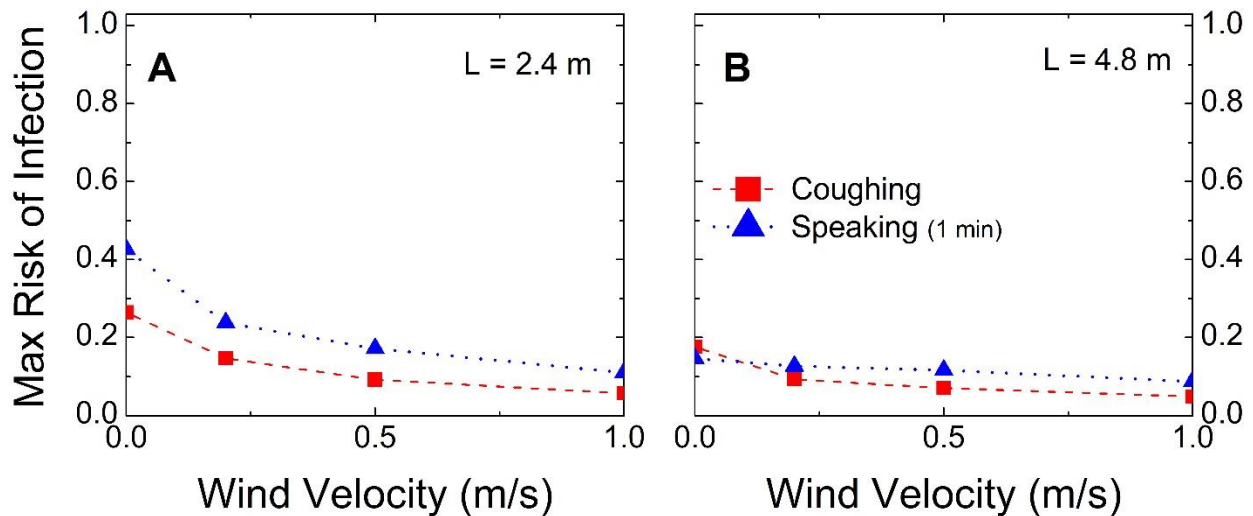
Figure 5-5 Maximum risk of infection from a cough (— – ■ – —), and speaking for 1 min (··· ▲ ···) by infected individual as the function of air velocity at physical separation of A.) 2.4 m, and B.) 4.8 m, when the wind is blowing towards the exposed person.

Typical values of the wind velocity in the outdoors are of the order of 1 m/s [64]. Air velocity in an indoor environment, due to ventilation and usage of fans, are usually on the order of 0.2 m/s

[65]. Air flow can affect both the virus concentration and the time a person is exposed, thus affecting the net respiratory deposition. The spread of droplets carrying infectious virus, can increase or decrease depending on the direction of airflow. The potentially most risky airflow direction is from the infected human towards the exposed individual. When, the airflow is in the direction of expiration, droplets can travel larger distances before significant settling take place. However, at higher air velocity, the droplets containing the infectious viruses pass through the location of the susceptible person faster and the person is exposed to these higher concentrations of viruses for a shorter period of time. The relative impact of airflow on the virus concentration and the time of exposure to higher concentration, determines the effect on the risk of transmission. Figure 5-5 shows the effect of wind velocity (towards the exposed person) on the risk of infection from a single cough, and speaking (1 min) from an infected individual at physical separation of 2.4 m, and 4.8 m. It can be seen that with increase in air velocity to 1 m/s, the risk of infection decreases for coughing and speaking (1 min) at both 2.4 m and 4.8 m. This implies that even though increase in air velocity results in the increase of viral concentration (less settling), the resulting decrease in exposure time dominates, and results in the lower net deposition of the infectious virus in the respiratory system of the exposed individual.

Since the velocity of the exhaled droplet jet reduces as the square of distance from the infected person (Eq. 5.6), the effect of background air flow on the droplet transport becomes more dominant as the droplet moves away from the infected person. If the direction of background air flow is from the exposed person towards the infected person, the transport of the expired droplets towards the exposed person is hindered. Therefore, when the air flow is in the direction opposite of expiration, the expired droplets cannot travel beyond a certain distance from the infected

individual, and the maximum distance that the droplets can travel in front of the infected person depends on the magnitude of air velocity. If there is a constant background air flow of 0.25 m/s in the direction opposite to expiration, the released droplets are not able to travel beyond 1.8 m (6 ft) and there will be no risk of transmission for the individuals standing beyond that distance (see Appendix B).

5.3.5   Effect of mask usage on risk of infection
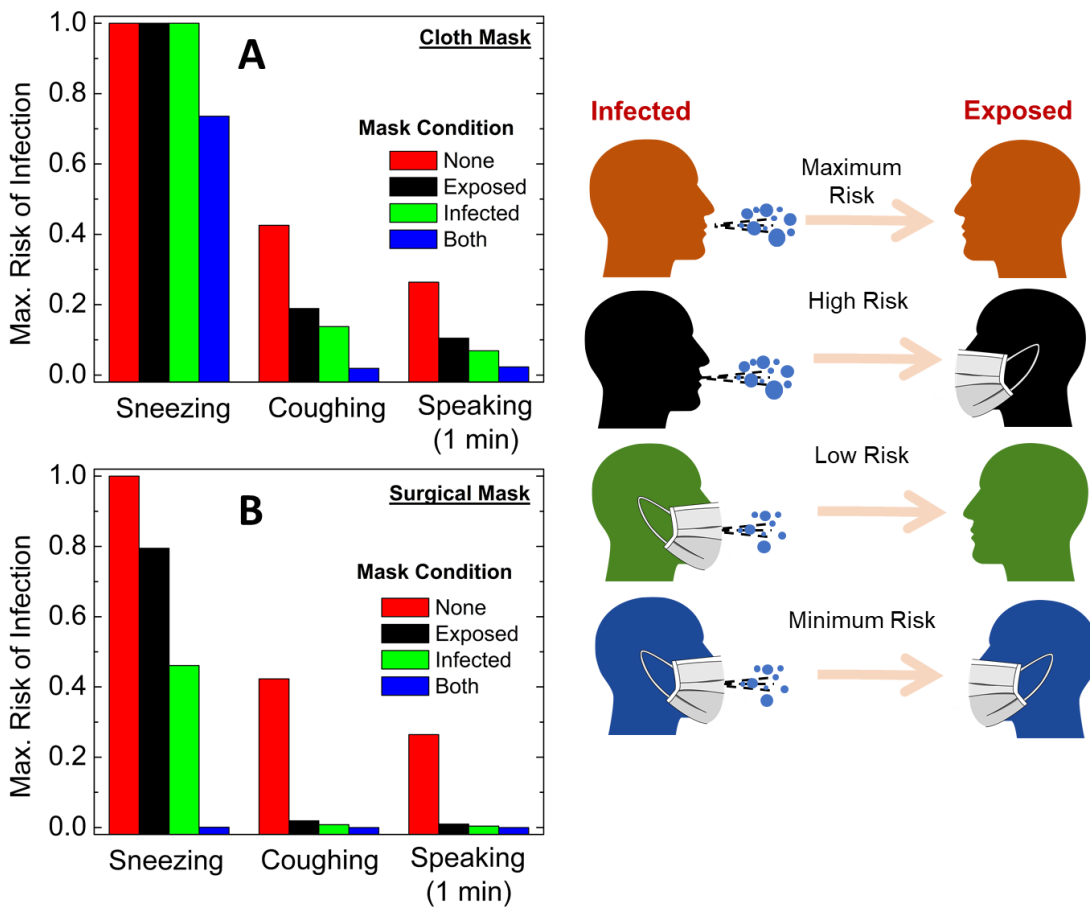
Figure 5-6 Effect of A) cloth mask and B) surgical mask on the risk of infection from sneezing, coughing, and speaking by infected individual at a distance of 2.4 m in the quiescent ambient. The risk is compared for four cases: a) when no one is wearing a mask, b) when only exposed person is wearing a mask, c) when only infected person is wearing a mask, and d) when both infected and exposed individual are wearing masks.

Face masks can be used as a way to control the spread of SARS-CoV-2, since they can reduce the net exposure to the infectious virus. The face mask worn by infected individual will reduce the emissions of the droplets into the air, while the mask worn by exposed individual will reduce the inhalation of these airborne droplets. It has also been reported that reduction in the virus deposition reduces the severity of illness from SARS-CoV-2 [66]. Figure 5-6. shows the effect of surgical masks and cloth masks (65%/35% cotton/polyester twill polyester/cotton blend 3, twill weave, 229 yarns inch^{-2}) on the risk of infection. The penetration efficiency of these masks is reported by Grinshpun et al. 2009 [67] and Zangmeister et al. 2020 [68] respectively (see Appendix B). There are four possible cases that were considered in this study: a) when no one is wearing a mask, b) when exposed person is wearing a mask, c) when infected person is wearing a mask, and d) when both the infected person and the person exposed are wearing masks. It can be seen that the risk of infection is highest when no one is wearing a mask followed by when only the exposed person is wearing a mask. The risk decreases significantly when the infected person is wearing a mask, and is lowest when both infected person and the person exposed are wearing masks. It is clear from Figure 5-6 that the face masks are more effective if the infected person is wearing a mask as compared to only the exposed person wearing a mask. This is because micrometer sized droplets upon emission (Appendix B) undergo evaporation when they become airborne, and the size of a large number of droplets reduces below 1 micrometer. The removal efficiency of the micrometer sized droplets by the facemasks is higher as compared to that of the sub-micrometer sized droplets (refer to Appendix B), the facemasks are therefore more effective in cutting off emissions near the source. The surgical masks are more effective than the cloth masks as they have lower particle penetration efficiency. Therefore in case of high risk situations, usage of masks with higher filtration efficiencies, like N95 and surgical masks, is

recommended. The filtration properties used in Figure 5-6 do not take into account the effect of air leaks that arise due to improper fit of the mask on the user's face. Leakages can significantly reduce effectiveness (see Appendix B); therefore, it is critically important that the masks are properly fit to minimize the leakage of air between the mask and the contours of the face.

5.4   Conclusions

The present study demonstrated that the airborne transmission of SARS-CoV-2 can be a significant mode of transmission of this disease. Using time scale analysis, it was shown that the droplets emitted by an infected person can remain suspended in the vicinity for several hours (2.2 hrs for 10 μm droplet), since the evaporation of the droplets increases their suspension time. These suspended droplets can travel a distance of several meters before settling; for example, a 10 μm droplet emitted by a cough can travel a distance of 27.4 m before it settles. These suspended droplets containing infectious viruses can be inhaled by a susceptible individual, deposit in the respiratory system and initiate the infection. The developed model was used to evaluate the risk of infection from coughing, sneezing and speaking, and it was shown that there is substantial risk of tranmission of infection from these expiratory activites even upto distance of 6 m. The presence of an air flow both towards and away from the direction of expiration was shown to reduce the risk from airborne transmission. The efficacy of masks to control the airborne transmission was demonstrated and it was found that the face masks are most effective when worn both by the infected and the exposed individual; but any person wearing a mask significantly reduces their risk to infection. The model equations developed in this study can also be used to design prevention and control measures so that the risk of infection form airborne transmission can be minimized.

5.5   References

1. *Worldometer* Website; https://www.worldometers.info/coronavirus/ (05/08/2021)

2. Chakraborty, I.; Maity, P. COVID-19 outbreak: Migration, effects on society, global environment and prevention. *Sci. Total Environ*. **2020**, 138882.

3. Tellier, R., Li, Y., Cowling, B. J., & Tang, J. W. (2019). Recognition of aerosol transmission of infectious agents: a commentary. *BMC infectious diseases*, *19*(1), 1-9.

4. Chan, J. F. W., Yuan, S., Kok, K. H., To, K. K. W., Chu, H., Yang, J., Xing, F., Liu, J., Yip, C.C.Y., Poon, R.W.S. & Yuen, K. Y. (2020). A familial cluster of pneumonia associated with the 2019 novel coronavirus indicating person-to-person transmission: a study of a family cluster. *The lancet*, *395*(10223), 514-523.

5. Zou, L., Ruan, F., Huang, M., Liang, L., Huang, H., Hong, Z., Yu, J., Kang, M., Song, Y., Xia, J. & Wu, J. (2020). SARS-CoV-2 viral load in upper respiratory specimens of infected patients. *New England Journal of Medicine*, *382*(12), 1177-1179.

6. Rothe, C., Schunk, M., Sothmann, P., Bretzel, G., Froeschl, G., Wallrauch, C., Zimmer, T., Thiel, V., Janke, C., Guggemos, W. & Hoelscher, M. (2020). Transmission of 2019-nCoV infection from an asymptomatic contact in Germany. *New England journal of medicine*, *382*(10), 970-971.

7. Li, R., Pei, S., Chen, B., Song, Y., Zhang, T., Yang, W., & Shaman, J. (2020). Substantial undocumented infection facilitates the rapid dissemination of novel coronavirus (SARS-CoV-2). *Science*, *368*(6490), 489-493.

8. Anfinrud, P., Stadnytskyi, V., Bax, C. E., & Bax, A. (2020). Visualizing speech-generated oral fluid droplets with laser light scattering. *New England Journal of Medicine*, *382*(21), 2061-2063.

9. Stadnytskyi, V., Bax, C. E., Bax, A., & Anfinrud, P. (2020). The airborne lifetime of small speech droplets and their potential importance in SARS-CoV-2 transmission. *Proceedings of the National Academy of Sciences*, *117*(22), 11875-11877.

10. Asadi, S., Wexler, A. S., Cappa, C. D., Barreda, S., Bouvier, N. M., & Ristenpart, W. D. (2019). Aerosol emission and superemission during human speech increase with voice loudness. *Scientific reports*, *9*(1), 1-10.

11. Morawska, L., & Cao, J. (2020). Airborne transmission of SARS-CoV-2: The world should face the reality. *Environment international*, *139*, 105730.

12. Chia, P. Y., Coleman, K. K., Tan, Y. K., Ong, S. W. X., Gum, M., Lau, S. K., Lim, X.F., Lim, A.S., Sutjipto, S., Lee, P.H. & Marimuthu, K. (2020). Detection of air and surface contamination by SARS-CoV-2 in hospital rooms of infected patients. *Nature communications*, *11*(1), 1-7.

13. Jiang, Y., Wang, H., Chen, Y., He, J., Chen, L., Liu, Y., Hu, X., Li, A., Liu, S., Zhang, P. & Hua, S. (2020). Clinical data on hospital environmental hygiene monitoring and medical staff protection during the coronavirus disease 2019 Outbreak. *MedRxiv*. doi:10.1101/2020.02.25.20028043.

14. Yuan, L., Zhi, N., Yu, C., Ming, G., Yingle, L., Kumar, G. N., Li, S., Yusen, D., Jing, C., Dane, W. & Ke, L. (2020). Aerodynamic characteristics and RNA concentration of SARS-CoV-2 aerosol in Wuhan hospitals during COVID-19 outbreak. *BioRxiv*. doi:10.1101/2020.03.08.982637.

15. Santarpia, J. L., Rivera, D. N., Herrera, V., Morwitzer, M. J., Creager, H., Santarpia, G. W., Crown, K.K., Brett-Major, D., Schnaubelt, E., Broadhurst, M.J. & Lowe, J. J. (2020).

Transmission potential of SARS-CoV-2 in viral shedding observed at the University of Nebraska Medical Center. *MedRxiv*. doi:10.1101/2020.03.23.20039446.

16. Lednicky, J. A., Lauzard, M., Fan, Z. H., Jutla, A., Tilly, T. B., Gangwar, M., ... & Wu, C. Y. (2020). Viable SARS-CoV-2 in the air of a hospital room with COVID-19 patients. *International Journal of Infectious Diseases*, *100*, 476-482.

17. Van Doremalen, N., Bushmaker, T., Morris, D. H., Holbrook, M. G., Gamble, A., Williamson, B. N., ... & Munster, V. J. (2020). Aerosol and surface stability of SARS-CoV-2 as compared with SARS-CoV-1. *New England journal of medicine*, *382*(16), 1564-1567.

18. Fears, A. C., Klimstra, W. B., Duprex, P., Hartman, A., Weaver, S. C., Plante, K. S., Mirchandani, D., Plante, J.A., Aguilar, P.V., Fernández, D. & Roy, C. J. (2020). Persistence of severe acute respiratory syndrome coronavirus 2 in aerosol suspensions. *Emerging infectious diseases*, *26*(9), 2168.

19. Kim, Y. I., Kim, S. G., Kim, S. M., Kim, E. H., Park, S. J., Yu, K. M., Chang, J.H., Kim, E.J., Lee, S., Casel, M.A.B. & Choi, Y. K. (2020). Infection and rapid transmission of SARS-CoV-2 in ferrets. *Cell host & microbe*, *27*(5), 704-709.

20. Chan, J. F. W., Yuan, S., Zhang, A. J., Poon, V. K. M., Chan, C. C. S., Lee, A. C. Y., Fan, Z., Li, C., Liang, R., Cao, J. & Yuen, K. Y. (2020). Surgical mask partition reduces the risk of noncontact transmission in a golden Syrian hamster model for Coronavirus Disease 2019 (COVID-19). *Clinical Infectious Diseases*, *71*(16), 2139-2149.

21. Bao, L., Gao, H., Deng, W., Lv, Q., Yu, H., Liu, M., Yu, P., Liu, J., Qu, Y., Gong, S. & Qin, C. (2020). Transmission of severe acute respiratory syndrome coronavirus 2 via

close contact and respiratory droplets among human angiotensin-converting enzyme 2 mice. *The Journal of infectious diseases*, *222*(4), 551-555.

22. Biswas, P., & Dhawan, S. (2020). Evaporation of Emitted Droplets Are An Important Factor Affecting the Lifetime of the Airborne Coronavirus. *Preprints* doi:10.20944/preprints202004.0523.v1.

23. Klompas, M., Baker, M. A., & Rhee, C. (2020). Airborne transmission of SARS-CoV-2: theoretical considerations and available evidence. *Jama*. doi:10.1001/jama.2020.12458.

24. Parienta, D., Morawska, L., Johnson, G. R., Ristovski, Z. D., Hargreaves, M., Mengersen, K., Corbett, S., Chao, C.Y., Li, Y. & Katoshevski, D. (2011). Theoretical analysis of the motion and evaporation of exhaled respiratory droplets of mixed composition. *Journal of aerosol science*, *42*(1), 1-10.

25. Wei, J., & Li, Y. (2015). Enhanced spread of expiratory droplets by turbulence in a cough jet. *Building and Environment*, *93*, 86-96.

26. Liu, L., Wei, J., Li, Y., & Ooi, A. (2017). Evaporation and dispersion of respiratory droplets from coughing. *Indoor air*, *27*(1), 179-190.

27. Gao, N. P., Niu, J. L., Perino, M., & Heiselberg, P. (2008). The airborne transmission of infection between flats in high-rise residential buildings: tracer gas simulation. *Building and Environment*, *43*(11), 1805-1817.

28. Wan, M. P., Sze To, G. N., Chao, C. Y. H., Fang, L., & Melikov, A. (2009). Modeling the fate of expiratory aerosols and the associated infection risk in an aircraft cabin environment. *Aerosol Science and Technology*, *43*(4), 322-343.

29. Redrow, J., Mao, S., Celik, I., Posada, J. A., & Feng, Z. G. (2011). Modeling the evaporation and dispersion of airborne sputum droplets expelled from a human cough. *Building and Environment*, *46*(10), 2042-2051.

30. Li, X., Shang, Y., Yan, Y., Yang, L., & Tu, J. (2018). Modelling of evaporation of cough droplets in inhomogeneous humidity fields using the multi-component Eulerian-Lagrangian approach. *Building and environment*, *128*, 68-76.

31. Wells, W. F. (1934). On air-borne infection. Study II. Droplets and droplet nuclei. *American Journal of Hygiene*, *20*, 611-18.

32. Yan, Y., Li, X., Shang, Y., & Tu, J. (2017). Evaluation of airborne disease infection risks in an airliner cabin using the Lagrangian-based Wells-Riley approach. *Building and environment*, *121*, 79-92.

33. Rudnick, S. N., & Milton, D. K. (2003). Risk of indoor airborne infection transmission estimated from carbon dioxide concentration. *Indoor air*, *13*(3), 237-245.

34. Knibbs, L. D., Morawska, L., & Bell, S. C. (2012). The risk of airborne influenza transmission in passenger cars. *Epidemiology & Infection*, *140*(3), 474-478.

35. Liao, C. M., Chang, C. F., & Liang, H. M. (2005). A probabilistic transmission dynamic model to assess indoor airborne infection risks. *Risk Analysis: An International Journal*, *25*(5), 1097-1107.

36. Friedlander, S. K. Smoke, dust, and haze 2000, Vol. 198. New York: Oxford University Press.

37. Biswas, P., Wu, C. Y., Zachariah, M. R., & McMillin, B. (1997). Characterization of iron oxide-silica nanocomposites in flames: Part II. Comparison of discrete-sectional model predictions to experimental data. *Journal of Materials research*, *12*(3), 714-723.

38. Savory, E., Lin, W. E., Blackman, K., Roberto, M. C., Cuthbertson, L. R., Scott, J. A., & Mubareka, S. (2014). Western Cold and Flu (WeCoF) aerosol study–preliminary results. *BMC research notes*, *7*(1), 1-11.

39. Nishimura, H., Sakata, S., & Kaga, A. (2013). A new methodology for studying dynamics of aerosol particles in sneeze and cough using a digital high-vision, high-speed video system and vector analyses. *PloS one*, *8*(11), e80244.

40. Chao, C. Y. H., Wan, M. P., Morawska, L., Johnson, G. R., Ristovski, Z. D., Hargreaves, M., Mengersen, K., Corbett, S., Li, Y., Xie, X. & Katoshevski, D. (2009). Characterization of expiration air jets and droplet size distributions immediately at the mouth opening. *Journal of aerosol science*, *40*(2), 122-133.

41. Nicas, M., Nazaroff, W. W., & Hubbard, A. (2005). Toward understanding the risk of secondary airborne infection: emission of respirable pathogens. *Journal of occupational and environmental hygiene*, *2*(3), 143-154.

42. Zhang, H., Sharma, G., Dhawan, S., Dhanraj, D., Li, Z., & Biswas, P. (2020). Comparison of discrete, discrete-sectional, modal and moment models for aerosol dynamics simulations. *Aerosol Science and Technology*, *54*(7), 739-760.

43. Dhawan, S., & Biswas, P. (2019). Sampling artifacts in denuders during phase partitioning measurements of semi-volatile organic compounds. *Aerosol Science and Technology*, *53*(1), 73-85.

44. Duguid, J. P. (1946). The size and the duration of air-carriage of respiratory droplets and droplet-nuclei. *Epidemiology & Infection*, *44*(6), 471-479.

45. Buckland, F. E., & Tyrrell, D. A. J. (1964). Experiments on the spread of colds: 1. Laboratory studies on the dispersal of nasal secretion. *Epidemiology & Infection*, *62*(3), 365-377.

46. Loudon, R. G., & Roberts, R. M. (1967). Droplet expulsion from the respiratory tract. *American Review of Respiratory Disease*, *95*(3), 435-442.

47. Fennelly, K. P., Martyny, J. W., Fulton, K. E., Orme, I. M., Cave, D. M., & Heifets, L. B. (2004). Cough-generated aerosols of Mycobacterium tuberculosis: a new method to study infectiousness. *American journal of respiratory and critical care medicine*, *169*(5), 604-609.

48. Yang, S., Lee, G. W., Chen, C. M., Wu, C. C., & Yu, K. P. (2007). The size and concentration of droplets generated by coughing in human subjects. *Journal of Aerosol Medicine*, *20*(4), 484-494.

49. Morawska, L., Johnson, G., Ristovski, Z., Hargreaves, M., Mengersen, K., Chao, C., Wan, M., Li, Y., Xie, X. & Katoshevski, D. (2008). Droplets Expelled during Human Expiratory Activities and their Origin. In *Proceeding of the 11th International Conference on Indoor Air Quality and Climate Change* (pp. 1-8). University of Denmark.

50. Xie, X., Li, Y., Sun, H., & Liu, L. (2009). Exhaled droplets due to talking and coughing. *Journal of the Royal Society Interface*, *6*(suppl_6), S703-S714.

51. Morawska, L. J. G. R., Johnson, G. R., Ristovski, Z. D., Hargreaves, M., Mengersen, K., Corbett, S., Chao, C.Y.H., Li, Y. & Katoshevski, D. (2009). Size distribution and sites of origin of droplets expelled from the human respiratory tract during expiratory activities. *Journal of Aerosol Science*, *40*(3), 256-269.

52. Zayas, G., Chiang, M. C., Wong, E., MacDonald, F., Lange, C. F., Senthilselvan, A., & King, M. (2012). Cough aerosol in healthy participants: fundamental knowledge to optimize droplet-spread infectious respiratory disease management. *BMC pulmonary medicine*, *12*(1), 1-12.

53. Han, Z. Y., Weng, W. G., & Huang, Q. Y. (2013). Characterizations of particle size distribution of the droplets exhaled by sneeze. *Journal of the Royal Society Interface*, *10*(88), 20130560.

54. ICRP. ICRP publication 66: human respiratory tract model for radiological protection. *Elsevier Health Sciences*, 1996, Vol. 66.

55. United States. Environmental Protection Agency. Office of Health, & Environmental Assessment. Exposure Assessment Group. Exposure factors handbook, 1989. Office of Health and Environmental Assessment, US Environmental Protection Agency, Vol. 90, No. 623106774.

56. Buonanno, G., Stabile, L., & Morawska, L. (2020). Estimation of airborne viral emission: Quanta emission rate of SARS-CoV-2 for infection risk assessment. *Environment International*, *141*, 105794.

57. Watanabe, T., Bartrand, T. A., Weir, M. H., Omura, T., & Haas, C. N. (2010). Development of a dose-response model for SARS coronavirus. *Risk Analysis: An International Journal*, *30*(7), 1129-1138.

58. L'Huillier, A. G., Torriani, G., Pigny, F., Kaiser, L., & Eckerle, I. (2020). Culture-competent SARS-CoV-2 in nasopharynx of symptomatic neonates, children, and adolescents. *Emerging infectious diseases*, *26*(10), 2494.

59. Wölfel, R., Corman, V. M., Guggemos, W., Seilmaier, M., Zange, S., Müller, M. A., Niemeyer, D., Jones, T.C., Vollmar, P., Rothe, C. & Wendtner, C. (2020). Virological assessment of hospitalized patients with COVID-2019. *Nature*, *581*(7809), 465-469.

60. Kleiboeker, S., Cowden, S., Grantham, J., Nutt, J., Tyler, A., Berg, A., & Altrich, M. (2020). SARS-CoV-2 viral load assessment in respiratory samples. *Journal of Clinical Virology*, *129*, 104439.

61. To, K. K. W., Tsang, O. T. Y., Leung, W. S., Tam, A. R., Wu, T. C., Lung, D. C., Yip, C.C.Y., Cai, J.P., Chan, J.M.C., Chik, T.S.H. & Yuen, K. Y. (2020). Temporal profiles of viral load in posterior oropharyngeal saliva samples and serum antibody responses during infection by SARS-CoV-2: an observational cohort study. *The Lancet Infectious Diseases*, *20*(5), 565-574.

62. Li, Y., Qian, H., Hang, J., Chen, X., Hong, L., Liang, P., Li, J., Xiao, S., Wei, J., Liu, L. & Kang, M. (2020). Evidence for probable aerosol transmission of SARS-CoV-2 in a poorly ventilated restaurant. *MedRXiv*. doi:10.1016/j.micinf.2020.08.004.

63. Pan, Y., Zhang, D., Yang, P., Poon, L. L., & Wang, Q. (2020). Viral load of SARS-CoV-2 in clinical samples. *The Lancet infectious diseases*, *20*(4), 411-412.

64. Beer, T. Beaufort wind scale. *Encyclopedia of Natural Hazards* 2013, 42-45.

65. Humphreys, M. A., & Nicol, J. F. (2000). Outdoor temperature and indoor thermal comfort: raising the precision of the relationship for the 1998 ASHRAE database of field studies. *Ashrae Transactions*, *106*(2), 485-492.

66. Gandhi, M.; Beyrer, C.; & Goosby; E. Masks Do More Than Protect Others During COVID-19: Reducing the Inoculum of SARS-CoV-2 to Protect the Wearer. *J. Gen. Int. Med.* **2020**, doi:10.1007/s11606-020-06067-8.

67. Grinshpun, S. A., Haruta, H., Eninger, R. M., Reponen, T., McKay, R. T., & Lee, S. A. (2009). Performance of an N95 filtering facepiece particulate respirator and a surgical mask during human breathing: two pathways for particle penetration. *Journal of occupational and environmental hygiene*, *6*(10), 593-603.

68. Zangmeister, C. D., Radney, J. G., Vicenzi, E. P., & Weaver, J. L. (2020). Filtration efficiencies of nanoscale aerosol by cloth mask materials used to slow the spread of SARS-CoV-2. *ACS nano*, *14*(7), 9188-9200.

Chapter 6. Enhancing the charging and capture efficiency of aerosols using an atmospheric-pressure, flow-through RF plasma with a downstream DC bias

Abstract

Electrostatic precipitators (ESPs) are widely employed in industry and indoor environments for the removal of aerosol particles. ESPs typically use a corona discharge to charge the particles and allow them to be removed by a DC electric field. However, corona discharges are weakly ionized plasmas with plasma densities of the order of 10^{14}-10^{16} #/m^3. In comparison, other types of atmospheric-pressure plasmas including radio frequency (RF) microplasmas are characterized by orders of magnitude higher plasma densities ~10^{20} #/m^3. We have recently shown that high charging efficiencies (>90%) can be achieved by these plasmas for particles larger than 100 nm, while the charging efficiency of particles smaller than 100 nm was low. A two-stage charging mechanism based on a characteristic time scale analysis suggested that while particles were predominantly charged negatively in the plasma volume, the relatively faster rate of loss of the electrons in the spatial afterglow resulted in neutralization by positive ions.

Here, we present a new design concept for aerosol particle charging in atmospheric-pressure plasmas: a DC field downstream of the plasma volume in the spatial afterglow to potentially remove the positive ions and prevent neutralization of the particles. The overall charge fraction and polarity were measured as a function of particle diameter at different downstream DC voltages of a flow-through, RF atmospheric-pressure plasma. We find that when the magnitude of the applied DC voltage was higher than a critical value, the charge fraction of particles increased, and the charge polarity shifted from bipolar to unipolarly negative. The results were supported by analyzing the characteristic timescales for neutralization by and loss to the walls of positive ions in the spatial afterglow at different downstream DC voltages.

6.1   Introduction

Several particle control technologies have been developed over the years to reduce our exposure to airborne particles that cause various health problems. Commercially, high-efficiency particulate air (HEPA) filtration and electrostatic precipitators (ESPs) are used to remove aerosol particles and inactivate bioaerosols (including several viruses) from the air in many indoor environments, including hospitals, offices, and aircraft cabins [1]. However, both of these technologies have serious limitations. HEPA filtration systems usually result in excessive operational costs, as the media filter in these systems need regular replacement and the large pressure drop requires additional power for air circulation [2]. Electrostatic precipitators (ESPs) are more economical, but have size-dependent collection efficiencies, and in particular, the efficiency in the nanometer size range is typically low because nanoparticles are difficult to charge [3, 4]. Many potentially harmful indoor aerosols such as viruses (including the SARS-COV-2 virus) and protein fragments lie in the nanometer size ranges [5], and it is therefore critical to modify existing technologies or develop low-cost alternatives that efficiently capture harmful, nanometer-sized aerosols.

In an ESP, aerosol particles are charged by gaseous ions that are typically produced by a corona discharge, which is a type of localized plasma created near an electrode surface by the partial breakdown of a gas in the presence of a relatively strong electric field [6]. Glow discharges are plasmas that are formed by complete gas breakdown and contain higher concentration of ions [7, 8]. Several reactive species present in glow discharges also have promise for directly inactivating pathogens [9]. Moreover, it is very easy to integrate flow-through versions of glow discharges operated at atmospheric pressure with existing particle control systems, to potentially address the

charging efficiency of nanoparticles. However, few studies exist on these types of plasmas for particle charging and particle control applications. Ion mobility spectrometry has been applied online to flow-through plasmas at atmospheric pressure [10] and low pressure [11, 12] and observed the presence of bipolarly-charged silicon nanoparticles after the spatial afterglow. Recently, Sharma et al. (2020) systematically characterized particle charging in AC- and RF-powered flow-through, atmospheric-pressure, plasma systems [13]. High charging efficiencies (>90%) were found for particles larger than 100 nm. However, the charging efficiency of particles smaller than 100 nm was low, with a charging efficiency of less than 40% for 20 nm sized particles and 0% for particles of size 10 nm. The charge distribution of particles exiting the plasma reactor was revealed to be bipolar with particles supporting multiple charges. A two-stage charging mechanism based on a characteristic time scale analysis suggested that while particles were predominantly charged negatively in the plasma volume, the relatively faster rate of loss of the electrons in the spatial afterglow (downstream of the plasma region) resulted in neutralization by positive ions, and even subsequent positive charging of some of the particles [13]. The effect was found to be larger for smaller particles because of their lower initial negative charge in the plasma volume. A potential strategy to improve the charge efficiency in these systems is to preserve the charging from the plasma volume by eliminating the ion-mediated neutralization in the spatial afterglow.

In this work, we present a new design concept for aerosol nanoparticle charging in plasmas: a DC field downstream of the plasma volume in the spatial afterglow to potentially remove the positive ions and prevent neutralization of the particles. To test the concept, magnesium sulfate ($MgSO_4$) nanoparticles generated by atomization were introduced into a RF-powered, flow-

204

through, atmospheric-pressure plasma and the overall charge fraction and charge distribution in terms of polarity were measured as a function of particle diameter at different downstream DC voltages. We find that when the magnitude of the applied DC voltage was higher (more negative) than -0.5 kV, the charge fraction of particles increased, and the charge polarity shifted from bipolar to unipolarly negative. The results were supported by analyzing the characteristic timescales for neutralization by and loss to the walls of positive ions in the spatial afterglow at different downstream DC voltages.

6.2   Materials and Methods

6.2.1   Aerosol generation and plasma reactor

Aerosol nanoparticles were generated by atomizing solution mixture of $MgSO_4$ ($\geq$ 99% pure, Sigma Aldrich) dissolved in DI water using a TSI Aerosol Generator (Model 3076) with argon (Ar) as the carrier gas ($\geq$ 99.998% pure, Sigma Aldrich). The atomized droplets were passed through a diffusion dryer to remove water and yield dry $MgSO_4$ nanoparticles. The salt concentration in the atomized solution was adjusted to control the size of particles in the sub-100 nm range; in our experiments, a geometric mean diameter of 40 nm was used. Following the diffusion dryer and upstream of the plasma reactor, the particle stream was passed through a charged particle remover (Upstream CPR) to ensure that the particles entering the plasma were initially charge neutral. The flow rate of the particle stream was maintained at 1 L/min through the plasma reactor.

The plasma reactor schematically shown in Figure 6-1 was a flow-through system consisting of a clear fused quartz tube (ID: 2 mm, OD: 3.2 mm) and three metal ring electrodes on the outside in a parallel configuration. Two electrodes were electrically connected to a RF power supply (RF VII Inc., Model RF-3 XII), with one outer electrode connected to the power side through a homemade L-type matching network and the middle electrode connected to electrical ground. The spacing between these electrodes was 2 cm. The other outer electrode spaced apart by 1.2 cm from the middle electrode was connected to the high voltage output of a DC power supply which shared the same electrical ground. The plasma was ignited by a high voltage AC power supply (PVM500-4000, Amazing1 Inc.).
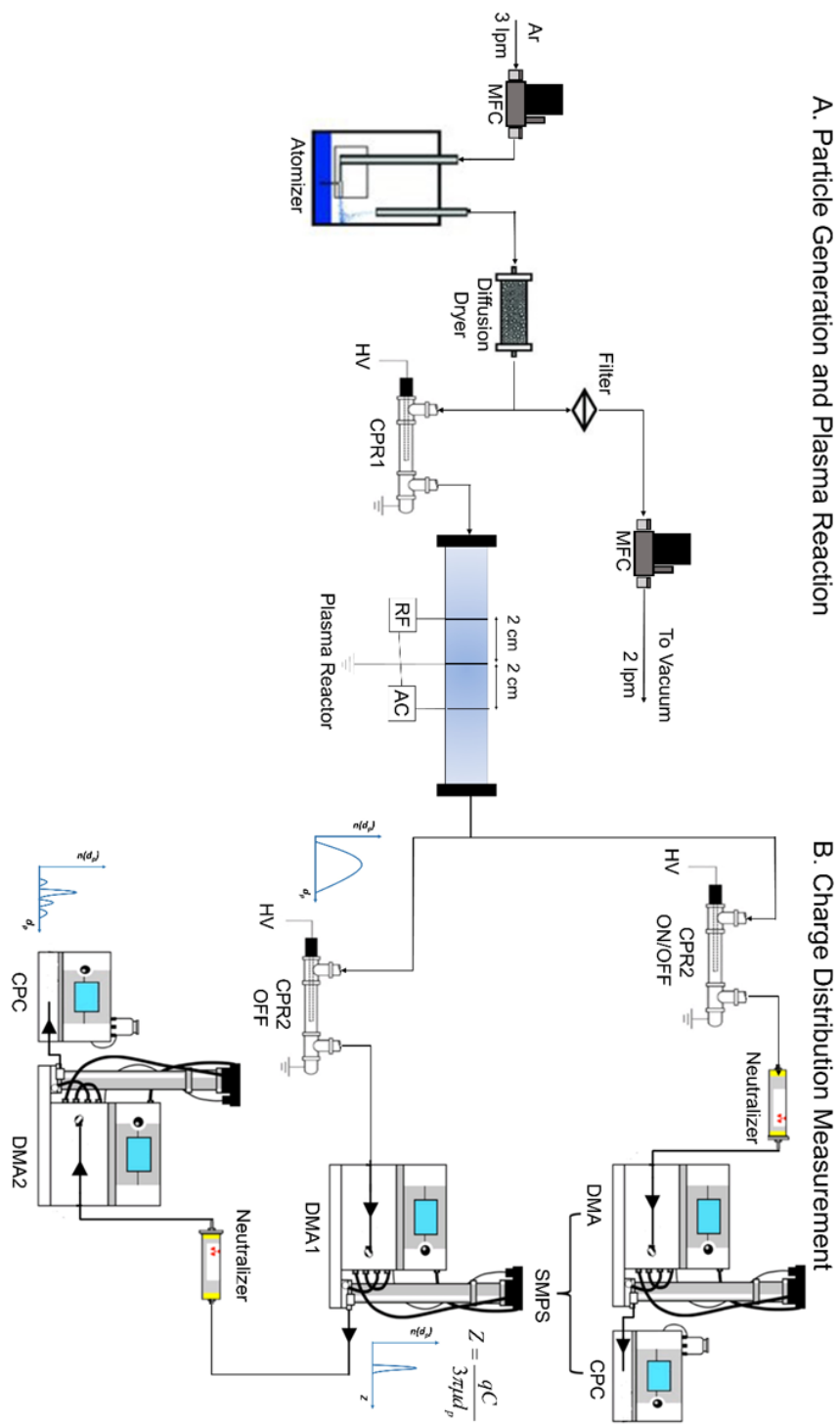
Figure 6-1 Experimental setup for A) particle generation and particle charging in a low-temperature, atmospheric-pressure, flow-through plasma with downstream DC bias; B) measurement of particle size distribution, overall particle charge fraction, and multiply charged particle distribution.

6.2.2   Plasma characterization

The electrical characterization of the RF plasma was performed using an RF power probe (Octiv Poly, Impedans Ltd.). The power probe is needed to measure the voltage and current waveforms in a RF plasma because of stray impedances in the high-frequency circuit. We developed a simplified equivalent circuit model to calculate the plasma resistance, and estimated the electron density from the plasma-fluid model. Additional details of these calculations, and the evaluated plasma properties (ion density and absorbed plasma power) are provided in the Sharma et al. (2020) [13].

6.2.3   Charge characterization

We systematically characterized the effect of a downstream DC bias on particle charging in a flow-through, atmospheric-pressure, RF plasma. The experimental setup is shown in Figure 6-1. Particle charging was assessed by the charging efficiency, which is defined as the fraction of particles that are charged, or the ratio of particles that attain any charge (either positive or negative, single or multiple) to the total number of particles entering the plasma. To measure the particle charge, the aerosol flow leaving the spatial afterglow was diluted by air at a flow rate of 2 L/min. The particle size distribution (PSD) and the charged particle fraction (either polarity) exiting the plasma reactor was obtained via a combination of a second charged particle remover (downstream CPR) and a scanning mobility particle sizer (SMPS). The initial PSD produced by the atomizer was measured in terms of a mobility diameter by the SMPS with the plasma and downstream CPR off. When the plasma and the downstream CPR were both turned on, the charge neutral (uncharged) PSD was obtained. The charged particle fraction was finally

calculated by subtracting the ratio of the neutral PSD and the initial PSD from unity. A similar charge characterization was then performed for different DC voltages in the spatial afterglow.

The polarity of particle charge exiting the plasma reactor was measured using a tandem differential mobility analyzer (TDMA) setup, consisting of two DMAs, a neutralizer, and a condensation particle counter (CPC). The first DMA (DMA1) is used to select particles of a desired mobility. The classified particle stream could contain different diameters depending on their charge state. This classified particle stream is then passed through a neutralizer to obtain a Fuchs charge distribution, followed by the second DMA (DMA2), where particles with different diameters and charge are separated, and then finally counted by the CPC. The relative peak heights were used to calculate the charge distribution. The polarity of DMA 1 can be switched between positive and negative polarity to measure negatively- and positively-charged particles, respectively. Here, we focused on the polarity of particles at two mean mobility diameters, 25 and 45 nm, as a function of the downstream DC voltage.

6.2.4   Time scale analysis

6.2.4 A. Calculation of characteristic neutralization time

The second stage, where particles exit the plasma and interact with a spatial afterglow, was modeled assuming the Fuchs theory of particle charging, and characteristic charging space-time or neutralization time in the second stage, $\tau_{neutralization}$, is estimated from the ion density and attachment coefficient of ions by [14, 15]:

$$\tau_{neutralization} = \frac{1}{\beta^+(d_p, q) n_{i,0}^+} \tag{6.1}$$

The attachment coefficient of ions to the particle, $\beta^+(d_p, q)$, with diameter d_p and elementary charge, q, is given by [14, 15]:

$$\beta^+(d_p, q) = \frac{\pi c_{ion}^+ \xi \delta^2 exp\left(-\frac{\phi(\delta)}{kT}\right)}{1 + exp\left(-\frac{\phi(\delta)}{kT}\right) \frac{c_{ion}^+ \xi \delta^2}{2 D_{ion}^+ d_p} \int_0^{\frac{d_p}{2\delta}} exp\left(-\frac{\phi\left(\frac{d_p}{2x}\right)}{kT}\right) dx} \tag{6.2}$$

where, c_{ion}^+ is the thermal velocity of ions (m/s), ξ is the collision coefficient between positive ions and negative ions, δ is the limiting-sphere radius, T is the gas temperature, and x is a dimensionless variable ranging from 0 to $d_p/2\delta$. The particle charge, q, at the exit of the plasma volume or at the beginning of second stage was calculated using orbit motion limited theory which is discussed in more detail in (Appendix C). The estimation of ion concentration in spatial afterglow is also discussed in (Appendix C).

The electrostatic potential energy $\phi(r)$ at distance r from the center of particle, is given by [14, 15]:

$$\phi(r) = \frac{e^2}{4\pi\varepsilon_0} \left\{ \frac{i}{r} - K \frac{d_p^3}{16r^2 (r^2 - (d_p/2)^2)} \right\} \tag{6.3}$$

where i is the number of elementary charges on the particle, and is positive if the charges of the

ion and the particle are of the same sign. For a perfectly conducting particle, $K = 1$, and for a

non-conducting particle, $K = 0$. The first term in Eq. 6.3 accounts for the Coulomb interaction

(attractive or repulsive) between the ion and the particles, and the second term accounts for the

attractive potential due to the polarization interaction of a sphere with a point charge. The

expression for limiting-sphere radius, δ, is given by [14, 15]:

$$\delta = \frac{d_p^3}{8\lambda_i^2}\left\{\frac{1}{5}\left(1+\frac{2\lambda_i}{d_p}\right)^5 - \frac{1}{3}\left(1+\frac{4\lambda_i^2}{d_p^2}\right)\left(1+\frac{2\lambda_i}{d_p}\right)^3 + \frac{2}{15}\left(1+\frac{4\lambda_i^2}{d_p^2}\right)^{5/2}\right\} \tag{6.4}$$

Using these equations, $\beta^+(d_p, q)$ is calculated and subsequently $\tau_{neutralization}$ was calculated.

We note that the neutralization time in the spatial afterglow will be a function of the particle size.

Here, we have simplified the calculation of the neutralization time by assuming a constant

geometric mean diameter of 45 nm as the representative size.

6.2.4 B. Calculation of characteristic loss time of ions

First, radial and axial electric field associated with the downstream DC bias was evaluated in the

afterglow region by using COMSOL. Figure 6-2 shows the COMSOL calculated values of radial

and axial electric field as the function of radial position and downstream distance from ground

electrode, when DC voltage of -0.5 kV is applied to third electrode. These calculations are used

to compute electrical force acting on ion in the afterglow region.
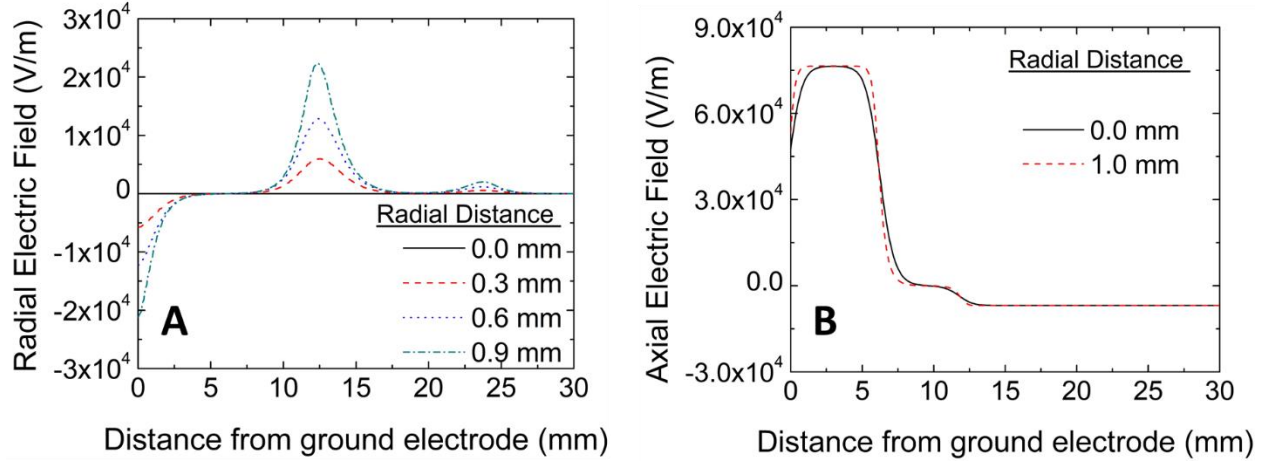
Figure 6-2 A) Radial and B) axial electric fields as a function of radial position and downstream distance from ground electrode when DC voltage of -0.5 kV is applied to third electrode.

The equation of motion was solved for argon ion while accounting for electrical force and drag force. The equation of motion of argon ion can be written as:

$$\frac{dv_r}{dt} = eE_r - \frac{3\pi\mu d_p}{C} v_r \tag{6.5}$$

$$\frac{dv_z}{dt} = eE_z - \frac{3\pi\mu d_p}{C} (v_z - v_{gas}) \tag{6.6}$$

Here, v_r and v_z are the radial and axial components of velocity of Ar ions, e is the elementary charge, E_r and E_z are the radial and axial components of the electric field, μ is the viscosity, d_p is the ion size, C is Cunningham slip correction factor and v_{gas} is the axial velocity of carrier gas. The initial position of ion was assumed to be at nearly the tube's center, at r = 0.1 mm, and the time to reach the tube's wall was calculated by solving Eq 6.5 and 6.6. These calculations were repeated for different DC voltages.

212

6.3   Results and Discussions

6.3.1   Charging characteristics
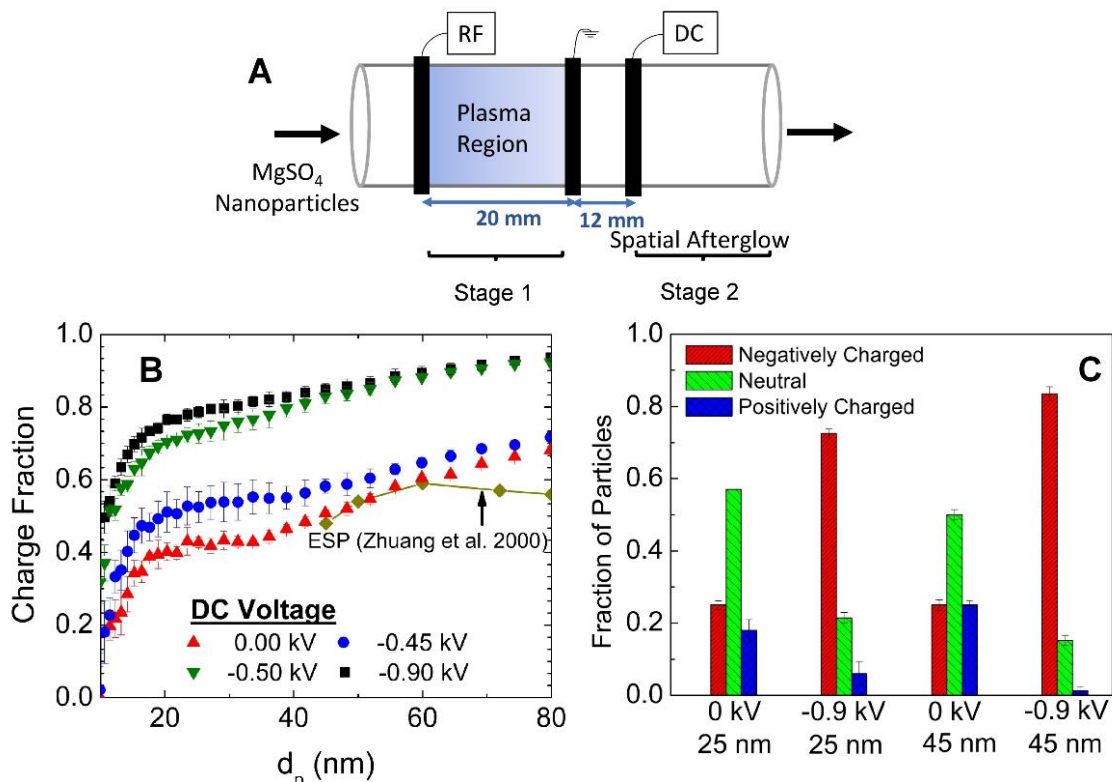
Figure 6-3 A) Schematic illustration of the RF-powered, flow-through, atmospheric-pressure plasma reactor with downstream DC bias used to study aerosol nanoparticle charging. B) Charge fraction of aerosolized $MgSO_4$ nanoparticles measured after plasma reactor as a function of particle diameter and different DC biases.   The collection efficiency of aerosolized NaCl particles measured after an ESP reported by Zhuang et al. (2000) is shown for comparison. C) Charge fraction of aerosolized $MgSO_4$ nanoparticles with 25 and 45 nm diameter after plasma reactor as a function of DC bias polarity.

The charging of particles exiting the plasma was initially characterized by the charged particle fraction. The DC voltage, applied to the third electrode, was varied to gauge the effect of downstream DC bias on particle charging. Figure 6-3 B shows the charge fraction of $MgSO_4$ particles exiting the RF plasma as a function of mobility diameter at different DC voltages. It can be seen from Figure 6-3 B that charge fraction increases with increasing diameter. At zero DC

voltage, the charge fraction of 10 nm particles is nearly zero; it increases to about 40% as the diameter increases to 20 nm, and is nearly 70% for 80 nm particles. Figure 6-3.B. shows that increasing the DC voltage from 0 kV to -0.45 kV does not result in significant difference in the total fraction of charged particles. A significant increase in charge fraction is observed when the DC voltage is increased to -0.5 kV. At an applied DC voltage of -0.5 kV, the charge fraction increases to nearly 35% for 10 nm particles, 70% for 20 nm particles and greater than 95% for 80 nm particles. Thus, -0.5 kV appears to be a threshold at which the charged particle fraction is enhanced. Any additional increase in DC voltage did not result in further change to the charged particle fraction.

In order to further understand the effect of downstream DC bias on particle charging, we characterized the polarity of the charge. Figure 6-3 C shows the charge distribution on $MgSO_4$ particles with 25 and 45 nm mean mobility diameters exiting the plasmas at two different DC voltages. At a DC voltage of 0 kV, the particles exhibit a bipolar charge distribution, which can be attributed to a two-stage charging mechanism in the plasma reactor that was previously reported (Sharma et al. 2020). Briefly, particles first acquire a predominantly negative charge in the plasma volume and subsequently, in the spatial afterglow, electrons are lost faster to the walls as compared to the positive ions because of their higher mobility, resulting in a larger flux of positive ions to the particles and neutralization. As can be seen from Figure 6-3 C, if a DC voltage of -0.9 kV is applied in the spatial afterglow, the fraction of positively charged particles becomes nearly zero and the particles are predominantly negatively charged. A possible explanation is that the negative DC bias decreases the flux of electrons or increases the flux of

positive ion to the walls and thus, limits or even eliminates neutralization of the particles, preserving the predominantly negative charge state of the particles leaving the plasma volume.

The distance between the third electrode with a DC bias and the ground electrode was also varied. At a distance of 1.2 cm, the critical DC voltage where particle charging efficiency was observed to dramatically increase was -0.5 kV. On increasing the electrode distance to 1.8 cm, the critical DC voltage increased to -2.5 kV, and at 2.4 cm, the DC bias was found to be ineffective up to a maximum of -5 kV. The experiments were also performed for positive DC bias; however, a positive DC voltage in the spatial afterglow was not found to have any effect on the charging characteristics of particles as compared to no bias. We note that the magnitudes of the DC voltages reported here could depend on many factors including the flow rate, reactor/electrode geometry, chemical composition of carrier gas, etc., but the overall trends should remain the same.

6.3.2   Characteristic time scale analysis
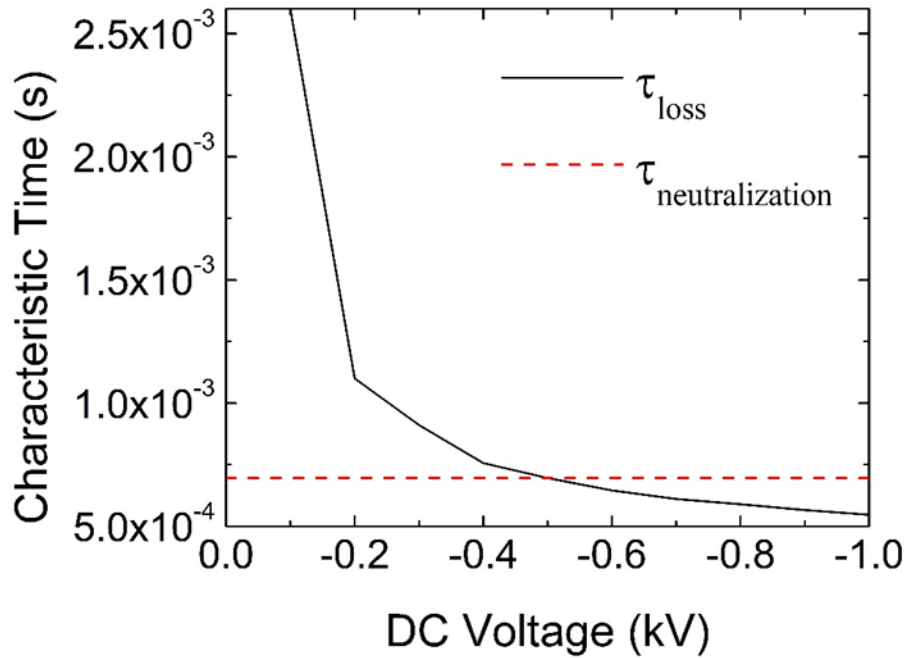
Figure 6-4 Calculations of characteristic times for positive ions colliding with and being lost to the reactor walls and colliding with and neutralizing negatively-charged nanoparticles in the spatial afterglow as a function of the DC bias voltage.

The experimental measurements indicate that the application of a negative DC field in the spatial afterglow reduces neutralization of particles, likely by decreasing the loss of electrons or increasing the loss of positive ions to the walls. To support and provide additional insight, the characteristic time for neutralization was compared to the characteristic loss time of positive ions as a function of the applied DC voltage. First, the electric potential distribution in the spatial afterglow was calculated using COMSOL. Then, while accounting for drag and electrical forces, Newton's second law (force balance expression) was solved to get the trajectory of the positive ions in the spatial afterglow and calculate the characteristic loss time of positive ions (τ_{loss}) as discusses in Section 6.2.3. The neutralization of negatively charged particles in the spatial afterglow, was modeled using Fuchs theory of particle charging. Briefly, the charge attained by

particles in the plasma volume was estimated first, and then using Fuchs theory of particle charging, the ion attachment coefficient was calculated. We note that the particle size could affect the neutralization time in spatial afterglow as larger particles possess more charge and would require more collisions or more time to be neutralized. We chose the 40 nm mobility diameter particles as a representative size to estimate the ion attachment coefficient. Sharma *et al*. (2020) reported the ion density in the same RF, flow-through, atmospheric-pressure plasma to be about 10^{20} m^{-3} [13]. The ion concentration in the spatial afterglow should be several orders of magnitude lower due to wall losses and electron-ion concentration recombination. However, the exact concentration is not known, and further experiments are required to measure it. For our purposes here, we varied the concentration and determined that a concentration of 2.5 x 10^{15} m^{-3} provided the best agreement between our characteristic time analysis and experimental results (Appendix C) which is consistent with the expected lower concentration than the plasma volume and literature values for an afterglow [16].

Figure 6-4 shows that the characteristic time of positive ion loss to the walls in the spatial afterglow region decreases as the magnitude of the DC voltage increases (more negative). When the DC voltage is $\geq$ -0.5 kV (more negative), the characteristic neutralization time for negatively-charged particles is longer than the time for loss of positive ions. Therefore, the charge fraction of particles will be higher, as the positive ions are lost relatively faster than the time required for particles to be neutralized, in agreement with experimental measurements. Figure 6-4 also shows that consistent with experiments, there is no further enhancement in positive ion removal rate as the DC voltage is increased beyond -0.5 kV.

6.3.3   Proposed mechanism
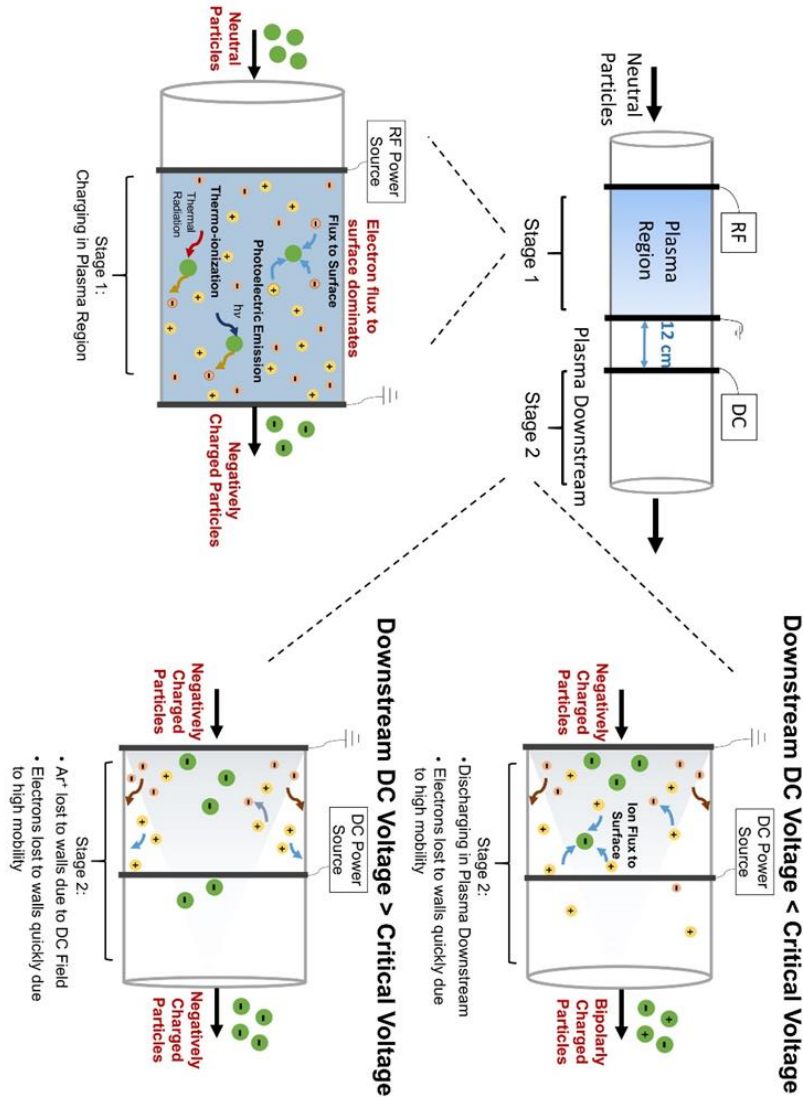
Figure 6-5 Schematic illustration of two stages within RF, flow-through, atmospheric-pressure plasma reactor with downstream DC bias: one, the main plasma volume where nanoparticles are predominantly charged negatively by the higher mobility electrons, and two, the spatial afterglow where positive ions neutralize and/or charge positively the negatively-charged particles when the DC bias voltage is less than a critical voltage (-0.5 kV), or where positive ions are removed and the negatively-charged particles are preserved.

218

We have previously proposed that particle charging in a flow-through, atmospheric-pressure plasma reactor is a two-stage process. The particles first pass through plasma volume which is quasi-neutral. Particles are predominantly charged negatively inside the plasma region because of the higher mobility of electrons compared to other charged species. The negative charge on particles in the plasma region will increase as the function of their size as larger particles are capable of holding more charge. After passing through the plasma volume, the particles exit through the spatial afterglow region [17-19], which is the region outside the RF and ground electrodes where ionization no longer takes place, but charged species remain [19]. In the spatial afterglow, electrons are quickly lost to the walls due to their very high mobility. Based on the experimental results and characteristic time scale analysis, the fate of negatively-charged particles in the afterglow depends on the magnitude of DC voltage applied to the third electrode, as shown in Figure 3. When there is no DC voltage or it is less than a critical voltage (less negative), loss of positive ions to the walls is relatively slow as compared to the characteristic neutralization time of the negatively-charged particles. Because of this, the negatively-charged particles exiting the plasma volume are neutralized and charged positively. This results in a bipolar distribution of charge on the particles at the reactor outlet. The neutralization effect was found to be larger for smaller particles because of their lower initial negative charge in the plasma region. However, when the applied DC voltage is higher than a critical voltage (more negative), the positive ions are lost to the walls relatively faster as compared to the characteristic neutralization time. In this case, positive ions are removed and unable to neutralize the negatively-charged particles exiting the plasma volume. Therefore, the particles retain their negative charge at the reactor outlet, and the fraction of particles carrying a charge is higher. The charge fraction increases with particle size as larger particles get higher initial negative charged

inside the plasma region. Although the proposed mechanism is supported by characteristic time calculations, other mechanisms could also be responsible for the experimental observations and were not considered in this study. We note that a similar picture could be described based on the DC voltage higher than a critical voltage (more negative) slowing the loss of electrons to the walls. Also, thermionic emission from quartz wall can take place near the DC electrode due to high temperature and application of negative electric field, which reduces the work function. Future studies are needed to verify the mechanism or the combination of mechanisms that affect particle charging in the afterglow region under the influence of negative electric field.

When the DC voltage was higher than the critical voltage, the overall charge fraction of particles was found to be very high for sub-100 nm particles, with a charging efficiency greater than 95% for 80 nm particles and greater than 70% for 20 nm particles. As can be seen from Figure 1.B., these efficiencies are very high as compared to traditional ESPs (Zhuang et al. 2000) which highlight the potential application of our flow-through, atmospheric-pressure plasma reactor with DC bias as a particle control device. Alternatively, the plasma reactor could be easily integrated with existing particle control systems to enhance their efficiencies at the smaller particle sizes. Moreover, further study of the potential inactivation of pathogens by the plasma could potentially lead to additional benefits.

6.4   Conclusions

In this work, we presented a new design concept for aerosol nanoparticle charging in plasmas: a DC field downstream of the plasma volume in the spatial afterglow to potentially remove the positive ions and prevent neutralization of the particles. Particle charging was systematically characterized for low temperature, atmospheric-pressure, flow-through plasmas with RF power couplings with a downstream DC Bias. The overall charge fraction and charge distribution in terms of polarity were measured as a function of particle diameter at different downstream DC voltages. We find that when the magnitude of the applied DC voltage was higher (more negative) than the critical voltage, the charge fraction of particles increased, and the charge polarity shifted from bipolar to unipolarly negative. The overall charge fraction of particles was found to be very high for sub-100 nm particles, with a charging efficiency greater than 95% for 80 nm particles and greater than 70% for 20 nm particles. The results were supported by analyzing the characteristic timescales for neutralization by and loss to the walls of positive ions in the spatial afterglow at different downstream DC voltages. Further studies are needed, to fully scale up this system and perhaps to lead to better understanding of particle charging in these plasma sources and control over charging for applications such as ESPs.

6.5　References

1. Kettleson, E. M., Ramaswami, B., Hogan Jr, C. J., Lee, M. H., Statyukha, G. A., Biswas, P., & Angenent, L. T. (2009). Airborne virus capture and inactivation by an electrostatic particle collector. *Environmental science & technology*, *43*(15), 5940-5946.

2. Gupta, A., Novick, V. J., Biswas, P., & Monson, P. R. (1993). Effect of humidity and particle hygroscopicity on the mass loading capacity of high efficiency particulate air (HEPA) filters. *Aerosol Science and Technology,* 19(1), 94-107.

3. Zhuang, Y., Kim, Y. J., Lee, T. G., & Biswas, P. (2000). Experimental and theoretical studies of ultra-fine particle behavior in electrostatic precipitators. *Journal of electrostatics*, *48*(3-4), 245-260.

4. Watanabe, T., Tochikubo, F., Koizurni, Y., Tsuchida, T., Hautanen, J., & Kauppinen, E. I. (1995). Submicron particle agglomeration by an electrostatic agglomerator. *Journal of Electrostatics*, *34*(4), 367-383.

5. Burnouf, T., Radosevich, M., Goubran, H. A., & Willkommen, H. (2005). Place of nanofiltration for assuring viral safety of biologicals. *Current Nanoscience*, *1*(3), 189-201.

6. Covert, D., Wiedensohler, A., & Russell, L. (1997). Particle charging and transmission efficiencies of aerosol charge neutralizes. *Aerosol Science and Technology*, *27*(2), 206-214.

7. Braithwaite, N. S. J. 2000. Introduction to gas discharges. *Plasma Sources Sci. Technol*. 9(4):517.

8. Tendero, C., Tixier, C., Tristant, P., Desmaison, J., & Leprince, P. (2006). Atmospheric pressure plasmas: A review. *Spectrochimica Acta Part B: Atomic Spectroscopy*, *61*(1), 2-30.

9. Wang, X. Q., Zhou, R. W., de Groot, G., Bazaka, K., Murphy, A. B., & Ostrikov, K. K. (2017). Spectral characteristics of cotton seeds treated by a dielectric barrier discharge plasma. *Scientific reports*, *7*(1), 1-9.

10. Sankaran, R. M., Holunga, D., Flagan, R. C., & Giapis, K. P. (2005). Synthesis of blue luminescent Si nanoparticles using atmospheric-pressure microdischarges. *Nano letters*, *5*(3), 537-541.

11. Chen, X., Ghosh, S., Buckley, D. T., Sankaran, R. M., & Hogan Jr, C. J. (2018). Characterization of the state of nanoparticle aggregation in non-equilibrium plasma synthesis systems. *Journal of Physics D: Applied Physics*, *51*(33), 335203.

12. Chen, X., Seto, T., Kortshagen, U. R., & Hogan Jr, C. J. (2020). Size and structural characterization of Si nanocrystal aggregates from a low pressure nonthermal plasma reactor. *Powder Technology*, *373*, 164-173.

13. Sharma, G., Abuyazid, N., Dhawan, S., Kshirsagar, S., Sankaran, R. M., & Biswas, P. (2020). Characterization of particle charging in low-temperature, atmospheric-pressure, flow-through plasmas. *Journal of Physics D: Applied Physics*, *53*(24), 245204.

14. Fuchs, N. A. (1963). On the stationary charge distribution on aerosol particles in a bipolar ionic atmosphere. *Geofisica pura e applicata*, *56*(1), 185-193.

15. Reischl, G. P., Mäkelä, J. M., Karch, R., & Necid, J. (1996). Bipolar charging of ultrafine particles in the size range below 10 nm. *Journal of Aerosol Science*, *27*(6), 931-949.

16. Xu, K. G., & Doyle, S. J. (2016). Measurement of atmospheric pressure microplasma jet with Langmuir probes. *Journal of Vacuum Science & Technology A: Vacuum, Surfaces, and Films*, *34*(5), 051301.

17. Couëdel, L., Samarian, A. A., Mikikian, M., & Boufendi, L. (2008). Dust charge distribution in complex plasma afterglow. *EPL (Europhysics Letters)*, *84*(3), 35002.

18. Wörner, L., Ivlev, A. V., Couëdel, L., Huber, P., Schwabe, M., Hagl, T., Mikikian, M., Boufendi, L., Skvortsov, A., Lipaev, A.M., & Molotkov, V.I. (2013). The effect of a direct current field on the microparticle charge in the plasma afterglow. *Physics of Plasmas*, *20*(12), 123702.

Chapter 7. Summary and Future Work

7.1   Summary

The main focus of my graduate work was to apply a thorough understanding of aerosol science, especially aerosol formation, growth dynamics, and their interaction with the surrounding media, to address the some of the issues faced by aerosol community. The challenges that were addressed in this study are summarized below.

7.1.1   Controlled synthesis of nanoparticles in aerosol reactors using liquid-to-particle synthesis process

The first section of my dissertation (Chapter 2 and 3) focused on understanding the particle formation in the aerosol reactors that employ liquid-to-particle conversion route (spray synthesis). Chapter 2 addresses the challenge of controlling morphology of particles synthesized via spray drying/pyrolysis. A model for simultaneous droplet heating, evaporation, and dynamics and transport of solute and particles within the droplet was developed, to investigate the effect of different conditions during spray drying on the dried particle morphology. The drying process was modelled in two separate stages in this work, initial drying stage before shell formation, and the transition stage, in which shell formation will modelled till the solid crust formation takes place. Using this model two cases were analyzed, 1) drying of droplet with dissolved solute, and 2) drying of droplet with suspended solids. The model developed in this study addresses several limitations of previously developed single droplet models in the literature, which neglected the shell growth and morphological development inside a droplet during spray drying. Another highlight of this work was the quantification of the impact of different material and operating parameters on the particle morphology, in terms of relative shell thickness. The model equations

developed in this study can be used to design the operating conditions of the spray processes so that the particles with desired morphology can be obtained.

Chapter 3 addresses the challenge of controlling the conductivity (or polymer conjugation length) of PEDOT (poly(3,4-ethylenedioxythiophene)) nanoparticles synthesized using aerosol vapor polymerization. Aerosol vapor polymerization (AVP) is a novel technique, which combines the vapor phase synthesis and liquid based synthesis approach, to synthesis PEDOT polymer nanoparticles. This study is the first attempt in the literature, to model the complex phenomena taking place during AVP, and predict the conductivity of the synthesized particles. The droplet drying model developed in Chapter 2 was advanced further to additionally account for monomer dynamics and transport in gas phase, and polymerization reaction inside the droplet. The effect of different process conditions, during AVP process, was examined on the average polymer chain length in the synthesized particles, which was correlated to the particle conductivity. The simulation results were in very close agreement with the experimental observations. The model equations developed in this study could be used to design the optimum operating conditions of the aerosol vapor polymerization process so that the PEDOT particles with desired conductivity can be obtained.

7.1.2   Aerosol transport and health impacts

The second section of my dissertation focused on understanding aerosol transport and improving pollutant sampling techniques to accurately assessing the impact of harmful aerosols on human health. Chapter 4 addresses the problem of artifacts associated with sampling semi-volatile organic compounds (SVOCs) using diffusion denuders. Several studies have been carried out in

the past to understand the artifacts caused by decomposition of a single component aerosol in the diffusion denuders. SVOCs exist in the atmosphere as a mixture of thousands of species, and there are not many studies that have examined the measurement artifacts arising from the evaporative loss of semi-volatile organic aerosols in the diffusion denuder. In this work, multicomponent SVOCs were modeled using the volatility basis set approach, which allowed for an elegant and unified framework for modeling multicomponent aerosols comprising of thousands of individual species. The developed model was used to investigate effect of the denuder design parameters and organic species properties, on the sampling artifacts, and it demonstrated that the sampling of a variety of SVOCs could result in significant particulate phase loss and excess gas adsorption due to aerosol evaporation in the denuder. The optimum operating conditions of the denuder were suggested in terms of dimensionless parameters such that the error due to sampling artifacts lie within an allowable limit (e.g. 10%). The model equations developed in this study could also be used to design a denuder so that the sampling artifacts are minimized.

Chapter 5 in my thesis focuses on accurate evaluation of the risk from airborne transmission of pathogens. Although several models exist in literature to estimate the risk of airborne, transmission of pathogens, they are limited in their scope. The models based on aerosol dynamics generally do not account for the initial viral load in the droplets and the virus viability, and hence fail to give any quantitative information regarding the risk of transmission; while the models based on dose-response approach to assess the risk of infection from airborne pathogens do not account for crucial aerosol dynamic processes that strongly impact the risk. This work overcomes the limitations of detailed aerosol models, and the virology-based dose response

models, by combining the two approaches. A comprehensive model for respiratory emissions of droplets, droplet evaporation, and transport due to diffusion, gravitational settling, and ambient air flow, was developed. The considerations for viral load in droplets and virus decay were accounted for in the model to determine the spatial and temporal concentration of viable virus exhaled by the infected individual. The exposure to viable virus and risk of infection was determined using respiratory deposition curves and dose-response approach. The effect of the different parameters such as viral load, physical separation, ambient air velocity, mask usage etc. was determined on the risk of infection transmission. The present study demonstrated that the airborne transmission of SARS-CoV-2 can be a significant mode of transmission of this disease. The model equations developed in this study are very general and can also be used to design prevention and control measures so that the risk of infection form any airborne transmission can be minimized.

7.1.3 Particle charging and particle capture

The third section of my dissertation focuses on the fundamental understanding of particle charging in a non-thermal plasma reactor, with a vision to incorporate plasma reactors in conjunction with the conventionally used particle capture devices, thereby increasing their efficiency for particle capture. Chapter 6 addresses the issue of low efficiency of sub 100 nm particle charging in atmospheric pressure plasma reactors due to neutralization in spatial afterglow. We tested a new design concept for enhancing aerosol nanoparticle charging in plasmas by introducing a DC field downstream of the plasma volume in the spatial afterglow to potentially prevent neutralization of the particles. The charging efficiencies improved very significantly by the addition of DC field. The overall charge fraction of particles was found to be

very high for sub-100 nm particles, with a charging efficiency greater than 95% for 80 nm particles and greater than 70% for 20 nm particles. The results were supported by analyzing the characteristic timescales for neutralization by and loss to the walls of positive ions in the spatial afterglow at different downstream DC voltages. The particle charging efficiencies in this work are very high as compared to traditional ESPs, which highlight the potential application of our flow-through, atmospheric-pressure plasma reactor with as a particle control device.

7.2　　Suggestions for future work

7.2.1　　Controlled synthesis of nanoparticles in aerosol reactors using reactive precursors

While the model developed in Chapter 2 focused on developing in-depth understanding of the particle formation during spray drying process using inert precursors to have better control over particle morphology, the future direction should be to focus on understanding the particle formation using spray techniques, when the reactive precursors are used. The presence of reactive precursor in the droplet can have additional effects like localized heating/cooling in the droplet, release of gaseous species etc. which can very significantly affect the morphology of synthesized particle. As a future direction, a robust model which incorporates the effect of all the possible scenarios during particle formation in spray pyrolysis, with simultaneous effects of droplet heating and evaporation, solute dynamics in the droplet, reaction dynamics and effect of localized gas release from reaction, etc., should be investigated in greater detail. The developed models should also be integrated with CFD simulations to represent realistic flows in different reactors.

7.2.2　　Understanding reaction kinetics of PEDOT polymerization

The good estimated of kinetic parameters are not available in the literature for PEDOT polymerization reaction using ferric initiator in an aqueous solution. The reaction kinetics parameters used in Chapter 3 were rough estimates based on experimental observations. Accurate values for the reaction parameters at different temperatures is needed to improve the accuracy of the model developed in Chapter 3, to model PEDOT synthesis using aerosol vapor

polymerization and predict particle conductivity. As a future direction, PEDOT polymerization could be carried out in a controlled batch reactor and the time evolution of the concentration of the oxidant could be measured. The modal approach for polymerization kinetics, developed in Chapter 3, could be used, and the reactor parameter could be estimating by fitting the model to fitted to experimentally obtained concentrations. The reaction parameters should be estimated at multiple temperatures to obtain the Arrhenius parameters.

7.2.3 Development of a dose-response model for SARS CoV-2

The model developed in Chapter 5 focused on understanding airborne transmission of SARS CoV-2. The dose-response relationship of SARS CoV-2 is still unknown, and an exponential dose-response model was used in this study based on dose-response relationship of SARS CoV-1. There is no dose-response model for SARS-CoV-2 available at the moment mainly due to unavailability of data sets challenging humans or animals with this virus. So, with time as more transmission datasets become available, the future studies should focus on developing accurate dose-response model for different SARS-CoV-2 variants. The exact knowledge of dose-response relationship will greatly improve the accuracy of the developed model to estimate the transmission risk.

7.2.4 Application of plasma reactor as a particle capture device

In Chapter 6, atmospheric pressure plasma reactor was explored as a possible charging tool for the development of particle capture technologies. In this study, argon gas was used as the aerosol carrier gas, since it is easy to ionize. Future studies should focus on characterizing atmospheric

pressure, flow through, non-thermal plasmas generated by ionizing different gases to represent more realistic situation in labs and industries. The effect of different gas compositions and different particle types on charging should be the focus of future, as the composition and the chemistry of the plasma is strongly dependent on the type of gas used to generate the plasma.

The potential application of using plasma afterglow to preferentially positively charge the aerosols should be examined. For this purpose, a cross-flow configuration where plasma afterglow mixes with the particle stream (air) in a cross-flow configuration, should be explored for particle charging.

Appendix A. Multi-modal model description

A.1   Background

The understanding of aerosol dynamics is essential in many applications, such as aerosol reactors, combustion, air quality control etc., for predicting the evolution of particulate systems, which is useful for in-depth understanding of the experimental measurements. Different aerosol dynamics phenomenon, such as chemical reaction, nucleation, condensation, coagulation, sintering, aggregate formation, and charging are described using general dynamic equation (GDE). Aerosol dynamic modelling involves computing the evolution of particle size distribution (PSD) by solving GDE. GDE is non-linear, partial integro-differential equation, therefore a general analytical solution often does not exist for GDE [1, 2]. Numerical approach is a better choice of solving GDE for the complex aerosol system. In the last few decades, different numerical schemes have been developed to solve GDE, which include method of moments, discrete model, sectional model, modal model etc. Each of these schemes have their own advantages and disadvantages.

Kruis, Kusters & Pratsinis (1993) [3] developed a simple unimodal (monodisperse) model to predict particle growth while accounting for the morphology using a fractal representation. The unimodal model is computationally efficient and also shows good agreements with the more accurate two dimensional sectional model predictions. This model fails to reflect the polydisperse characteristics of the particles when particle generation and growth occur simultaneously, as in many aerosol reactor systems. To overcome this problem, Jeong & Choi (2003) [4] proposed an extension to the unimodal model by using a bimodal approach and obtained reasonable agreement with more accurate models when new particle generation exists. The accuracy of bimodal model fails when the system evolves for a longer period of time. The

number of modes in the modal model can be increased for better accuracy but the computational time also increases with the number of modes. The development of generalized multi-model approach to solve general dynamics equation is discussed in this section.

A.2   Multi-Modal Model Development

(a)

(b)

$$\varepsilon_{i,j,k} = \frac{v_{k+1} - (v_i + v_j)}{v_{k+1} - v_k}$$

$$\varepsilon_{i,j,k+1} = 1 - \varepsilon_{i,j,k}$$

$$\varepsilon_{i,j,l} = 0 \quad \forall\, l \neq k\ or\ k + 1$$
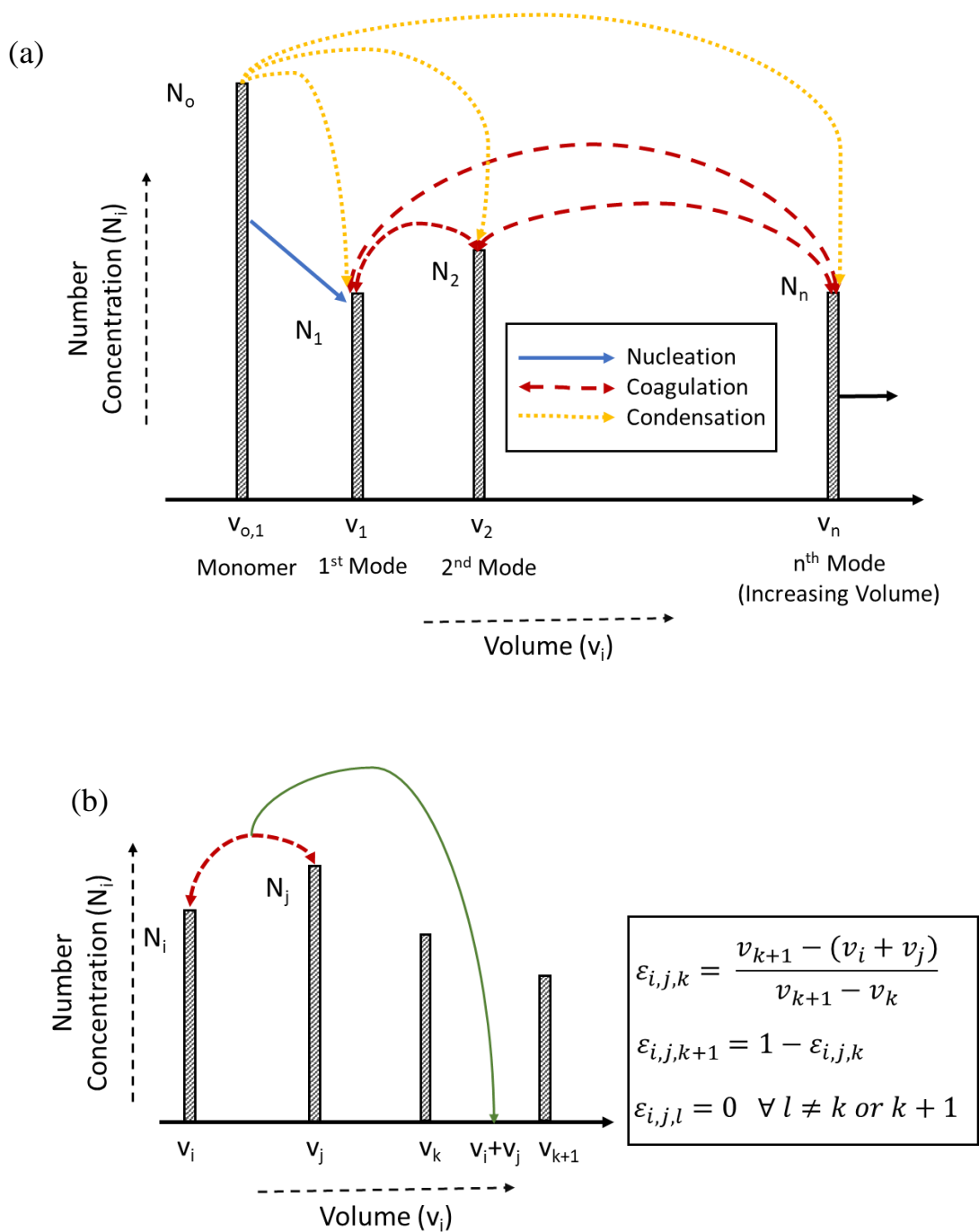
Figure A-1 The schematic of modal model (a) general description of modal model (b) assigning a volume to its adjacent nodes.

The general dynamic equation (GDE) is given by [1]:

$$\frac{\partial n(v,t)}{\partial t} + \nabla \cdot n(v,t)\boldsymbol{u} + \frac{\partial(Gn)}{\partial v} - I(v^*)\delta(v - v^*)$$
$$= \frac{1}{2}\int_0^v \beta(v - \tilde{v}, v)n(v - \tilde{v}, t)n(\tilde{v}, t)d\tilde{v}$$
$$- n(v,t)\int_0^\infty \beta(\tilde{v}, v)n(\tilde{v}, t)d\tilde{v} \tag{A.1}$$

The first term on the left-hand side (LHS) is the rate of change of the particle size distribution (PSD) in the particle volume interval, v to $v + dv$, the second term on the LHS considers the aerosol convection in the background fluid, the third term on the LHS accounts for particle condensation at rate G, and the last term on the LHS describes the formation of new particles of critical volume v^* at rate I (Biswas et al., 1997). The terms on the right-hand side describe the effect of Brownian coagulation.

In this work, a computationally simple and generalized modal model for single component aerosol formation and growth is proposed, which is shown in Figure A-1. The nucleation, coagulation, and surface growth of particles are accounted for in this modal model and the developed model is generalized to incorporate "n" modes. Thus, the GDE is equivalently solved by obtaining N_i and V_i as below:

$$\frac{dN_i}{dt} = \frac{dN_i}{dt}\bigg|_{coag} + \frac{dN_i}{dt}\bigg|_{nucl} \tag{A.2}$$

238

$$\frac{dV_i}{dt} = \frac{dV_i}{dt}_{coag} + \frac{dV_i}{dt}_{cond/evap} , \qquad (A.3)$$

where N_i is the number concentration of particles and V_i is the total particle volume corresponding to i^{th} mode for $1 \le i \le n$. The rate of change of N_k due to coagulation is given by (for $k < n$):

$$\frac{dN_k}{dt}_{coag} = -N_k \sum_{j=1}^{n} \beta_{j,k} N_j + \frac{1}{2} \sum_{i=1}^{n} \beta_{i,i} N_i N_i \varepsilon_{i,i,k} + \sum_{i=2}^{n} \sum_{j=1}^{i-1} \beta_{i,j} N_i N_j \varepsilon_{i,j,k} , \qquad (A.4)$$

where $\beta_{i,j}$ is coagulation coefficient between mode i and j and ε is the apportionment factor. If the particle volume formed via collision of particles from mode i and j lies between two nodes, the new particle is split into two adjacent nodes in accordance with mass conservation. $\varepsilon_{i,j,k}$ is the fraction of the particle formed via collision of particles from mode i and j that is apportioned to mode k as shown in Figure A-1 B. The net change in volume of all the internal modes is given by:

$$\frac{dV_k}{dt}_{coag} = v_k \frac{dN_k}{dt}_{coag} , \quad \text{for } k < n, \qquad (A.5)$$

where v_k is the volume of a single particle in mode k, i.e. $v_k = V_k/N_k$. If collision results in the formation of a particle with a volume higher than that of the last mode *'m'*, then the particle can

be assumed to be laid in last mode 'n'. The volume 'v_n' is increased in accordance with mass conservation. The rate of change of number concentration and volume for last mode 'n' due to coagulation is given by ($k = n$):

$$\frac{dN_n}{dt}_{coag} = -\frac{1}{2}\beta_{n,n}N_nN_n + \frac{1}{2}\sum_{i=1}^{n-1}\beta_{i,i}N_iN_i\varepsilon_{i,i,n} + \sum_{i=2}^{n-1}\sum_{j=1}^{i-1}\beta_{i,j}N_iN_j\varepsilon_{i,j,k},$$ (A.6)

$$\frac{dV_n}{dt}_{coag} = \frac{v_n}{2}\sum_{i=1}^{n-1}\beta_{i,i}N_iN_i\varepsilon_{i,i,n} + v_n\sum_{i=2}^{n-1}\sum_{j=1}^{i-1}\beta_{i,j}N_iN_j\varepsilon_{i,j,k}.$$ (A.7)

Further, condensation or evaporation of the vapor results in the change of volume of the mode and does not result in change of the number concentration. The rate of change of the total volume for k^{th} mode due to condensation/evaporation is given by:

$$\frac{dV_k}{dt}_{cond/evap} = \frac{G_C G_{FM}}{G_C + G_{FM}}N_k,$$ (A.8)

where G_C and G_{FM} are the particle growth rates in the continuum and free molecular regime respectively. The nucleation will lead to the production of particles of critical size (v^*). The volume of a single particle in the first mode is set to be greater than or equal to the critical size v^*. The rate of change of number concentration and volume for the first mode due to nucleation is given by:

$$\frac{dN_1}{dt}\bigg|_{nucl} = I\frac{v^*}{v_k}\delta(k-1),$$ (A.9)

$$\frac{dV_1}{dt}\bigg|_{nucl} = Iv^*\delta(k-1).$$ (A.10)

Monomers are involved in nucleation and surface growth of particles. A monomer balance is necessary to account for monomer concentration changes due to nucleation, condensation, and evaporation, which is given as:

$$\frac{dN_0}{dt} = J_0 - \frac{1}{v_1}\sum_{k=1}^{m}\frac{dV_k}{dt}\bigg|_{cond} - I\frac{v^*}{v_1},$$ (A.11)

where J_0 is the monomer generation rate.

A.3 References

1. Hidy, G. M. (2011). Sheldon K. Friedlander. Aerosol Science and Technology: *History and Reviews*, 33.

2. Seigneur, C., Hudischewskyj, A. B., Seinfeld, J. H., Whitby, K. T., Whitby, E. R., Brock, J. R., & Barnes, H. M. (1986). Simulation of aerosol dynamics: A comparative review of mathematical models. *Aerosol Science and Technology*, 5(2), 205-222.

3. Kruis, F. E., Kusters, K. A., Pratsinis, S. E., & Scarlett, B. (1993). A simple model for the evolution of the characteristics of aggregate particles undergoing coagulation and sintering. *Aerosol science and technology*, 19(4), 514-526.

4. Jeong, J. I., & Choi, M. (2003). A simple bimodal model for the evolution of non-spherical particles undergoing nucleation, coagulation and coalescence. *Journal of Aerosol Science*, 34(8), 965-976.

Appendix B. Supplementary Material for Chapter 5

B.1　Size distribution of droplets emitted during expiration

Table B-1 Summary of studies that report size distribution of droplets expired during coughing, sneezing, and speaking

Reference	Respiratory Behavior	Method	Size Resolution
Duguid et al. 1946[1]	Coughing, Sneezing and Speaking	Solid impaction	1 to 1500 µm
Buckland et al. 1964[2]	Coughing, and Speaking	Liquid impaction	~1 to 860 µm
Loudon & Roberts 1967[3]	Coughing, and Speaking	Solid impaction	~10 to 1500 µm
Fennelly et al. 2004[4]	Coughing	Solid impaction	0.65 to 7 µm
Yang et al. 2007[5]	Coughing	APS and SMPS	~0.5 to 30 µm
Morawska et al. 2008[6]	Breathing, Speaking, and Coughing	APS	~0.5 to 20 µm
Chao et al. 2009[7]	Coughing, and Speaking	Interferometric Mie imaging	1 to 1500 µm
Xie et al. 2009[8]	Coughing	Solid impaction	~1 to 1500 µm
Morawska et al. 2009[9]	Coughing	APS	~0.5 to 20 µm

Johnson et al. 2011[10]	Speaking, and Coughing	APS and DDA	0.3 to 1000 µm
Zayas et al. 2012[11]	Coughing	He-Ne laser	0.1 to 1 µm
Han et al. 2013[12]	Sneezing	Laser particle analyzer	~10 to 1000 µm
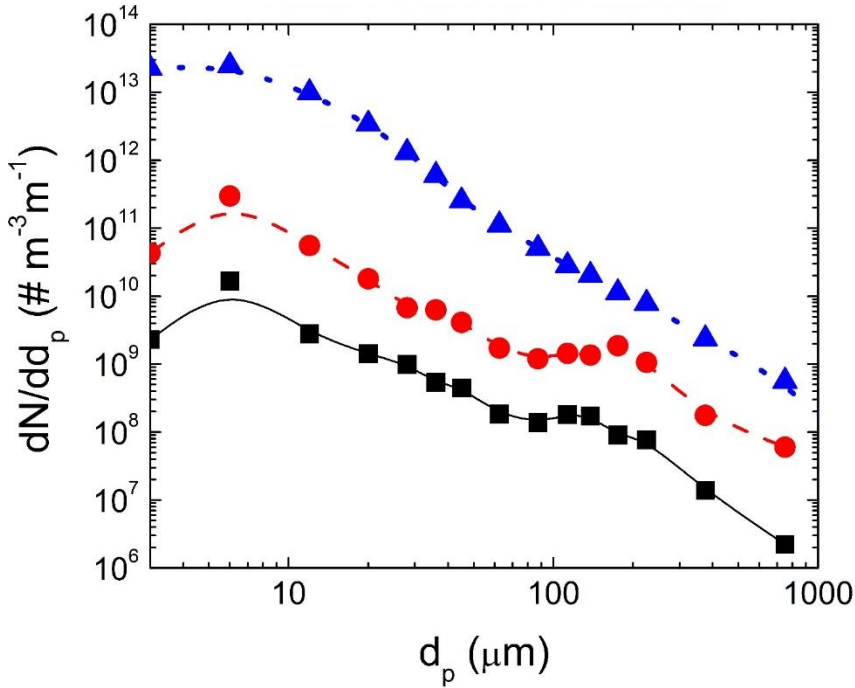
Figure B-1 Size Distribution of Particles Emitted During Speaking [7], Coughing [7], and Sneezing [1] used in this study. The symbols denote the experimentally measured values, while the lines are the basis splines fitted to the measured data (——■—— Speaking, – – ● – – Coughing, ⋯▲⋯ Sneezing).

Several studies have reported distribution of the sizes and numbers of particles emitted during speaking, coughing, and sneezing. Table B-1. summarizes the expiration activities, methods, and results of some of the previous literature. These studies employed different methods and the findings are inconsistent among different studies possibly due to measurement artifacts

introduced by experimental device, measurement methods and evaporation effects. Optical measurements should be most accurate as they eliminate some measurement biases. Most of these studies report only the sizes distribution of emitted particles while the total number concentration of exhaled droplets is not reported. The particle size distributions from Chao et al [7] and Duguid [8] were used in this study and these are shown in Figure B-1.

B.2 Evaporation and Settling Calculations

For particle smaller than ~ 140 µm, the evaporation time of the emitted or exhaled droplet must be considered to accurately calculate their lifetime (or settling time). The evolution of the diameter of droplet was first evaluated. The ambient temperature and relative humidity were assumed to be 298 K and 50% respectively. Then, the vertical position of droplet was estimated using the equation of motion, given by:

$$\frac{dy}{dt} = \overrightarrow{u_{ext}} \qquad\qquad (B.1)$$

where, y is the vertical position of the droplet, and $\overrightarrow{u_{ext}}$ is the velocity of droplet due to external forces which in this case is gravity. $\overrightarrow{u_{ext}}$ is the function of diameter of droplet which changes with time due to evaporation. Solving Eq. 5.8 gives the diameter of the droplets as the function of time ($d_p(t)$) which can be substituted in Eq. B.1. At t = 0, the droplet starts from the mouth of the infected person at height of the person ('H' which is typically 1.75 m). Eq. B.1 is solved using this initial condition to get the vertical position of the droplet as the function of time ($y(t)$). The lifetime or the settling time corresponds to the time when the droplets reaches the ground ($y = 0$). The lifetime is evaluated as the function of emitted droplet diameter and reported in Figure 5-2 A.

Validation for life-time calculation: Marr et al 2018 [13] calculated the settling time for a droplet initially 10 µm in diameter containing 9 mg ml salt as NaCl and 3 mg ml protein at RHs of 100%, 90% and 64% and it was reported that the droplet shrinks to 2.8 mm at 90% RH and to

1.9 mm at less than 64% RH and the calculated life time were 8 min, 102 min and 216 min. The life time reported by Marr et al 2018 [13] are higher than those reported in this study because evaporation was assumed to be instantaneous. However, the droplet initially starts as larger diameter which evaporate and settles simultaneously. The settling time of 2.8 µm droplet and 1.9 µm (non- evaporating) were calculated to be 103 min and 220 min, which is similar to those reported by Marr et al 2018 [13]. Therefore, both settling equation and evaporation equation needs to be solved simultaneously to accurately determine droplet lifetime.

Table B-2 Comparison of settling time (1.5 m) of evaporation droplet of 10 µm at 303 K & different RH

	Marr et al 2018[13]		This work	
RH	**Final Particle Size**	**Life time**	**Final Particle Size**	**Life time**
100	10 µm	8 min	10 µm	8.3 min
90	2.8 µm	102 min	2.7 µm	78 min
64	1.9 µm	216 min	1.7 µm	113 min

B.3   Trajectory Calculation

The trajectory of the droplets in the quiescent ambient was determined by solving the equation of motion while simultaneously considering droplet evaporation and settling. The lifetime of the droplets and their vertical position as the function of time, was calculated first using the procedure in Section B.2. The horizontal position of droplet ('x') was estimated using the equation of motion, given by

$$\frac{dx}{dt} = \overrightarrow{u_{expiration}}$$

(B.2)

The expression for $\overrightarrow{u_{expiration}}$ for coughing is given by Eq. 5.6. $\overrightarrow{u_{sneeze}}$ was assumed to be same as $\overrightarrow{u_{cough}}$ and $\overrightarrow{u_{speech}}$ was assumed to be same as $\frac{1}{3}\overrightarrow{u_{cough}}$. At t = 0, x = 0 and Eq. B.1, Eq. B.2 and Eq. 5.8 are simultaneously solved. The horizontal distance traversed before settling is given by 'x' at t = $t_{lifetime}$. The horizontal distance traversed by droplets before settling as the function of emitted droplet diameter was evaluated and is shown in Figure 5-2 B. The horizontal distance traversed by particles of size 10 µm and 100 µm sized droplet emitted during coughing, sneezing and speaking is given in Figure B-2. The life time of the 100 µm droplet is 44 s and it can travel a distance of 1.6 m and 4.9 m when released during speaking and coughing/sneezing respectively; while the 10 µm droplet can stay suspended for 2.2 hrs and can travel a distance of 9.1 m and 27.4 m when released during speaking and coughing/sneezing respectively.
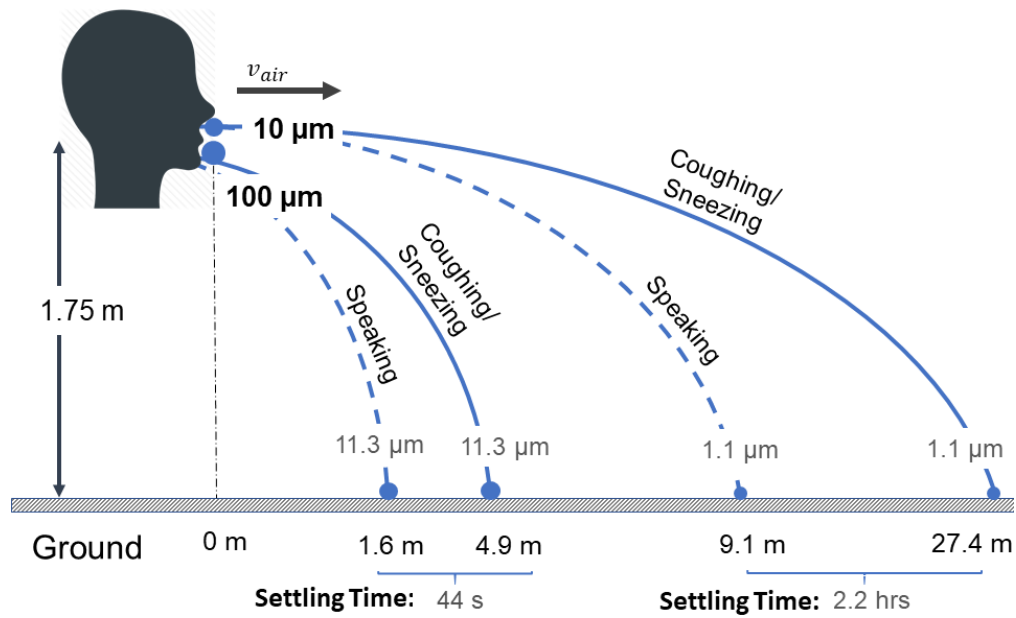
Figure B-2 Horizontal distance traversed by droplets of size 10 & 100 µm, emitted during coughing/sneezing (solid line) and speaking (dashed line) in quiescent ambient. The ambient temperature and relative humidity were assumed to be 298 K and 50% respectively, with air velocity of $\frac{0.875}{(x+0.333)^2}$ during coughing/sneezing and $\frac{0.292}{(x+0.333)^2}$ during speaking.

B.4   Emission Rate

The number concentration of droplets emitted during exhalation activities used in this study is given in Figure B-1. About 0.4 L of air is exhaled in a cough and sneeze which lasts for ~ 500 ms. The air volume expired during speech is almost a third of the volume expired during cough, within same time (500 ms). Constant emission rate was assumed during the time of emission. To simplify, the emissions from infected person $\dot{N}_i(x, y, z, t)$ was considered to be composed of superposition of 'n' impulse emissions at small time intervals 'dt' given by Eq. 5.13.

To calculate the impulse emission at t = 0, first the total particles emitted during exhalation were obtained by multiplying the number concentration with the total volume exhaled. Then, the particles released during each impulse emission can be obtained by dividing total particles number by 'n'. And, the number concentration at the mouth (x = 0, y = H = 1.75 m, z = 0) at t = 0, was evaluated by dividing the number of particles released during each impulse emission to the differential volume considered in the model (*dx* x *dy* x *dz*). The differential volume in our simulation was 2cm x 2cm x 2 cm as the approximate area of open mouth is 2cm x 2cm.

B.5　　Effect of Height on Risk of Infection
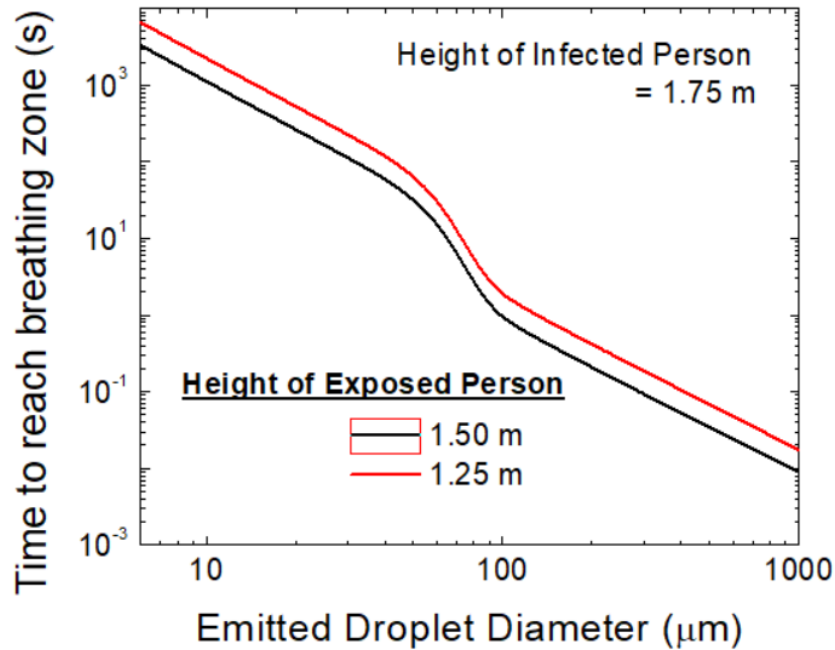
Figure B-3 Time to reach the breathing zone of exposed individual of different heights as the function of emitted droplet diameter.

The height of infected person was assumed to be 1.75 m which is typical average height. The risk of infection will also depend on height of the person exposed. Figure B-3 shows the time emitted droplet take to reach the breathing zone as the function of height of exposed person. It can be seen that larger droplets can quickly reach the breathing zone while the droplets smaller than 10 µm can take few hours to reach the breathing zone of exposed person of smaller heights (1.25 m and 1.5 m). Thus at closer distance, shorter individual (as compared to infected person) will be exposed to larger droplets, while at larger distances, exposure to small airborne droplet will take place.
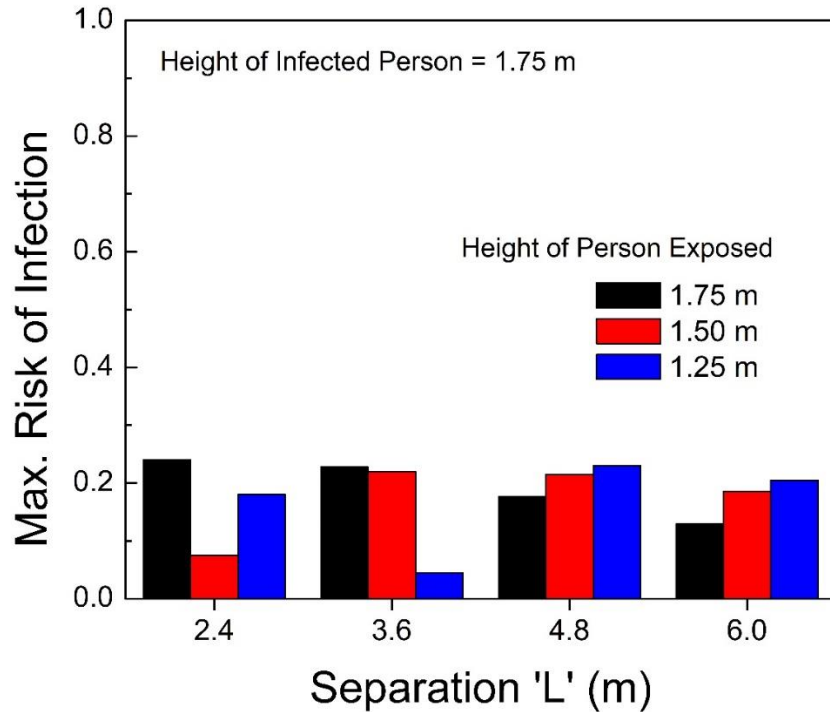
Figure B-4 Risk of infection from coughing at different physical separations for different heights, 1.75 m, 1.50 m and 1.25 m, of person exposed.

Figure B-4 shows the risk of infection from coughing at different heights, 1.75 m, 1.50 m and 1.25 m, as the function of physical separation. The particles are emitted at the height of 1.75 m and at that height, the risk decreases as the separation increases, as can be seen in Figure B-4. This is because with distance, more settling takes place. However, there is no clear trend in the risk of infection at the heights of 1.50 m and 1.25 m. The infectious viruses reach the lower heights due to the settling of the droplets, and the larger droplets faster than the smaller droplets. Since, the emitted droplet size distribution is not monotonic (Figure B-1), the distribution of virus over different droplets size ranges will not be monotonic and not have a clear trend. Therefore, there is no clear trend in the risk of infection as the function of height. It can be seen from Figure B-4 that the risk of infection can be as high as 20% at the height of 1.50 m and 1.75 m even at the physical separation of 6.0 m.

B.6   Effect of Air Mixing and Dilution on Risk of Infection
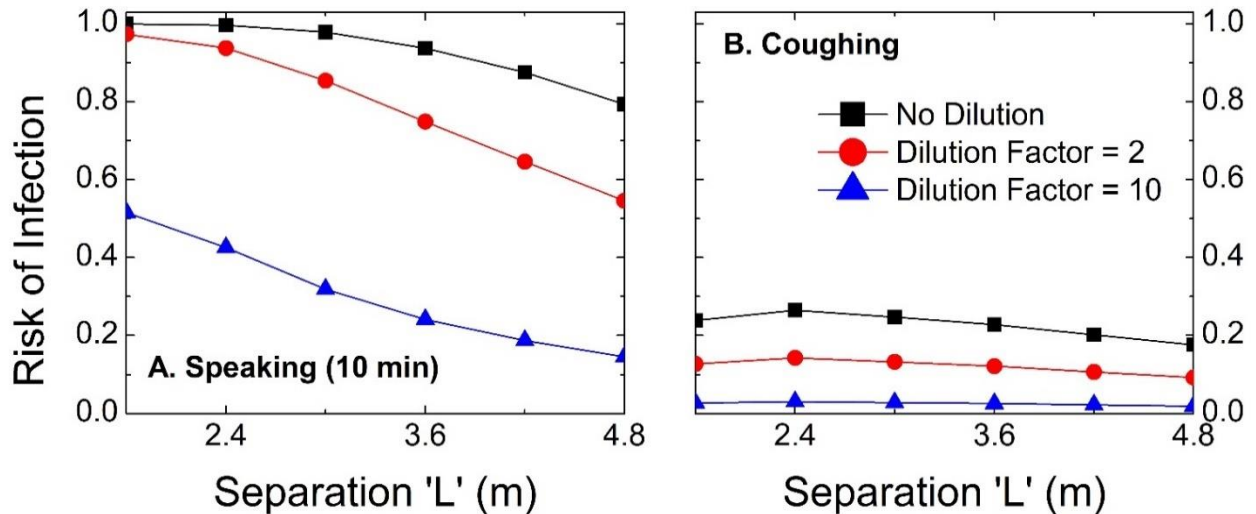
Figure B-5 Risk of infection from A) speaking (10 min) and B) coughing, at different physical separation at different dilution factors.

The base case considered in this study (Figure 5-6) represents a worst-case scenario i.e. when infected individual is directly in front of the person exposed and the surrounding air is stagnant or there is no dilution by mixing. The dilution due to ventilation and air flow can decrease the concentration of airborne droplets and thus reduce the risk of infection. The risk of infection was calculated for different dilution factors (ratio of total air to the air contaminated with droplets) and Figure B-5 shows the effect of dilution on the risk of infection from (A) speaking (10 min) and (B) coughing. It can be seen from Figure B-5 that with the increase in dilution, the risk of transmission decreases. Thus, improvements to ventilation and air flow can reduce the risk of airborne transmission of the SARS-CoV-2 virus.

B.7 Effect of wind on transmission, when wind is in the direction towards infected person

The wind in the direction from exposed person to infected person can reduce the transport of expired droplets. When, the wind is in the direction opposite of expiration, the expired droplets cannot travel beyond a certain distance from infected individual, which depends on the magnitude of wind velocity. The evolution of velocity of the expired droplet on exhalation is given by:

$$m_{droplet}(t)\frac{du_{droplet}}{dt} = -3\pi\mu d_p(t)(u_{droplet} - u_{air}) \tag{B.3}$$

where $m_{droplet}$ is droplet mass, $u_{droplet}$ is droplet velocity, μ is air viscosity, d_p is droplet diameter, and u_{air} is air velocity given by Eq. 4. Eq. S3 can be solved simultaneously with evaporation equation (Eq. 8) to obtain droplet's velocity as the function of time. The initial velocity of droplet is given by $u_{expiration}$ at x = 0. The droplet velocity will decrease as it moves horizontally. The position at which droplet's velocity becomes zero is the maximum distance that the droplet can travel in front of infected person. The position of droplets is given by

$$\frac{dx}{dt} = u_{droplet} \tag{B.4}$$

Eq. B.3, B.4 and 5.8 are solved simultaneously and 'x' is evaluated where velocity of droplets is zero. At the wind velocity of 0.25 m/s towards infected person, the maximum distance that the droplets can traverse is 1.8 m in front of the infected person.

B.8   Penetration efficiency of Masks

The penetration efficency of surgical masks (both sealed and leakage) is reported by Grinshpun et al. 2009 [14]   and penetration efficiency of cloth mask (65%/35% cotton/polyester twill polyester/cotton blend 3, twill weave, 229 yarns inch^{-2}) is reported by Zangmeister et al. 2020 [15]. The regression was used to fit the equations to penetration efficiency (*PE*) data as the function of particle size, as presented in these studies. The regression equations are given by:

$$PE_{surgical,leak} = (36.24 \pm 1.46) \times exp\left(-\left(\frac{ln(d_p) - (-16.05 \pm 0.23)}{(3.054 \pm 0.544)}\right)^2\right) \qquad (B.5)$$

$$PE_{surgical,sealed} = (7.02 \pm 0.231) \times exp\left(-\left(\frac{ln(d_p) - (-16.73 \pm 0.61)}{(4.5 \pm 1.138)}\right)^2\right) \qquad (B.6)$$

$$PE_{cloth,sealed} = (82.28 \pm 1.14) \times exp\left(-\left(\frac{ln(d_p) - (-16.48 \pm 0.08)}{(4.534 \pm 0.251)}\right)^2\right) \qquad (B.7)$$

These regression equations for have the adjusted $R^2 > 0.97$.

B.9   Effect of Mask Leakage on Risk of Transmission
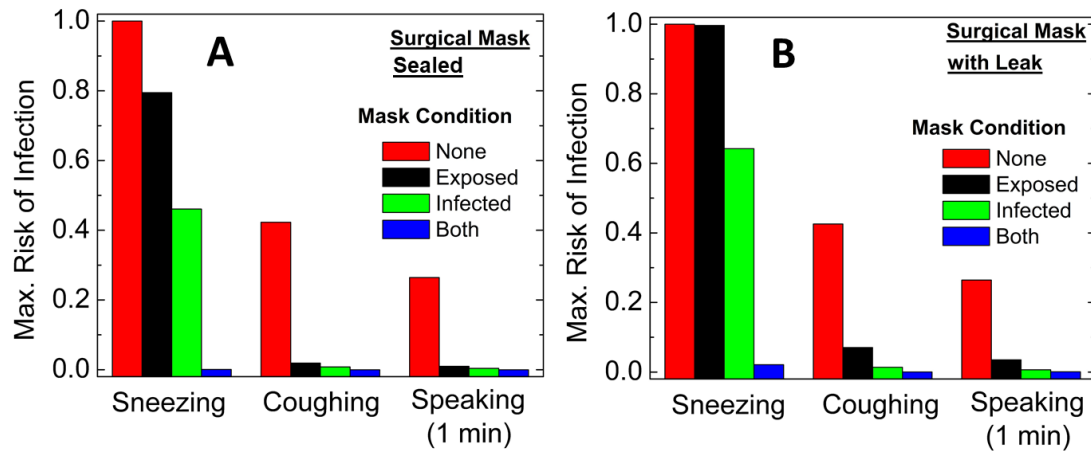
Figure B-6 Effect of A) sealed surgical mask, and B) surgical mask with face seal leakage, on the risk of infection from sneezing, coughing, and speaking by infected individual at a distance of 2.4 m in the quiescent ambient. The risk is compared for four cases: a) when no one is wearing mask, b) when only exposed person is wearing mask, c) when only infected person is wearing mask, and d) when both infected and exposed individual are wearing mask.

Leakages can significantly reduce mask effectiveness. The penetration of particles through mask is higher in the presence of leaks as compared to a properly sealed mask (Eq B.5-B.7). Figure B-6 shows the effect of properly sealed surgical mask and surgical mask with leakage on the risk of infection. It can be seen that the risk of infection increases significantly in the presence of leakages. Therefore, it is critically important that mask are properly fit to minimize leakage of air between the mask and the contours of the face.

B.10 Viral Load Considerations

The total viral loading in droplets is a mystery. The viral concentration varies depending on the region in the respiratory system from where the droplets are produced. Since the emitted respiratory droplet size also depends on the region in the respiratory tract from where the droplets are produced, the mean viral concentration varies with the droplet size. There are no studies in the literature which report in detail the dependance of viral concentration as a function of emitted droplet size. Due to lack of experimental data and rigorous models, the concentration of virus in the mouth (saliva/sputum) was used as a representative of the concentration in the droplets emitted during the expiratory activities.

Several studies assume that the number of viruses in emitted droplets follow a Poisson distribution [16-19]. If V_{load} is the average concentration (RNA copies/mL) of the virus in the respiratory fluids, then the average number of viruses in a droplet of diameter 'd_p' can be expressed as

$$N_{av} = V_{load}\frac{\pi}{6}d_p^{\,3} \qquad\qquad (B.3)$$

In these studies [16-19], it is assumed that the probability 'P_n' that a droplet will actually contain 'n' viral copies follows from the one parameter Poisson distribution, having mean N_{av} and standard deviation $\sqrt{N_{av}}$:

$$P_n = \frac{N_{av}^{\,n}\exp\left(-N_{av}\right)}{n!} \qquad\qquad (B.4)$$

It follows that the probability of containing no virus at all (n = 0) will be $\exp(-N_{av})$. The risk of infection depends directly on the total numbers of infectious viruses deposited in the respiratory system of the exposed person, and not the number of droplets with infectious virus. Therefore, to get an estimate of the number of infectious viruses deposited in the respiratory region of exposed person, the number of droplets (of different sizes) deposited were first calculated using respiratory deposition curve and then multiplied by the average number of infectious viruses in the droplets.

B.11 References

1. Duguid, J. P. (1946). The size and the duration of air-carriage of respiratory droplets and droplet-nuclei. *Epidemiology & Infection*, *44*(6), 471-479.

2. Buckland, F. E., & Tyrrell, D. A. J. (1964). Experiments on the spread of colds: 1. Laboratory studies on the dispersal of nasal secretion. *Epidemiology & Infection*, *62*(3), 365-377.

3. Loudon, R. G., & Roberts, R. M. (1967). Droplet expulsion from the respiratory tract. *American Review of Respiratory Disease*, *95*(3), 435-442.

4. Fennelly, K. P., Martyny, J. W., Fulton, K. E., Orme, I. M., Cave, D. M., & Heifets, L. B. (2004). Cough-generated aerosols of Mycobacterium tuberculosis: a new method to study infectiousness. *American journal of respiratory and critical care medicine*, *169*(5), 604-609.

5. Yang, S., Lee, G. W., Chen, C. M., Wu, C. C., & Yu, K. P. (2007). The size and concentration of droplets generated by coughing in human subjects. *Journal of Aerosol Medicine*, *20*(4), 484-494.

6. Morawska, L.; Johnson, G.R.; Ristovski, Z.; Hargreaves, M.; Mengersen, K.L.; Chao, C.; Wan, M.P.; Li, Y.; Xie, X.; Katoshevski, D. Droplets expelled during human expiratory activities and their origin. *In Størm-Tejsen, P., Olesen, B. W., Wargocki, P., Zukowska, D., Toftum, J. (Eds.), Proceedings of the 11th international conference on indoor air quality and climate. Indoor air 2008, Copenhagen, Denmark, Paper ID: 1023, ISBN: 9788778772701.*

7. Chao, C. Y. H., Wan, M. P., Morawska, L., Johnson, G. R., Ristovski, Z. D., Hargreaves, M., Mengersen, K., Corbett, S., Li, Y., Xie, X. & Katoshevski, D. (2009).

Characterization of expiration air jets and droplet size distributions immediately at the mouth opening. *Journal of aerosol science*, *40*(2), 122-133.

8. Xie, X.; Li, Y.; Sun, H.; Liu, L. Exhaled droplets due to talking and coughing. *JR Soc. Interface,* **2008,** 6. S703–S714.

9. Morawska, L. J. G. R., Johnson, G. R., Ristovski, Z. D., Hargreaves, M., Mengersen, K., Corbett, S., Chao, C.Y.H., Li, Y. & Katoshevski, D. (2009). Size distribution and sites of origin of droplets expelled from the human respiratory tract during expiratory activities. *Journal of aerosol science*, *40*(3), 256-269.

10. Johnson, G. R., Morawska, L., Ristovski, Z. D., Hargreaves, M., Mengersen, K., Chao, C. Y. H., Wan, M.P., Li, Y., Xie, X., Katoshevski, D. & Corbett, S. (2011). Modality of human expired aerosol size distributions. *Journal of Aerosol Science*, *42*(12), 839-851.

11. Zayas, G., Chiang, M. C., Wong, E., MacDonald, F., Lange, C. F., Senthilselvan, A., & King, M. (2012). Cough aerosol in healthy participants: fundamental knowledge to optimize droplet-spread infectious respiratory disease management. *BMC pulmonary medicine*, *12*(1), 1-12.

12. Han, Z. Y., Weng, W. G., & Huang, Q. Y. (2013). Characterizations of particle size distribution of the droplets exhaled by sneeze. *Journal of the Royal Society Interface*, *10*(88), 20130560.

13. Marr, L. C., Tang, J. W., Van Mullekom, J., & Lakdawala, S. S. (2019). Mechanistic insights into the effect of humidity on airborne influenza virus survival, transmission and incidence. *Journal of the Royal Society Interface*, *16*(150), 20180298.

14. Grinshpun, S. A., Haruta, H., Eninger, R. M., Reponen, T., McKay, R. T., & Lee, S. A. (2009). Performance of an N95 filtering facepiece particulate respirator and a surgical

mask during human breathing: two pathways for particle penetration. *Journal of occupational and environmental hygiene*, *6*(10), 593-603.

15. Zangmeister, C. D., Radney, J. G., Vicenzi, E. P., & Weaver, J. L. (2020). Filtration efficiencies of nanoscale aerosol by cloth mask materials used to slow the spread of SARS-CoV-2. *ACS nano*, *14*(7), 9188-9200.

16. Hogan, C. J., & Biswas, P. (2011). Monte Carlo simulation of macromolecular ionization by nanoelectrospray. Journal of the American Society for Mass Spectrometry, 19(8), 1098-1107.

17. Hogan, C. J., Kettleson, E. M., Ramaswami, B., Chen, D. R., & Biswas, P. (2006). Charge reduced electrospray size spectrometry of mega-and gigadalton complexes: whole viruses and virus fragments. Analytical chemistry, 78(3), 844-852.

18. Jeon, S., Oberreit, D. R., Van Schooneveld, G., & Hogan, C. J. (2016). Nanomaterial size distribution analysis via liquid nebulization coupled with ion mobility spectrometry (LN-IMS). Analyst, 141(4), 1363-1375.

19. Anand, S., & Mayya, Y. S. (2020). Size distribution of virus laden droplets from expiratory ejecta of infected subjects. Scientific Reports, 10(1), 1-9.

Appendix C. Supplementary Material for Chapter 6

C.1   Initial particle size distribution of MgSO₄ particles entering the plasma reactor expiration
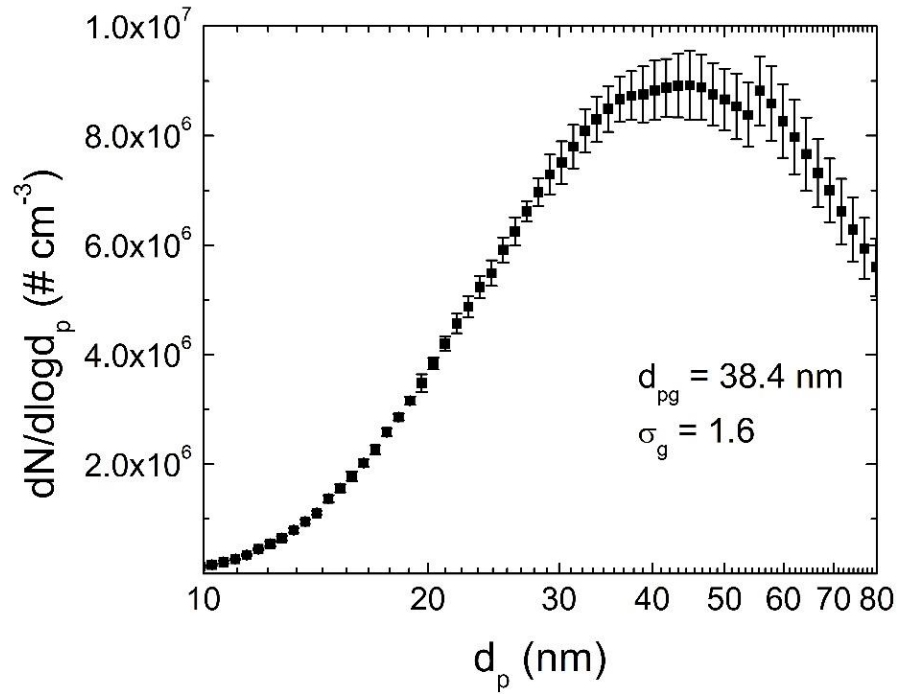

Figure C-1 Representative particle size distribution of neutral MgSO$_4$ particles entering the plasma reactor. The geometric mean diameter (d$_{pg}$) is 38.4 nm and the geometric standard deviation (σ$_g$) is 1.6.

C.2 Approach for the calculation of particle charge in plasma volume

Assuming that the emission processes (thermo- and photoionization) are relatively less significant compared to charging by electrons and ions, the charge of a particle (Q) as a function of space-time (τ) inside the plasma volume is given by [1]:

$$\frac{dQ}{d\tau} = \pi d_p^2 (J_i - J_e) \tag{C.1}$$

where J_e and J_i are the electron and ion flux densities to the particle surface, respectively, and can be described by the following equations [1]:

$$J_e = \frac{1}{4} n_e v_e \exp\left(\frac{e\phi_p}{kT_e}\right) \tag{C.2}$$

$$J_i = \sqrt{\frac{\pi}{2}} n_i v_i \left(\frac{\lambda_i}{d_p}\right) \left|\frac{e\phi_p}{kT_i}\right| \tag{C.3}$$

where v_e and v_i are the electron and ion velocities, respectively, T_i is the mean ion temperature, k is the Boltzmann's constant, $\lambda_i = k_B T_i / \sqrt{2}\sigma_i P$ is the mean free path of ions, and ϕ_p is the surface potential of the particle given by [1]:

$$\phi_p = \frac{eQ}{2\pi\varepsilon_0 d_p} \exp\left(-\frac{d_p}{2\lambda_D}\right) \tag{C.4}$$

and λ_D is the Debye length and is given by:

$$\lambda_D = \sqrt{\frac{\varepsilon_0 k T_e}{n_e e^2}} \qquad\qquad (C.5)$$

Qualitatively, the flux of electrons to the particle surface is higher than that of ions due to the higher mobility of electrons as compared to ions and thus particles very quickly (*i.e.*, at initial times after entering the plasma) charge negatively. As the negative charge increases, the electron flux to the particle surface decreases because of Coulombic repulsion, and concomitantly, the ion flux to the particle surface increases because of Coulombic attraction. Eventually, the electron and ion flux to the particle surface become equal and the particle obtains an equilibrium charge. The equilibrium charge can be obtained by solving for Q when $J_i = J_e$.

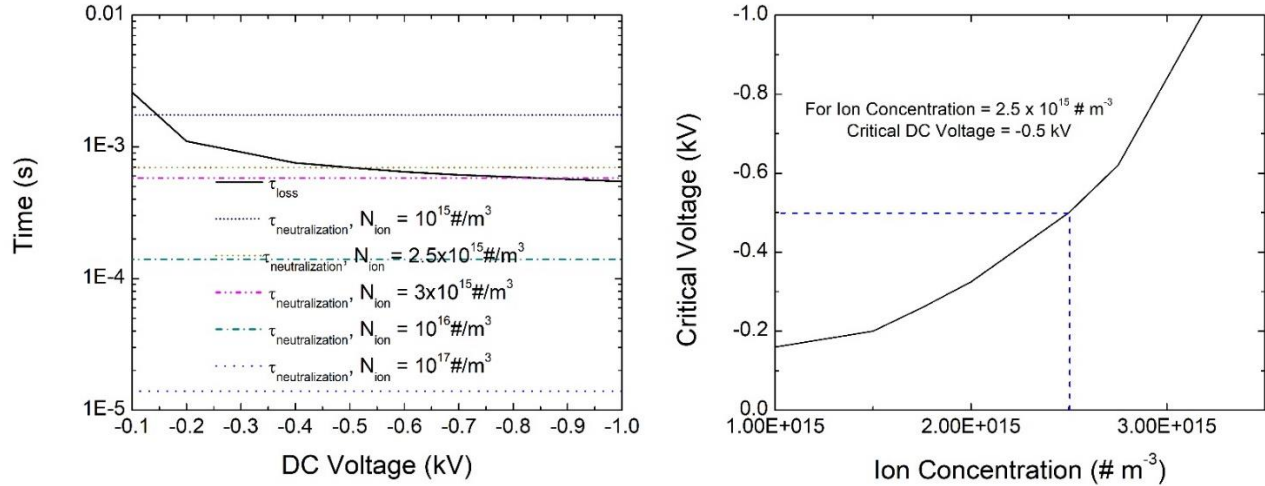## C.3 Approach for estimation of ion concentration in spatial afterglow

Figure C-2 Calculations of characteristic times for positive ions colliding with and being lost to the reactor walls and colliding with and neutralizing negatively-charged nanoparticles in the spatial afterglow as a function of the DC bias voltage at different afterglow ion densities. B. Critical DC voltage as a function of afterglow ion density.

The properties of the spatial afterglow of the flow-through, RF atmospheric-pressure plasma studied here are not completely known at this time. Our approach is to use the ion density in the plasma as a starting point, which based on quasineutrality is the same as the measured electron density of 10^{20} m^{-3} [2], and then assume lower values in the spatial afterglow. We repeated the calculations for several ion densities and the plots for neutralization time are shown in Figure C-2 A. We then compared the modeling results with experiments and find that for an ion density of 2.5 x 10^{15} m^{-3} in the spatial afterglow region, the neutralization time is greater than the loss time of Ar+ ions at the experimentally-measured critical DC voltage of -0.5 kV (Figure C-2 B). Based on this analysis, we have obtained an estimate of the ion density in the spatial afterglow, which agrees with the expected lower ion density as compared to the plasma and literature values for

the afterglow of an atmospheric-pressure plasma jet [3], and future work is needed to experimentally verify the exact value.

C.4   References

1. Uner, N. B., & Thimsen, E. (2018). Low temperature plasma as a means to transform nanoparticle atomic structure. *Plasma Sources Science and Technology*, *27*(7), 074005.

2. Sharma, G., Abuyazid, N., Dhawan, S., Kshirsagar, S., Sankaran, R. M., & Biswas, P. (2020). Characterization of particle charging in low-temperature, atmospheric-pressure, flow-through plasmas. *Journal of Physics D: Applied Physics*, *53*(24), 245204.

3. Xu, K. G., & Doyle, S. J. (2016). Measurement of atmospheric pressure microplasma jet with Langmuir probes. *Journal of Vacuum Science & Technology A: Vacuum, Surfaces, and Films*, *34*(5), 051301.

Appendix D. Computational Codes

A number of computer codes and simulation programs have been developed throughout the work presented in this dissertation. A subset of these codes and programs are available for download from the author's profile on GitHub: https://github.com/sukrant9

A list of the developed codes and programs, along with a brief description of each, is provided below.

1. **SprayDry:** A MATLAB code for predicting morphology of particle synthesized using spray drying. The code numerically solves droplet heating/evaporation and coupled particle/solute dynamics (valid for both dissolved and suspended species) inside the droplet. The code also solves for the shell growth and thickening process. For more details, also refer to Chapter 2.

2. **PEDOT_AVP:** A MATLAB code for predicting average chain length and conductivity of PEDOT particles synthesized using aerosol vapor polymerization. The code numerically solves droplet heating/evaporation, coupled gas phase transport, as well as particle/solute dynamics and polymerization reaction inside the droplet. For more details, also refer to Chapter 3.

3. **Denuder_Artifacts:** A MATLAB code for estimating the sampling artifacts during phase partitioning measurements of a multi-component aerosol using denuder. The code numerically solves coupled advection-evaporation equations for multi-component species in both gas and particulate phase. For more details, also refer to Chapter 4.

4. **CoV2_Transport:** A MATLAB code that solves for the spatiotemporal evolution of exhaled droplets in the vicinity of the infected person while accounting for droplet emissions, evaporation, advection and settling. For more details, also refer to Chapter 5.

Appendix E. Curriculum Vitae

Sukrant Dhawan

Department of Energy, Environmental and Chemical Engineering

Washington University in St. Louis, St. Louis, MO, 63130

Phone: +1-314-295-1500; Email: sukrant@wustl.edu

EDUCATION

Washington University in St. Louis   (2016-2021)

- Ph.D. Candidate in Energy, Environmental and Chemical Engineering

- Advisor: Dr. Pratim Biswas

- Thesis: "Particle and Droplet Dynamics in Aerosol Reactors and Environmental Systems"

- GPA: 4.0/4.0

Princeton University, USA   (2019)

- CEFRC Combustion Summer School

Indian Institute of Technology, Bombay   (2012-2016)

- Bachelor of Technology with honors in Chemical Engineering

- Minor in Electrical Engineering

- GPA: 8.02/10

SCHOLARSHIPS

- McDonnell International Academy Scholar   (2016-2021)

- Bayer Corporate Fellow   (2017-2021)

RESEARCH EXPERIENCE

Graduate Research Assistant

Supervisors: Professors Pratim Biswas, Richard Axelbaum, Rajan Chakrabarty, Jian Wang and

Julio D'Arcy

- *Particle and Droplet Dynamics in Aerosol Reactors and Environmental Systems*

INDUSTRIAL TRAINING/ INTERNSHIPS

Reliance Industries Ltd., Patalganga   (May-July 2015)

- Worked to understand the basic operations and processes of Purified Terepthalic Acid (PTA)

  plant.

- Identified and tackled the problem of drainage of liq. hydrocarbons owing to the inefficiency

  of pumps in the LPG Recovery Section of Para-Xylene Plant.

Essar Steel Ltd., Hazira   (May-June 2014)

- Worked on HVAC engineering project for the installation of dust extraction system in Sinter

  Plant.

- Identified the critical positions in the plant which required fume hoods and calculated the

  pump and power requirements for the operation of suggested dust extraction system.

TEACHING EXPERIENCE

- Served as Teaching Assistant for 3 graduate courses: Aerosol Science and Technology,

  Advanced Topics in Aerosol Science & Technology, and Transport Phenomenon in EECE.

  (2017-2020)

- Managed and taught recitation sessions and graded exams/projects. Also, delivered lecture on climate effects of aerosols in Aerosol Science and Technology graduate course

PROFESSIONAL AND ACADEMIC SERVICE

- Served as Environmental, Health and Safety Coordinator of the laboratory responsible for internal training, hazardous waste management, and ensuring rule abidance. (2017-2020)
- Served as Conference Session Co-Chair, "Instrumentation and Methods X - Samplers and Sensors" AAAR 36th Annual Conference, 2017
- Served as Student Assistant and ensured the smooth functioning of workshops at AAAR 36th Annual Conference, 2017
- Served as a Reviewer for the Journal of Aerosol Science and Aerosol Science and Technology
- Represented Washington University in McDonnell Academy International Symposiums held at Beijing, China   (2018)

PUBLICATIONS

1. **Dhawan, S.,** & Biswas, P. (2019). Sampling artifacts in denuders during phase partitioning measurements of semi-volatile organic compounds. *Aerosol Science and Technology*, *53*(1), 73-85.
2. Sharma, G., **Dhawan, S.,** Reed, N., Chakrabarty, R., & Biswas, P. (2019). Collisional growth rate and correction factor for TiO2 nanoparticles at high temperatures in free molecular regime. *Journal of Aerosol Science*, *127*, 27-37.

3. Sharma, G.*, Abuyazid, N.*, **Dhawan, S.***, Kshirsagar, S., Sankaran, R. M., & Biswas, P. (2020). Characterization of particle charging in low-temperature, atmospheric-pressure, flow-through plasmas. *Journal of Physics D: Applied Physics*, *53*(24), 245204. (*Equal Contribution)

4. **Dhawan, S.,** Vidwans, A., Sharma, G., Abuyazid, N. H., Mohan Sankaran, R., & Biswas, P. (2020). Enhancing charging and capture efficiency of aerosol nanoparticles using an atmospheric-pressure, flow-through RF plasma with a downstream DC bias. *Aerosol Science and Technology*, *54*(11), 1249-1254.

5. Zhang, H., Sharma, G., **Dhawan, S.,** Dhanraj, D., Li, Z., & Biswas, P. (2020). Comparison of discrete, discrete-sectional, modal and moment models for aerosol dynamics simulations. *Aerosol Science and Technology*, *54*(7), 739-760.

6. Biswas, P., & **Dhawan, S.** (2020). Evaporation of Emitted Droplets Are an Important Factor Affecting the Lifetime of the Airborne Coronavirus. *Preprints.org*

7. **Dhawan, S.,** & Biswas, P. (2021). Aerosol Dynamics Model for Estimating the Risk from Short-Range Airborne Transmission and Inhalation of Expiratory Droplets of SARS-CoV-2. *Environmental Science & Technology*.

8. **Dhawan, S.,** & Biswas, P. A numerical model to predict morphology of nanoparticles synthesized using spray pyrolysis. Submitted to *Drying Technology*.

9. Okonkwo, O., **Dhawan, S.,** & Biswas, P. Controlled Synthesis of Alumina in Spray Flame Aerosol Reactor. Submitted to *Journal of the American Ceramic Society.*

10. **Dhawan, S.,** Vidwans, A. & Biswas, P. Modeling PEDOT formation using aerosol vapor polymerization to predict synthesized particle conductivity. Under Preparation.

11. **Dhawan, S.,** Vidwans, A. & Biswas, P. Selective positive charging of aerosols using afterglow of atmospheric pressure, flow-through RF plasma. Under Preparation.

SELECTED PRESENTATIONS

1. **Sukrant Dhawan** and Pratim Biswas. Evaluation of Sampling Artifacts in Phase Partitioning Measurements of Semi-Volatile Organic Compounds in Denuders, *Platform Presentation, 36ᵗʰ Annual American Association of Aerosol Research Conference, 2017*

2. **Sukrant Dhawan,** Girish Sharma and Pratim Biswas. Investigation of the Role of Charging on the Particle Growth during Combustion in Spray Flame Aerosol Reactor, *Poster Presentation, 10ᵗʰ International Aerosol Conference, 2018*

3. Girish Sharma, **Sukrant Dhawan**, Zhichao Li, David I. A. Dhanraj, and Pratim Biswas. Comparison of Different Aerosol Dynamics Models Based on Accuracy and Computational Time, *Poster Presentation, 10ᵗʰ International Aerosol Conference, 2018*

4. **Sukrant Dhawan** and Pratim Biswas. Numerical model to predict the morphology of particle synthesized via spray pyrolysis, *Platform Presentation, 37ᵗʰ Annual American Association of Aerosol Research Conference, 2019*

5. Girish Sharma, Nabiel Abuyazid, **Sukrant Dhawan**, R. Mohan Sankaran, Pratim Biswas. Charge characterization of nanoparticles exiting nonthermal atmospheric pressure plasmas. *Poster Presentation, American Association of Aerosol Research, 37th Annual Conference, 2019*

6. **Sukrant Dhawan,** Huang Zhang, Renhui Ruan, and Pratim Biswas. Multiscale Models for Aerosol Transmission of Highly Infectious SARS-CoV-2 Novel Coronavirus., *Platform Presentation, 38th Annual American Association of Aerosol Research Conference, 2020*

7. **Sukrant Dhawan**, Abhay Vidwans, Nabiel Abuyazid, R. Mohan Sankaran, Pratim Biswas The Addition of a Downstream DC Bias to an Atmospheric-pressure, Flow-through RF Plasma for Enhanced Charging of Aerosol Nanoparticles. *Platform Presentation, 38th Annual American Association of Aerosol Research Conference, 2020*

8. Onochie Okonkwo, **Sukrant Dhawan**, Pratim Biswas Controlled Synthesis of Alumina in a Spray Flame Aerosol Reactor. *Platform Presentation, 38th Annual American Association of Aerosol Research Conference, 2020*